

**Cecilia Levy**

Light Propagation and Reflection off Teflon  
in Liquid Xenon Detectors for the  
XENON100 and XENON1T Dark Matter Experiments

**-2014-**



Experimentelle Physik

Dissertationsthema

Light Propagation and Reflection off Teflon  
in Liquid Xenon Detectors for the  
XENON100 and XENON1T Dark Matter Experiments

Inaugural-Dissertation

zur Erlangung des Doktorgrades der Naturwissenschaften  
im Fachbereich Physik  
der Mathematisch-Naturwissenschaftlichen Fakultät  
der Westfälischen Wilhelms-Universität Münster

vorgelegt von

Cecilia Levy

aus Besançon, Frankreich

-2014-

Dekan:	Prof. Dr. M. Donath
Erster Gutachter:	Prof. Dr. C. Weinheimer
Zweiter Gutachter:	Prof. Dr. J.P. Wessels
Tag der mündlichen Prüfung:	27/05/2014
Tag der Promotion:	27/05/2014





# ABSTRACT

Today's universe is thought to be composed of about 25% of a new, non-baryonic and weakly interacting type of matter, dark matter. Many theories predict the existence of dark matter, amongst them, supersymmetry (SUSY). The preferred dark matter candidate from SUSY is the stable neutralino, a weakly interacting massive particle (WIMP).

To this day, many experiments have set to try and detect dark matter, directly or indirectly. Amongst these experiments, the XENON program has led the field for many years by looking for interactions between a WIMP and a target nucleus in a dual phase liquid xenon time projection chamber (TPC) as a detector. The current phase of the experiment, XENON100, which used 100 kg of target material, has now reached its sensitivity goal and the next phase, the much bigger XENON1T experiment which will contain over 2 tons liquid xenon, is under construction at the LNGS underground laboratory in Italy.

In this work, an essential part of the analysis done for the XENON100 results is presented. These light yield studies led to a 3D correction map of the light yield in the XENON100 detector and to a value for the light yield at 122 keV between  $2.24 \pm 0.009$  and  $2.31 \pm 0.062$  pe/keV which was used as a crucial cross check for the final value used in the XENON100 data analysis.

In addition, in order to do R&D for XENON1T, a Monte Carlo simulation of a small TPC built in Muenster has been developed, and preliminary simulations on light yield and calibrations have been performed. This simulation package can now be used by anyone who wishes to study in depth detector response.

In a last part, measurements were done using a reflectivity setup to measure the reflectivity off of teflon of VUV light and investigate the impact of the teflon thickness on the reflectivity. An average reflectivity of  $73 \pm 7\%$  was found, while no major dependence was found between teflon thickness and reflectivity for teflon thicknesses superior to 3 mm.

Finally, the previous setup was adapted to be usable in liquid xenon and measure the reflectivity off of teflon in liquid xenon, which was found not to behave like the reflectivity in vacuum but to follow a model much more dependent on incident angles giving reflectivities ranging from 20% to 100% for low and high incident angles respectively.



*To my husband...*

*"Physics isn't the most important thing. Love is."*

*Richard Feynman*

## ACKNOWLEDGMENTS

First and foremost, I would like to thank my advisor, Prof. Weinheimer, for allowing me to pursue a PhD, giving me the opportunity to work in the project I wanted and sharing (at least part of!) his deep knowledge and understanding of physics with me. And also, for forcing me to not just be satisfied with superficial and inexact explanations but dig deeper to understand the basic underlying physics concepts in my work.

Second I would like to thank the Muenster XENON group, Ethan, Stephan, Alex, Michael, Sergej and Christian H., who have all been super nice and helpful to me during these years. I also would like to thank the secretaries Mrs Erdmann and Mayer, for their patience in helping me deal with the many administrative problems I've encountered along the way!

I also would like to thank my family, my mother and Taty, my godmother and Alice who have all taken so much interest in what I do and have encouraged me and helped me to get this far in life, ever since I was a baby.

My friends, who have been a moral support even from far away and even if we don't talk often are always there for me. A special mention goes to my oldest friend, Agnes, who has spent many hours on the phone with me, listening to my endless complaining and frustration and allowed me to vent and keep my sanity while always offering many sound advices which have helped me many times!

Last but most important, I would like to thank my husband, who has lived through this with me, instant by instant, ever present and ever loving, no matter what. And I just would like to thank him for simply being the wonderful man he is.

# CONTENTS

<i>Abstract</i> . . . . .	vi
<i>Dedication</i> . . . . .	viii
<i>Acknowledgments</i> . . . . .	x
<i>Table of Contents</i> . . . . .	xi
<i>List of Figures</i> . . . . .	xvi
<i>List of Tables</i> . . . . .	xxv
<b>Chapter 1. Introduction</b> . . . . .	1
<b>Chapter 2. Dark Matter: Theory and Search</b> . . . . .	5
2.1 First Indications for the Existence of Dark Matter . . . . .	5
2.1.1 Galactic Scale: Rotation Curves . . . . .	5
2.1.2 Galaxy Cluster Scale: Gravitational Lensing . . . . .	7
2.2 Dark Matter Origins . . . . .	11
2.2.1 The Cosmological Standard Model: $\Lambda$ CDM . . . . .	11
2.2.2 Large Scale Structure Formation . . . . .	13
2.3 Dark Matter Density . . . . .	14
2.3.1 The Cosmic Microwave Background . . . . .	15
2.3.2 Big Bang Nucleosynthesis . . . . .	23
2.3.3 Supernova Studies . . . . .	26
2.4 Where to look for Dark Matter? . . . . .	27
2.5 Dark Matter Theory Beyond the Standard Model of Particle Physics . . . . .	28
2.5.1 Properties of Dark Matter . . . . .	28
2.5.2 The WIMP Miracle . . . . .	28
2.5.3 Supersymmetry . . . . .	30

2.5.4	Other Extensions to the Standard Model And Non-WIMP Dark Matter Candidates . . . . .	35
2.6	Experimental Detection . . . . .	37
2.6.1	Indirect Searches . . . . .	37
2.6.2	Direct Searches . . . . .	41
2.6.3	The DAMA/LIBRA Controversy . . . . .	49
2.6.4	Dark Matter in Colliders . . . . .	49
2.7	Summary . . . . .	51
<b>Chapter 3. The XENON100 Experiment . . . . .</b>		<b>53</b>
3.1	The XENON Program . . . . .	55
3.1.1	XENON10 . . . . .	55
3.1.2	XENON100 . . . . .	55
3.1.3	XENON1T . . . . .	56
3.1.4	XENONnT . . . . .	56
3.1.5	Dual Phase Xenon TPC . . . . .	56
3.1.6	Choice of Xenon as Liquid Scintillator . . . . .	58
3.2	Principle of Ionization and Scintillation . . . . .	61
3.2.1	The Scintillation Process . . . . .	61
3.2.2	Ionization Yield . . . . .	62
3.2.3	Scintillation Yield . . . . .	63
3.3	Technical Description of the XENON100 Experiment . . . . .	64
3.3.1	The Detector . . . . .	64
3.3.2	Shielding . . . . .	65
3.3.3	Cooling System . . . . .	67
3.3.4	Recirculation System . . . . .	68
3.3.5	Distillation System . . . . .	69
3.3.6	PMTs . . . . .	72
3.3.7	Data Acquisition . . . . .	74
3.4	Calibration of the Detector . . . . .	77
3.4.1	PMT Calibration . . . . .	77
3.4.2	Electron Drift Lifetime . . . . .	78

3.4.3	Energy Calibration . . . . .	79
3.5	Detector Response to Backgrounds and Particle Identification . . . . .	82
3.5.1	Neutrons . . . . .	82
3.5.2	Gammas . . . . .	83
3.5.3	Particle Identification . . . . .	84
3.6	Data Analysis . . . . .	87
3.6.1	Position Correction . . . . .	87
3.6.2	Data Quality Cuts . . . . .	88
3.6.3	Profile Likelihood Analysis . . . . .	88
3.7	Dark Matter Search Results . . . . .	90
<b>Chapter 4. Light Yield Studies for the XENON100 Experiment . . . . .</b>		<b>93</b>
4.1	Introduction to Light Yield . . . . .	93
4.2	Measuring the Light Collection Efficiency and Light Yield . . . . .	95
4.2.1	Choosing a Calibration Source . . . . .	95
4.2.2	Gamma Interactions . . . . .	96
4.2.3	S1 Spectrum . . . . .	98
4.3	3D $r\theta z$ Maps of the Light Yield . . . . .	100
4.4	Evolution of the LY over Time . . . . .	103
4.5	Quantifying the Asymmetry . . . . .	103
4.6	Cause of the Asymmetry . . . . .	105
4.7	3D Correction Function . . . . .	106
4.7.1	Method . . . . .	106
4.7.2	Quality Checks . . . . .	108
4.8	Applying the Correction Function to the Data . . . . .	111
4.8.1	$^{137}\text{Cs}$ Data . . . . .	112
4.8.2	40 keV Lines from AmBe Data . . . . .	115
4.8.3	Xenon Activated Lines - 164 keV . . . . .	117
4.8.4	Comparison of the Effect of the Correction Function on All Three Types of Data	120
4.9	Light Yield at 122keV . . . . .	123
4.9.1	Light Yield at 662, 40 and 164 keV . . . . .	123
4.9.2	Light Yield at 80 keV . . . . .	124

4.9.3	Extracting the Light Yield at 122 keV . . . . .	124
4.10	Conclusion . . . . .	129
<b>Chapter 5. Monte-Carlo Simulations of the Muenster TPC . . . . .</b>		<b>131</b>
5.1	The Muenster TPC . . . . .	131
5.2	A GEANT4 Simulation of the Muenster TPC . . . . .	132
5.2.1	The Detector Geometry . . . . .	133
5.2.2	Particle Tracking and Basic Detector Response . . . . .	134
5.3	Scintillation Light Propagation . . . . .	136
5.3.1	2D Light Yield Map . . . . .	136
5.3.2	3D Maps of the Light Yield . . . . .	137
5.3.3	Influence of the Absorption Length in Xenon on the Light Yield . . . . .	139
5.3.4	Influence of the PTFE reflectivity on the Light Yield . . . . .	139
5.4	Gamma Simulations . . . . .	140
5.5	Conclusion . . . . .	144
<b>Chapter 6. Teflon Reflectivity Studies in Vacuum . . . . .</b>		<b>147</b>
6.1	Introduction and Motivation . . . . .	147
6.2	Basic Theory of Reflectivity . . . . .	148
6.3	The Setup . . . . .	149
6.3.1	The Light Assembly . . . . .	150
6.3.2	The Main Vacuum Chamber . . . . .	152
6.4	XENON100 Teflon Sample Cut in Steps . . . . .	155
6.4.1	The Sample . . . . .	156
6.4.2	Calibration . . . . .	156
6.4.3	Influence of the thickness on the reflectivity . . . . .	162
6.4.4	Full Transparency of the teflon . . . . .	169
6.4.5	Reflectivity of the teflon . . . . .	169
6.4.6	Conclusion . . . . .	182
<b>Chapter 7. Teflon Reflectivity Studies in Liquid Xenon . . . . .</b>		<b>185</b>
7.1	Introduction and Motivation . . . . .	185
7.2	The Setup in Liquid Xenon . . . . .	185

---

7.2.1	The Tube in Liquid Xenon . . . . .	187
7.2.2	Movement and Degrees of Freedom . . . . .	192
7.2.3	Data Acquisition . . . . .	197
7.3	Measurements and Analysis . . . . .	198
7.3.1	Calibration of the PMT . . . . .	198
7.3.2	X Calibration . . . . .	199
7.3.3	Y Calibration . . . . .	200
7.3.4	Z Calibration . . . . .	201
7.3.5	Vacuum Measurements . . . . .	202
7.3.6	Gas Xenon Measurements . . . . .	210
7.3.7	Liquid Xenon Measurements . . . . .	213
7.4	Conclusion . . . . .	225
<b>Chapter 8. CONCLUSION And Outlook . . . . .</b>		<b>229</b>
<b>Appendix . . . . .</b>		<b>233</b>
<b>Bibliography . . . . .</b>		<b>239</b>

# LIST OF FIGURES

2.1	Rotation curve of galaxy NGC 3198 from [1]. . . . .	6
2.2	The principle of gravitational lensing. . . . .	8
2.3	Gravitational rings in galaxies from the BOSS survey [2]. . . . .	9
2.4	Weak gravitational lensing effect in the Abell2218 galaxy cluster. The images of the background galaxies are distorted and stretched around the cluster’s center. Credit: NASA, ESA, Richard Ellis (Caltech) and Jean-Paul Kneib (Observatoire Midi-Pyrenees, France) . . . . .	10
2.5	Map of the gravitational potential of the Bullet Cluster 1E0657-558 from [3]. . . . .	10
2.6	The famous pie of today’s universe. Credit: NASA / WMAP Science Team. . . . .	12
2.7	Representation of the top down (left) and bottom up (right) scenarios for the formation of large structure of the universe [4]. . . . .	13
2.8	Dark matter power spectra for different amounts of hot dark matter [5]. . . . .	15
2.9	The temperature fluctuations of the Cosmic Microwave Background as observed by the WMAP satellite [6] . . . . .	18
2.10	The angular power spectrum of the CMB [6] . . . . .	20
2.11	Values for the $\Lambda$ CDM parameters from WMAP [6] . . . . .	22
2.12	Mass fraction of ${}^4\text{He}$ and relative abundance of ${}^3\text{He}$ , ${}^2\text{H}$ , and ${}^7\text{Li}$ as a function of baryon density, compared to the WMAP results [7]. . . . .	26
2.13	Combined results of clusters of galaxies, CMB and supernovae studies [8]. . . . .	27
2.14	Evolution of the WIMP number density $Y$ in the early universe from $\Lambda$ CDM model [9]. . . . .	29
2.15	Feynman Diagrams from WIMP annihilation into two photons. a) fermion sfermion loops, b) charged Higgs chargino loops, c) chargino W-boson loops [10]. . . . .	38
2.16	AMS-02 positron fraction compared with other satellite data and theoretical model [11]. . . . .	41
2.17	Feynmann diagram for spin-dependent interactions from [12]. . . . .	43
2.18	Feynmann diagram for spin-independent interactions from [12]. . . . .	44
2.19	The DAMA/LIBRA modulation signal from [13]. . . . .	49
2.20	Results on the missing transverse energy from the ATLAS experiment. [14]. . . . .	50
3.1	Location of the XENON100 experiment at LNGS. . . . .	53
3.2	Various underground laboratories around the world . . . . .	54

3.3	The XENON10 Detector . . . . .	55
3.4	The XENON100 Detector [15] . . . . .	56
3.5	The XENON1T Detector . . . . .	57
3.6	Principle of a dual phase xenon time projection chamber . . . . .	57
3.7	Example of a PMT hit pattern for an S2 signal. . . . .	58
3.8	Differential WIMP spin independent scattering rate for several targets with $m_\chi = 100\text{GeV}$ and $\sigma_p = 10^{-44}\text{cm}^2$ [16] . . . . .	60
3.9	Principle of Scintillation for LXe . . . . .	61
3.10	Ionization yield from nuclear recoils at different electric fields [17] . . . . .	63
3.11	Technical drawing of the XENON100 TPC. . . . .	64
3.12	The shielding structure of the XENON100 experiment. The copper, polyethylene and two lead layers are clearly visible while the water boxes are starting to show on top. . . . .	66
3.13	Drawing of the cooling system of the XENON100 experiment [15] . . . . .	67
3.14	Drawing of the gas recirculation system of the XENON100 experiment [15] . . . . .	69
3.15	Picture of the bottle rack while recuperation is ongoing. The bottles are frozen with LN2. . . . .	70
3.16	Schematical drawing of the krypton distillation column [15]. . . . .	71
3.17	Packing material of the inside of the distillation column. . . . .	71
3.18	Schematics of the principle of a PMT . . . . .	72
3.19	The top PMT array of the XENON100 TPC. . . . .	73
3.20	The bottom PMT array of the XENON100 TPC. . . . .	73
3.21	Quantum efficiency of the top, bottom and veto PMTs used in XENON100 [15] . . . . .	74
3.22	Sensitivity to blue light (SKb) versus quantum efficiency (QE) for the HAMAMATSU R8520 PMTs used in XENON100. . . . .	75
3.23	Schematics of the data acquisition system of XENON100 [15]. The black circles indicate a false input. . . . .	76
3.24	Waveform encoded with zero length [18]. . . . .	77
3.25	Typical gain calibration spectrum [15]. . . . .	78
3.26	Calculation of the electron lifetime from the S2 signal of a $^{137}\text{Cs}$ source. [15]. . . . .	79
3.27	Relative scintillation efficiency measured for different experiments [19] . . . . .	81
3.28	Attenuation coefficient in xenon for the photoelectric effect, Compton scattering and pair production [20]. . . . .	83

3.29	Electronic (top) and nuclear (bottom) recoil bands from $^{60}\text{Co}$ and $^{232}\text{Th}$ (top) and $^{241}\text{AmBe}$ (bottom) calibration data, respectively, using the discrimination parameter $\log_{10}(S2/S1)$ as a function of nuclear recoil equivalent energy (keV <sub>nr</sub> ) according to equation 3.5. Colored lines correspond to the median of both bands, blue for electronic recoils and red for nuclear recoils. The vertical lines correspond to the WIMP search window while the long dashed line is a software threshold of 300 pe. [21]. . . . .	85
3.30	WIMP region of interest superimposed with nuclear recoil and electronic recoil calibration data. The top dotted green line corresponds to 99.75% ER rejection, the bottom top dotted green light corresponds to the 97% NR quantile. The left dashed blue line and the right green dotted line correspond to the energy window for WIMP recoil energy. The small blue dashed line in the bottom left corner shows the negligible impact of the $S2 > 150$ pe threshold cut. . . . .	86
3.31	Stopping power for alpha particles in $^{131}\text{Xe}$ [20]. . . . .	87
3.32	Profile likelihood analysis. The blue dots are the electronic recoils from a $^{60}\text{Co}$ calibration source. The red dots are the nuclear recoils from an $^{241}\text{AmBe}$ calibration source. The thin lines represent the j bands of the analysis, while the two thick lines are the median of the nuclear recoil and electronic recoil bands. The dashed vertical lines represent the relevant S1 parameter range [22]. . . . .	89
3.33	The two events from the XENON100 225 live days results. Right: as seen in the WIMP ROI with the calibration bands. Left: as seen on the physical detector . . . .	90
3.34	Results on spin-independent scattering from 225 live days of data by XENON100 [23] . . . .	91
4.1	The 2D light collection efficiency map for the XENON100 detector [15]. . . . .	94
4.2	Coarse LCE(x,y,z) map for the bottom part of the TPC. The black circle represents the edge of TPC. . . . .	95
4.3	Spectra of the S1 light (pe) in the detector from a $^{137}\text{Cs}$ calibration for initial scatters opposite the source position (top left), in the center of the TPC (top right) and next to the source position (bottom). . . . .	99
4.4	Example of S1 spectra with associated fits used to calculate and make the light yield map. .	101
4.5	Light yield maps for the 9 z slabs of the TPC from top to bottom (z ranges from 0 to -303 mm) . . . . .	102
4.6	Ratio of the light yield maps of run 10 over those of run 8 from top to bottom of the TPC. .	103

4.7	Light yield as a function of the azimuthal angle $\theta$ for different vertical slabs $z$ of the TPC and radial rings $r$ .	104
4.8	Reduced $\chi^2$ for each $z,r$ ring of the TPC	105
4.9	Superposition of the light map with the PMT array. PMTs marked with a cross are broken.	106
4.10	Intuitive description of the correction function for one $z$ slab.	107
4.11	Check of the validity of the correction function for a random test function.	109
4.12	Comparison of the old (run 8) 2D correction function using AmBe (left) with the new 3D correction function using $^{137}\text{Cs}$ . The 3D function has been brought back to 2D (right). The ordering of the curves from top to bottom corresponds to positions in the detector ( $z$ slabs) from bottom ( $z=-303$ mm) to top ( $z=0$ mm).	110
4.13	Behavior of the correction factor. Top Left: at the top of the TPC. Top Right: at the bottom of the TPC. Bottom Left: in the center region of the TPC. Bottom Right: at the edges of the TPC.	111
4.14	Behavior of the 3D correction factor as a function of $\theta$ . Left: at the top of the TPC. Right: at the bottom of the TPC.	112
4.15	Corrected light yield maps from top ( $z=0$ mm) to bottom ( $z=-303$ mm) of the TPC. Left: 2D correction. Right: 3D correction	113
4.16	Corrected light yield as a function of $\theta$ for the bottom of the TPC.	114
4.17	Quality factor of the light yield for no correction, the 2D correction function and the 3D correction function. Left: Overall TPC. Right: Bottom of the TPC.	115
4.18	Effect of the correction function on the $^{137}\text{Cs}$ spectra for random datasets, for the overall detector (left) and the bottom part of the TPC (right)	115
4.19	Spectra from AmBe. Left: the whole spectrum. Right: zoom on the region of interest corresponding to the 40 keV line	116
4.20	S1 distribution and fit for the 40 keV line from AmBe data	117
4.21	Corrected light yield maps using the 2D (left) and 3D (right) correction function for top and bottom of the detector for the 40 keV line from AmBe.	118
4.22	Quality factor for the 2D and 3D correction applied to the same AmBe data at the top of the detector (left) and the bottom of the detector (right)	118
4.23	Parameter space and line selection for the 164 keV activated line from AmBe calibration	119
4.24	S1 distribution and fit for the 164 keV xenon activated line	120

4.25	Corrected light yield maps using the 2D (left) and 3D (right) correction function for top and bottom of the detector for the 164 keV activated xenon data . . . . .	121
4.26	Quality factor for the 2D and 3D correction applied to the same 164 keV line from AmBe data at the top of the detector (left) and the bottom of the detector (right) . . . . .	121
4.27	Light yield residuals between 3D and 2D correction for $^{137}\text{Cs}$ data (left), 40 keV AmBe data (middle) and 164 keV AmBe Data (right) . . . . .	122
4.28	Comparison between the RMS of the 2D and 3D corrections applied to all data types. . . . .	122
4.29	Parameter space and line selection for the 80 keV gamma emission from AmBe . . . . .	124
4.30	Spectrum corresponding to the 80 keV line from AmBe . . . . .	125
4.31	NEST model for the scintillation yield in liquid xenon [24] . . . . .	126
4.32	Field quenching at 662 keV [25] (left), and at 9.4, 32 and 122 keV [26] (right) . . . . .	126
4.33	Field quenching for a 530V/cm electric field . . . . .	127
4.34	The NEST model at 530V/cm in liquid xenon found by applying the correction of figure 4.33 to the NEST model of figure 4.31 . . . . .	127
4.35	Fit of the XENON100 data using the NEST model with an error analysis based on the actual calculated errors . . . . .	128
4.36	Fit of the XENON100 data using the NEST model with an error analysis based on the reduced $\chi^2$ . . . . .	129
5.1	Sectional view of the technical drawing of the TPC encased in the inner cryostat.[27] . . . . .	132
5.2	Mechanical drawing of the outer vacuum vessel with the TPC encased inside and the cooling tower located outside.[27] . . . . .	133
5.3	The simulated TPC and its cryostat with the major components visible, the pmts, copper rings, meshes and teflon holders.(left) Side view. (right) Perspective view. . . . .	134
5.4	Visualization of the final simulated detector geometry . . . . .	135
5.5	Example of the propagation of a non-interacting particle through the whole detector. . . . .	136
5.6	Light collection efficiency in the Muenster TPC. . . . .	137
5.7	Light yield maps in the muenster TPC from top (z=0 mm) to bottom (z=-169 mm) of the TPC . . . . .	138
5.8	Absorption length influence on the average light yield in the detector . . . . .	139
5.9	Influence of the reflectivity on the light yield . . . . .	140
5.10	Decay scheme of $^{137}\text{Cs}$ [28]. . . . .	141
5.11	Decay scheme $^{57}\text{Co}$ [28]. . . . .	141

5.12	Decay scheme of $^{60}\text{Co}$ [28]. . . . .	141
5.13	$^{137}\text{Cs}$ spectrum from simulation. . . . .	142
5.14	$^{57}\text{Co}$ spectrum from simulation. . . . .	143
5.15	$^{60}\text{Co}$ spectrum from simulation. . . . .	143
5.16	Events (first scatter) position in the Muenster TPC for three different gamma sources. Top left: $^{137}\text{Cs}$ . Top right: $^{57}\text{Co}$ . Bottom: $^{60}\text{Co}$ . . . . .	144
6.1	Schematic of specular (blue) and diffuse (red) reflection processes. . . . .	149
6.2	Schematic view of the reflectivity setup under vacuum. . . . .	150
6.3	The light assembly of the reflectivity setup. . . . .	150
6.4	Spectrum emitted by the McPherson model 632 deuterium lamp. Courtesy of McPherson. . . . .	151
6.5	Principle of diffraction through two slits showing the relevant parameters of equation 6.3 [29] . . . . .	152
6.6	The inside of the McPherson model 218 monochromator with the main features and the light path indicated by the dashed lines. . . . .	152
6.7	The inside of the vacuum chamber. Left: once the top flange has been removed, the outer cold shield is visible. Middle: When the lid of the outer cold shield is removed, the anodized inner cold shield remains. Right: After removing the lid of the inner cold shield, the rotatable PMT in its copper case and the collimator are clearly visible. . . . .	153
6.8	The central bottom feedthrough allowing rotational movement of the PMT around the chamber. . . . .	154
6.9	The central top feedthrough allowing rotational and translational movement of the teflon in the vacuum chamber. . . . .	154
6.10	Diagram showing the inside of the main vacuum chamber of the reflectivity setup at Muenster university. . . . .	155
6.11	Orientation of the setup . . . . .	155
6.12	Photo of the XENON100 teflon sample cut in steps which is used in the reflectivity setup . . . . .	156
6.13	Setup position to perform the beam spot measurement. . . . .	157
6.14	Beam spot calibration . . . . .	157
6.15	Setup for the rough x calibration. . . . .	158
6.16	Rough X calibration . . . . .	158
6.17	Angle Alignment . . . . .	158
6.18	Z Calibration . . . . .	159
6.19	X Calibration . . . . .	160

6.20	Verification of the z calibration using the x calibration. Note that in reality the teflon moves, not the beam. Due to the diameter of the beam, depending on where the beam shines on the teflon, the intensity read by the PMT will differ. . . . .	161
6.21	Definition of the incident angle $\theta_i$ . . . . .	162
6.22	Setup position to perform the Y Calibration . . . . .	162
6.23	Y Calibration . . . . .	163
6.24	Raw data from the teflon positioned at $80^\circ$ incident angle over the entire height of the teflon. Linear scale. . . . .	164
6.25	Raw data from the teflon positioned at $80^\circ$ incident angle over the entire height of the teflon. Logarithmic scale. . . . .	164
6.26	Rate of the specular component as a function of the vertical position of the sample for an $80^\circ$ incident angle. . . . .	165
6.27	Zoom of figure 6.26 . . . . .	166
6.28	Rate versus thickness of the sample for $80^\circ$ incident angle. . . . .	167
6.29	Sample position and specular reflection for $70^\circ$ incident angle. . . . .	168
6.30	Rate versus thickness of the sample for a $70^\circ$ incident angle . . . . .	168
6.31	Diagram of the setup for full transparency measurements . . . . .	170
6.32	Full transparency . . . . .	170
6.33	Diagram showing the important scattering angles in the reflectivity process. $\mathbf{r}_i$ represents the incident beam, $\mathbf{r}$ the direction of the reflected beam, $\mathbf{r}_s$ the direction of perfect specular reflection and $\alpha$ the spread angle between $\mathbf{r}_s$ and $\mathbf{r}$ . . . . .	171
6.34	Diagram showing the three observable angles in the laboratory coordinates . . . . .	173
6.35	Raw data - Beam incident on the second (5 mm) teflon step. . . . .	176
6.36	Fits on the background subtracted data - Beam incident on the 5 mm thick teflon step. From left to right, top to bottom: normalization, $\theta_i=80, 70, 60, 50, 45, 40, 30^\circ$ . . . . .	177
6.37	Reflectivity model on unpolished molded teflon at 175 nm [30]. . . . .	178
6.38	Total, specular and diffuse reflectivities of the 9.5 mm thick teflon. . . . .	178
6.39	Total, specular and diffuse reflectivities of the 5 mm thick teflon. . . . .	179
6.40	Total, specular and diffuse reflectivities of the 3 mm thick teflon. . . . .	179
6.41	Total, specular and diffuse reflectivities of the 2 mm thick teflon. . . . .	179
6.42	Total, specular and diffuse reflectivities of the 1 mm thick teflon. . . . .	180
6.43	Average reflectivity of the Xe100 step sample as a function of the thickness of the sample. .	180

---

6.44	Comparison of the output of both analysis methods to the data . . . . .	181
7.1	Principle of the reflectivity setup . . . . .	186
7.2	Inside the main chamber . . . . .	187
7.3	Light transmission for synthetic quartz glass made with UV-grade fused silica [31] . . . . .	188
7.4	Effect of the quartz tube on the incident light . . . . .	189
7.5	The sealing of the quartz tube. Left: the top flange with the xenon supply and return lines welded to it. Middle: the bottom flange, with the holes to screw the teflon holder in place. Right: the final assembly with the tube sealed and the teflon and teflon holder inside . . . . .	190
7.6	Xenon phase diagram [32] . . . . .	191
7.7	The tube and xenon liquefaction assembly. . . . .	192
7.8	Simplified picture of the motion assembly. . . . .	193
7.9	The stainless steel tube which allows the chamber to be maintained under vacuum while moving the quartz tube assembly. . . . .	193
7.10	The flange allowing the rotational motion of the xenon assembly. Left: top part, outside the main vacuum chamber. Right: bottom part, inside the main vacuum chamber. . . . .	194
7.11	A photo of the motion assembly with the bearings, spacers and angle marker clearly visible. The motor valve is also visible in the back as well as the chains linked to the pulley for the lifting movement and the xenon supply lines. . . . .	195
7.12	The full reflectivity setup as viewed from the outside. . . . .	196
7.13	A photo of the trigger logic for data acquisition. From left to right, the high voltage supply, the LED, the counter timer and the fast amplifier. . . . .	197
7.14	A typical PMT signal; in yellow, the signal once amplified; in blue, the yellow signal once inverted and digitized. The amplitude scale is for yellow: 100 mV/div and for blue: 500 mV/div. The time scale is 100 ns/division. . . . .	197
7.15	The orientation of the PMT. Top view. . . . .	198
7.16	Setup to perform the PMT calibration in the X direction. . . . .	199
7.17	X calibration of the PMT . . . . .	199
7.18	Setup for the y calibration . . . . .	200
7.19	Y calibration of the PMT using the rod as a point of reference . . . . .	201
7.20	Z calibration of the PMT . . . . .	202
7.21	Normalization data through the quartz tube in vacuum . . . . .	203
7.22	Schematic view of the angles needed to calculate the incident angle . . . . .	204

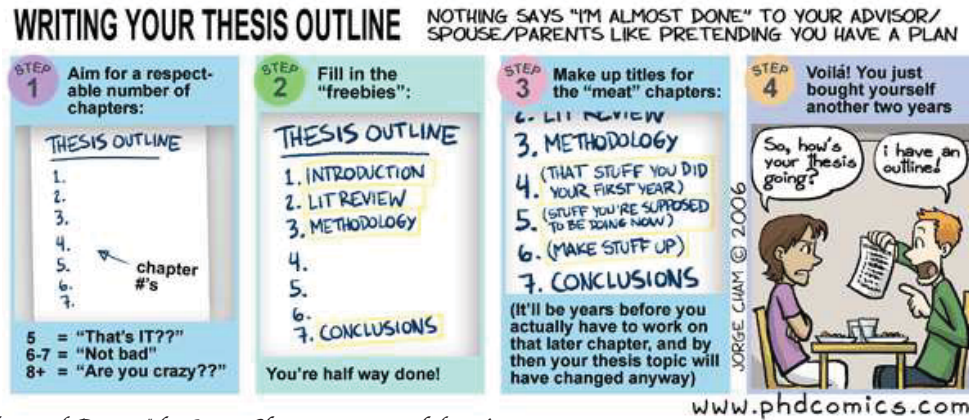
7.23	Setup for the PTFE alignment data . . . . .	205
7.24	PTFE alignment data through the tube under vacuum. Note that a teflon scale angle of $47^\circ$ corresponds to an incident angle of $76^\circ$ . . . . .	205
7.25	Raw Data of the reflection off of the teflon in vacuum. The dip around $10^\circ$ is due to the rod position around the quartz tube. . . . .	206
7.26	Position of the rods around the quartz tube. . . . .	207
7.27	Fits to the raw data in vacuum . . . . .	208
7.28	Reflectivity in vacuum through quartz tube . . . . .	209
7.29	Total, specular and diffuse reflectivities of the 3 mm thick teflon in the original vacuum setup. The data for the cold and warm measurements lie on top of one another. . . . .	209
7.30	Normalization data through the quartz tube in gas xenon . . . . .	210
7.31	PTFE alignment data through the tube under gas xenon . . . . .	211
7.32	Raw Data of the reflection off of the teflon in both cold and warm gas xenon . . . . .	212
7.33	Fits to the data in cold GXe . . . . .	213
7.34	Total, specular and diffuse reflectivities of the 3 mm thick teflon under both cold and warm gas xenon. . . . .	214
7.35	Normalization data through the quartz tube in liquid xenon . . . . .	214
7.36	PTFE alignment data through the tube under liquid xenon . . . . .	216
7.37	Raw Data of the reflection off of the teflon in liquid xenon . . . . .	217
7.38	Comparison between data in LXe and in vacuum for selected angles . . . . .	218
7.39	Effect of an artificial tilt on the quartz tube . . . . .	219
7.40	Raw data under LXe for three different teflon spots . . . . .	220
7.41	Raw data comparison before and after an accidental power outage which changed the state of the LXe . . . . .	221
7.42	Fits to the reflectivity data in LXe . . . . .	223
7.43	Reflectivity of 178 nm light in LXe . . . . .	224
A.1	The change in reference frame and the measured angles. The coordinate system is chosen such that a the tilt angle is described by a rotation about the x axis. . . . .	234

# LIST OF TABLES

2.1	Summary of the current dark matter search experiments . . . . .	48
4.1	Light yield values for the different energy lines . . . . .	124
6.1	Z positions corresponding to the different sample steps . . . . .	160
6.2	Parameters values of the fits corresponding to figure 6.36 (5 mm thick step). The top line is for the normalization measurement of the incident light with the teflon sample out of the way. . . . .	177
7.1	Reduced $\chi^2$ for the fits to the vacuum data through the quartz tube. The first reduced $\chi^2$ value corresponds to the normalization data (no reflection off teflon) . . . . .	207
7.2	Reduced $\chi^2$ for the fits to the GXe data. The first reduced $\chi^2$ value corresponds to the normalization data (no reflection off teflon) . . . . .	212
7.3	Reduced $\chi^2$ for the fits to the data in LXe. The first reduced $\chi^2$ value corresponds to the normalization data (no reflection off teflon) . . . . .	222



# Chapter 1. INTRODUCTION



*Piled Higher and Deeper* by Jorge Cham [www.phdcomics.com](http://www.phdcomics.com)

Hypothesized by Fritz Zwicky over 70 years ago, dark matter is now thought to constitute up to 26% of the total energy of the universe while the visible matter merely accounts for about 5%. The remaining energy of the universe would be accounted for by the so called dark energy. While numerous evidences that dark matter exists have been found, the dark matter particle itself still remains to be discovered.

An ideal dark matter candidate should have several properties. It should be non-baryonic, massive, stable on cosmological time scale, charge neutral, non-relativistically moving, weakly interacting and it should have the correct abundance.

Following this, theories predict the existence of various dark matter candidates, such as the WIMP (Weakly Interacting Massive Particle), the axion, the gravitino or the sterile neutrino. Normal neutrinos however can not constitute the bulk of dark matter as not only are they moving relativistically but their total mass would only account for a small fraction of the missing mass of the universe.

One of the favorite theory predicting dark matter is called supersymmetry (SUSY). Dark matter, as predicted by SUSY, is the object of numerous experiments all around the world which are relentlessly trying to detect it, either directly using recoil experiments, indirectly using gamma-ray or neutrino telescopes or using colliders. This task happens to be extremely daunting, principally because dark matter is thought to interact only very weakly with ordinary matter. However, for the first time in history, experiments, such as the ones using liquid noble detectors, are now capable of probing the phase space predicted by SUSY.

The XENON100 experiment is one of the world's leading experiments on dark matter searches. It has the potential to discover dark matter by directly looking for nuclear recoils in the detector after the interactions between the target material and the dark matter particles. Like all other experiments, XENON100 has to deal with different external backgrounds which could mimic a dark matter signal in the detector. Therefore a very precise understanding of the detector and of the underlying physics is necessary to develop a correct analysis capable of identifying the source of a signal. This is achieved by precise data analysis, Monte-Carlo simulations and dedicated small scale laboratory experiments. The XENON100 experiment has now reached its designed sensitivity and has released its most recent results in 2012. However, the search goes on as a new, bigger and more sensitive experiment has been designed and is now being built. This new experiment, in its working principle identical to XENON100, is called XENON1T.

In this thesis, results will be presented on a small yet important part of the XENON100 analysis program, on simulations from a smaller, almost identical detector and on a new experiment dedicated to analyze the reflectivity of certain materials. The analysis studies have helped XENON100 achieve the best limit in the world in its area of sensitivity as of the time of publication in 2012, while the simulations and experimental work will help in the construction of the upcoming XENON1T experiment.

In the following chapter, an overview of dark matter theory and experiments will be given. The convincing evidence for the existence of dark matter including the rotation curves of galaxies, gravitational lensing, measurements of the cosmic microwave background and supernova studies will be presented. Dark matter properties as well as a short explanation of the theory which fits it best, supersymmetry, will be given. Falling from this theory (and others), the most likely dark matter candidates, will be introduced. Finally an overview of some of the different experiments searching for dark matter and their mode of operation will be discussed.

The third chapter will present the XENON100 experiment in detail. It will cover the detector's operational principles, the detector's response to different signals, the analysis used to extract such a signal and finally the detector's sensitivity and its most recent results.

Chapter 4 is dedicated to the light yield analysis done on XENON100 data. A 3D light yield map and correction function will be described, and its performance and impact on the XENON100 results will be discussed. Additional light yield measurements used for the determination of the nuclear recoil energy scale are also presented.

Chapter 5 introduces the first results from a Monte-Carlo simulation of a small version of the

XENON100 detector built at the University of Muenster. This simulation package, done in GEANT4, is heavily inspired from the XENON100 simulation package.

Chapter 6 presents important and necessary results from a vacuum experiment at Muenster University designed to measure the reflectivity and transparency properties of teflon, a material used in the building of the XENON100 and XENON1T detectors.

Chapter 7 is a direct follow up of chapter 6 and introduces a new improved reflectivity setup, based on the original one, but modified to measure the reflectivity in liquid xenon instead of vacuum. The first results from this new setup are also presented, including a new model for reflectivity in liquid xenon.

Finally the last chapter will conclude this thesis by summarizing and discussing its results and suggesting improvements for the future of the experiment.



## Chapter 2. DARK MATTER: THEORY AND SEARCH



“I almost wish I hadn't gone down that rabbit-hole —and yet—and yet— it's rather curious, you know, this sort of life!”

— Alice

*Piled Higher and Deeper* by Jorge Cham [www.phdcomics.com](http://www.phdcomics.com)

### 2.1 First Indications for the Existence of Dark Matter

#### 2.1.1 Galactic Scale: Rotation Curves

After the pioneering idea of Zwicky [33], it was Vera Rubin in the 1970s who presented the first conclusive evidence for the existence of dark matter by analyzing the rotation curves of spiral galaxies [34]. The rotation curve of a galaxy represents the dependence between the velocity of stars and objects in a galaxy with respect to their distance from its center. By following classical Newtonian dynamics, the gravitational force should compensate the centripetal force such that:

$$F_G = F_c \quad (2.1)$$
$$\frac{G_N M(< r) m}{r^2} = \frac{m v_{circ}^2}{r}$$

where  $F_G$  is the gravitational force and  $F_c$  the centripetal force,  $m$  is the mass of the orbiting object,  $v_{circ}$  is the orbital velocity,  $G_N$  the gravitational constant and  $M(< r)$  the mass within a

distance  $r$  from the center, under the simplifying assumption of a radial symmetric mass distribution. Solving equation 2.1 for  $v_{circ}$  gives:

$$v_{circ} = \sqrt{\frac{G_N M(< r)}{r}} \quad (2.2)$$

According to equation 2.2 the orbital velocity of stars drops at larger distances and because most of the luminous mass is concentrated within the galactic bulge, it was thus expected that after a short distance the rotation curve of spiral galaxies would drop.

However, Rubin's results demonstrated that this was not the case. The orbital velocity of most stars remained constant even at distances much greater than the galactic bulge, distances which extended to the galactic halo as shown in figure 2.1. Since the bulk of the luminous mass is concentrated within the galactic center, this observation implied that there had to be extra, non visible mass densities at large radii as described by equation 2.3, thus suggesting the presence of a new form of massive matter: dark matter.

$$v_{circ} \sim constant \rightarrow M(< r) \propto r \rightarrow \rho \propto \frac{1}{r^2} \quad (2.3)$$

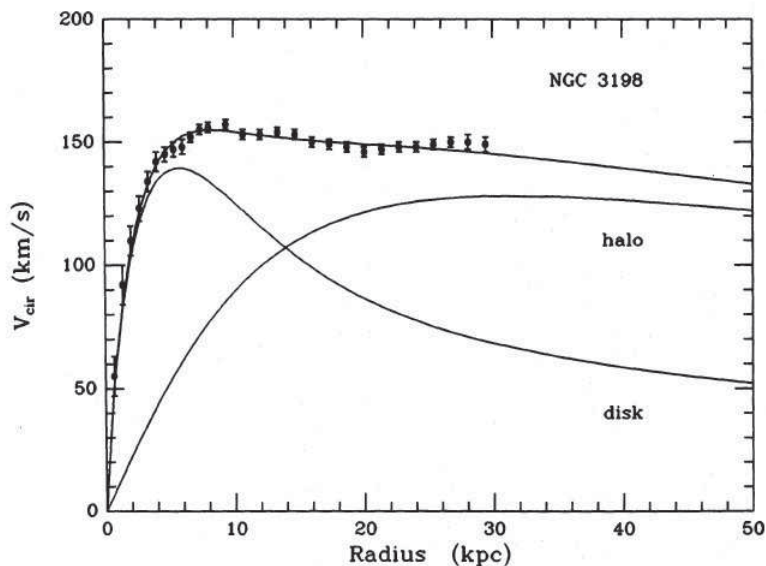


Figure 2.1: Rotation curve of galaxy NGC 3198 from [1].

Figure 2.1 illustrates this last point by displaying the rotation curve of the galaxy NGC 3198, determined by the galaxy's velocity, as observed using the 21 cm line from the neutral hydrogen spectrum beyond the visible disk [1]. This 21 cm line occurs when the spins of the proton and the electron of the lowest orbital energy state of atomic hydrogen change from aligned to anti-aligned

thus emitting in the process a photon with a vacuum wavelength of 21 cm in free space. This is a highly suppressed transition with a very low probability however due to the great abundance of hydrogen in the universe, this 21 cm line constitutes a rather stable cosmological beacon. Because this line is especially narrow due to its long lifetime, its width as observed from Earth can be directly linked to the velocity of the emitting object as it is the result of the doppler shift from the motion of said object. The rotation curve of a galaxy is then obtained by measuring this 21 cm line at different points in the galaxy.

Figure 2.1 shows both the observational data points with error bars and the contributions from the visible disk and a galactic halo including dark matter. At small distances the observed rotation curve follows the rotation curve predicted from the disk containing most of the visible mass as described previously by equation 2.2. However, at large distances, the observed rotation curve is mostly dissociated from the disk's and follows the rotation curve of a galactic halo which would contain more mass than visible according to equation 2.3. It is then clear that the rotation curves of spiral galaxies imply that most of the galactic halo is made of a non-luminous halo, a dark matter halo about the central area.

### 2.1.2 Galaxy Cluster Scale: Gravitational Lensing

Further evidence for the existence of dark matter has been obtained using a phenomenon called gravitational lensing [3]. This occurs when the light coming from a far away bright source is gravitationally bent, before reaching the observer, by a massive object such as a cluster of galaxies which behaves like a lens as shown on figure 2.2.

Gravitational lensing is generally described by the lens equation [35]:

$$\mathbf{y} = \frac{D_{OS}}{D_{OL}}\mathbf{x} - D_{LS}\boldsymbol{\alpha}(\mathbf{x}) \quad (2.4)$$

where  $\mathbf{y}$  is the true position of the source in the source plane,  $D_{OS}$  is the distance from the observer to the source,  $D_{OL}$  is the distance from the observer to the lens,  $D_{SL} = D_{OS} - D_{OL}$  is the distance from the source to the lens, and  $\boldsymbol{\alpha}(x)$  is the deflection angle at a position  $\mathbf{x}$  on the image plane.

The use of gravitational lensing to calculate the mass of a foreground cluster of galaxies (lens) was first introduced by Zwicky in 1937 [36] and is now one of the primary method used. Indeed, the deflection angle  $\boldsymbol{\alpha}(x)$  varies depending on the mass within a given projected radius  $\mathbf{x}$  on the image

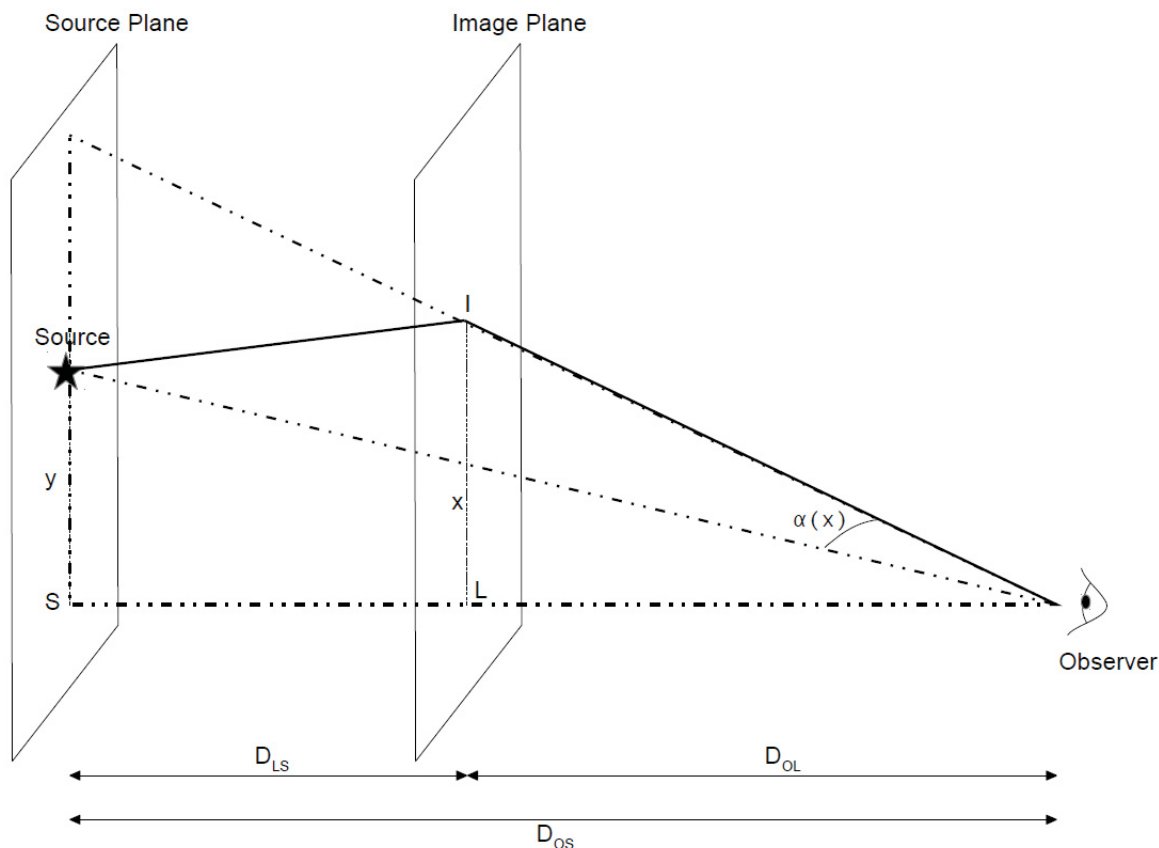


Figure 2.2: The principle of gravitational lensing.

plane according to equation 2.5 where  $G$  is the gravitational constant and  $c$  the speed of light [35], with the approximation of a point-like lens with mass  $M_L$ .

$$\alpha = \frac{4GM_L}{c^2 x} \quad (2.5)$$

Because most of the mass of a galaxy or cluster of galaxies is contained within the hot gas and not within the stars, and because the hot gas emits x-rays by combination of bremsstrahlung radiation, caused by the acceleration of free electrons by protons and helium nuclei, and emission lines from highly ionized heavy elements, calculating the mass of a cluster of galaxies requires x-ray images of that cluster [37].

### ***Strong Gravitational Lensing***

Strong gravitational lensing occurs in clusters with high mass density and can indicate the presence of more mass than can be accounted for from conventional matter. This effect, which gave the first discovery of gravitational lensing, is easily identified in the sky by spectacular gravitational arcs, rings or multiple images of lensed quasars. An example of strong gravitational lensing is shown

on figure 2.3 which displays a system of two galaxies SDSS J1631+1854, one in the foreground and one in the background, taken by the BOSS survey. While the left panel shows the original image, with the foreground galaxy in the center and the rings around it coming from the distant background galaxy, the right panel shows the same image after subtraction of a model for the lens surface brightness, thus clearly showing the residual light coming from the source, being bent around the lens, which clearly extends well beyond the luminous mass of the foreground galaxy. Comparison of the mass of the foreground galaxy as measured by gravitational lensing and luminosity yields an excess of gravitational mass compared to luminous mass. This confirms that the mass of galaxies is dominated by dark matter.

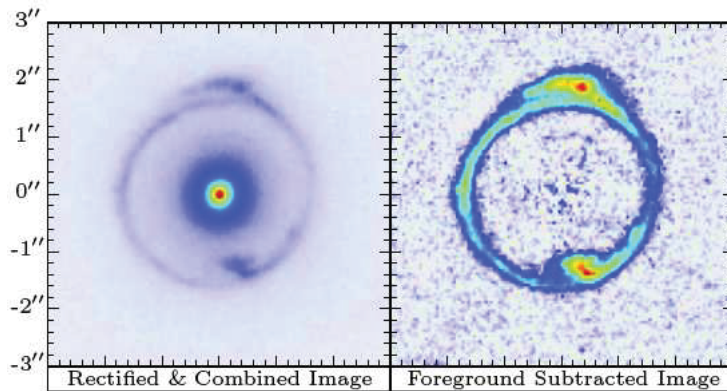


Figure 2.3: Gravitational rings in galaxies from the BOSS survey [2].

### ***Weak Gravitational Lensing***

Weak gravitational lensing which is characterized by the distortion of an image whose light has passed through a strong gravitational well, corresponds to much less powerful lenses and is thus not as easily identified as strong gravitational lensing. The distortion is actually too small to be detected when it comes from a single background source, consequently observing weak gravitational lensing requires to use a wide ensemble of background sources aligned around the lens, making its observation a statistical process [38]. A very good example of weak gravitational lensing comes from the observation of the Abell NGC2218 cluster, shown here on figure 2.4. This cluster acts as a very powerful lens, distorting and even multiply imaging background galaxies into long arcs stretched around the cluster's center.



Figure 2.4: Weak gravitational lensing effect in the Abell2218 galaxy cluster. The images of the background galaxies are distorted and stretched around the cluster's center. Credit: NASA, ESA, Richard Ellis (Caltech) and Jean-Paul Kneib (Observatoire Midi-Pyrenees, France)

### *The Bullet Cluster*

Another very particular example of weak gravitational lensing is found in the Bullet cluster 1E0657-558 presented in figure 2.5. The Bullet cluster consists of two clusters of galaxies which have collided in the past and constitutes until now probably the most compelling evidence for the existence of dark matter by using a system where visible matter and dark matter are spatially located at different points [3].

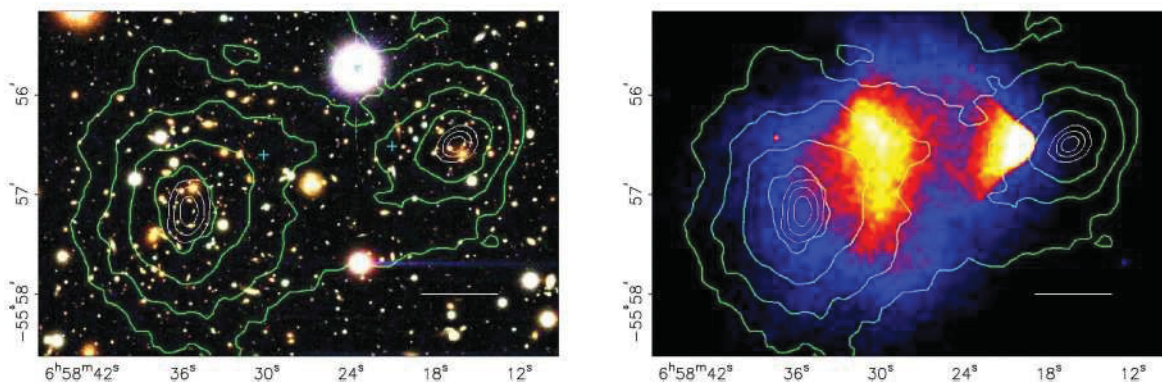


Figure 2.5: Map of the gravitational potential of the Bullet Cluster 1E0657-558 from [3].

On the left of figure 2.5 is a color image of the cluster taken by Magellan. On the right is an x-ray image of the same cluster taken by the Chandra telescope with the hot red zones corresponding to the hot plasmas and the blue zone corresponding to cold matter like stars. The green contours are the reconstruction of the gravitational potentials from gravitational lensing measurements. In a typical cluster, stars, plasma and dark matter are symmetrically distributed around the center. However, in the collision of two clusters, the collisionless stars decouple from the two plasmas as the

plasmas are slowed by ram pressure due to their collision with one another [3].

When producing a map of the gravitational potential if no dark matter is present, the maximum mass density should correspond spatially to the dominant visible matter, the plasma, which in the case of the Bullet cluster, is offset from the spatial position of the other galaxies. However, if dark matter is present and dominant and assuming it is collisionless, the maximum mass density on the map should correspond to the spatial position of the collisionless galaxies. This is indeed the case for the Bullet cluster. In the Chandra image, the slowed down plasmas from the two galaxies do not coincide with the green contours showing the two higher mass density points in that region of the sky. These contours however, do coincide with the stars' center of the Magellan image, thus indicating the presence of dark matter.

## ***2.2 Dark Matter Origins***

At this point, the case for dark matter is rather strong. So before going further into more evidences and start characterizing dark matter, it is useful to take a step back and wonder about the actual origins of dark matter. Other than the empirical proof of the existence of dark matter, dark matter is an inherent component to the standard cosmological model.

### ***2.2.1 The Cosmological Standard Model: $\Lambda$ CDM***

The  $\Lambda$ CDM (Lambda Cold Dark Matter) model is the standard cosmology model which uses general relativity as the appropriate gravitational theory on cosmological scales. The  $\Lambda$ CDM model describes the universe as containing a dark energy component parametrized by the cosmological constant  $\Lambda$  and cold (non-relativistic) dark matter. It is the simplest model known to match most cosmological observations including the anisotropy of the cosmic microwave background (CMB), the large scale structure in the distribution of galaxies, the measured abundance of hydrogen, helium and lithium, and the expansion rate of the universe. These observations will be explained in more details in the following sections.

The  $\Lambda$ CDM model, in its simplest form, contains six basic parameters, the dark energy density, the dark matter density, the baryon density, the amplitude of primordial fluctuations of the space curvature, the reionization optical depth and the slope of the scalar perturbation spectrum [6]. While the meaning of the first three parameters is self explanatory, some precision needs to be added about the last three.

The reionization optical depth measures how far back in time the reionization process happened. This process happened after stars form, when they are energetic enough to partially ionize the diffuse neutral hydrogen remaining in the universe. Since the physics underlying this process is not fully understood, the reionization depth is not known precisely and is thus left as a free parameter of the  $\Lambda$ CDM model.

Primordial density fluctuations are necessary in the early universe to allow galaxy formation around them. Without them, the universe would be completely homogeneous and no large scale structure would have ever been formed. Once again, because the amplitude of these perturbations is unknown, they are left as a free parameter.

Finally, the spectral index of the primordial density fluctuations is linked to the physical size of the aforementioned density fluctuations. Indeed, their size could vary depending on the scale at which they are looked at.

It is really remarkable that these six parameters are sufficient to describe the universe as we know it, at least at first order. Indeed, the  $\Lambda$ CDM model contains many more parameters, like for example, the neutrino density, however these describe only perturbations from the basic model.

According to the  $\Lambda$ CDM model, the universe is divided in three major components, 71.4% consists of dark energy, 24% of dark matter and 4.6% of baryons as represented in the famous pie of the universe on figure 2.6 [6].

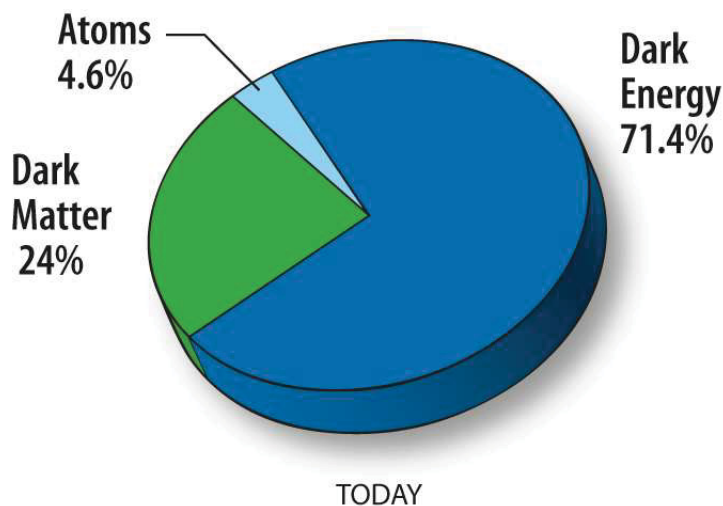


Figure 2.6: The famous pie of today's universe. Credit: NASA / WMAP Science Team.

### 2.2.2 Large Scale Structure Formation

The  $\Lambda$ CDM scenario, as its name indicates, requires dark matter to be cold so moving non-relativistically. Such a requirement comes from the study of large scale structure formations in the universe such as galaxies and clusters of galaxies. There are two possibilities to explain the structure of the universe as we see it today from the photon decoupling epoch. In a first case, called the top down scenario, it is assumed that in the early universe radiation smoothed out matter density fluctuations forming large pancakes. At the time of recombination (photon decoupling) the pancakes accreted matter and grew until their eventual collapse and fragmentation into smaller scale structures such as galaxies. This scenario, which took billions of years, leads to a rather homogeneous universe which would look like sheets of galaxies with voids between the sheets and clusters of galaxies at the sheets' intersections.

A second case, called bottom up scenario, hypothesizes that small scale structures like galaxies formed first to then clumped together due to gravitational forces into larger structures such as bigger galaxies and eventually clusters of galaxies. An intuitive description of these two scenarios is shown on figure 2.7.

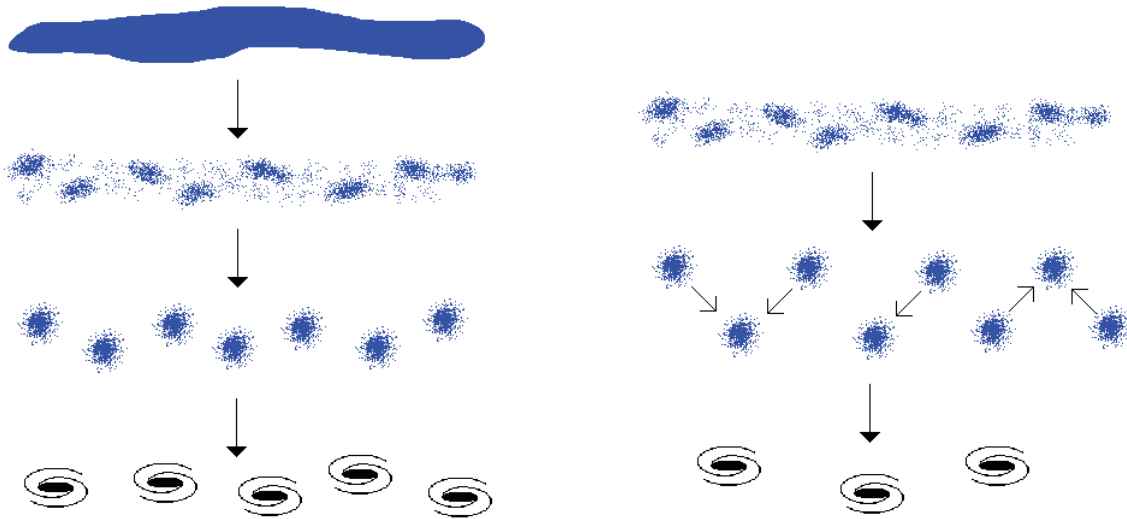


Figure 2.7: Representation of the top down (left) and bottom up (right) scenarios for the formation of large structure of the universe [4].

When observing the universe today, it is quite clear that galaxies are not evenly distributed like the top down scenario would expect but rather have sharp features with weak connecting filaments. In addition, clusters of galaxies are still forming today, while stars are known to be over 10 billion years old. These two arguments make the bottom up scenario much more likely to be the accurate one.

The more interesting features of these two scenarios is that they both require dark matter however

with different properties. The top down scenario requires hot dark matter to provide large and smooth features. Indeed relativistically moving weakly interacting particles would not clump together but just smooth out the density distribution. On the other hand, the bottom up scenario requires dark matter to be cold as slow moving matter would clump on small scales. The clumps would then grow and clump together to form galaxies.

Figure 2.8 shows such a phenomenon where the non-linear dark matter power spectrum as a function of the wavenumber  $k$  is shown for various amount of hot dark matter and superimposed with actual data from the APM galaxy [39]. The power spectrum is the fourier transform of the matter distribution and thus indicates the frequency with which matter clumps are found over a certain length scale which is the inverse of the wavenumber. Depending on the amount of hot dark matter included in the model, the matter fluctuations vary a lot on small scales. In the cold dark matter model, matter fluctuations still persist on small scales (red curve of figure 2.8) which is consistent with the bottom up scenario, while they disappear progressively as hot dark matter is added (green, blue, cyan and magenta curves) until they are completely gone thus giving a smoothed density distribution, consistent with the top down scenario [5].

Consequently because the bottom up scenario seems to match the observations the best and because it is clear that hot dark matter couldn't lead to the large scale structures we see today, it is thought that dark matter is essentially cold. It is to be noted however that the cold dark matter only model has still to answer some challenging problems. Indeed cold dark matter predicts the formation of cusps in the halos' density distribution which have not yet been observed [40]. Another problem is the prediction of the number of satellites as well as the frequency of massive galaxies which is much higher than observed. Because of these challenges, new hybrid theories of combinations of hot and cold or warm dark matter have started to emerge. However, the cold dark matter scenario still remains the dominant theory, especially because it gives excellent dark matter candidates. This will be emphasized and explained in later sections.

### ***2.3 Dark Matter Density***

Now that both empirical evidences and the  $\Lambda$ CDM model have established that dark matter is an intrinsic component to the universe, it becomes important to be able to tell in what quantity dark matter is present and to put a number on its relic density. Measuring the actual value of the dark matter relic density of the universe was done by studying the anisotropy of the Cosmic Microwave

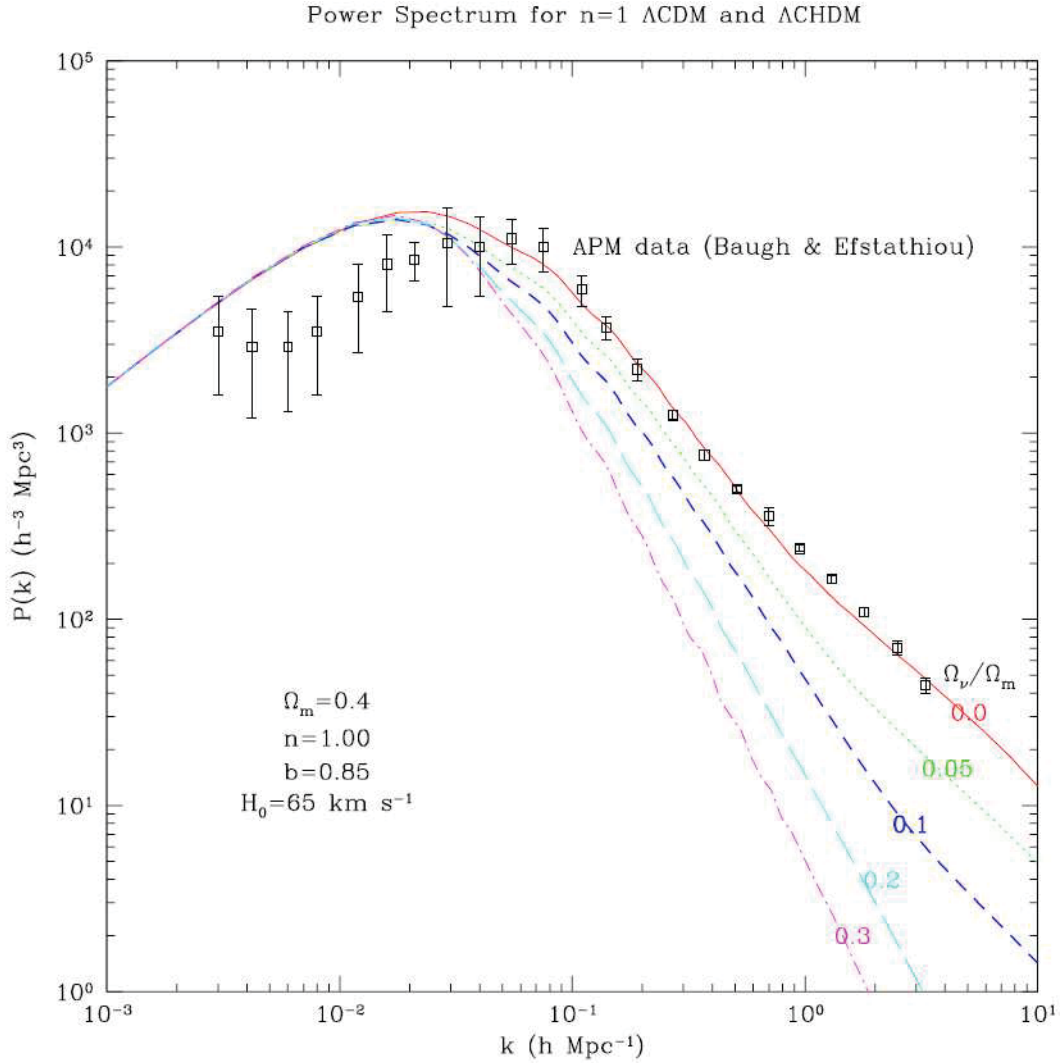


Figure 2.8: Dark matter power spectra for different amounts of hot dark matter [5].

Background (CMB) using the WMAP and Planck satellites [6] [41].

### 2.3.1 The Cosmic Microwave Background

The CMB is a common name for the thermal radiation left over from the early universe or free relic photons. These photons are the oldest light in the universe as they come from the epoch of recombination and photon decoupling some 380,000 years after the Big Bang. The CMB consists of a nearly perfect isotropic black body radiation, the best ever measured in nature, with fluctuations in the spectrum smaller than the  $10^{-4}$  level and with an average temperature of 2.725 K [42] as first measured by the COBE satellite [42].

### *Origins of the CMB*

In its very early, radiation dominated era, the universe was opaque. Indeed it was made of an homogeneous, very energetic plasma containing mutually scattering photons, baryons and electrons. At that stage, electrons and baryonic matter were coupled and in equilibrium with the photons and interactions between them were governed by equation 2.6 [37].



Equation 2.6 is a reversible reaction where on one hand, protons and electrons undergo radiative recombination to create an hydrogen atom in a ground or excited state and on the other hand, hydrogen is photoionized into a proton electron plasma, thus making the ratio ionized hydrogen to unionized hydrogen a temperature dependent value, at thermal equilibrium.

As the universe expanded, it cooled down until the point where it reached the ionization energy of hydrogen  $Q=13.6$  eV. At that point, the average CMB photon can no longer photoionize hydrogen and the formation of stable hydrogen atom should be enabled, a moment in time known as recombination. However, because there are so much more CMB photons than baryonic matter (about  $5 \cdot 10^{10}$  more) the high energy photon content of the exponential tail of the black body spectrum of figure ?? cannot be neglected and keeps the rate of photoionization very high. In addition, because baryonic matter and photons are still coupled, the rate of photoionization is maintained in statistical equilibrium with the rate of radiative recombination. Consequently recombination does not happen when the universe reached the ionization energy of hydrogen.

Instead, the recombination temperature, the temperature at which recombination happens and stable atomic hydrogen formation is enabled, depends not only on the ionization energy  $Q$ , but also on the baryon to photon ratio  $\eta$  and on the degree to which the baryonic content of the universe is ionized  $X$ , where  $X = 1$  when the baryonic content is fully ionized and  $X = 0$  when it consists entirely of neutral atoms. Defining the moment of recombination such as the moment where the baryonic content of universe is half ionized ( $X=1/2$ ) leads to a recombination temperature of about 0.3 eV or 3740 K [37].

At this point however, photons and baryonic matter are still coupled. It's only at the time of photon decoupling that photons become truly free. In addition to reaction 2.6, when the universe was fully ionized, photons mainly interacted with electrons via Thomson scattering, a reversible reaction which consists in a transfer of momentum and energy between the photon and the electron and is

shown in equation 2.7.

$$\gamma + e^- \leftrightarrow \gamma + e^- \quad (2.7)$$

At the epoch of recombination, the electron density suddenly decreased drastically as electrons combined with protons to form stable hydrogen atoms. Because the mean free path of a photon  $\lambda$ , which is the average distance a photon travels before scattering off of an electron, depends on the number of electrons  $n_e$ , as shown on equation 2.8 where  $\sigma_e = 6.65 \cdot 10^{-29} m^2$  is the Thomson scattering cross-section, the lower the electron density, the higher the mean free path.

$$\lambda = \frac{1}{n_e \sigma_e} \quad (2.8)$$

As long as the photon mean free path is shorter than the Hubble distance  $c/H$ , which is the spatial distance over which two points can be connected by a photon, the photons and electrons stay coupled at the same temperature and the photons stay in thermal equilibrium with the electrons as well as with the protons due to reaction 2.6. When that is no longer the case, and the photon mean free path becomes larger than the Hubble distance, or equivalently the scattering rate between photons and electrons becomes smaller than the rate of expansion of the universe, photons decouple and can no longer interact with electrons. At this time of photon decoupling, which is found to have happened at a redshift  $z \simeq 1100$  corresponding to temperatures 3000 K, the universe becomes transparent and photons and baryons are no longer compelled to have the same temperature. These now free photons have been roaming the universe since the time of last scattering, the time at which a photon underwent its last scattering from an electron, and it is these photons which constitute the CMB with a density of  $4.11 \cdot 10^8 m^{-3}$ .

In addition, it happens that these photons have a mean energy comparable to the vibration or rotation energy of small molecules like H<sub>2</sub>O. Consequently, these photons can very easily interact on Earth after having roamed the universe for billions of years and be detected as the CMB.

Another happy consequence of photon decoupling is that it enabled large structure formation. Indeed, because the universe is no longer made of an homogeneous plasma but rather of two decoupled gases, one made of photons and the other of neutral hydrogen, baryons can collapse gravitationally and form condensed objects such as planets, stars and galaxies [37].

### *Anisotropies of the CMB*

Since the epoch of photon decoupling and last scattering, the CMB photons have been propagating through the universe. However, not all the CMB photons underwent their last scattering simultaneously, a phenomenon which gave rise to the temperature fluctuations that are observed today in the CMB. Many experiments have been mapping these temperature fluctuations over a decade. After the 4 years mission of the Cosmic Background Explorer (COBE) [43] and its subsequent results in 1999, a 45 times more sensitive satellite, the Wilkinson Microwave Anisotropy Probe (WMAP), was launched in 2001 to map out the tiny temperature fluctuations of the CMB over the full sky. In 2012, WMAP released its results from 9 years of observation of the CMB [6]. The subsequent CMB full sky map shown on figure 2.9, shows temperature fluctuations on a scale as small as  $0.2^\circ$  on the sky. On this map, the different colors match the different temperatures and densities, the red regions are warmer and denser by about  $400\mu K$  than the blue regions. Note that another new and more sensitive satellite, the Planck satellite [41], was launched in 2009. While the Planck data and results are already available, they have not yet been peer reviewed and consequently the results from the 9 years of observation by WMAP are presented in this work instead.

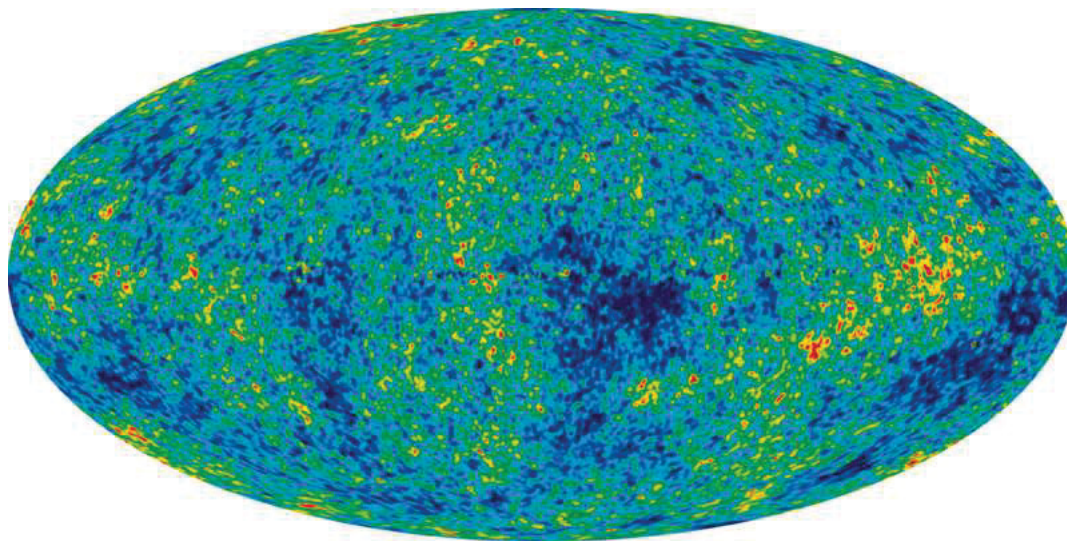


*Figure 2.9:* The temperature fluctuations of the Cosmic Microwave Background as observed by the WMAP satellite [6]

The temperature fluctuations shown on figure 2.9, depending on their size, have two different origins. Large scale fluctuations, at angular scales greater than  $1^\circ$ , come from the gravitational effect from primordial density fluctuations in the distribution of non baryonic dark matter prior and at the time of last scattering. Indeed, at that time, the universe is matter dominated and the density of dark matter is much higher than the density of the photons which in turn is higher than the

density of the baryons. Consequently, dark matter dominates the gravitational potential at the time of last scattering, and the fluctuations in this gravitational potential gives rise to potential wells. A photon, which at the time of last scattering is at a minimum potential in the well, will need more energy to get out of the well. This photon will then be redshifted and consequently, colder. This case corresponds to the blue (colder) regions in the CMB map of figure 2.9. Conversely, if a photon at the time of last scattering is at a maximum in the well, it will need less energy to get out and will thus appear blueshifted and gives rise to the red (warmer) regions in the CMB map. This is known as the Sachs Wolfe effect. The temperature fluctuations of the CMB thus give a map of the gravitational potential fluctuations at the time of last scattering.

Smaller scale fluctuations, of the order of less than  $1^\circ$ , are more complicated as the effect of photons and baryons must be taken into account. As mentioned above, prior to photon decoupling, the photon baryon fluid moves under the gravitational influence of the non baryonic dark matter. If this photon baryon fluid is in a dark matter potential well, it falls to the center and under the action of gravity, gets compressed. As it gets compressed, however, its pressure rises. This happens until the pressure is high enough that it exceeds the effect of gravity and the photon baryon fluid starts expanding outwards. While expanding the pressure starts decreasing again until it's too small and the fluid goes back to being compressed by the well gravity, and the process repeats itself. These inward outward compression and expansion give rise to acoustic oscillations as this motion is that of a simple harmonic oscillator. In addition, depending on whether the photon baryon fluid is at maximum or minimum compression, its density is higher or lower than average and so, at the time of photon decoupling and last scattering, the liberated photons are hotter or colder, thus blueshifted or redshifted, and causing the small angular scale fluctuations in the map of the CMB (figure 2.9).

Now that the origins of the fluctuations are understood, they need to be characterized over the entire visible sky. This is done using two dimensional spherical harmonics functions  $Y_{lm}(\theta, \phi)$  defined as equation 2.9 where  $P_l^m$  are Legendre polynomials,  $-l \leq m \leq l$  and  $l$  is defined as  $l = 0, \dots, \infty$  and is the multipole which represents a given angular scale in the sky  $\alpha = \pi/l$ . Consequently, the larger the angular scale the smaller the value of  $l$ .  $l = 0$  is thus an overall constant which represents the average temperature over the whole sky, while  $l = 1$  has an angular scale  $\alpha = 180^\circ$  and is the angular dipole which is in fact a simple Doppler shift resulting from the motion of the satellite relative to the rest frame of the CMB, in which the CMB is isotropic. This dipole can be corrected for by accounting for the motion of the Earth relative to the Hydra-Centaurus supercluster, the closest supercluster to the Earth. The CMB map of figure 2.9 is obtained after subtraction of this dipole anisotropy in the

CMB.

$$Y_{lm} = \sqrt{\frac{2l+1}{4\pi} \frac{(l-m)!}{(l+m)!}} P_l^m(\cos\theta) e^{im\phi} \quad (2.9)$$

The temperature fluctuations over the entire sky can then be represented in terms of  $Y_{lm}$  as equation 2.10 where  $a_{lm}$  are coefficients representing the amplitude of the fluctuations and  $T(\theta, \phi)$  is the general function representing the fluctuations over the whole sky.

$$T(\theta, \phi) = \sum_{l=0}^{l=\infty} \sum_{m=-l}^l a_{lm} Y_{lm}(\theta, \phi) \quad (2.10)$$

From equation 2.9 and 2.10, a multipole dependent power spectrum of these fluctuations,  $C_l$ , can be defined as

$$C_l = \frac{1}{2l+1} \sum_{m=-l}^l \langle |a_{lm}|^2 \rangle \quad (2.11)$$

This angular power spectrum, plotted as a function of the multipole  $l$  from WMAP in figure 2.10 [6], gives then invaluable information about the matter density of the early universe and allows to calculate the values of the fundamental six parameters of the  $\Lambda$ CDM cosmological model as well as the perturbative parameters such as the neutrino mass fraction.

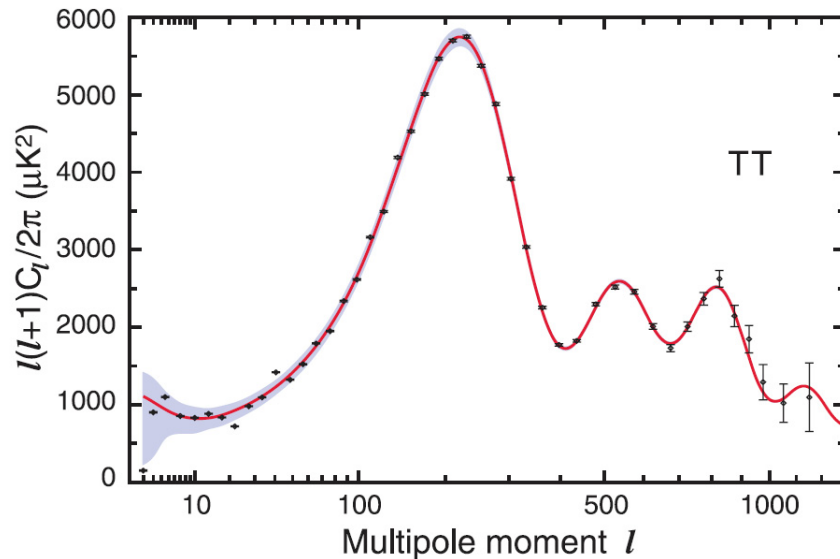


Figure 2.10: The angular power spectrum of the CMB [6]

While the whole angular power spectrum will not be explained here, its main features will be introduced. First, each “bump” on the power spectrum corresponds to maximum compression and

rarefaction (when a photon has undergone one full oscillation) alternatively. For example, the first peak corresponds to regions that have undergone half an oscillation in the time between recombination and last scattering, and are thus at maximum compression, while the second peak is due to regions that have undergone one full oscillation and are thus at rarefaction, and so forth and so on. Note also that large scale fluctuations with  $\theta > 1^\circ$  indeed appear for values of  $l < 180$ , as should be the case. Second, the main acoustic peak appears at value slightly less than  $1^\circ$  ( $l = 200$ ). The angular scale of the first peak, and so its position, is related to the physical distance of the source, called the angular diameter distance, through the physical distance the photons travel. Since this distance depends on the expansion rate of the universe, the location of the first peak is very sensitive to this expansion rate and can be used to measure it. The location of the first peak at  $l = 200$  is consistent with a flat universe where the total energy density of the universe is  $\Omega_{tot} = 1$ .

In addition to the geometry of the universe, the baryon density is also given by the angular power spectrum of the CMB. The maximum compression reached in the potential well depends also on the baryon mass. If the baryon mass is bigger, there is more inertia and the baryon photon fluid is more compressed. Rarefaction on the other hand does not depend on the baryon mass. Consequently, the relative height of the compression peaks (first, third, fifth...) to rarefaction peaks (second, fourth, sixth...) is dependent on the baryon density.

As for the third (and higher) peak of the power spectrum, it gives information on the total density of non relativistic matter. Indeed, if the universe had only radiation, at maximum compression, the photons would continue to redshift with the expanding universe and the gravitational potential would decay away, thus making the temperature fluctuations much bigger than they would be. However, non relativistic matter does not redshift so its gravitational potential does not decay, which thus would lead to smaller fluctuations and smaller peaks. This thus allows the determination of the density of non relativistic matter in the universe.

The actual values of the parameters calculated from the CMB angular power spectrum from the WMAP results are shown on figure 2.11 [6]. From this, two very important conclusions can thus be drawn. First the dark energy component of the universe  $\Omega_\Lambda$  is much larger than the others, confirming that dark energy is the main component of the universe. Second,  $\Omega_c h^2$  is much larger than  $\Omega_b h^2$  confirming that dark matter does exist and that it must be non-baryonic. The WMAP data is thus in complete agreement with the  $\Lambda$ CDM (Lambda Cold Dark Matter) model and requires the existence of both dark matter and dark energy.

Parameter	Symbol	WMAP <sup>a</sup>
<b>6-parameter <math>\Lambda</math>CDM fit parameters<sup>c</sup></b>		
Physical baryon density	$\Omega_b h^2$	$0.02264 \pm 0.00050$
Physical cold dark matter density	$\Omega_c h^2$	$0.1138 \pm 0.0045$
Dark energy density ( $w = -1$ )	$\Omega_\Lambda$	$0.721 \pm 0.025$
Curvature perturbations ( $k_0 = 0.002 \text{ Mpc}^{-1}$ ) <sup>d</sup>	$10^9 \Delta_{\mathcal{R}}^2$	$2.41 \pm 0.10$
Scalar spectral index	$n_s$	$0.972 \pm 0.013$
Reionization optical depth	$\tau$	$0.089 \pm 0.014$
Amplitude of SZ power spectrum template	$A_{\text{SZ}}$	$< 2.0$ (95% CL)
<b>6-parameter <math>\Lambda</math>CDM fit: derived parameters<sup>e</sup></b>		
Age of the universe (Gyr)	$t_0$	$13.74 \pm 0.11$
Hubble parameter, $H_0 = 100h \text{ km/s/Mpc}$	$H_0$	$70.0 \pm 2.2$
Density fluctuations @ $8h^{-1} \text{ Mpc}$	$\sigma_8$	$0.821 \pm 0.023$
Velocity fluctuations @ $8h^{-1} \text{ Mpc}$	$\sigma_8 \Omega_m^{0.5}$	$0.434 \pm 0.029$
Velocity fluctuations @ $8h^{-1} \text{ Mpc}$	$\sigma_8 \Omega_m^{0.6}$	$0.382 \pm 0.029$
Baryon density/critical density	$\Omega_b$	$0.0463 \pm 0.0024$
Cold dark matter density/critical density	$\Omega_c$	$0.233 \pm 0.023$
Matter density/critical density ( $\Omega_c + \Omega_b$ )	$\Omega_m$	$0.279 \pm 0.025$
Physical matter density	$\Omega_m h^2$	$0.1364 \pm 0.0044$
Current baryon density ( $\text{cm}^{-3}$ ) <sup>f</sup>	$n_b$	$(2.542 \pm 0.056) \times 10^{-7}$
Current photon density ( $\text{cm}^{-3}$ ) <sup>g</sup>	$n_\gamma$	$410.72 \pm 0.26$
Baryon/photon ratio	$\eta$	$(6.19 \pm 0.14) \times 10^{-10}$
Redshift of matter-radiation equality	$z_{\text{eq}}$	$3265_{-105}^{+106}$
Angular diameter distance to $z_{\text{eq}}$ (Mpc)	$d_A(z_{\text{eq}})$	$14194 \pm 117$
Horizon scale at $z_{\text{eq}}$ (h/Mpc)	$k_{\text{eq}}$	$0.00996 \pm 0.00032$
Angular horizon scale at $z_{\text{eq}}$	$l_{\text{eq}}$	$139.7 \pm 3.5$
Epoch of photon decoupling	$z_*$	$1090.97_{-0.86}^{+0.85}$
Age at photon decoupling (yr)	$t_*$	$376371_{-4111}^{+4115}$
Angular diameter distance to $z_*$ (Mpc) <sup>h</sup>	$d_A(z_*)$	$14029 \pm 119$
Epoch of baryon decoupling	$z_d$	$1020.7 \pm 1.1$
Co-moving sound horizon, photons (Mpc)	$r_s(z_*)$	$145.8 \pm 1.2$
Co-moving sound horizon, baryons (Mpc)	$r_s(z_d)$	$152.3 \pm 1.3$
Acoustic scale, $\theta_* = r_s(z_*)/d_A(z_*)$ (degrees)	$\theta_*$	$0.5953 \pm 0.0013$
Acoustic scale, $l_* = \pi/\theta_*$	$l_*$	$302.35 \pm 0.65$
Shift parameter	$R$	$1.728 \pm 0.016$
Conformal time to recombination	$\tau_{\text{rec}}$	$283.9 \pm 2.4$
Redshift of reionization	$z_{\text{reion}}$	$10.6 \pm 1.1$
Time of reionization (Myr)	$t_{\text{reion}}$	$453_{-64}^{+63}$
<b>7-parameter <math>\Lambda</math>CDM fit parameters<sup>i</sup></b>		
Relativistic degrees of freedom <sup>j</sup>	$N_{\text{eff}}$	$> 1.7$ (95% CL)
Running scalar spectral index <sup>k</sup>	$dn_s/d \ln k$	$-0.019 \pm 0.025$
Tensor to scalar ratio ( $k_0 = 0.002 \text{ Mpc}^{-1}$ ) <sup>l</sup>	$r$	$< 0.38$ (95% CL)

Figure 2.11: Values for the  $\Lambda$ CDM parameters from WMAP [6]

### 2.3.2 Big Bang Nucleosynthesis

It is noteworthy to mention that before COBE and its capacity to measure the precise density of baryons in the universe, studies of the Big Bang Nucleosynthesis (BBN) had already determined the baryon density in the universe and come to the conclusion that it was too low to make out the bulk of the universe.

BBN refers to this period of time in the formation of the universe between 100 seconds and 15 min after the big bang, where atomic nucleus formation was enabled. To correctly understand this process, it is necessary to go back when the universe was about 0.01 s old at a temperature  $T = 10^{11}K$  or  $kT \simeq 10MeV$ , where only a tiny portion of the initial protons and neutrons have survived radiative annihilation and the universe is made only of bosons, leptons, anti-leptons and the remaining neutrons and protons. At that stage, the relative number of neutrons and protons is in equilibrium and governed by weak reactions [44]:

$$\nu_e + n \leftrightarrow e^- + p \quad (2.12)$$

$$\bar{\nu}_e + p \leftrightarrow e^+ + n \quad (2.13)$$

$$n \rightarrow e^- + p + \bar{\nu}_e \quad (2.14)$$

At such high temperature  $T$ , the nucleons move non relativistically and so the ratio between the number of neutrons  $N_n$  and protons  $N_p$  can be described by a Boltzmann distribution as shown on equation 2.15 where  $Q$  is the mass difference between neutron and proton so 1.293 MeV and  $k$  is the Boltzmann constant.

$$\frac{N_n}{N_p} = \exp\left(\frac{-Q}{kT}\right) \quad (2.15)$$

At the universe expands, around  $t=0.1$  s and  $kT \simeq 3MeV$ , reactions 2.12, 2.13 and 2.14 start coming out of equilibrium and neutrinos decouple, a process very similar to photon decoupling explained in the previous paragraph.

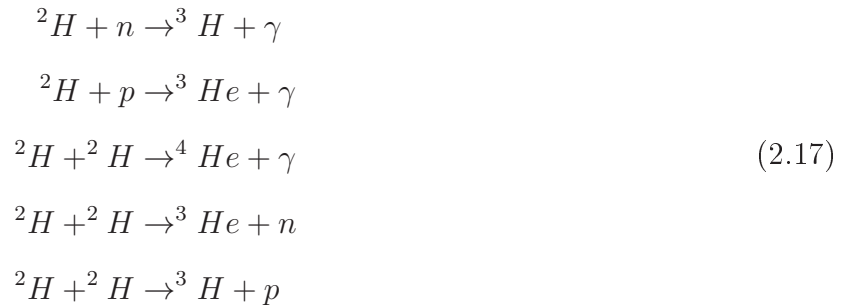
From the moment of neutrino decoupling, protons and neutrons are no longer created by reactions 2.12 and 2.13, a freeze-out which happens at 0.8 MeV, the remaining neutrons decay via reaction 2.14 and nucleosynthesis can begin, producing deuterium via reaction 2.16 where  $Q = 2.22MeV$  is

the binding energy of deuterium.



However, at that point reaction 2.16 is reversible and due to the plethora of photons around, deuterium ( ${}^2H$ ) is destroyed as soon as it is formed, thus not only preventing stable deuterium to form and consequently permanent nucleosynthesis to happen, but also maintaining the ratio neutron to proton in equilibrium due to a cross section much larger than for the one of reaction 2.14.

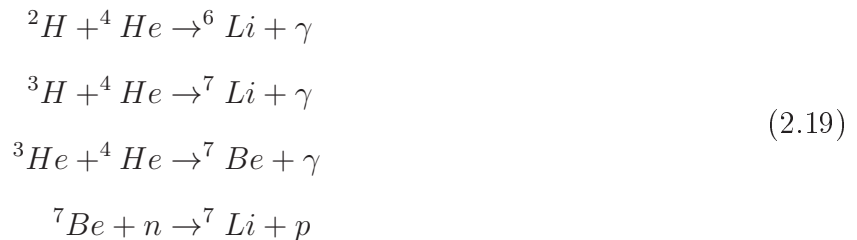
It's only at  $t \sim 100$  s, when the universe has a temperature  $kT \simeq 0.1 \text{ MeV}$  that equation 2.16 becomes irreversible, deuterium is no longer frozen out and permanent nucleosynthesis happens. Once deuterium is formed, it can react and form light nuclei such as helium,  ${}^3He$  or  ${}^4He$  and tritium  ${}^3H$ , for example via reactions 2.17 [37].



However,  ${}^3He$  or  ${}^3H$  usually don't stay as such but are converted to  ${}^4He$  via reactions 2.18.



Once  ${}^4He$  is formed, it can react with other light nuclei and create heavier nuclei such as  ${}^6Li$  or  ${}^7Li$ , the only stable isotopes of lithium, and beryllium  ${}^7Be$  via reactions 2.19.



It is very important to note that all of the reactions that can occur once deuterium has been

formed have temperature dependent cross sections and calculating the precise yield of each isotope is a very complex process which goes far beyond the scope of this work.

As there are no stable nuclei with an atomic number of 8, the chain stops here and nucleosynthesis stops around  $t \sim 1000$  s where the temperature of the universe is about 0.03 MeV. Indeed at that point, the temperature becomes too low and nuclei can't overcome the Coulomb barrier that separates them. Formation of heavier nuclei will have to wait for stellar fusion to happen. In addition, the mean lifetime of a neutron in free space is 14.7 min, so any neutrons which have not been used to form a nucleus decay via reaction 2.14. At the end of nucleosynthesis, nearly all baryons consist of protons and  ${}^4\text{He}$  nuclei and only small amount of  ${}^2\text{H}$ ,  ${}^3\text{H}$ ,  ${}^3\text{He}$  and even smaller amounts of  ${}^6\text{Li}$ ,  ${}^7\text{Li}$  and  ${}^7\text{Be}$ , which is in turn converted into  ${}^7\text{Li}$  via electron capture.

The major result from this is that the relative abundance of light nuclei to hydrogen is frozen in time and so by measuring their abundance now, their primordial abundance is effectively measured. The primordial abundance of elements is obtained by observing metal-poor, extra-galactic, ionized hydrogen regions of space for  ${}^4\text{He}$ , remote cosmological clouds for  ${}^2\text{H}$ , metal-poor and halo stars for  ${}^7\text{Li}$  and giant molecular cloud regions for  ${}^3\text{He}$  [7].

This relative abundance is directly linked to the baryons to photons ratio  $\eta$ . Indeed, from reaction 2.16, a higher  $\eta$  would mean that the temperature at which nucleosynthesis occurs,  $T_{nuc}$ , is also higher, thus making nucleosynthesis start earlier and consequently last longer. Since nucleosynthesis is, in any case, time limited due to the ever decreasing density and temperature of the universe, an earlier start means a more efficient production of  ${}^4\text{He}$  and so smaller amounts of deuterium and  ${}^3\text{He}$  leftover. By using a Monte-Carlo (MC) and varying  $\eta$  the relative abundance of  ${}^4\text{He}$ ,  ${}^3\text{He}$ ,  ${}^2\text{H}$ , and  ${}^7\text{Li}$  as a function of  $\eta$  can be produced. This is shown on figure 2.12 [7].

Note that for the case of  ${}^4\text{He}$ , the mass fraction  $Y$  is used instead of the relative abundance. This comes from the fact that  $Y$  is extremely easy to calculate from temperature dependent neutron to proton ratio  $f = N_n/N_p$  (see equation 2.15) according to equation 2.20 [37].

$$Y = \frac{2f}{1+f} \quad (2.20)$$

In figure 2.12, the mass fraction of  ${}^4\text{He}$  and the relative abundance of helium, deuterium and lithium with respect to hydrogen, computed thanks to a complex MC on the basis of the cross-sections involved, are plotted as a function of the baryon to photon ratio  $\eta$  and of the physical baryon density  $\Omega_b h^2$ . The green hatched areas represent the relative abundances as observed and measured in different astrophysical sites like mentioned above ( ${}^3\text{He}$  is omitted because the data was

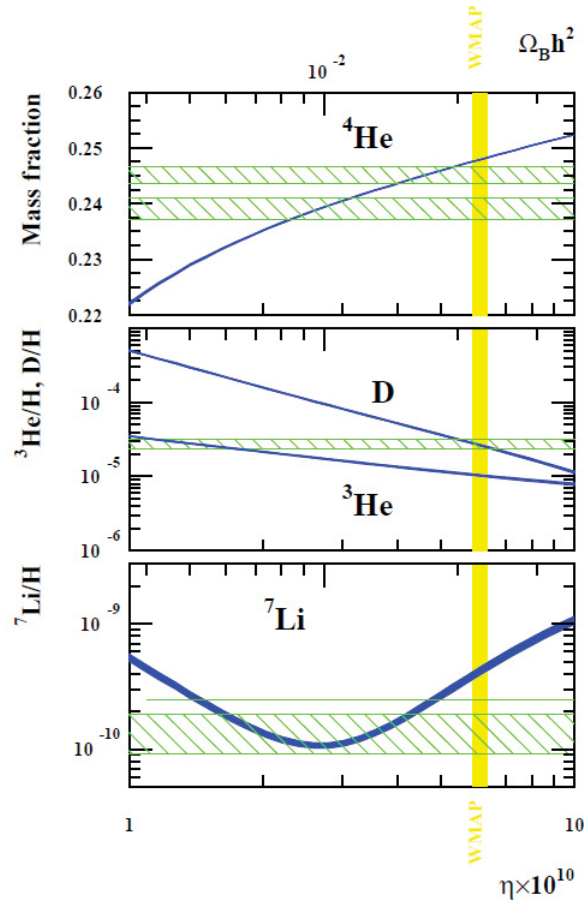


Figure 2.12: Mass fraction of  ${}^4\text{He}$  and relative abundance of  ${}^3\text{He}$ ,  ${}^2\text{H}$ , and  ${}^7\text{Li}$  as a function of baryon density, compared to the WMAP results [7].

found unreliable [7]). While not precise, these BBN measurement allowed to place limits on the baryon density such as  $0.005 < \Omega_b h^2 < 0.025$ , thus implying that most matter in the universe had to be non-baryonic. This is completely in agreement with the WMAP results (in yellow) which led to  $\Omega_b h^2 = 0.02264 \pm 0.0005$  [6].

### 2.3.3 Supernova Studies

A totally different approach to measure the cosmological parameters is to use type Ia supernovae and their redshifts by means of a space telescope like the Hubble Space Telescope (HST) [8]. These types of supernovae are preferred as they are the best high luminosity "standard candles", which simply means that their luminosity is known. Supernovae studies were thus used to demonstrate the accelerating expansion rate of the universe. It was indeed expected that distant supernovae should appear brighter than their redshifts would suggest. However, the opposite was observed, thus implying an expanding universe. Because this expansion is driven by the cosmological parameter  $\Lambda$

or dark energy, supernovae studies allow to put limits on the density of matter  $\Omega_m$  and energy  $\Omega_\Lambda$  in the universe. The results shown in equation 2.21 [8] are consistent with WMAP [6].

$$\begin{aligned}\Omega_m &= 0.25_{-0.06}^{+0.07}(\text{statistical}) \pm 0.04(\text{identified systematic}) \\ \Omega_\Lambda &= 0.75_{-0.07}^{+0.06}(\text{statistical}) \pm 0.04(\text{identified systematic})\end{aligned}\tag{2.21}$$

## 2.4 Where to look for Dark Matter?

By combining all the limits from the rotation curves of clusters of galaxies, CMB measurements and supernovae studies, figure 2.13 is obtained. There is remarkable agreement between these three very different techniques. The three datasets intersect in one region which matches the  $\Lambda$ CDM cosmological model and requires the existence of dark matter, thus making it the preferred region of interest for dark matter searches.

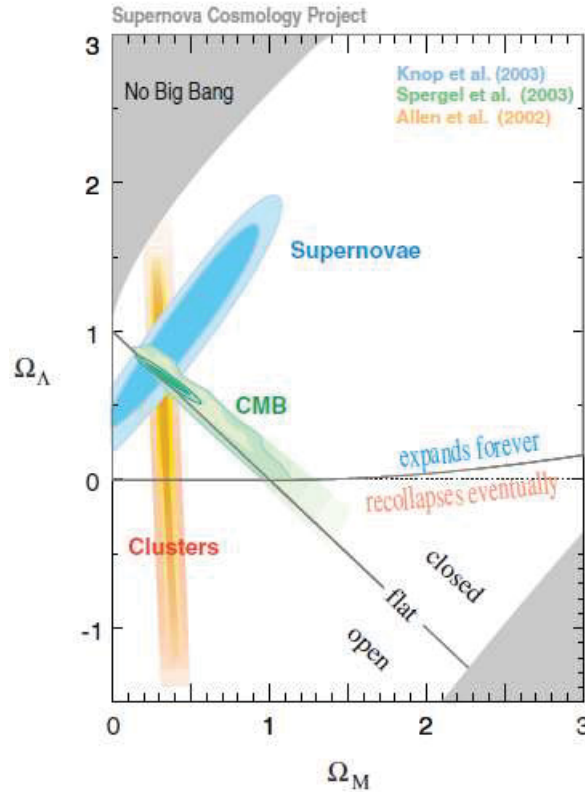


Figure 2.13: Combined results of clusters of galaxies, CMB and supernovae studies [8].

## 2.5 Dark Matter Theory Beyond the Standard Model of Particle Physics

### 2.5.1 Properties of Dark Matter

From the observational evidence of dark matter described in the previous sections several properties of dark matter can be implied:

- It must be stable on cosmological time scales otherwise it would have decayed by now.
- Dark matter must have been created with the correct abundance.
- It is non baryonic as shown by BBN and WMAP.
- Dark matter should be cold (CDM), or at least not hot, [45], meaning that it moves non relativistically, to fit the current accepted models.
- Due to the previous argument and because it is observed through gravitational effects, dark matter has to be massive.
- It is most likely charge neutral or electro-magnetic interactions must be strongly suppressed as otherwise, we would have already detected it.
- Finally, under the assumption that otherwise it would have been detected already, dark matter is thought to interact very weakly with ordinary matter. However dark matter is assumed to interact with standard model particles, otherwise it would have been difficult to create in the early universe.

### 2.5.2 The WIMP Miracle

A very general candidate for non-baryonic and cold dark matter is called the Weakly Interacting Massive Particle or WIMP. The WIMP is an ideal cold dark matter candidate because not only it happens to have the proper abundance to be cold dark matter but also the interactions which give the WIMP the correct density, also make it detectable. This happy coincidence is called the WIMP miracle.

In the  $\Lambda$ CDM scenario, in the early times during the radiation dominated era, the universe was constituted of a plasma in thermal equilibrium due to pair production and annihilation from particle-anti-particle collisions. The same as any other particle anti-particle pairs, WIMPs were pair-produced

and would annihilate at the same rate, thus preserving the equilibrium. This happened when the plasma temperature was much higher than the WIMP mass.

As the universe expanded, the plasma temperature decreased with decreasing photon energy until it finally was less than the WIMP mass, thus allowing WIMPs to be produced only from particle anti-particle collision with enough energy. Indeed, since WIMP production follows a Boltzmann distribution, the reduction in production was exponential by a factor  $e^{-m_\chi c^2/kT}$ . Simultaneously, with the expanding universe, the number density of particles decreased thus leading to decreasing production and annihilation rates. When the WIMP annihilation rate became smaller than the expansion rate of the Universe and at the same time when the mean free path of WIMP producing collisions became smaller than the Hubble radius (distance beyond which an object recedes from an observer at a speed higher than  $c$ ), production and annihilation of WIMPs stopped and has stayed constant since then. This is referred to as the freeze-out of the Universe. Consequently, the WIMP density normalized to a comoving volume which is expected today is the same as the relic density from the WIMP of the early universe. Figure 2.14 illustrates this process.

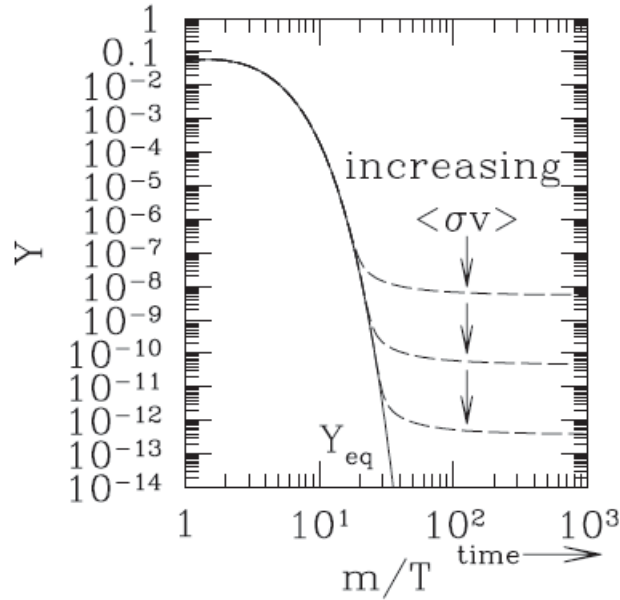


Figure 2.14: Evolution of the WIMP number density  $Y$  in the early universe from  $\Lambda$ CDM model [9].

At high temperatures  $T$ , where the plasma is in thermal equilibrium, the WIMP number density  $Y$  follows its equilibrium value  $Y_{eq}$ . However, this becomes less and less the case with decreasing temperatures where  $Y_{eq}$  becomes exponentially suppressed, until finally, at the freeze out temperature, the WIMP number density  $Y$  completely decouples from  $Y_{eq}$  and becomes stable. In addition, figure 2.14 links WIMP annihilation cross section  $\sigma$  with their relic density. Indeed, because WIMPs with

stronger interactions will take longer to decouple, higher annihilation cross section will result in smaller relic density. Consequently, relic density  $\Omega_{DM}$  and WIMP annihilation cross section are linked according to equation 2.22 where  $h$  is the normalized Hubble expansion rate, and  $\langle \sigma_{ann}v \rangle$  the velocity averaged total annihilation cross section.

$$\Omega_{DM}h^2 \simeq \frac{3 \times 10^{-27} cm^3/s}{\langle \sigma_{ann}v \rangle} \quad (2.22)$$

Coincidentally, from equation 2.22, a weak scale for the WIMP annihilation cross section results in the observed dark matter relic density. This constitutes the WIMP miracle.

### 2.5.3 Supersymmetry

It has been known for a long time that the Standard Model (SM) of particle physics, the global theory governing the world of sub-atomic physics is inexact or incomplete. Indeed, the SM has many unexplained or unsatisfactory elements to it. For example, the SM does not explain gravity nor the scale difference between gravity and the weak interaction (the so-called hierarchy problem, described later in this work), nor does it explain the matter antimatter asymmetry of the universe. It also does not incorporate dark matter but predicts way too much dark energy, and finally predicts massless neutrinos which is now known to be false. Consequently, to solve or at least overcome some of these problems, new theories, new models beyond the SM are being developed.

One of the best motivated extension to the SM is supersymmetry (SUSY). SUSY is a model which relates exchange particles, bosons and the constituents of matter, fermions to one another. To do so, it predicts the existence of supersymmetric partners called sparticles to all known fermions and bosons that would only differ by a spin of a half. The superpartners of bosons are thus fermions and vice versa.

The appeal of SUSY is that by linking matter particles and force carriers, it unifies the strong, weak and electromagnetic forces at high energies, solves the hierarchy problem and provides a natural mechanism for electroweak symmetry breaking, which will be discussed later. In addition, under certain conditions, SUSY may also provide adequate dark matter candidates. Finally SUSY appears to be at an energy level accessible by experiments, making it an ideal model to be tested.

It is noteworthy to mention that there are several levels within SUSY and it is possible to have more than one kind of supersymmetry transformation leading to as many as 105 free parameters. However, the first and simplest level of SUSY which requires only one transformation is called

the Minimal Supersymmetric Standard Model (MSSM) and is today the favored and most probed supersymmetric model as it has only 4.5 free parameters. However this is relatively fast changing as the Large Hadron Collider (LHC) still has found no clue of supersymmetry thus making theorists wonder if the MSSM is not a too simplified model [12].

*Electroweak Symmetry Breaking* Another key point worth mentioning is that, just like the Standard Model, SUSY must be broken in order to conserve electroweak symmetry breaking (EWSB). The need for an electroweak theory comes from the fact that if the Standard Model respected symmetry, the uncharged gauge bosons, the photon and the  $Z^0$  should have the same mass, which is clearly not the case. Consequently, the gauge symmetry of the Standard Model is a broken symmetry. The electroweak theory, developed in 1979 by Glashow, Salam and Weinberg postulates that the weak and electromagnetic interactions are unified at high energies while at low energies, the weak and the electromagnetic interactions are simply two different manifestations of this unified electroweak interaction. It is this behavior in the transition from high to low energies that is called symmetry breaking. This electroweak theory has proven to be right especially when it accurately predicted the mass of the Z boson, which was subsequently found in 1983. However, while it is clear that the symmetry is broken, the big question was how is it broken. This question was answered by the theory of the Higgs mechanism, which postulates that mass is acquired by the interaction of particles with a Higgs field through the exchange of a spin 0 particle, the Higgs boson. This theory has been confirmed with the discovery of the Higgs boson in 2012.

However, when extending the SM to SUSY, the Higgs mechanism has to be modified slightly. Indeed, SUSY does not work with the SM as it is now but instead requires the addition of 4 other Higgs bosons to the SM, otherwise the theory would have gauge anomalies. In the current SM, there is only one Higgs doublet with one neutral and one charged complex component, with a total of 4 degrees of freedom. The  $Z^0$  and  $W^{+-}$  gauge bosons have absorbed three of them, acquiring mass in the process. The remaining degree of freedom is the scalar Higgs boson  $H^0$ . However, if that were the case in SUSY, this would give only one Higgsino (the superpartner of the Higgs) and the summed hypercharge of each generation of fermion would not be conserved anymore. Adding an extra doublet allows to create a second Higgsino with opposite hypercharge, thus making SUSY an anomaly free theory.

*Hierarchy Problem* One of the most prominent problems of the SM is the so called hierarchy problem. Simply put, the question which puzzles physicists is why is the weak force  $10^{32}$  times larger

than gravity. Or why is the Higgs boson so much lighter than the Planck mass?

Indeed, from perturbation theory, the Higgs mass  $m_H$  should be close to the Planck mass due to large radiative corrections to its mass  $\Delta m_H$  coming from its interaction with heavy particles, especially the top quark. This is represented in equation 2.23 where  $m_0$  is the bare mass which is at the Planck scale.

$$m_H = m_0 + \Delta m_H \quad (2.23)$$

In a bit more detail, any particle is thought to couple with the Higgs field. This is represented by the Yukawa coupling  $\lambda_f$ . Additionally, the coupling of fermions to the Higgs field gives an interaction term and because the mass of a fermion is proportional to  $\lambda_f$ , the Higgs boson will couple more to heavy particles. Consequently, the largest corrections to the Higgs mass are given by the Higgs' interactions with heavy particles. The corrections to the mass of the Higgs boson are given by:

$$\Delta m_H^2 = -\frac{|\lambda_f|^2}{8\pi^2}[\Lambda_{UV}^2 + \dots] \quad (2.24)$$

where  $\Lambda_{UV}$  is the ultraviolet cutoff beyond which the SM is not valid anymore.

From equation 2.24, it is then clear that if  $\lambda_f$  is large, the radiative correction would also be very large and so should the Higgs mass be. However, the Higgs mass was found to be very small in comparison, at 125 GeV, which implies very fine tuning where the radiative corrections cancel the bare mass almost perfectly.

Introducing SUSY however, allows to solve this problem. Indeed, if to each fermion, a bosonic superpartner is introduced, and assuming that the coupling to the Higgs stays the same, for that superpartner equation 2.24 would become

$$\Delta m_H^2 = \frac{|\lambda_f|^2}{8\pi^2}[\Lambda_{UV}^2 + \dots] \quad (2.25)$$

The change of sign between equation 2.24 and 2.25 is simply due to the spin statistics theorem which describes bosons and fermions by their wavefunctions and spins.

Thus, in a model where each fermion has a boson superpartner and vice-versa, the total contribution to the Higgs mass becomes zero, thus explaining its low mass. In addition, because SUSY is broken, sparticles which should have identical masses, do not, thus implying that the cancellation is not perfect and that the mass scale for these superpartners is at the mass scale of the new particles, presumed to be at the TeV scale [46].

*R-Parity* Another, motivation for SUSY, more relevant to this work, is the observation that the lightest supersymmetric particle (LSP) derived from SUSY is heavy, neutral and stable and appears to be an excellent dark matter candidate.

With the introduction of superpartners both lepton and baryon quantum numbers are not conserved anymore. Without them being conserved, protons, being the lightest baryon, should be able to decay but the observational data clearly indicates that protons are stable with a half-life of about  $10^{33}$  years [47]. Consequently something had to be added to SUSY to keep the proton stable, this something is a new quantum number called R-parity.

R-parity is a multiplicative quantum number which has a value of 1 for all the SM particles and a value of -1 for all the superpartners since they must have the same value of B and L as their SM counterparts. Also, R-parity is of course conserved in interactions. It is represented as

$$R = (-1)^{3B+L+2s} \quad (2.26)$$

where B is the baryon number, L the lepton number and s the spin of the particle.

Conservation of R-parity has two very important consequences. Firstly collisions of SM particles will always produce sparticles in pairs while sparticles will only decay into an odd number of sparticles. Secondly, heavier sparticles can only decay into lighter sparticles. This second consequence has an even more important corollary which predicts that the LSP cannot decay and hence has to be stable, in the same way that baryon conservation predicts that protons must be stable in the SM.

The LSP, provided that it can match dark matter properties, is a naturally viable dark matter candidate. Under the assumption that it had once been in thermal equilibrium in the early universe, the LSP is thought to have a mass inferior to 1 TeV and should thus be reachable by collider experiments.

### ***Supersymmetric Dark Matter Candidates***

What particles from the MSSM could qualify as a dark matter LSP? If the LSP was electrically charged it would bind to conventional matter and would thus be readable detectable. The same holds for a strongly interacting LSP. Because it has not been observed in any experiment, the LSP is thus thought to be neutral and to interact very weakly with matter. However, even with these conditions, several candidates still arise from the MSSM. Note that of course all these candidates have the proper thermal relic abundance and relic density associated with dark matter.

*The Sneutrino* The sneutrino as its name indicates is the supersymmetric partner of the neutrino. As neutrinos have a spin  $1/2$ , sneutrinos would have spin  $0$ . Sneutrinos have however been proven to be non viable dark matter candidates [48]. For the sneutrino to match the WIMP relic density, it should have a mass between  $550$  GeV and  $2.3$  TeV. With such heavy masses, sneutrinos would be expected to interact rather strongly with heavy nuclei and should thus have been already detected in direct dark matter searches using such nuclei [48]. Consequently sneutrinos with such masses are excluded. Note that the possibility of light sneutrinos was also discarded by results from the LEP collaboration [49].

*The Gravitino* The gravitino,  $\tilde{G}$ , is yet another DM candidate although it is not a necessary ingredient for SUSY. Indeed, the gravitino is the hypothetical SUSY partner of another hypothetical particle, the graviton, which would be the gauge boson mediating gravity. But because there is no way to detect the graviton, its existence is purely speculative and so it is also for the gravitino. That said, in the hypothesis that the graviton does exist, its superpartner, the gravitino, would be a fermion with spin  $3/2$ . Contrary to other LSPs, the gravitino is not expected to have been in thermal equilibrium in the early universe because it interacts only via gravity. However, the gravitino could have been produced in the early universe during collisions or decays from heavier sparticles. Because gravitinos only have gravitational-strength interactions, gravitinos are expected to come mostly from decays of the next to lightest supersymmetric particle (NLSP), thus making the nature of the NLSP an important question to answer. As of now, some candidates for the NLSP in a gravitino LSP scenario are the stau and the stop, both of which should have a distinctive signature in colliders. However, since the gravitino interacts only gravitationally, it is not directly detectable in dark matter searches.

*The Neutralino* The preferred LSP candidate is the lightest neutralino. In the MSSM there are four neutralinos, each being a linear combination of the superpartners of the neutral gauge bosons ( $W^0$  and  $B$ , whose superposition give the photon and the  $Z$ ) and Higgs bosons: the wino  $\tilde{W}^3$ , the bino  $\tilde{B}$  and two higgsinos  $\tilde{H}_1$  and  $\tilde{H}_2$ .

The composition of the neutralinos is, as stated before, a linear combination of these four fields:

$$\chi = \alpha\tilde{B} + \beta\tilde{W}^3 + \gamma\tilde{H}_1 + \delta\tilde{H}_2 \quad (2.27)$$

where  $\alpha, \beta, \gamma$  and  $\delta$  are mixing coefficients.

Depending on the region of the supersymmetric parameter space realized in nature, the neutralino may be more bino-like, wino-like or higgsino-like.

It is to be noted that neutralinos are Majorana particles implying that they are their own anti-particle. Additionally, the neutralinos are expected to interact (ever so slightly) with matter, making them directly detectable.

#### ***2.5.4 Other Extensions to the Standard Model And Non-WIMP Dark Matter Candidates***

While for the past decade SUSY has been largely favored, the question of other extensions to the SM is now resurfacing due to the unexpected lack of results on SUSY at the LHC. There are many other theories which could explain the existence of dark matter and only a few are presented here. In addition to those, other theories are Little Higgs Dark Matter, Technicolour, Mirror Dark Matter, WIMPonium, SuperWIMPs etc...

#### ***Axions***

Axions have initially been postulated by the Peccei-Quinn theory to solve the strong CP problem. CP symmetry is the product of two symmetries, the charge conjugation C and the parity P. The charge conjugation changes the charge of a particle thus transforming it into its anti particle while parity is a mirror like transformation. CP symmetry was found not to be conserved for weak interactions and CP violation has now been observed for different particles in different experiments [50], [51]. It is now thought that while CP symmetry is violated the underlying CPT symmetry is an exact symmetry, where T is the time reversal symmetry stating that if a motion is allowed, so is the inverse motion. With this in mind, there are no reasons why CP symmetry should be conserved in the strong interaction, as there are some terms in the Lagrangian which could break the symmetry. However, no trace of CP violation has been found in the strong interaction. This phenomenon is what is referred to as the strong CP problem. To solve this, Peccei-Quinn introduced the idea that, by adding an extra symmetry to the Standard Model (called Peccei-Quinn symmetry) which would be spontaneously broken, the CP violating term in the strong interaction would be canceled. The introduction of this new field gives a new particle, the axion.

Axions are predicted to be light (less than 1 eV), neutral and have low interaction cross sections to the weak and strong interactions. Because axions could also be produced in the right amount to match dark matter, they are a natural candidate for dark matter. Axions are in principle detectable

as they can decay into photons in the presence of a strong magnetic field or couple to electrons by the axio-electric effect. Currently, the experiment ADMX is trying to detect axion dark matter in the local galactic halo. This experiment ran for 2 years and found no sign of axions in a  $1.9 \mu\text{eV}$  to  $3.53 \mu\text{eV}$  range. It is now being upgraded and will resume its search in the spring of 2014 [52].

### ***Extra Dimensions***

Another proposed extension to the SM is to introduce extra dimensions to solve the hierarchy problem rather than use SUSY. This is called the Kaluza-Klein theory and has the particularity that it also includes the existence of DM under the form of KK particles. The KK theory was first proposed to link gravity and electromagnetism by extending general relativity to 5 dimensions (one extra spatial dimension). The basics of the theory describes the universe as having a fourth spatial dimension curled up in a small circle, so that a particle moving around that circle will return to its original position. The size of the dimension is given by the size of the circle, or how much distance does a particle have to cover until it goes back to its original position [53]. This extra dimension is thus a compact set, and the phenomenon of having a space-time with compact dimensions is referred to as compactification. Due to this compactification, the momentum along the extra-dimension is a discrete quantity which leads to Kaluza-Klein (KK) resonances in the particle spectrum. Therefore, each Standard Model particle is accompanied by a so called KK tower, an ensemble of heavier partners with the same quantum numbers and spin. Just as in SUSY, the lightest KK particle would be stable and be a candidate for dark matter. At low energies, only massless particles could be produced but after a certain threshold, extra dimensions would show up. These extra dimensions could then be produced and observed in colliders [54], however no hints of extra dimensions have been found to this day.

### ***Sterile Neutrinos***

Finally, dark matter could be made of hypothetical particles called sterile neutrinos, which have been postulated as a new type of heavy neutrino. In the same way that neutrinos are now known to have three oscillating flavors, it is suspected that a fourth flavor could explain small discrepancies in neutrino counts at several reactors and be the answer to the dark matter question. These heavy neutrinos would have a mass of a few keV and would constitute warm dark matter, that is, moving semi-relativistically. Several experiments are now trying to detect them such as Minos [55] or the upcoming KATRIN experiment [56].

## 2.6 *Experimental Detection*

While there are many candidates for DM and many different experiments trying to detect DM in one form or another, WIMPs and in particular the SUSY LSP neutralino, being in principle easier to detect than other candidates, are still the preferred candidate and consequently the major part of the DM experiments are tuned to look for this particular form of dark matter. In the next section, the emphasis is put on such experiments.

WIMPs can interact in two different ways. They can either annihilate with another neutralino, usually to fermion-antifermion pairs, gauge boson pairs or final states containing Higgs bosons, or they can scatter off a nucleus. Assuming WIMPs annihilate in the early universe, the cross section of WIMP interactions with ordinary matter can be calculated as shown by equation 2.22. Experiments sensitive to these cross sections can be built to look either for annihilation products or evidence of scattering by direct coupling to the spin of the particle (spin-dependent interaction) or by direct coupling to the nucleus (spin-independent interaction). Therefore WIMPs should in principle be detectable in experiments. Consequently there is a plethora of different experiments using different detection techniques that are currently trying to detect WIMPs.

### 2.6.1 *Indirect Searches*

One way to detect dark matter is to search for its annihilation products which can be in the form of neutrinos, gamma rays, electron-positron pairs, antiprotons or antinuclei. A WIMP passing through the Sun, the Earth or any dense object has a higher probability to scatter elastically, lose energy in the process and thus become gravitationally bound when its velocity drops below the relevant escape velocity. Consequently, WIMPs are thought to accumulate at the center of such objects thus increasing the probability of annihilation. Therefore, all indirect searches look in favorable locations, usually at the center of a massive object, where the probability of annihilation is the greatest.

#### *Gamma Ray Telescopes*

Very good candidates as dark matter annihilation products are high energetic gamma rays. Indeed, because photons are not bound, telescopes can be pointed at the source of such gamma rays in order to detect them. These gamma rays would come from neutralinos annihilation according to the Feynman diagrams shown in figure 2.15.

Also, because the typical velocity of WIMPs in the halo is a thousand times smaller than  $c$ , it

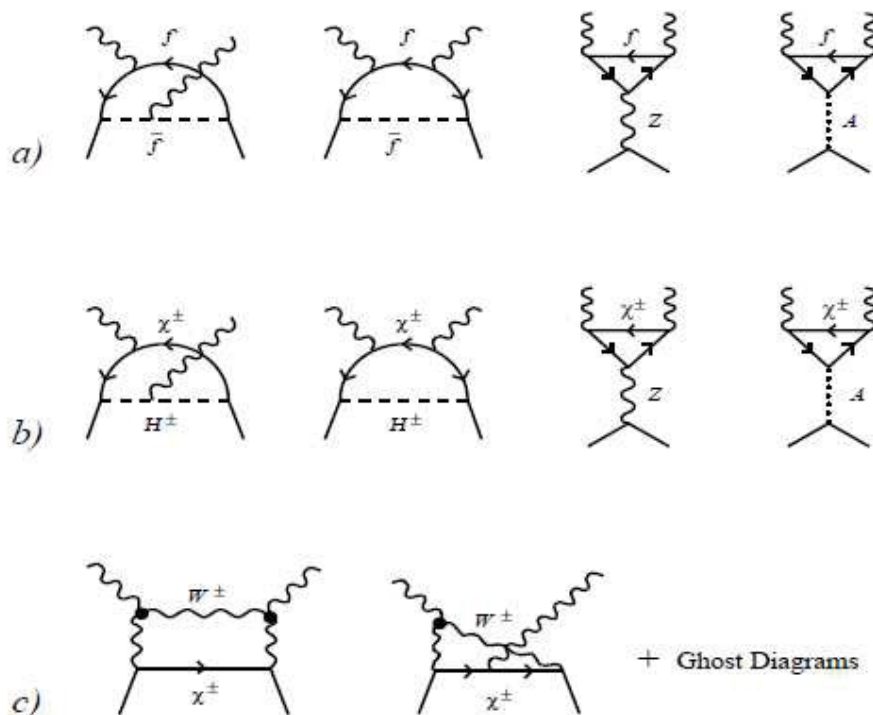


Figure 2.15: Feynman Diagrams from WIMP annihilation into two photons. a) fermion sfermion loops, b) charged Higgs chargino loops, c) chargino W-boson loops [10].

is expected that WIMP annihilation will produce monochromatic photons at an energy equal to the WIMP mass (10 GeV - 1 TeV) [12]. Because there are no known sources of gamma rays of that strength, the observation of such high energy monochromatic gamma rays would be a clear dark matter signal.

To look at gamma ray sources, experiments use telescopes both space based and ground based.

Space based telescopes have the advantages of looking directly at the gamma rays without interference from the Earth's atmosphere and of having a much wider field of view. The Fermi gamma rays telescope (formerly GLAST) [57], which was launched in 2008, is such a telescope. It tracks gamma rays by looking at the characteristic positron-electron pairs emitted from the interaction of a gamma ray with a dense layer of tungsten. Since its launch, Fermi has made many interesting discoveries, most notably the fact that background gamma ray sources are responsible for only  $16\% \pm 9\%$  of the gamma-ray background radiation indicating that something else, possibly dark matter, must provide most of gamma ray background [58]. As of today, the Fermi collaboration has not found a conclusive hint on dark matter, however their new results impact the range of particle masses over which dark matter thermal production in the early universe would have been possible [59].

Unlike space based telescopes, ground based telescopes are subject to a lot of interference from

the Earth's atmosphere. Also because gamma-rays are not penetrative enough, ground based telescopes cannot hope to detect them directly. However, detection becomes possible when looking at the Cherenkov light and/or secondary particles coming from the passage of gamma rays in the atmosphere. That said, particles other than gamma rays, such as normal cosmic rays, can emit such a signature. The success of a ground based gamma ray telescope thus lies in the ability to distinguish the Cherenkov light produced by the gamma rays from those produced by cosmic rays. To make this distinction, the observed Cherenkov light is compared to numerical simulations of atmospheric showers. One such ground based experiment is the VERITAS telescope [60] which looks at the gamma ray emission from objects which are expected to have a large dark matter abundance, such as dwarf galaxies. Recently, VERITAS discovered a TeV gamma-ray emission from a supernova remnant [61], however, no detected gamma ray emission has been related to dark matter [62].

### *Neutrino Telescopes*

Neutrinos are an indirect product of WIMP annihilation. They come from the decays of the leptons, quarks, gauge bosons and Higgs bosons, which make up most of the annihilation products of WIMPs. Such neutrinos are for example produced in the Sun, where WIMPs became gravitationally bound after scattering elastically off of the nuclei in the Sun. Because these neutrinos escape the Sun with minimal absorption they could constitute a very distinct dark matter signal. Additionally, looking for neutrinos to identify dark matter has the advantage of being independent from many astrophysical constraints. Indeed, the present WIMP annihilation rate in the Sun is given by equation 2.28 [35] and depends only on the WIMP capture rate in the Sun  $C_{\odot}$ , the age of the Solar System  $t_{\odot}$  and the annihilation cross section times the relative WIMP velocity per volume  $A_{\odot}$ , thus leaving out any dependency on structure or variation in the local dark matter density. It is also completely independent from the dark matter distribution or from any galactic properties such as radiation fields.

$$\Gamma = 0.5C_{\odot} \tanh^2(\sqrt{C_{\odot}A_{\odot}t_{\odot}}) \quad (2.28)$$

In fact, equation 2.28 is maximized when  $\sqrt{C_{\odot}A_{\odot}t_{\odot}} \gg 1$  which corresponds to an equilibrium between annihilation and capture rates. Knowing that the age of the solar system is about 4.5 billion years, this condition is fulfilled, thus meaning that today annihilation and capture rate are indeed in equilibrium. This leads to the fact that the WIMP annihilation rate in the Sun  $\Gamma$  today depends

only on the WIMP capture rate in the Sun  $C_{\odot}$  and is independent of even the WIMP annihilation cross section [35]:

$$\Gamma = 0.5C_{\odot} \quad (2.29)$$

Consequently various DM candidates' signals can be predicted reliably in a neutrino telescope, allowing for a broad testing of different models.

Because of their weak interaction rate, neutrinos can be detected on Earth only in very quiet (background free) environments. This is why most high energy neutrino telescopes are under ice like IceCube [63], or under the sea like ANTARES [64], which make use of a vast volume of water as their detectors to increase the probability of observing rare interactions while shielding out most cosmic rays. When neutrinos interact with water or ice, they emit secondary particles such as muons through charged current interactions, which themselves create Cherenkov light. This light is detected by very large arrays of photomultipliers.

As of now, neither the IceCube, nor the ANTARES collaboration have reported a dark matter discovery. The latest results of IceCube however, especially in the spin-dependent regime, have put stringent limits on the dark matter cross section [65].

### *Positron and anti-proton experiments*

Like neutrinos, positrons and anti-protons are yet another potential secondary product of dark matter particle annihilation. However, unlike neutrinos or gamma rays, these particles cannot be found by directly pointing a telescope to their source. Indeed, positrons and anti-proton are charged particles and consequently by the time they reach Earth, their path has been diverted by galactic magnetic fields, making it impossible to track down their origin. To try and detect dark matter products in the form of antimatter, satellite detectors like PAMELA [66] or AMS-02 [67] have been launched. Assuming that most sources of antimatter are known, these experiments look for antimatter excess in their spectra which would indicate a new unknown anti-matter source, like WIMP annihilation for example. The PAMELA experiment saw signs consistent with dark matter in an excess of positrons above 10 GeV and up to 100 GeV [68].

However, further analysis of the results has revealed that this excess of positron comes from a previously unknown anti-proton radiation belt around the Earth [69]. The antiparticles forming the belt are products of the interaction of cosmic rays with the Earth atmosphere which seem to

accumulate at altitudes of several hundreds kilometers above the surface of the Earth, right in the line of sight of PAMELA. This is as of now, the most abundant source of antiprotons near the Earth [69].

The other experiment, AMS-02 has just released results in March 2013 [70]. Their data, with unprecedented accuracy, closely follows the PAMELA data and also displays a striking unexplained excess of high energy positrons which would be consistent with positrons coming from dark matter annihilation. Figure 2.16 shows the data from AMS-02 superimposed with the data from PAMELA and Fermi-LAT, another satellite, as well as the theoretical range for positron fraction (the grey region on figure 2.16). This clearly shows an increase above what is expected from positrons produced in cosmic-ray interactions. In addition, the positron fraction spectrum exhibits no fine structure while showing a slope decrease of an order of magnitude between the range 10-250 GeV and 20-250 GeV. Because no anisotropy in the positron to electron ratio are found either, all these features combined really hint to a new phenomenon, such as dark matter annihilation. However, the signal is not conclusive enough to discard other explanations [70].

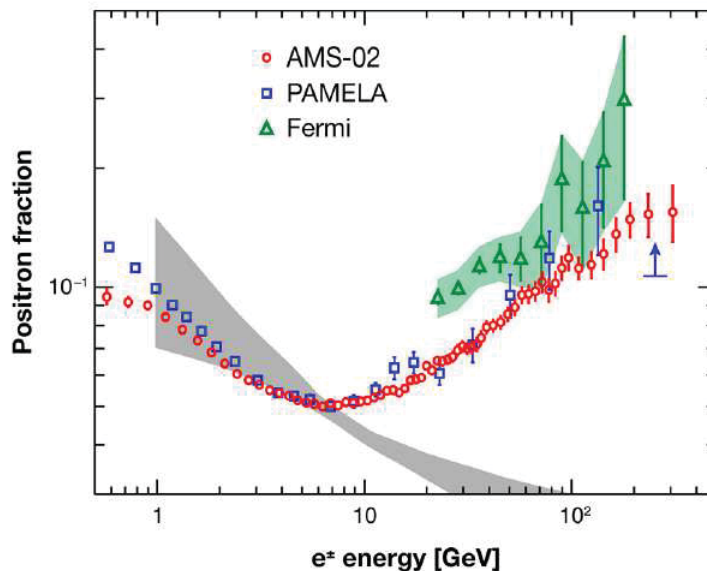


Figure 2.16: AMS-02 positron fraction compared with other satellite data and theoretical model [11].

### 2.6.2 Direct Searches

While indirect searches look for products of WIMP annihilation, many experiments are trying a much more direct approach to tackle the dark matter problem. They hope to discover dark matter particles by directly looking at their interactions, mostly through elastic scattering with the nuclei

of an appropriate target material. This target material depends on the type of detector and also on the type of interaction expected.

Because WIMPs interactions are expected to be extremely rare, to try to isolate WIMPs from the sea of particles which hit the Earth every day and constitute a dominant source of background, such as cosmic ray products or neutrinos and muons produced from air showers, most direct searches experiments are located in mines deep underground or in tunnels under mountains. The crucial point of all direct search experiment is to be able to remove or identify as much background as possible from the detectors. Depending on the type of detector, this is achieved through various techniques. The goal of direct search experiments is thus to have a completely quiet, background free environment where only a handful of interactions per year will happen. Each of these interactions is expected to have a specific signature which matches the ones of the particles of the SM, the hope being that some of these interactions will not be identifiable because they are the signature of a new type of previously undiscovered matter.

There are two types of possible elastic dark matter interaction with a target nucleus, either the WIMP will couple to the spin of the nucleus which will be referred to as a spin-dependent interaction, or the WIMP will couple coherently to all nucleons in the nucleus which is then referred to as a spin-independent interaction. Spin dependency depends on the target nucleus. A target with an odd number of nucleons like  $^{19}\text{F}$  or  $^{131}\text{Xe}$ , having a non-zero spin, is sensitive to both spin-dependent and spin-independent interactions while a target nucleus like  $^{40}\text{Ar}$  which has a spin zero, is sensitive to only spin-independent interactions. Consequently some targets having both even and odd isotopes like xenon are excellent as they are highly sensitive to both spin-dependent and spin-independent interactions. In any case, the fundamental property to be determined is the elastic scattering cross section  $\sigma$  which is a measure of the probability that a WIMP will scatter elastically from the target nucleus. This cross section is what allows then to determine the detection rate in both direct and indirect searches. It is noteworthy to emphasize that the derivation of this cross section is model-dependent and that the following holds for specific theories only, such as SUSY.

### ***Spin-Dependent Interaction Cross Section***

As mentioned above, in a spin-dependent interaction, the spin of the WIMP couples directly with the spin of the nucleus. Feynman diagrams describing spin-dependent interactions are shown on figure 2.17

For spin-dependent interactions, the differential cross section can be written as:

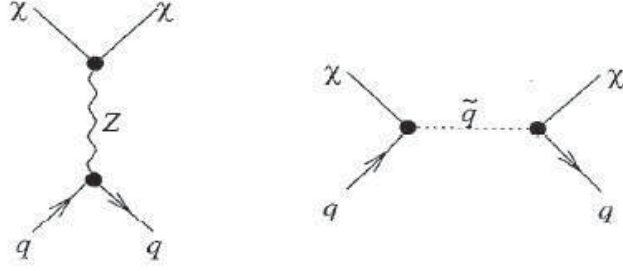


Figure 2.17: Feynmann diagram for spin-dependent interactions from [12].

$$\frac{d\sigma}{d|\mathbf{q}|^2} = G_F^2 \frac{C}{v^2} F^2(|\mathbf{q}|) \quad (2.30)$$

where  $G_F$  is the fermi coupling constant which describes the strength of the fermi interaction,  $C$  is a dimensionless number carrying all the particle physics model information,  $v$  is the velocity of the WIMP relative to the target,  $\mathbf{q}$  is the momentum transfer and  $F$  is the so called form factor. The form factor is a key parameter as its form changes depending on the type of interaction. Simply put, the form factor is a measure of the coherency of the interaction or how well, depending on its energy and thus on its momentum transfer, an incoming WIMP will see the structure of the nucleus. In the limit of the momentum transfer approaching zero, so when a WIMP has such a small energy and a long de Broglie wavelength that it will only see the nucleus as a uniform ball, the WIMP and the target nucleus form a macroscopic two body collisional system where the form factor has no impact anymore and is thus set to one. In the case of a spin dependent interaction, the form factor describes the coupling of the WIMP with the different spin parts of the nucleus (mainly the proton and neutron, the electron contribution to the spin being much more spread out and thus negligible).

In equation 2.30, the dimensionless number  $C$  is given by the following equation:

$$C = \frac{8}{\pi} \Lambda^2 (J)(J+1) \quad (2.31)$$

where  $J$  is the total angular momentum and  $\Lambda$  is described by

$$\Lambda = \frac{1}{J} [a_p \langle S_p \rangle + a_n \langle S_n \rangle] \quad (2.32)$$

where  $\langle S_n \rangle$  and  $\langle S_p \rangle$  are the expectation values of the spin content of the neutron and proton group respectively in the nucleus and  $a_p$  and  $a_n$  are the coupling constants. These expectation values and couplings are calculated using nuclear models and are the constituents of the form factor. Note however, that there are many different models to calculate form factors and that some of them

differ greatly [12].

As a consequence of the importance of the form factor in the cross section determination, experiments looking for spin-dependent interactions will favor target nuclei such as fluorine, which have a high  $C$  and a high form factor.

### ***Spin-Independent Interaction Cross Section***

Feynman diagrams describing a spin independent interaction are shown in figure 2.18. In this figure, a neutralino interacts with a quark by exchanging a higgs boson  $H$  or by producing a virtual squark. The only difference with a spin-dependent interacting is the exchange of a Higgs instead of a  $Z$  boson [12].

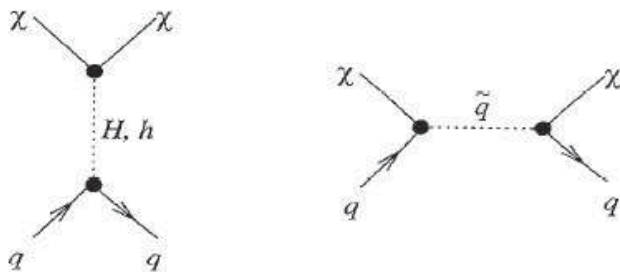


Figure 2.18: Feynman diagram for spin-independent interactions from [12].

In the case of spin independent interactions, the form factor differs greatly from the spin-dependent one. Indeed, because no spin structure needs to be resolved, the nucleon operators simply count the number of nucleons making the form factor proportional to the number of the nucleons and thus making heavy material ideal target for spin-independent interactions in the limit of  $q^2 = 0$ .

While the form factor is still equal to one at zero momentum transfer, at non zero momentum transfer it is simply the Fourier transform of the nucleon density [12]. Typically, the most common form factor used for heavy nuclei such as xenon is the Woods-Saxon form factor given by [71]:

$$F(q) = \left( \frac{3j_1(qR_1)}{qR_1} \right)^2 e^{-(qs)^2} \quad (2.33)$$

where  $j_1$  is the first spherical bessel function,  $q$  is the momentum transferred,  $R_1$  is an effective nuclear radius and  $s$  is the nuclear skin thickness.

The differential cross section, while essentially in the same form as equation 2.30, needs to incorporate this new form factor. The  $C$  value of equation 2.30 thus becomes:

$$C = \frac{1}{\pi G_f^2} [Z f_p + (A - Z) f_n] \quad (2.34)$$

where  $G_f$  is the fermi constant,  $Z$  is the number of protons,  $A$  is the number of nucleons and  $f_p$ ,  $f_n$  are the neutralino couplings to protons and neutrons respectively.

This leads to the differential cross section of:

$$\frac{d\sigma}{d|\mathbf{q}|^2} = \frac{1}{\pi v^2} [Z f_p + (A - Z) f_n]^2 F^2(q) \quad (2.35)$$

where  $v$  is the velocity of the WIMP with respect to the target and  $q$  is the momentum transferred from the WIMP to the nucleus [12].

For heavy nuclei with  $m_\chi \gg m_N$ ,  $f_p = f_n$  so the cross section becomes proportional to the square of the nucleus atomic number  $A$ , making once again heavy nuclei, such as xenon, favorable targets for spin-independent interactions.

### **Event Rate**

With the definition of the form factor for both spin dependent and spin independent interactions and with the appropriate cross section, the differential event rate per nuclear recoil energy  $E_R$  expected in a detector can be calculated by:

$$\frac{dR}{dE_R} = \frac{\rho_0}{m_N m_\chi} \int_{v_{min}}^{\infty} v f(v) 2m_N \frac{d\sigma}{d|\mathbf{q}|^2} dv \quad (2.36)$$

where  $\rho_0$  is the local WIMP density,  $m_N$  the mass of the target nucleus,  $m_\chi$  the mass of the WIMP,  $d\sigma/d|\mathbf{q}|^2$  is the differential cross section and  $f(v)$  is the WIMP speed distribution in the detector frame normalized to unity [72], which contains all the astrophysical uncertainties. Note that  $E_R$  is the nuclear recoil energy or energy transfer and is related to  $q$  via

$$q = \sqrt{2m_N E_R} \quad (2.37)$$

Because of the heavy mass of the WIMP, any elastic scattering will happen in a non-relativistic frame. Consequently the recoil energy  $E_R$  can be expressed as a function of the scattering angle  $\theta$  in the frame of the center of mass and as a function of the reduced mass  $\mu_N$  and the nucleus mass  $m_N$  as laid out in equation 2.38.

$$E_R = \frac{\mu_N^2 v^2 (1 - \cos\theta)}{m_N} \quad (2.38)$$

Finally, integrating equation 2.36 over all possible recoil energies gives the total event rate expected per kilogram per day in the detector.

### **Detection**

As mentioned before, direct detection of dark matter requires WIMP-nuclei elastic scattering. The recoiling nuclei can then usually be detected by the following processes: scintillation and/or ionization and/or heat deposition. Many experiments combine two of these processes in order to optimize background discrimination.

In these experiments, if a neutralino deposits enough energy when scattering elastically off of the target nucleus, the latter can induce the emission of electrons (ionize), photons (scintillate) or phonons (heat). The preferred materials are noble gases for scintillation experiments, high purity semi-conducting crystals for ionization experiments and bolometers or superheated liquids for heat deposition experiments.

*Noble Gases Experiments* The typical noble gases used in DM direct searches experiments are xenon and argon. Experiments using liquid noble gases include XENON100 and XENON1T, ZEPLIN-III, XMASS, LUX, DarkSide, ArDM and DEAP-3600.

These experiments can be categorized in single or double phase experiments. Single phase experiments, such as DEAP-360 and XMASS, are essentially a big volume (usually spherical) filled with noble liquid, surrounded by photosensors to detect a scintillation signal from an interaction.

Double phase experiments, like XENON100 or DarkSide, use their target material in both liquid and gas state and observe both scintillation and ionization signals by again using photosensors.

Also xenon experiments have the advantage to be able to probe both spin-dependent and spin-independent regime due to the presence of both odd and even isotopes in the xenon. Argon experiments however, are limited to spin-independent searches.

In general, liquid noble detectors are very attractive as while performing extremely well, they are also rather cheap and easily scalable to larger size. Note that as of now, the most sensitive experiments looking for dark matter are the liquid noble experiments XENON100, to which the next chapter will be dedicated, and LUX.

*Cryogenic Experiments* Crystal targets like germanium or silicon are another material of choice for DM experiments such as CDMS, EDELWEISS, CRESST and CoGeNT. Because of the material choice, these experiments are mainly suited for spin-independent searches. The principle of operation of these detectors is to cool down these crystals to cryogenic temperatures so that a particle interaction will heat them up by very small but detectable amounts that will give a first signal. A second signal is given by the ionization or scintillation coming from the interaction.

To detect the heat, these experiments operate a target material at low temperature where the heat capacity  $C$  follows from Debye's law in equation 2.39 where  $T$  is the temperature in K and  $\theta_D$  is the Debye temperature.

$$C \left(\frac{T}{\theta_D}\right)^3 \quad (2.39)$$

By operating at low temperature, the heat capacity becomes very small, yielding large temperature variations for small energy depositions. To detect the heat, transition edge sensors (TES) are typically used. These are made of superconducting material and are operated at the transition temperature between normal and superconducting regimes. The resistivity then varies drastically for very small temperature changes. This technique allows single phonon detection with an incredibly good energy resolution.

Cryogenic experiments are amongst the oldest dark matter experiments and were leading the search for a while. However due to their expensive cost and the difficulty of scaling to large volume, they are now letting the way to liquid noble experiments.

*Superheated Liquid Experiments* The last type of dark matter experiments, such as PICASSO or COUPP, are best performing in the spin-dependent regime by using as target nuclei, superheated liquids, which are materials which stay liquid at temperatures at which they should be gaseous, such as a compound of fluorine. An interaction with such a droplet will provide enough energy to provoke a phase transition from liquid to gas, drastically increasing the droplet volume. By suspending the droplets in a gel, this transition gives rise to a pressure wave which is transmitted through the gel and detected by piezoelectric sensors.

*Summary and other experiments* Finally, as a summary, table 2.1 lists many of the current experiments in the field, both spin-dependent and spin-independent. Each of the experiments is categorized according to the type of detection it uses and by its target nuclei.

Experiment	Type	Target Nucleus
ArDM	ionization + scintillation	gas/liquid argon
CDMS	ionization + heat deposition	germanium and silicon crystals
CRESST	heat deposition + scintillation	sapphire crystals and calcium tungstate
CoGeNT	ionization	germanium crystals
COUPP	heat deposition	$CF_3I$
DAMA/LIBRA	scintillation	sodium iodide crystals
DARKSIDE	ionization + scintillation	gas/liquid argon
DEAP/CLEAN	scintillation	liquid argon
EDELWEISS	ionization + heat deposition	germanium crystals
KIMS	scintillation	CsI crystals
LUX	scintillation + ionization	gas/liquid xenon
NAIAD	scintillation	sodium iodide crystals
PANDAX	ionization + scintillation	gas/liquid xenon
PICASSO	heat deposition	$C_4F_{10}$
SIMPLE	heat deposition	$C_2ClF_5$
XENON	ionization + scintillation	gas/liquid xenon
XMASS	scintillation	liquid xenon
ZEPLIN III	scintillation + ionization	gas/liquid xenon

Table 2.1: Summary of the current dark matter search experiments

*Annual Modulation* Another experiment, DAMA/LIBRA, uses a somewhat different technique than all the other experiments. It looks at a modulation in the event rate as a function of time. This modulation comes from the revolution of the Earth around the Sun and the motion of the latter in the galaxy. Since dark matter has no net velocity in the galaxy, in summer when the Earth moves in the same direction as the Sun and through the dark matter halo, an increase in the relative velocity between dark matter and the target material should be observed. In the winter, it should be the opposite. Since the rate is dependent on the relative velocity, there should be a higher rate in summer than in winter. This is indeed what DAMA/LIBRA sees as shown in figure 2.19, where at low energy an annual modulation is seen with the expected phase and period. However, it is worth noting that while the fact that DAMA/LIBRA does see an annual modulation is undeniable, the cause of this annual modulation has not been found nor conclusively proven to be dark matter.

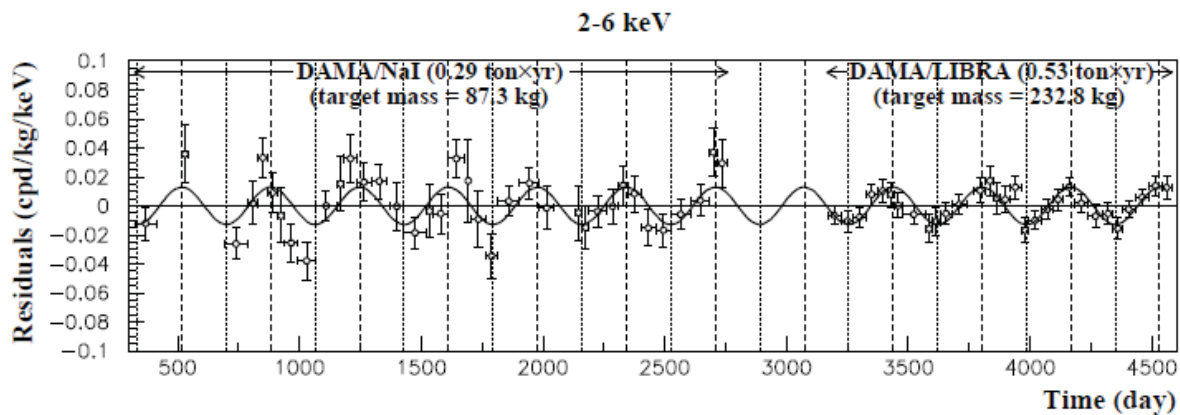


Figure 2.19: The DAMA/LIBRA modulation signal from [13].

### 2.6.3 The DAMA/LIBRA Controversy

Until now there has been only one claim for the discovery of dark matter via direct detection which was made very early on by the DAMA/LIBRA collaboration. Other experiments, such as CoGeNT, have seen an excess of events near threshold, that could be interpreted as a dark matter signal, however the CoGeNT results have now been found to be due to an unexpected background rather than dark matter [73]. In addition, all other experiments, using various detection techniques, have since then refuted these claims. Some like KIMS or CDMS looked at annual modulation signals and found nothing conclusive placing a limit on the annual modulation rate of less than 0.06 event per keV per kg per day in the 5-11.9 keV nuclear recoil energy range at the 99% confidence level [74], limit inconsistent with the DAMA or CoGeNT findings. Others like XENON100, and more recently LUX, which have a much higher sensitivity altogether also rejected this claim [23] [75] even in the theoretical case of inelastic dark matter [76]. Still others like CRESST, did see something [77] but after careful analysis have now declared that it was due to background. EDELWEISS also published new results highly constraining the DAMA/CoGeNT claims [78] while collider experiments also greatly constrained the possibility of low mass WIMPs. In the spin-dependent sector, the PICASSO experiment recently also ruled out the DAMA claim [79].

All these divergent results from the so many completely different experiments make the DAMA/LIBRA claim for dark matter less and less believable each passing year.

### 2.6.4 Dark Matter in Colliders

With the LHC being turned on in 2011, and the discovery of the Higgs boson in 2012, collider experiments at the LHC like ATLAS and CMS are now naturally turned partly towards the search

for dark matter. The working principle of the LHC is to create a plethora of particles by colliding very high energy protons or heavy ions together, the goal being to detect all the SM particles as well as new previously undiscovered particles. In the more relevant case of ATLAS and CMS detectors, DM particles can be produced in two ways, in cascade decays from heavier unstable supersymmetric particles and by pair-production [14]. The DM particles can then be detected in a calorimeter via an analysis of the missing transverse momentum. Indeed, because of the tremendous energy release in such processes, the energy between hadrons is constantly exchanged and the information on the initial momentum of the colliding hadrons along the beam axis is lost. However, because particles start in the beam axis, the initial momentum of the particles traveling perpendicular (transverse) to the beam is known to be zero. Consequently, if a collision results in a net momentum in the transverse direction, it means that something else, such as neutrinos or new undetectable particles, has been created in the process. Since SM neutrino cross sections are well understood, an excess relative to this expectation would be evidence for a new non-interacting particle. The big advantage of such an approach is obviously that it is model independent, however it is also based on two major assumptions, that WIMPs are pair-produced and that any new particles mediating the interaction between WIMPs and SM are too heavy to be produced directly [14].

Until now, while the LHC experiments probed several interaction channels as shown on figure 2.20, they have seen no sign at all of any dark matter signal, thus raising the possibility that the theoretical extensions to the SM are not adequate and that new, very different theories must be devised.

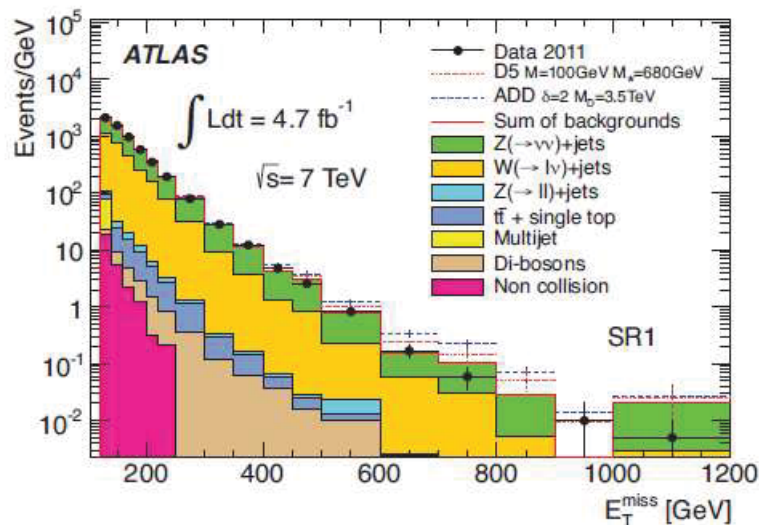


Figure 2.20: Results on the missing transverse energy from the ATLAS experiment. [14].

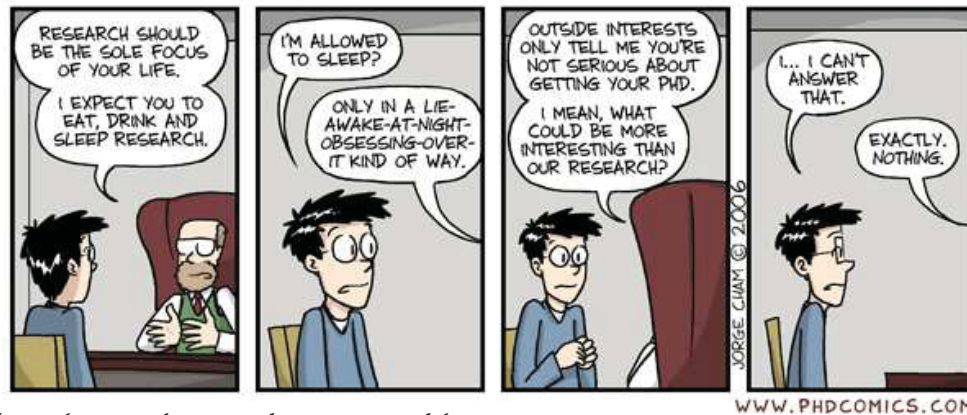
---

## 2.7 Summary

As shown by CMB and SN studies, the universe is currently seen as made of about 5% visible matter, 26% of dark matter and 69% dark energy. For now, dark energy eludes scientists but dark matter may be about to become a solved mystery. There is more and more convincing evidence that dark matter exists, and many experiments are making great progress trying to detect it directly or indirectly. A very nice feature of dark matter is that it fits into SUSY, the favorite extension to the SM. If dark matter is a SUSY particle, then it is the LSP such as the neutralino. Experiments are always aiming at better sensitivities and limits to try to detect the WIMP LSP which will lead to either a discovery or to a revision of the current theory. In any case, experiments are now pushing forward to try and solve the dark matter enigma in the next years. Leading amongst them are noble liquids detectors such as the ones used in the LUX experiment and the XENON project.



## Chapter 3. THE XENON100 EXPERIMENT



*Piled Higher and Deeper* by Jorge Cham [www.phdcomics.com](http://www.phdcomics.com)

The XENON100 experiment is the second step in the phased project XENON. It has now reached its scientific goal in the search for dark matter and is being used as testing device for the upcoming experiment XENON1T. Located at a depth of 3600 mwe (meter water equivalent) at the Gran Sasso National Laboratory (LNGS) in Italy below the Gran Sasso mountain peak, it benefits from a very good shielding from cosmic ray muons with a muon flux reduced by six order of magnitudes [80] compared to the surface. Those muons would otherwise be a non-negligible source of background. Figure 3.1 shows the placement of the actual XENON100 experiment in the laboratory.



Figure 3.1: Location of the XENON100 experiment at LNGS.

While LNGS is not the deepest underground laboratory in the world as seen on figure 3.2, the protection it offers coupled to the unique self shielding properties of the XENON detectors is sufficient

to reach a background level low enough to conduct a dark matter detection experiment at the frontier of modern sensitivity.

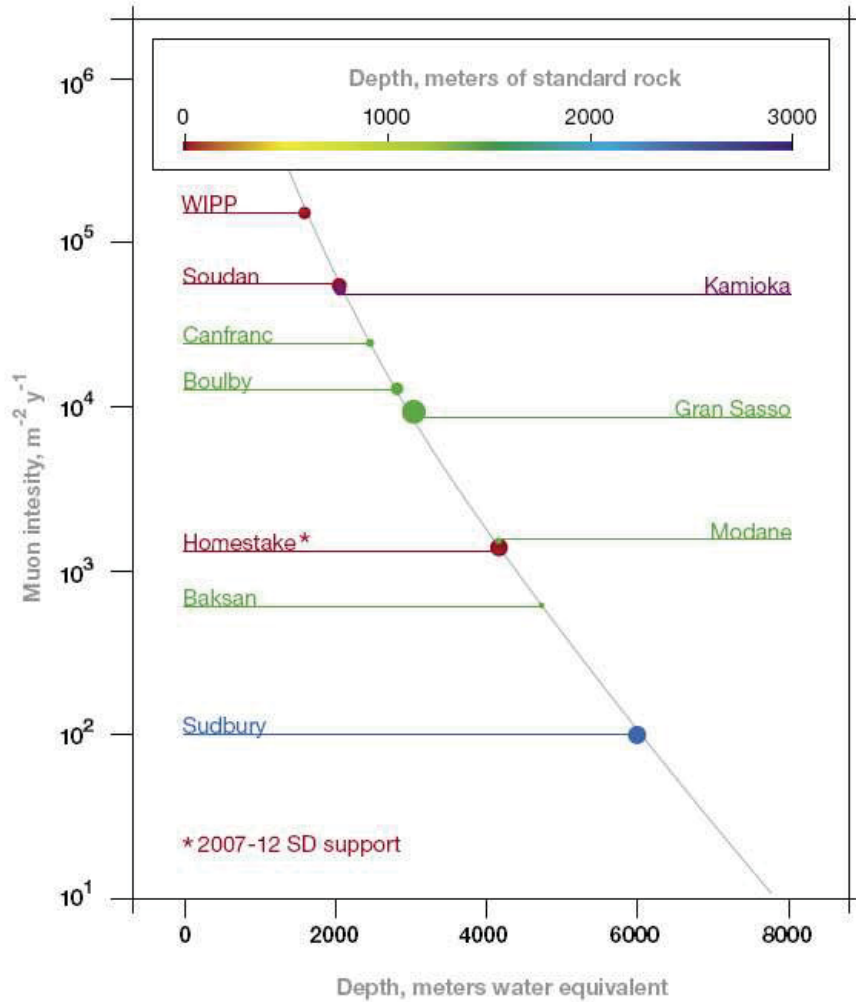


Figure 3.2: Various underground laboratories around the world

The experiment consists of one detector containing about 165 kg of xenon surrounded by a passive shield, made of copper, polyethylene, lead and water. The shield ensures that most residual particles which could contribute to an eventual background are stopped.

Detector operation consists of several runs, which are long periods of data taking. A new run is started each time the detector is opened and changes are made to the hardware. During each run, many datasets are taken, some in the presence of radioactive sources to calibrate the detector, and others, just as is, to probe the background and try to detect a dark matter signal.

### 3.1 The XENON Program

While many dark matter experiments using different technologies were already in the field, none were using liquid scintillators. In 2001, the idea of a dual phase time projection chamber (TPC) as a detector using xenon as an active target was proposed by Elena Aprile [81]. The first experiment using this technology, XENON10, used a detector containing around 10 kg of xenon. It was soon followed by a 100 kg scale detector (XENON100). The next step, XENON1T, currently ongoing, is to build a detector containing about 1 ton of xenon. The project has now been extended to include a fourth phase, a multi-ton detector called XENONnT.

#### 3.1.1 XENON10

The XENON10 detector, shown on figure 3.3, developed extremely fast and in 2007, the first results from the XENON10 experiment were published [82] while establishing a world leading limit of  $9 \cdot 10^{-44} \text{cm}^2$  on the WIMP-nucleon cross section, thus making it a viable new technology for the search of dark matter and imposing the most competitive constraints on dark matter searches at the time.

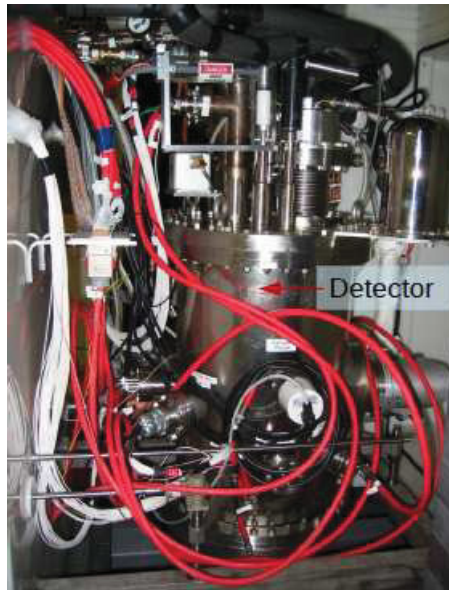


Figure 3.3: The XENON10 Detector

#### 3.1.2 XENON100

The XENON100 detector, shown on figure 3.4 which has already reached its scientific goal was built between 2007 and 2009 and started taking data in 2009, releasing in the process several world

best sensitivities in 2010 [21], 2011 [19] and 2012 [23] but without a significant signal above the expected background. These results have probed a non-negligible chunk of the predicted SUSY parameter space, and have set limits on the WIMP-nucleon cross section with the current limit at  $\sigma < 2.0 \cdot 10^{-45} \text{cm}^2$ .



Figure 3.4: The XENON100 Detector [15]

### 3.1.3 XENON1T

Finally, the ongoing step in the XENON project is the XENON1T detector, as shown on figure 3.5 which is currently being built and should start taking science data in 2015. With its 1 ton fiducial volume of liquid xenon and much lower background, this detector will increase the sensitivity to the WIMP-nucleon cross section by two orders of magnitude, with a projected sensitivity of  $2 \cdot 10^{-47} \text{cm}^2$ .

### 3.1.4 XENONnT

While XENON1T is being designed and constructed, an even bigger version of XENON1T, called XENONnT is now in development. This multi-ton detector would be an upgrade to XENON1T and would use the same existing infrastructure as XENON1T.

### 3.1.5 Dual Phase Xenon TPC

In all the phases of the experiment, the detector used is a special case of Time Projection Chamber (TPC), a dual phase xenon TPC, whose working principle is schematized on figure 3.6. It consists of a cylinder made of a highly reflective material, teflon in this case filled with liquid xenon with a gaseous phase on top. Radiation induces electron or nuclear recoils in the xenon, which produce

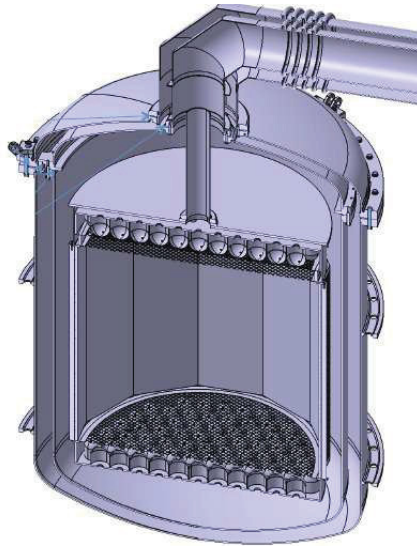


Figure 3.5: The XENON1T Detector

scintillation (light) and ionization (electrons) signals. The scintillation signal is promptly detected by photomultiplier tubes (PMTs) at the top and bottom of the detector and is called the S1 signal. The ionized electrons are drifted along the chamber by an externally applied electric field until they reach the gas phase and are extracted into the gas phase by a much stronger electric field. They are then accelerated by the same electric field and produce a second scintillation signal upon colliding with xenon atoms. This second scintillation signal is then collected by the PMTs and called S2. This S2 signal is often referred to as proportional scintillation as its size is directly proportional to the number of extracted electrons.

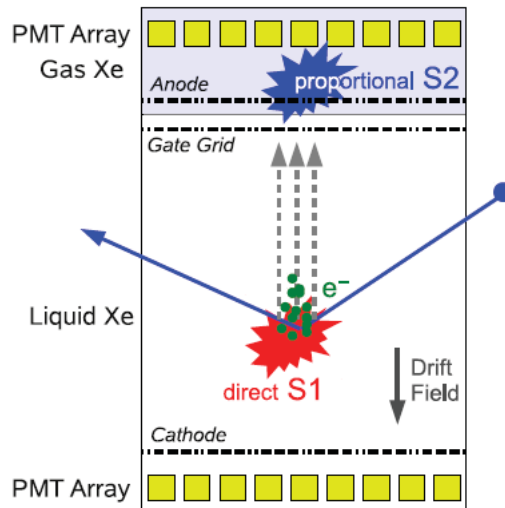


Figure 3.6: Principle of a dual phase xenon time projection chamber

### 3D Position Reconstruction

Such a detector is a powerful tool as it allows 3D position reconstruction of the events. Because electrons drift vertically, the x-y location of the S2 signal is the same as the S1 signal. In addition, because the S2 light is generated just below the top PMT array, x and y coordinates of an event can be determined from the top PMT hit pattern of the S2 signal which is then very localized as shown on figure 3.7. The resolution for such a reconstruction is in the case of XENON100, less than 3 mm [19].

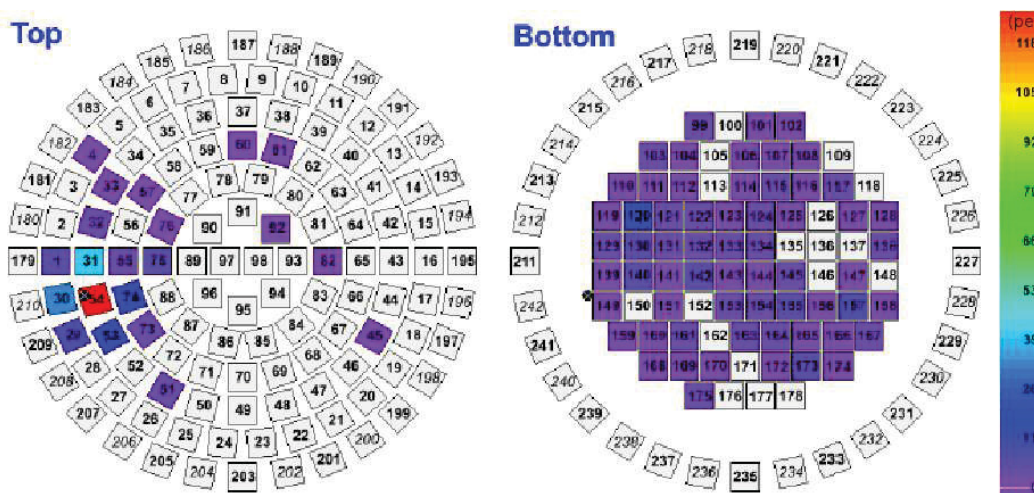


Figure 3.7: Example of a PMT hit pattern for an S2 signal.

As for the z-position of an event, it can simply be inferred from the S1-S2 time separation. Indeed, the time difference between an S1 and its corresponding S2 signal is the time it took an electron to drift upwards to the gas phase. Because the constant drift speed is measured to be  $1.73 \text{ mm } \mu\text{s}^{-1}$  [15] and because the light travel time is instantaneous on this scale, the distance undergone by the electron can be easily and accurately calculated with a resolution of less than 0.3 mm [19]. This time element is the reason why the XENON detector is referred to as a TPC.

#### 3.1.6 Choice of Xenon as Liquid Scintillator

When the XENON program started, the majority of the dark matter detectors were semiconductors, such as those used in the CDMS experiment. As seen in the previous chapter, this type of detectors use heat and ionization and/or scintillation to try and detect a dark matter signal, however, they are limited as cryogenic detectors are usually expensive and not easily scalable. Moreover, discovering dark matter with only one type of detector would be suspicious and so there was a definite need to find an alternative method of detection. The use of scintillators such as noble liquids, provided such

an alternative by exploiting a unique feature of noble liquids which is to be both excellent scintillators and ionizers.

Among noble liquids, three are today in use as dark matter detectors, liquid xenon (LXe), liquid argon (LAr) and liquid neon (LNe), however because the latter is a much poorer ionizer, the emphasis is usually put on using either LXe or LAr. The XENON program, as its name indicates, gave preference to xenon ( $Z=54$ ) over argon ( $Z=18$ ) for many different reasons. The high atomic number of xenon gives it amazing self-shielding properties against external gamma radiation which is attenuated at the edges of the detector, allowing the center of the detector to be background free. This very powerful propriety of xenon allows then for a background reduction through fiducialization, i.e by selecting only events from the quiet center of the detector.

In addition to a high atomic number, LXe also has a high density which makes it a much better detector medium since a large target mass can be contained in a small detector, leading to an increased sensitivity. Its high density also provides the non-negligible advantage to make LXe very compact and thus easily scalable. Moreover, LXe gives scintillation light at 178 nm, which implies that it can be directly detected by photomultiplier tubes (PMTs) as they can utilize a quartz window that is transparent at this wavelength and a bialkali photocathode with a high quantum efficiency of more than 30%. This is not the case for LAr which thus requires wavelength shifting in the detection process. Additionally, unlike LAr or cryogenic crystals, LXe requires cryogenics temperatures only around  $-100^{\circ}C$  which make the handling of the detector much easier.

Many other qualities make LXe the target of choice. First the spin independent WIMP scattering rate at low recoil energies, which is the range of interest to find dark matter in the XENON100 experiment, is much better for LXe than for other noble liquids. This is shown on figure 3.8, where the differential scattering rate is calculated according to equation 3.1 [16] [83]:

$$\frac{dR}{dQ} = \frac{\sigma_p \rho_0 A^2}{\sqrt{\pi} v_0 m_\chi m_p^2} F^2(Q) \frac{k_0}{k_1} \times \left[ \frac{\sqrt{\pi} v_0}{4v_e} \left( \text{erf}\left(\frac{v_{min} + v_e}{v_0}\right) - \text{erf}\left(\frac{v_{min} - v_e}{v_0}\right) \right) - \exp\left(\frac{-v_{esc}^2}{v_0^2}\right) \right] \quad (3.1)$$

where  $Q$  is the recoil energy,  $\rho_0 = 0.3 \text{ GeV}/\text{cm}^3$  is the local dark matter density,  $A$  is the number of nucleons,  $m_\chi$  is the WIMP mass,  $m_p$  is the mass of the proton,  $v_{min} = (Qm_N/2m_r^2)^{-1/2}$  is the minimum WIMP velocity that can produce a recoil of energy  $Q$  with  $m_N$  the mass of the nucleus and  $m_r$  the reduced mass,  $v_{esc} = 544 \text{ km}/\text{s}$  is the escape velocity of WIMPs in the Milky Way,  $v_0 = 220 \text{ km}/\text{s}$  is the speed of the sun about the center of the galaxy,  $v_e$  is the relative speed of the

earth and sun through the galaxy,  $F(Q)$  is the form factor as explained in the previous chapter and  $k_0$  and  $k_1$  are constants linked through:

$$k_1 = k_0 \left[ \operatorname{erf}\left(\frac{v_{esc}}{v_0}\right) - \frac{2v_{esc}}{\sqrt{\pi}v_0} \exp\left(-\frac{v_{esc}^2}{v_0^2}\right) \right] \quad (3.2)$$

The recoil rates shown in figure 3.8 show two features. At low recoil energy, the rate scales with  $A^2$ , as expected from equation 3.1. However, the form factor, which is the Fourier transform of the mass distribution of the nucleus, depends on the type of target and describes the loss of coherence for the scatter as a function of recoil energy. Consequently, the slope of the spectrum is different for different targets. In particular, xenon has a zero in the form factor due to destructive interference at a recoil energy around 100 keV because of the large size of the xenon nucleus, while for smaller atoms like Ar and Ge the zero is at much higher energies (not shown on figure 3.8). Thus, at low recoil energies, Xe is the target of choice, while at higher energies the rate falls below that of lighter isotopes. In order to take advantage of the high rate for Xe, a low energy threshold is necessary.

Second, xenon consists of about half odd numbered isotopes thus allowing for both spin-dependent and spin-independent interactions which of course gives it an advantage over LAr which can mostly probe spin-independent scatters, as it contains only traces of odd isotopes. Another very interesting propriety is that LXe has no long lived isotopes, except for  $^{136}\text{Xe}$  which has a half life of  $2.165 \cdot 10^{21}$  years [84], thus making xenon a very radioactive free medium. A final advantage is that despite being more expensive than LAr, LXe is still relatively cheap and can be found easily.

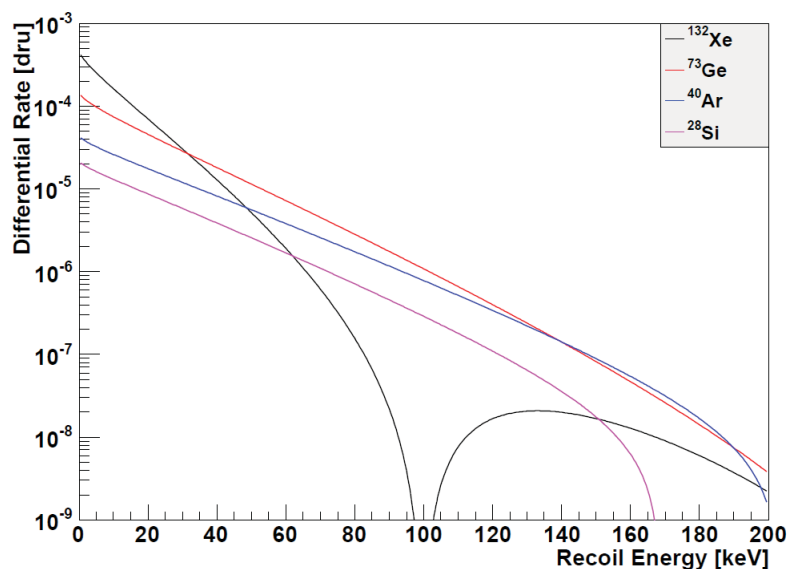


Figure 3.8: Differential WIMP spin independent scattering rate for several targets with  $m_\chi = 100\text{GeV}$  and  $\sigma_p = 10^{-44}\text{cm}^2$  [16]

### 3.2 Principle of Ionization and Scintillation

To understand the signal generation of the XENON100 experiment, it is important to understand the underlying basic physics principles pertaining to ionization and scintillation, and how they are implemented in this detector.

When a particle passes through the detector, it can interact with the electron cloud or the nucleus of an atom. In the case of gamma radiation, the interaction with the electron cloud dominates, and the available interactions are the photoelectric effect, Compton scattering, and if the gamma energy is greater than twice the electron mass, pair production. For neutrons and WIMPs, the dominant interaction is a coherent scatter off of the nucleus. Gammas thus induce electron recoils (ER) while neutrons and WIMPs produce nuclear recoils (NR). The recoiling electron or nucleus, as it travels, excites and ionizes other xenon atoms due to collisions to ultimately give out scintillation light. The non-trivial process leading up to this scintillation light is schematized on figure 3.9 and explained in details in the next section.

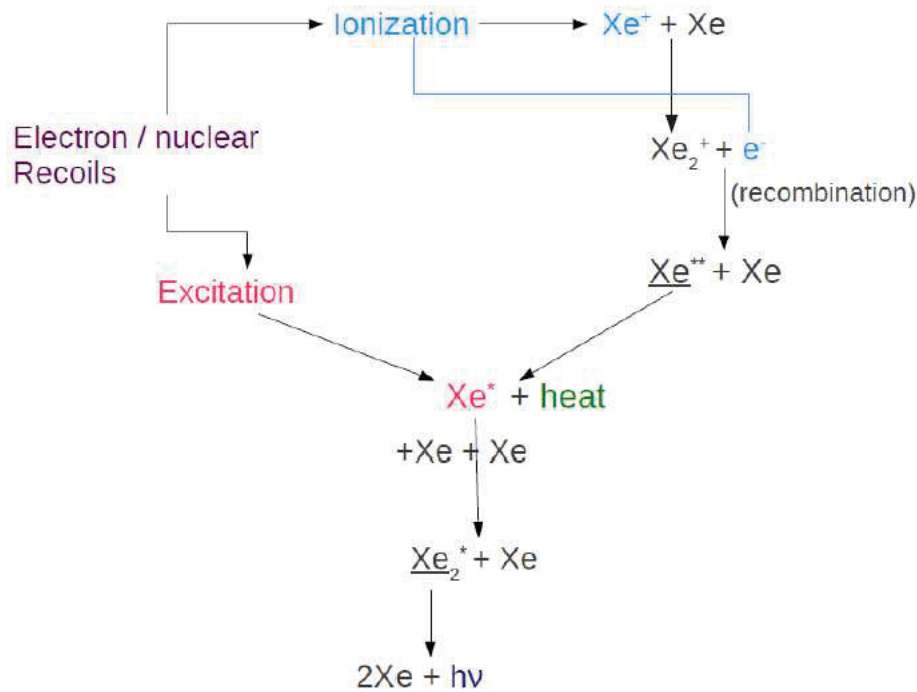


Figure 3.9: Principle of Scintillation for LXe

#### 3.2.1 The Scintillation Process

Scintillation is a luminous radiation of a material induced by exposure to radiation. In noble liquids, it arises from the decay of excited atoms ( $Xe^*$ ) to the ground state ( $Xe$ ). The excitation can happen

either by directly exciting the atom, or by the recombination of ionized electrons. However, the excited atoms do not decay directly to the ground state, but go through an intermediate step.

The intermediate state is created in two ways. In the first case, when an excited atom interacts with another atom (Xe), they combine to create an excited dimer ( $Xe_2^*$ ), a bound state consisting of one excited and one ground state xenon atom. This dimer is then de-excited and returns to a dissociative ground state where the dimer is separated into two monomers ( $2Xe$ ). This de-excitation is accompanied with the emission of a single ultra-violet (UV) photon.

This intermediate step is extremely important because the reaction 3.3 is irreversible.



This means that xenon atoms in the ground state can't be excited directly to this state, and therefore xenon is transparent to its own scintillation light.

In the second case, the ionized atom ( $Xe^+$ ) interacts with an atom creating an ionized dimer ( $Xe_2^+$ ). This dimer can then recombine with the free electron coming from the initial ionization. The products of this recombination consist of an highly excited atom ( $Xe^{**}$ ) and a stable atom (Xe). The highly excited atom decays to a lower excited state ( $Xe^*$ ) via heat dissipation. Finally, the latter excited atom undergoes the process described above in the first case, creating a dimer ( $Xe_2^*$ ) and then releasing a UV photon.

### 3.2.2 Ionization Yield

In the presence of an electric field, some of the ionized electrons can be drifted and collected separately, giving a distinct ionization signal. These electrons then do not have the possibility of recombining, and thus reduce the scintillation signal. There is therefore an anti-correlation between the scintillation and ionization signals due to the fluctuations in the amount of electrons that recombine.

In addition, the electron ion recombination process does not have a 100% probability to happen and sometimes, the ionizing electron does not recombine with an ion. Because of the denser tracks of nuclear recoils, their probability of electron-ion recombination is higher than for electronic recoils, making it harder to collect the ionizing electrons.

The ionization yield  $Q_y$  is simply defined as the number of observed electrons per unit recoil energy ( $e^-/keVr$ ) and thus depends on the strength of the applied electric field. It has been measured for nuclear recoils by [17] for different electric fields as shown on figure 3.10. The increase at low energies

can be explained by the drop in recombination rate due to the decrease of the electronic stopping power at these energies [35].

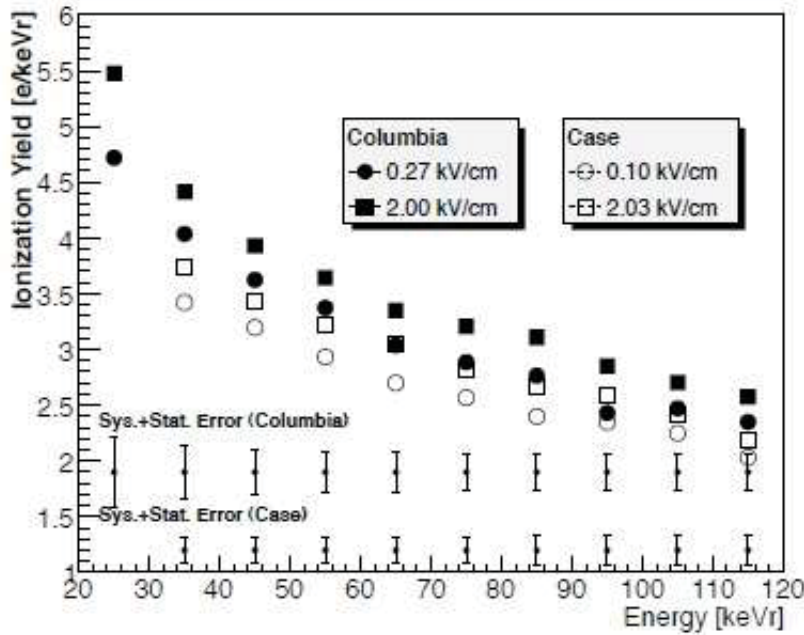


Figure 3.10: Ionization yield from nuclear recoils at different electric fields [17]

Because the S2 scintillation process is based on the ionization yield, the higher the ionization yield of a material, the better. This ionization yield is given by the average energy needed to produce an ion-electron pair,  $W$ . A smaller  $W$  will thus yield more ionization. This is yet another advantage of using LXe over LAr, as LXe has a  $W$  of 15.6 eV versus 23.6 eV for LAr.

The ionization yield is an interesting feature as it can be measured with much better statistics than the scintillation yield, especially at lower energies, because the S2 signal is an amplified and much stronger signal than S1. This potentially allows detectors to be more sensitive to WIMP detection at low energies.

### 3.2.3 Scintillation Yield

The scintillation yield for electron and nuclear recoils is the number of scintillation photons created per energy deposited. This is closely related to the energy calibration, which includes both the scintillation yield and the efficiency of collecting and detecting these photons. This will be described in detail in section 3.4.3.

### 3.3 Technical Description of the XENON100 Experiment

After having introduced the XENON program and the main characteristics common to all phases of the experiment, it is important to focus on the current experiment, XENON100. A review of the experiment will be given, containing details pertaining to both software and hardware.

#### 3.3.1 The Detector

A technical drawing of the inside structure of the XENON100 detector is shown on figure 3.11 and its various features are explained in this section.

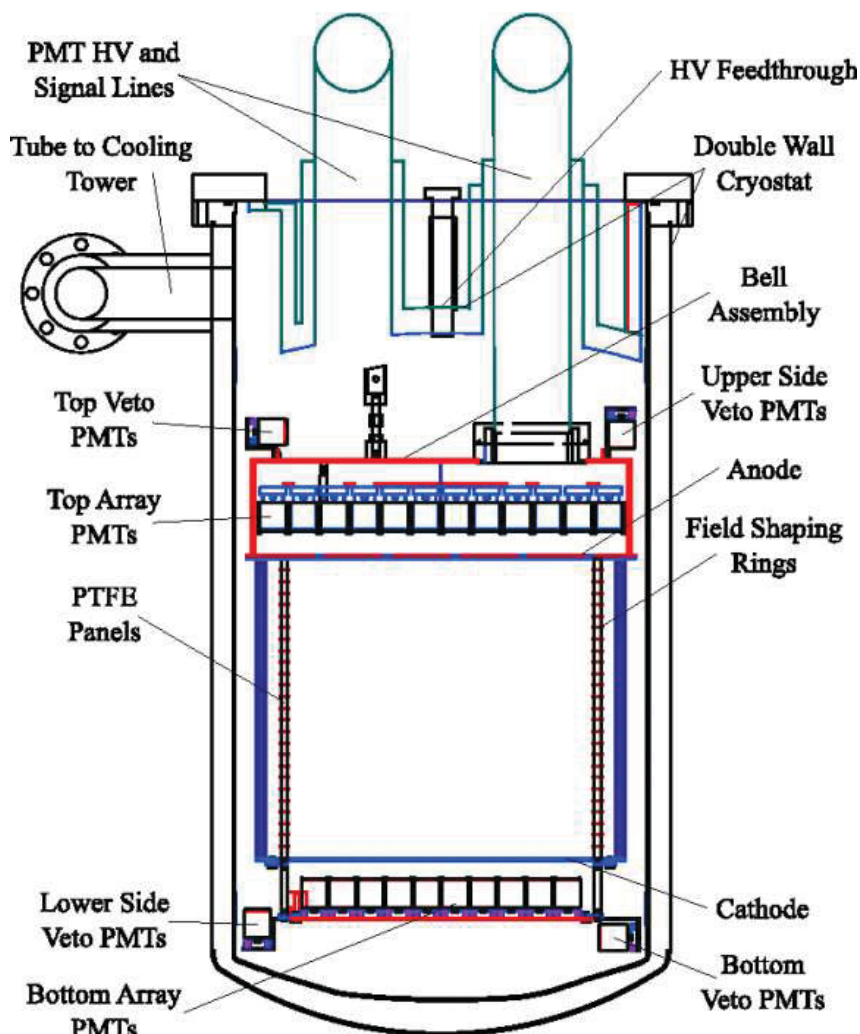


Figure 3.11: Technical drawing of the XENON100 TPC.

As previously mentioned, the XENON100 detector is made of a dual-phase time projection chamber (TPC) contained in a low activity stainless steel double walled cryostat. In between this double wall, a vacuum is applied which allows the system to be thermally isolated from the external world. This vacuum is what allows the xenon to stay in a stable liquid state. The cryostat itself is linked to

the outside by two lines on the side allowing for xenon liquefaction, while a third line at the top of the cryostat brings in clean gas and a last line at the bottom takes out liquid xenon to circulate it and clean it from impurities. The cryostat is thus mostly filled with liquid xenon, while the top-most part is filled with gaseous xenon adding up to a total of 165 kg of xenon.

The TPC, which has a diameter and height of 30 cm, is totally submerged in liquid xenon, however, while the region above the TPC is filled with liquid, a diving bell allows the top-most part of the TPC to contain gaseous xenon by maintaining an overpressure. The liquid xenon surrounding the TPC acts as an active veto and offers an additional background shield. The TPC itself is made of a low radioactivity white teflon reflector especially sensitive to VUV light with low activity copper holders visible on figure 3.4.

PMTs are located at the top and bottom of the TPC. At the bottom of the TPC is located an array of 80 closely packed pmts whose function is to detect the light from scintillation in the liquid (S1) while at the top a second array of 98 PMTs, arranged in circular pattern is there to detect the proportional scintillation signal (S2). An extra 64 PMTs are located outside and around the TPC at the bottom and top of the cryostat so as to detect the light in the veto.

The electric field (E1), which allows to drift the ionization electrons to the gaseous part of the TPC, is achieved by applying a negative bias voltage to a stainless steel cathode located 17 mm above the bottom PMT array. This cathode is made from a transparent mesh so as to not hinder the detection of the light by the PMTs. Below the cathode, about 2 mm from the bottom PMTs, is placed a screening mesh whose function is to screen any field at the PMTs. A series of low activity copper rings are placed inside around the TPC. These are used as field shaping rings and allow a uniform electric field of 530 V/cm to be maintained in the TPC. The electric field is stopped around 2.5 mm below the liquid level by another transparent mesh called gate mesh, while an anode, also made of a transparent mesh and located 2.5 mm above the liquid level usually at a voltage of 4.4 kV, creates an accelerating electric field about 17 times stronger than E1. Another screening mesh, located 2.5 cm from the top of the TPC, ensures again of no electric field at the PMTs.

### 3.3.2 Shielding

As mentioned above, the detector has to be protected from external radiation coming from the environment. For that purpose, in addition to the 99.9998% muon and cosmic ray attenuation from being located underground at LNGS [80], it is surrounded by a passive shield which is made of several layers of different materials. An external 20 cm thick layer of water boxes is first implemented on the

top and four sides to shield against muon induced neutrons as well as neutrons from decays of  $^{238}\text{U}$ ,  $^{235}\text{U}$ ,  $^{232}\text{Th}$  and their daughters in the rock and the concrete. An inner 20 cm thick lead layer is then added to shield for the gammas from  $^{238}\text{U}$ ,  $^{232}\text{Th}$  and  $^{40}\text{K}$  decays in the rock and the concrete, with the innermost 5 cm being made of ancient lead with extremely low intrinsic radioactivity. This is followed by a 20 cm thick inner polyethylene layer to shield against the neutrons from  $^{210}\text{Pb}$ ,  $^{238}\text{U}$  and  $^{232}\text{Th}$  decays in the lead layer. Finally an inner 5 cm thick layer of electrolytic copper is put into place to shield for the gammas from the polyethylene layer. Figure 3.12 shows the actual shield used in the experiment.



Figure 3.12: The shielding structure of the XENON100 experiment. The copper, polyethylene and two lead layers are clearly visible while the water boxes are starting to show on top.

### Radon Shielding

While the shielding structure reduces every source of external background, it is powerless against radon inside the shield. Radon ( $^{222}\text{Rn}$ ) is a naturally occurring radioactive element coming from the decay chain of  $^{238}\text{U}$ , making it an inevitable background. While the laboratory itself attempts to reduce the radon by constantly blowing up fresh air from outside the mountain into the underground facility, it is by no means a radon-free environment and the radon levels are still too high for the purpose of dark matter searches. To reduce the radon rate to an acceptable level of less than  $1\text{Bq}/\text{m}^3$ ,

nitrogen gas is continuously blown inside the shielding structure. The nitrogen takes the place of the radon which is thus pushed outside the shield. To ensure that the radon level stays low, it is constantly monitored and measured with an upper limit of  $1\text{Bq}/\text{m}^3$ .

### 3.3.3 Cooling System

When the detector is enclosed in the shield, the main structure visible from the outside is the so called cooling tower. Cooling is required in XENON100 to be able to maintain the xenon in a liquid state which happens at  $-93^\circ\text{C}$  and 2.25 bar. The schematics of such a cooling system is shown on figure 3.13.

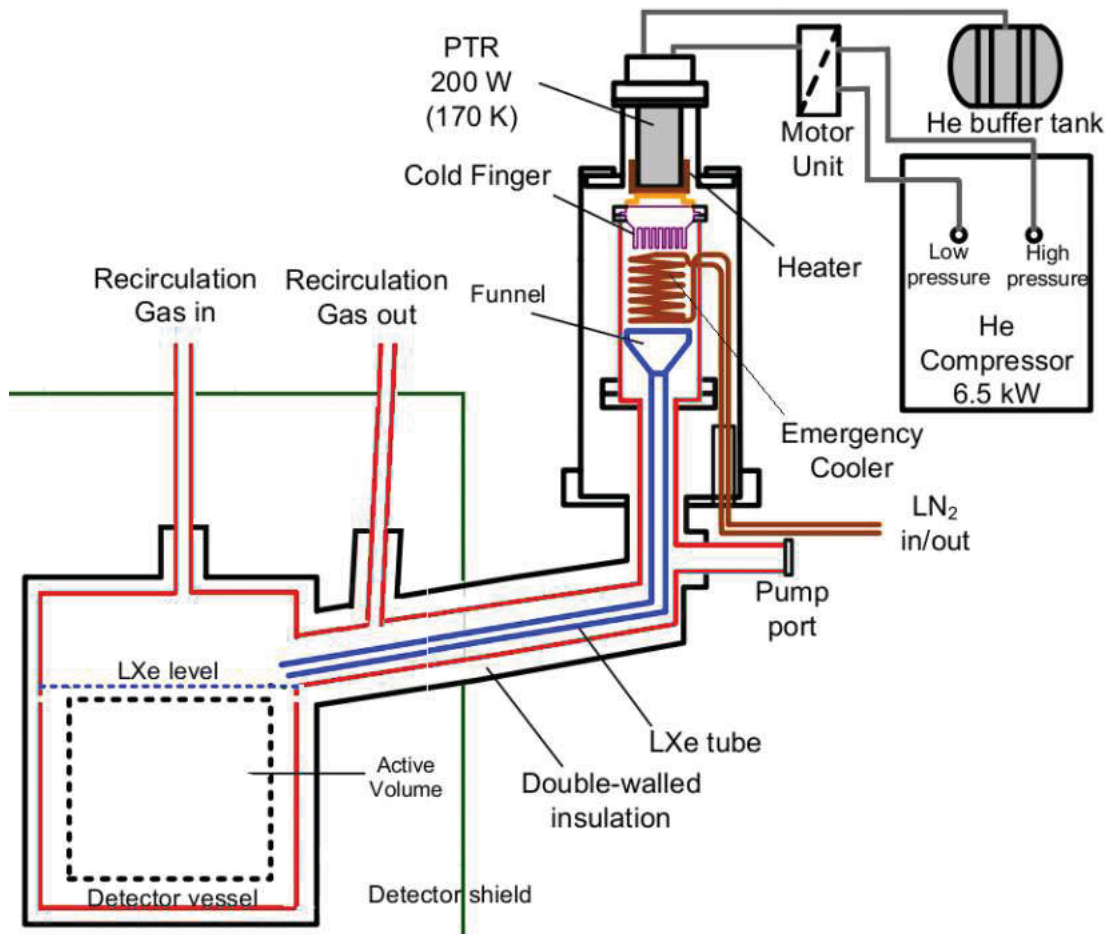


Figure 3.13: Drawing of the cooling system of the XENON100 experiment [15]

The main components of such a system are a pulse tube refrigerator (PTR), which consists in a piston capable of increasing or decreasing gas pressure as it moves, a helium compressor which, connected to a continuously running motor, can pressurize helium, a cold finger, which generates a cold surface, a heater and an emergency cooler. The detector is connected to the cooling tower

assembly through vacuum insulated pipes which come off right above the liquid level, allowing xenon gas to fill up the cooling system.

During normal operation of the system, the helium compressor supplies power to the PTR by pressurizing helium. Once a sufficient amount of helium gas has been introduced in the PTR, the piston of the PTR is moved up, expanding the helium gas in the process, thus decreasing the pressure and cooling down the system. A cylindrical copper block is attached to the PTR cold head to seal off the detector from the PTR. This block of copper is thus cooled down at the same temperature as the cold head and can be used as cold finger to be in contact with the xenon gas. At this contact, the xenon gas condensates and the now liquid xenon drops into a funnel linked to a small pipe inside the bigger vacuum insulated pipe, thus filling the detector. To make sure that the cold finger doesn't get too cold and that a temperature of  $-100^{\circ}\text{C}$  is maintained, a heater is installed between the PTR cold head and the cold finger.

In case of emergency where the primary cooling process would not work anymore, another system takes over. This is done using liquid nitrogen (LN2). A stainless steel coil, placed around the cold finger in order to be at all times in contact with LXe, is linked to an emergency dewar always filled with LN2. When the pressure surpasses a certain set point, the dewar automatically releases nitrogen, thus cooling down the coil which then takes on the role of cold finger.

### **3.3.4 Recirculation System**

The performance of the detector depends on the purity of the system, consequently the xenon is constantly purified using a recirculation system which is shown on figure 3.14. When the xenon sits in the detector it cleans it by detaching impurities from its walls. These impurities are then found in the xenon and they need to be disposed of. To do this, the recirculation system is linked to the bottom of the detector where it takes the LXe out, which evaporates due to an increase of temperature. The gas is then pushed through the system via a KNF membrane pump through a heated zirconium getter which removes impurities by chemical bonding. After passing the getter, the GXe is thus cleaned and sent back to the top of the cryostat where it can then undergo the process of liquefaction as explained in subsection 3.3.3.

Another feature of the recirculation system is a pumping port to which a vacuum pump can be attached. This is used before the first filling of the detector when the lines must be pumped down and vacuum must be created before introducing any xenon in them.

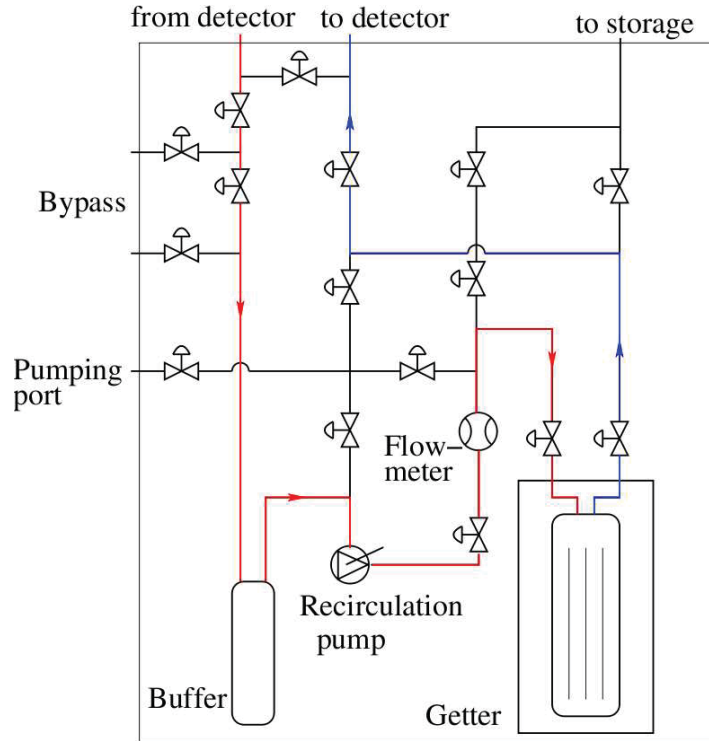


Figure 3.14: Drawing of the gas recirculation system of the XENON100 experiment [15]

### Recuperation

The recirculation system is also used in case of recuperation. In case of problems, the detector might need to be emptied and the xenon must be recuperated. For this, the recirculation system has to be rerouted to go towards storage bottles instead of back into the detector. The bottles stand in buckets which are filled with LN<sub>2</sub>, thus allowing the GXe to freeze in the bottles. Figure 3.15 show the bottle rack while recuperation is going on. Rerouting is of course possible by simply closing the last valve leading to the gas layer of the cryostat while opening the valve leading to the bottle rack thus forcing the GXe to go that way.

#### 3.3.5 Distillation System

As mentioned above in section 3.1.6 xenon has no long lived isotope and because it is a noble gas, it is intrinsically very pure. This statement is true with the exception of  $^{85}\text{Kr}$  which is one isotope of natural krypton ( $^{nat}\text{Kr}$ ) with an abundance of  $^{85}\text{Kr}/^{nat}\text{Kr}$  of  $10^{-11}$  and is naturally present in the atmosphere as a fission product and is present in trace amounts in commercial xenon.  $^{85}\text{Kr}$  decays into  $^{85}\text{Rb}$  with a half life of 10.756 years and a 99.57% branching ratio emitting beta rays with an endpoint energy of 687 keV in the process.  $^{85}\text{Rb}$  is stable and doesn't constitute a danger for the detector however the electrons from the decay become a non-negligible source of background which



Figure 3.15: Picture of the bottle rack while recuperation is ongoing. The bottles are frozen with LN2.

can be calculated as 20 events/keV/kg/day or 20 differential rate unit (dru) in the region of interest for dark matter searches for  $^{nat}Kr$  at the ppm level. Because such a background would be dominant and would render the operation of the detector impossible, the xenon needs to be purified to lower the  $^{nat}Kr$  level to 100ppt, which would then give a rate of 0.002 dru thus rendering the krypton background sub-dominant [15]. To reach such a low level of contamination, a distillation column, whose principle is shown on figure 3.16 was installed by the XENON100 detector. The GXe coming from the detector is first passed through a cooler to be liquefied and then is sent to the middle of the column. A condenser at the top and a heater at the bottom continuously liquefy and boil the xenon in the column. Because of the much higher saturation pressure of krypton at these temperatures, the krypton preferentially moves up the column allowing a separation of the two gases. In the meantime, the LXe at the bottom of the column, which has now a reduced concentration in Kr, is ready for use in the experiment.

The column is designed to have a multiple stage distillation, also called rectification, following a McCabe Thiele diagram [85] to give a  $^{nat}Kr$  reduction factor of 1000. Depending on the start and end concentration to be achieved by the distillation, the McCabe-Thiele is used to calculate the length of the column by calculating how many theoretical stages are needed for the desired decrease in concentration. In the case of XENON100, 6 theoretical cell stages were needed. The active part

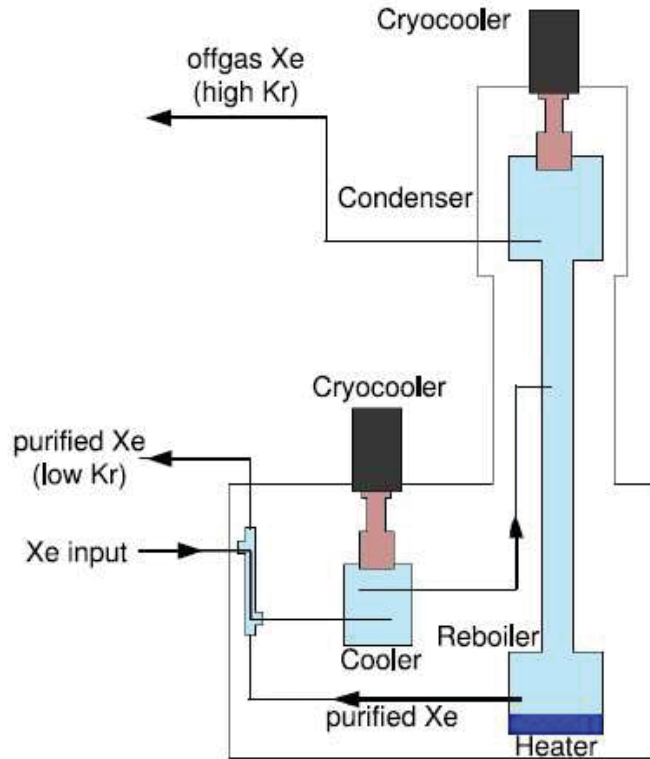


Figure 3.16: Schematical drawing of the krypton distillation column [15].

of the column is made of stainless steel packing material tightly braided in 3 dimensions as shown on figure 3.17, to increase the condensation surface.



Figure 3.17: Packing material of the inside of the distillation column.

After running all the xenon through the column, the concentration of  $^{nat}Kr$  in xenon was found to be  $19 \pm 4$  ppt [23], thus meeting the needs of a low background experiment.

While this column was sufficient for XENON100, it will no longer work for XENON1T as the amount of xenon to be distilled will be a factor 10 higher and the purification speed of 0.6 kg/h will not be fast enough anymore. A bigger column which will have a separation factor of  $10^5$  is thus being tested to meet the needs of XENON1T.

### 3.3.6 PMTs

By being the light collection tools, the PMTs are extremely important in XENON100 and thus deserve to have a bit more information stated about them.

A PMT is a device which detects, amplifies and converts incoming photons into an electrical signal. Upon contact with a photon, a photocathode emits an electron via the photoelectric effect. These electrons are accelerated by an electric field, multiplied thanks to a system of dynodes and finally converted into a measurable signal. The drawing of the principle of a PMT is shown on figure 3.18.

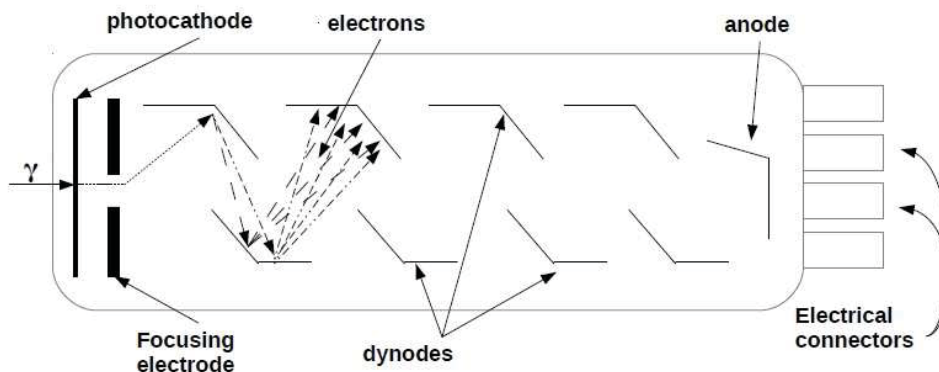


Figure 3.18: Schematics of the principle of a PMT

The PMTs used in XENON100 are the HAMAMATSU R8520-06-Al 1 inch square which were selected for their low radioactivity and for their relatively small size, thus allowing better position resolution [86]. To be able to operate at temperatures reaching  $-110^{\circ}\text{C}$ , the PMTs have a special bi-alkali photocathode and are optimized to be more sensitive to 178 nm scintillation light [18].

There is a total of 242 PMTs on XENON100, divided into a top array, a bottom array and a veto array. The top array is located at the top of the TPC in the gaseous layer and is composed of 98 PMTs arranged in a circular pattern to improve the resolution of the radial position reconstruction as shown on figure 3.19. The light collection efficiency is not deteriorated much by this pattern as the holding structure is made of PTFE which acts as a reflector. The radius of this circular pattern is bigger than the TPC's to improve position reconstruction at the edges.

The bottom array, located at the very bottom in the liquid layer of the TPC, is made of 80 PMTs arranged in square so as to maximize the light collection efficiency, as shown on figure 3.20.

The last 64 PMTs are located in the veto region of the detector equally separated between top and bottom. The arrangement of these pmts is different than for the TPC PMTs and is made so that the light from top, bottom and sides of the active veto can be simultaneously detected. This is

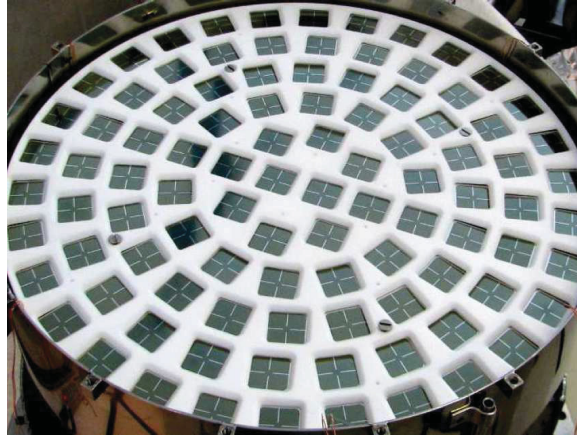


Figure 3.19: The top PMT array of the XENON100 TPC.

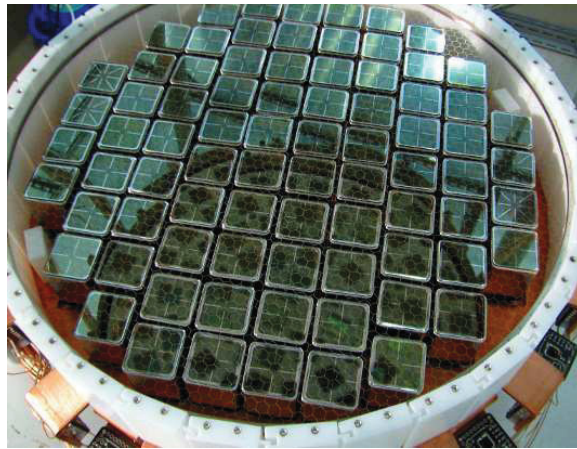


Figure 3.20: The bottom PMT array of the XENON100 TPC.

done by alternatively pointing the PMTs inward and down for the top PMTs and inward and up for the bottom PMTs.

### ***Quantum Efficiency***

A characteristic of PMTs which must be discussed is the so called quantum efficiency (QE) which is a measure of how well electrons leave the photocathode after a photon has reached it. This number is provided by the company who made the PMTs (in this case Hamamatsu). The results as presented on figure 3.21 indicate that the top array has an average of 25% while the bottom array has a higher QE of about 33% and the veto array about 23%.

The higher QE value for the bottom array is necessary as the S1 signal needs higher photostatistics in order to be able to improve the energy threshold beyond which the knowledge of the detector is good enough that events can be recorded and analyzed. Note that the QE measurements have big uncertainties as it is a difficult measurement to carry out, consequently Hamamatsu does not

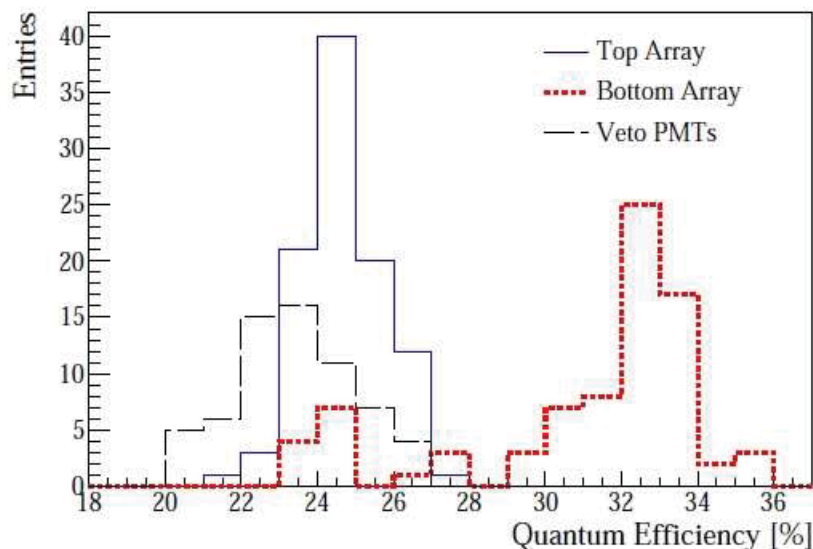


Figure 3.21: Quantum efficiency of the top, bottom and veto PMTs used in XENON100 [15]

measure QE directly. Rather they measure the photocathode’s sensitivity to blue light (Skb) which is correlated with QE as shown on figure 3.22. As can be seen, the error on the correlation is rather big which is why QE is not known precisely.

### 3.3.7 Data Acquisition

The XENON100 data acquisition (DAQ) system, whose drawing can be seen in figure 3.23 governs the trigger logic of the experiment. All the 242 PMTs give out a signal which is amplified 10 times by Phillips PS776 amplifiers. The amplified signal is then digitized by 31 CAEN V1724 flash ADCs with 100 MHz sampling rate, 14 bit resolution, and 40 MHz bandwidth.

The first step in recording an event is to recognize a signal as such. This is done using only the 68 inner top array PMTs and the 16 inner bottom PMTs, whose individual signals are summed up in Phillips 740 fan-ins and passed through a shaping amplifier (Spec Amp) to determine if the summed signal is a multiple coincidence on PMTs, which would lead to an S1, or just noise on a single channel. To do this, the shaping amplifier integrates the input signal to give out an output signal with an integration time constant of  $1 \mu\text{s}$ . At this point, a discriminator (Discr) is used to check if this integral is above or below a software fixed threshold. If it is above, the signal is identified as a trigger (Trig).

When a signal has been tagged as a trigger, another subsystem of the DAQ takes over, to make sure and avoid pile up events. The ADCs will then trigger (ADCTrig) only if a signal was considered an event by the trigger and if the ADC did not trigger in the last 0.5 ms. During the 0.5 ms holdoff,

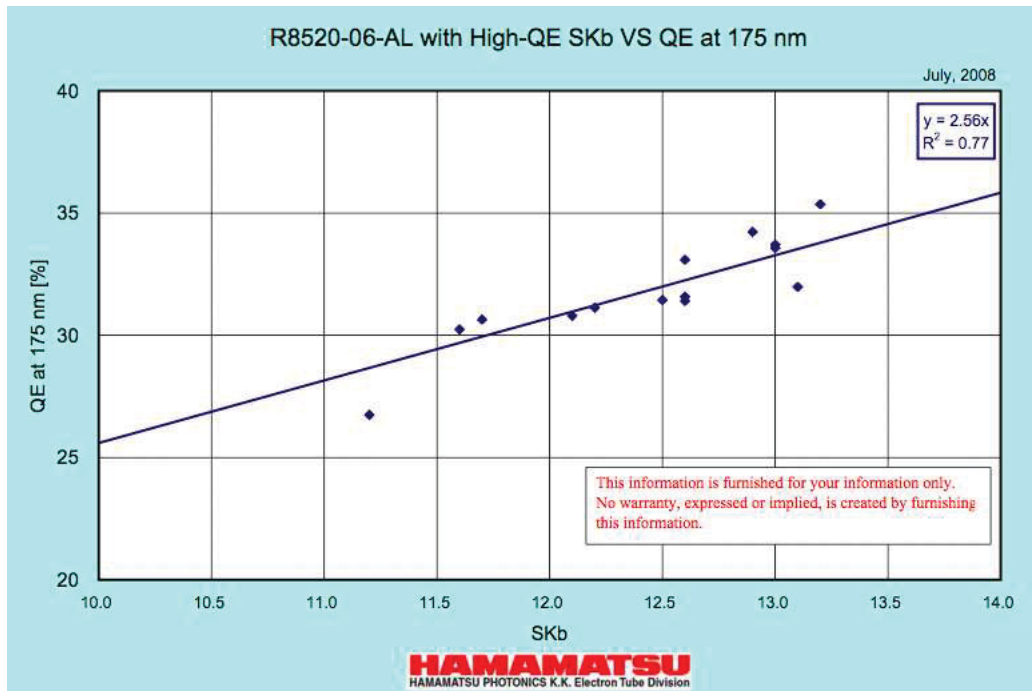


Figure 3.22: Sensitivity to blue light (SKb) versus quantum efficiency (QE) for the HAMAMATSU R8520 PMTs used in XENON100.

the ADCs send out a busy signal thus preventing ADC triggering.

Finally to keep track of time and count events, a timing subsystem is in place, which uses a clock to record real time, livetime and deadtime. The livetime and deadtime are recorded if the ADCs respectively are not sending or are sending out a busy signal.

### *Deadtime-Less Mode*

The DAQ operation can be optimized as the ADCs allow deadtime-less mode. Deadtime is mostly induced by the transfer time between the ADCs' memory and the computer. If the ADCs did trigger only when they are not transferring data, a lot of data would be lost. To avoid this, the ADCs must record signals at all times. To do this without loss, the signals are continuously recorded on the memory of the ADCs which is made of a circular buffer with 512 kB of available space for each PMT channel. As the signals are being recorded, the previous signals are being transferred to the computer so that when the buffer is full, it just loops back and new signals are being recorded on top of older, already transferred ones.

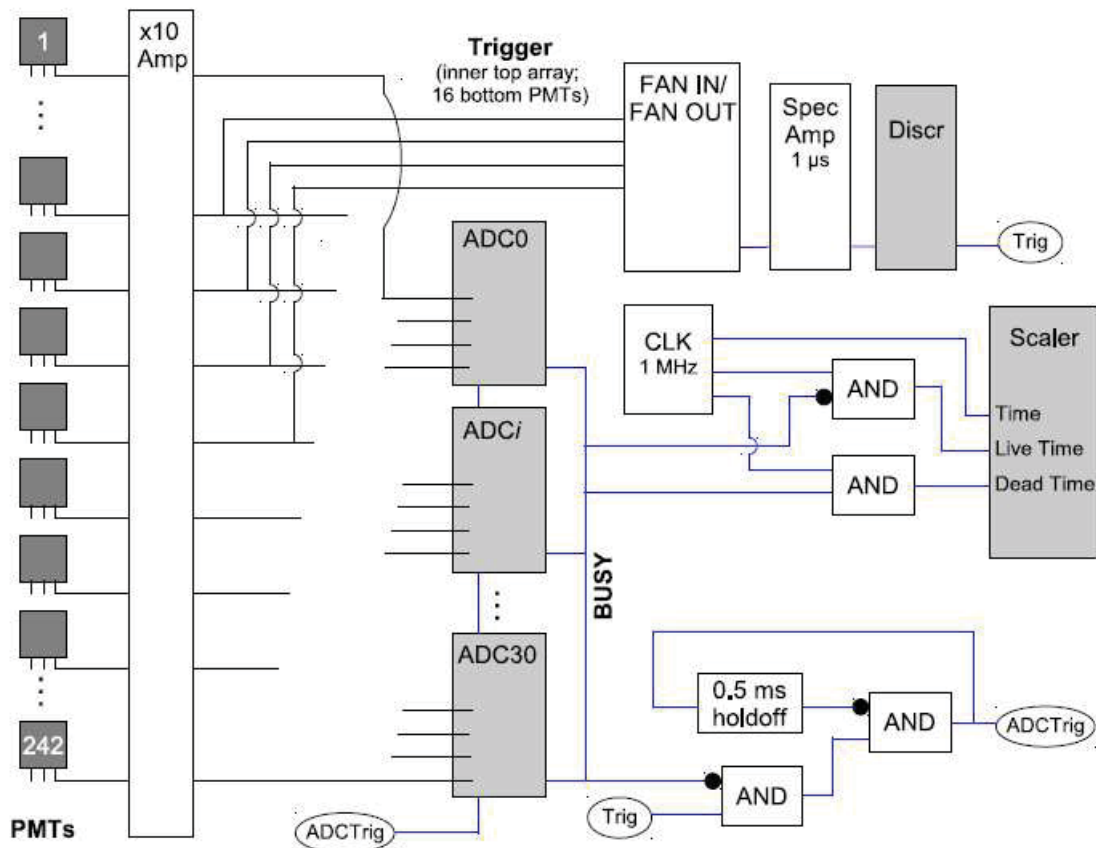


Figure 3.23: Schematics of the data acquisition system of XENON100 [15]. The black circles indicate a false input.

### Zero Length Encoding

To ensure that no signal is missed, it is important to have a large enough acquisition window. The drift time of the ionization electron being 175  $\mu\text{s}$  maximum, the window is set at 400  $\mu\text{s}$ , so more than twice as much. Moreover the trigger is placed at the center of the window so that it records always 200  $\mu\text{s}$  before and after the event. This is necessary so that if the trigger occurs due to a S1, the S2 signal which comes 175  $\mu\text{s}$  later is also recorded and vice versa. Only this way, is it insured that the full signal (S1 and S2) are always recorded. However, because the acquisition window is so wide, most of the digitized waveform is just background noise, which is uninteresting for the purpose of the experiment. Consequently this background increases considerably the data size and so, because it isn't of any particular interest, it is necessary to try to remove it in order to minimize data size as much as possible. To do so, the zero length encoding algorithm (ZLEA) is used. Each waveform is mostly composed of noise, and of at least one S1 and one S2 peak, which constitute almost entirely the data of interest. The ZLEA gets rid of the sizable noise by recording only data that is above a software set threshold, plus 50 samples (500 ns) before and after this above threshold region. To be

able to reconstitute the entire waveform afterwards, the ZLEA records the time in between each peak thus allowing to reproduce their relative position. The baseline is also reconstituted as one value, as the information about the fluctuations have been lost. Figure 3.24 shows an example of waveform encoded with zero length, where three PMTs triggered and only the region around the peaks was recorded while the remainder of the waveform was in fact replaced by a single baseline.

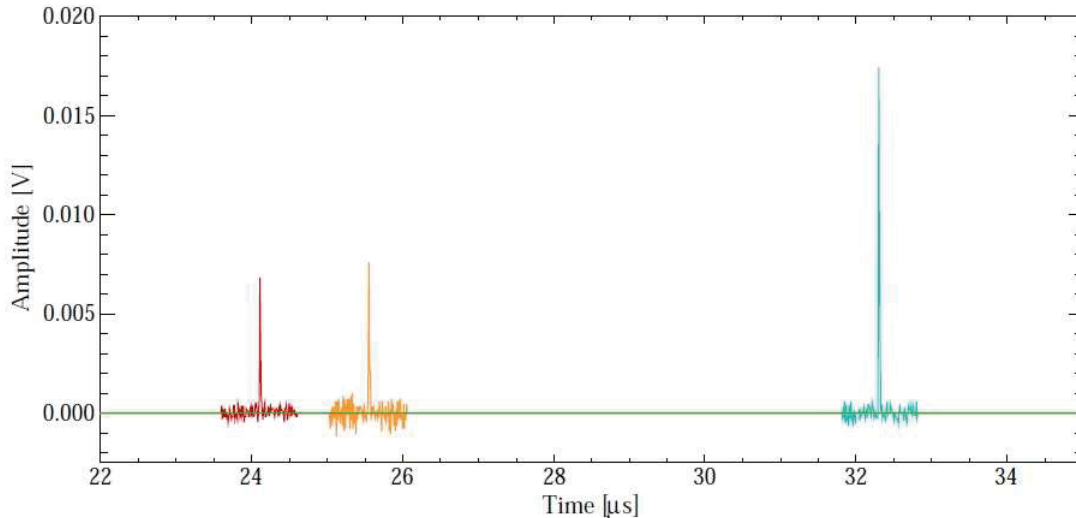


Figure 3.24: Waveform encoded with zero length [18].

### 3.4 Calibration of the Detector

To fully understand the experiment a series of calibrations are carried out frequently. These allow to monitor the response of the detector to diverse particles such as gammas and neutrons, as well as the behavior over time of certain sub-systems such as the PMTs.

#### 3.4.1 PMT Calibration

As explained in section 3.3.6, PMTs are a vital part of the experiment as all the information about an event comes directly from them. The PMTs have not been changed since 2008 so it is important to understand their behavior over time, whether they simply break down or became noisy. In addition to the simple monitoring of the condition of the PMTs, their individual performance are parametrized through gain calibrations. The gain is a measure of how well a PMT amplifies the signal from an incoming photon and is taken as the ratio of the charge output from the PMT to the charge coming off the photocathode. Knowing the gain is thus necessary to convert back from a signal in ADC counts to a signal in photoelectrons, which is essential for data analysis.

Gain calibrations are performed weekly for all 242 PMTs using a blue nanosecond pulse LED located outside the detector and linked to the inside via optical fibers. The fibers are located uniformly throughout the detector and the veto so as to ensure an homogeneous light distribution. A trigger is set on each pulse, whether or not the PMT receives a photon. Additionally the intensity of the light is set low enough that a PMT receives a photon only on less than 5% of the events, thus avoiding contamination from coincident photoelectrons, which also means that the charge coming off the photocathode is one single photoelectron. As for the charge output of the PMT, it is measured by integrating the spectrum over the pulse duration. The gain spectrum is thus obtained by rescaling the charge output by the charge of the electron. A typical gain calibration spectrum as shown on figure 3.25, presents two contributions, a noise peak on the left, of no interest, corresponding to these triggers where the PMT did not see a signal, and the single photoelectron peak on the right. It is by fitting this latter peak and extracting the mean value from the fit that the gain is then determined. Overall, the average gain is very stable within  $\pm 1\%$ , indicating that the PMTs are still performing adequately. More details about the calibration procedure and results can be found in [16] and in [87].

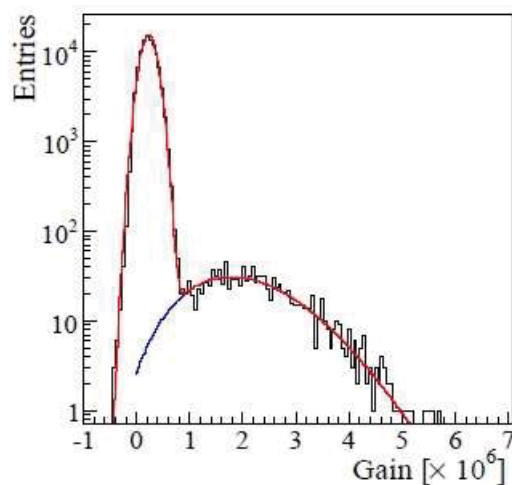


Figure 3.25: Typical gain calibration spectrum [15].

### 3.4.2 Electron Drift Lifetime

Another crucial parameter in the experiment is the electron drift lifetime  $\tau_e$ , which corresponds to the time after which  $1/e$  drifting electrons will have been captured by impurities. It can be calculated for each impurity element according to equation 3.4 where  $m_{Xe}$  is the mass of a xenon atom,  $C$  is the concentration of the impurity,  $k$  is the electron attachment rate of the impurity,  $\rho_{Xe}$  is the density of xenon and so  $\rho_{Xe}/m_{Xe}$  is the number density of xenon atoms.

$$\tau_e = \frac{m_{Xe}}{C \cdot \rho_{Xe} k} \quad (3.4)$$

The electron lifetime is thus a direct measure of the purity of the LXe and is directly linked to the intensity of the S2 signal and the drift time. The more impurities, the lesser the electron lifetime and the intensity of the S2. Typical values for oxygen in xenon are  $k = 10^{11} \text{ mol}^{-1} \text{ L s}^{-1}$  and  $C = 10^{-9}$ .

The electron lifetime is determined by exponentially fitting S2 signals as a function of the drift time as shown on figure 3.26. To do this, a  $^{137}\text{Cs}$  source emitting 662 keV gammas is used. Such a source presents a spectrum with two contributions, a clear peak corresponding to a full energy peak of the 662 keV gamma and a smaller peak due to Compton scattering. Details on this source and its properties will be given in chapter 4. The S2s used for the calculation of the electron lifetime, correspond to the S1s in the full absorption peak of the Cs spectrum. The drift time can then be easily calculated by taking the difference in positions between the corresponding S1s and S2s.

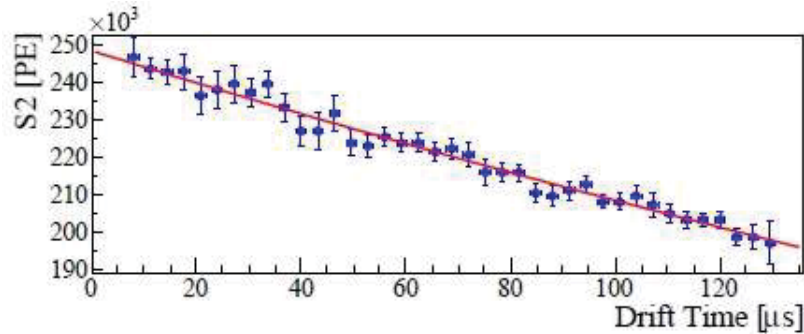


Figure 3.26: Calculation of the electron lifetime from the S2 signal of a  $^{137}\text{Cs}$  source. [15].

In the example of figure 3.26, the electron lifetime is calculated to be  $556 \mu\text{s}$ , so almost three times as much as the maximum drift time for the maximal drift length of 300 mm, thus ensuring that charge signals from the bottom of the TPC reach the gas phase. Such a calibration is performed weekly to ensure of the stability of the detector and of the capacity to drift charges.

### 3.4.3 Energy Calibration

The signals S1 and S2 read by the PMTs are converted to units of photoelectrons (pe) i.e. the number of electrons coming from one photon entering the PMT as described in section 3.4.1. However to be able to analyze the data, knowing the number of photoelectrons from an interaction is not sufficient and it is necessary to be able to determine the energy of the actual recoil. Because of the different xenon response to nuclear and electronic recoils the same amount of energy deposited will give a different number of pe whether the interactions was nuclear or electronic. Consequently two

energy scales are defined, respectively in units of keVnr (keV nuclear recoil) and keVee (keV electron equivalent). To complicate the matter, the conversion factor between pe and energy is not a constant but a function dependent on that same deposited energy. Consequently dedicated measurements and calibrations are performed to be able to determine these functions.

### ***Electron Recoil Energy Scale keVee***

The electron recoil energy scale, or electron equivalent energy is important because the dominant background in the detector manifests itself as electronic recoils, while a potential dark matter signal would manifest itself as nuclear recoil. This energy scale is determined by using several gamma sources whose energy is well known, such as  $^{137}\text{Cs}$ . By fitting the full absorption peak, one can obtain the photoelectrons to energy conversion for this particular energy. Doing this for several sources and then fitting a model to the points allows to determine the conversion over the entire energy scale. When the unit keVee is used it means that this conversion has already been applied to the data. Note that this energy scale depends also on the purity and the light yield of the detector, and thus gamma calibrations have to be performed weekly.

### ***Nuclear Recoil Energy Scale keVnr***

The nuclear recoil energy scale is an S1 only energy scale and is of utmost importance as WIMPs are expected to scatter coherently off of the nucleus. This energy scale is non-linear because it is determined by nuclear quenching. Additionally neutron sources emit a spectrum of energies instead of one specific energy, making it much harder to measure. The conversion between scintillation signal S1 in pe and energy of nuclear recoil  $E_{nr}$  as shown on equation 3.5 is thus not a simple factor but several parameters which themselves must be well known.

$$E_{nr} = \frac{S1 \cdot W}{\epsilon} = \frac{S1}{LY_{122keV}} \frac{1}{L_{eff}(E_{nr})} \frac{S_{ee}}{S_{nr}} \quad (3.5)$$

In this equation,  $\epsilon$  is the efficiency of collecting the scintillation photons,  $W$  is the average energy to produce a scintillation photon,  $L_{eff}$  is the so called relative scintillation efficiency which will be defined in the next subsection,  $LY_{122keVee}$  is in units of pe/keVee and is the light yield for electron recoils at 122 keVee and  $S_{ee}$  and  $S_{nr}$  are the field quenching factors for electron and nuclear recoils whose values depend on the strength of the electric field applied.

*Relative Scintillation Efficiency*  $L_{eff}$   $L_{eff}$  is thus a crucial parameter to determine the nuclear recoil energy scale and needs to be defined as precisely as possible. It itself depends on the nuclear recoil energy and is defined as in equation 3.6 where  $LY_{er}$  is the light yield for electron recoils of energy  $E_{nr}$  and  $LY_{122keVee}$  is again the light yield for electron recoils at 122 keVee. This last point will be explained furthermore in the next chapter.

$$L_{eff}(E_{nr}) = \frac{LY_{er}(E_{nr})}{LY_{122keVee}} \quad (3.6)$$

$L_{eff}$  has historically been related to the 122 keV  $\gamma$  rays emitted by a  $^{57}Co$  source at zero electric field. Several dedicated experiments have been set up to try and measure  $L_{eff}$  but disagreement arose especially at low energies where no data is available [88] [89] [90] [91] [92]. For LXe,  $L_{eff}$  has been measured only up to 3 keVr [88]. Below this value, various extrapolations have been used. The global fit to all data points from different experiments is shown on figure 3.27.

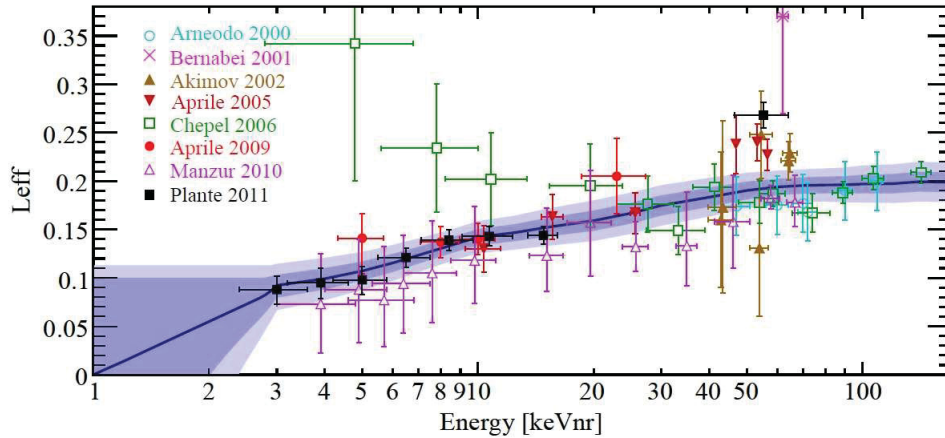


Figure 3.27: Relative scintillation efficiency measured for different experiments [19]

However, the choice of extrapolation can and has been questioned [93]. Indeed, if the extrapolation were not correct at low energy, then the nuclear recoil energy scale would be wrong at these energies which would have a non negligible impact on the sensitivity of the experiment at low energies. However, the impact of this has been minimized as the fit and the extrapolation are treated in a profile likelihood (PL) analysis [22] which accounts for the systematics in the measurements and in the extrapolation. More details on this PL analysis will be given in section 3.6.3.

### 3.5 Detector Response to Backgrounds and Particle Identification

To be able to detect dark matter, the detector's response to every signal must be very well known so as to be able to discriminate the background events from a possible dark matter signal. As already mentioned, the detector's response differs greatly depending on the type of incident particle, due to the relative size between scintillation signal S1 and proportional signal S2. In the following, this will be explained in more details and all major sources of background will be considered.

#### 3.5.1 Neutrons

Neutrons are by far, the most important background as their interaction gives rise to a nuclear recoil and thus mimics a dark matter signal. Consequently they are shielded against by being deep underground, by surrounding the detector with water and polyethylene and by choosing low radioactivity materials. All these precautions lead to a background of less than 1 neutron per year and so a few neutrons still manage to pass into the detector, mostly coming from muons and from the surrounding materials, through  $(\alpha, n)$  reactions and spontaneous fission. All these neutrons have very different energies and the detector's response to them is thus different.

For energies higher than 1 MeV, neutrons mainly interact via elastic scattering with Xe nuclei thus producing simple nuclear recoils. These neutrons constitute an irreducible background, however, because of their high energy and a mean free path of about 10 cm, they are very likely to scatter multiple times in the detector and thus be easily rejected as background.

However at neutron energies of about 1 MeV, inelastic scattering starts to occur mainly via interactions of the type  ${}^AXe(n, n'){}^AXe^*$ . The product of this interaction is an excited Xe nucleus which eventually decays by emitting gamma-rays. While most of the time, this decay happens relatively fast (on the order of 0.1 ns), sometimes, as in the case of  ${}^{129}\text{Xe}$  and  ${}^{131}\text{Xe}$ , it happens days after the irradiation due to their long lifetime. Indeed, low order transitions to the ground state are forbidden, thus resulting in long lifetimes.

For energies lower than 100 keV, elastic scattering remains the main process however the nuclear recoils coming from these interactions are usually too small to be measured. In addition to elastic scattering, radiative capture,  ${}^AXe(n, \gamma){}^{A+1}\text{Xe}^*$ , also occurs.

While neutron elastic scattering constitutes an irreducible background, neutron inelastic scattering do not as the emitted  $\gamma$  rays have an energy far beyond the range of interest. In addition, because the favored process for this interaction is excitation, interacting neutrons will give a much bigger S1

than S2 signal, making these interactions easily identifiable.

However, the gammas emitted from neutron inelastic scattering are used as a powerful calibration tool for the detector as will be shown in the next chapter. Indeed by using a neutron source, these gammas which otherwise would be too low energy to penetrate the detector, are emitted directly into the detector and thus allow a uniform calibration.

### 3.5.2 Gammas

Depending on their energy, gamma rays interact with the electronic cloud surrounding a nucleus in three different processes, the photoelectric effect, the Compton effect and the pair production effect, which all produce electron recoils. All three processes are shown on figure 3.28 which presents the attenuation coefficient in xenon as a function of the energy of the incident gamma.

It can be seen that in the region of interest from 600 keV to 1 MeV, Compton scattering is the dominant effect. Additionally, while a gamma ray is completely absorbed in the case of the photoelectric effect and pair production, it may continue its trajectory in the case of Compton scattering and interact many more times thus producing new electrons. Consequently Compton scattering is the main interaction process in the detector and electronic recoils from low energy Compton scatters constitutes the biggest external electronic background. This will be extensively explained in the next chapter.

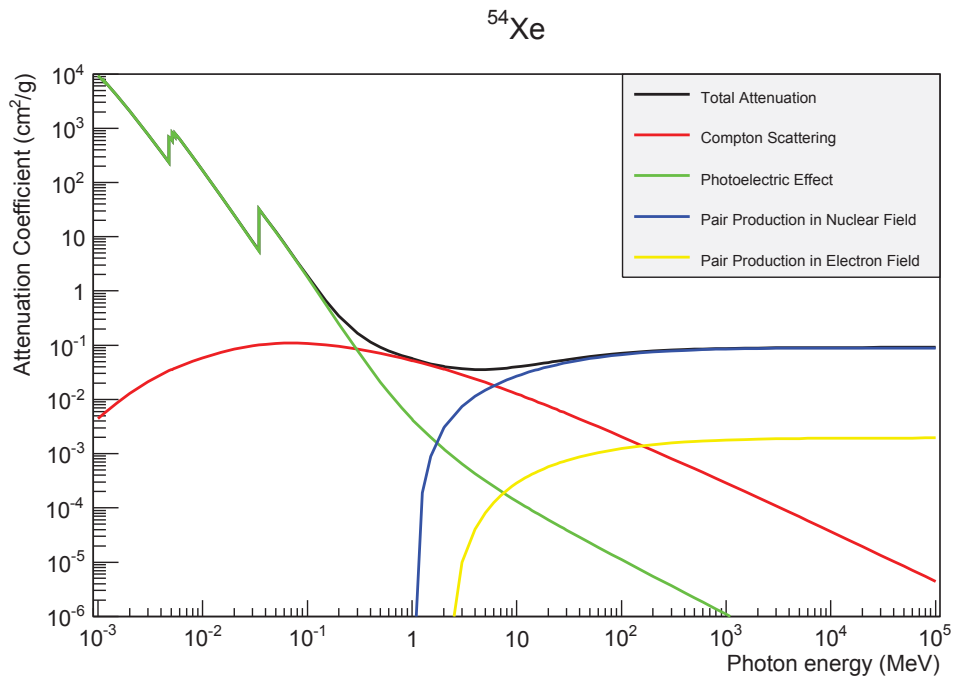


Figure 3.28: Attenuation coefficient in xenon for the photoelectric effect, Compton scattering and pair production [20].

### 3.5.3 Particle Identification

It is to be noted that XENON100 does not identify per say the type of interacting particles but instead identifies the type of interaction so whether it gives nuclear or electronic recoils. In addition, any identification is purely statistical, meaning that an event is identified as ER or NR based on the probability that it is one or the other.

#### *Nuclear and Electronic Recoils*

When understanding interactions from nuclear or electronic recoils in the detector, obvious discrimination means arise which are based on using the ratio between S1 and S2 signals. As mentioned before, S1 signals come from the prompt scintillation in the liquid xenon and S2 signals come from the extracted ionization signal that generates proportional scintillation in the gas phase. Also because of the amplification in the proportional scintillation, S2 signals are always much bigger than S1 signals. In addition, the ionization yield is different for electron and nuclear recoils, an S2 signal coming from an initial nuclear recoil is going to be smaller than an S2 signal coming from an initial electronic recoil. Consequently, the ratio S2/S1 will always be much smaller for nuclear recoils than for electronic recoils.

To clearly visualize this discrimination effect, the detector must be submitted to a high flux of neutrons and gammas. For this purpose an  $^{241}\text{AmBe}$  neutron source and a  $^{60}\text{Co}$  and  $^{232}\text{Th}$  gamma source are used. Figure 3.29 shows the S2/S1 ratio distribution as a function of energy for both sources.

While it is clear that the median for NR (red in figure 3.29) is much lower than for ER (blue in figure 3.29), there is no precise boundary for both bands. Consequently, the discrimination between ER and NR is not completely straight forward. Indeed, the ER band leaks into the NR band making particle identification more difficult and thus constituting an irreducible electron recoil background. To solve that and remove this background, all the NR above the median line (red) are removed thus giving a 50% NR acceptance and 99.75% of the ER are rejected [23].

### WIMP

Because WIMPs are expected to interact via nuclear recoil, the region of interest for the search for WIMPs, shown in figure 3.30 has to be in the nuclear recoil band (lower green dotted line) and well below the electronic recoil band (upper green dotted line). Additionally it has to be between the

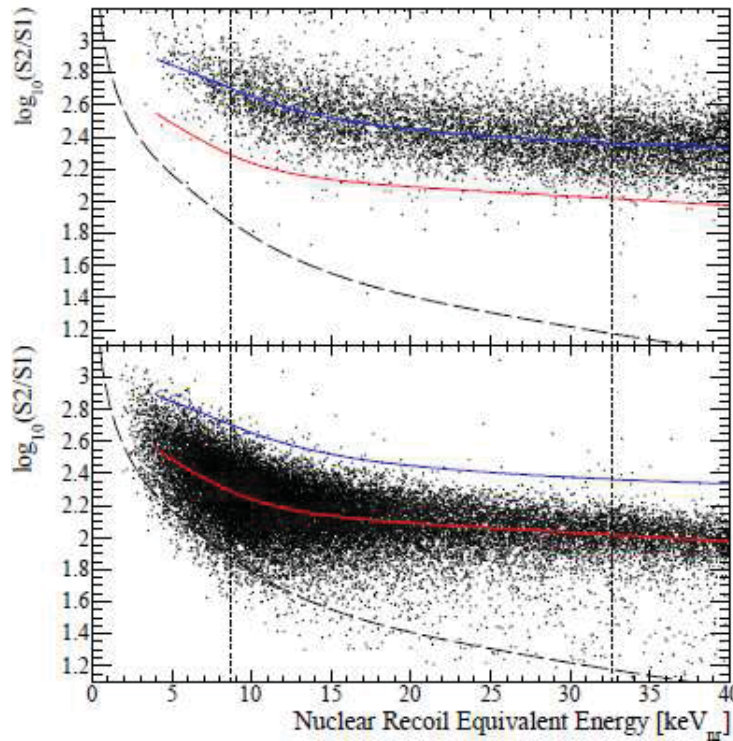


Figure 3.29: Electronic (top) and nuclear (bottom) recoil bands from  $^{60}\text{Co}$  and  $^{232}\text{Th}$  (top) and  $^{241}\text{AmBe}$  (bottom) calibration data, respectively, using the discrimination parameter  $\log_{10}(S2/S1)$  as a function of nuclear recoil equivalent energy (keVnr) according to equation 3.5. Colored lines correspond to the median of both bands, blue for electronic recoils and red for nuclear recoils. The vertical lines correspond to the WIMP search window while the long dashed line is a software threshold of 300 pe. [21].

range of recoil energies expected for WIMP interactions. It has been chosen between 6.6 and 30.5 keVnr (left dashed blue line + right green dotted line) as shown on figure 3.30.

In this figure, the bands are shown in a flattened space where the mean of the electron recoil band (blue curve in figure 3.29) has been subtracted. This is done to flatten the background so that a nuclear recoil signal is more obviously identifiable.

### Alphas

Alpha particles come mostly from the decay of radioactive elements and have high typical energy of about 5 MeV. There are two sources of alphas, decays from the xenon itself and decays which occurred somewhere in the surrounding materials. As shown on figure 3.31, the stopping power for alphas in xenon is very high of the order of  $10 \text{ MeV cm}^2\text{g}^{-1}$ , which means that if an alpha interaction happens inside the detector, it is essentially pointlike. The energy released in such an interaction is so large that any alpha interaction happening in these conditions is easily identifiable and discriminated against.

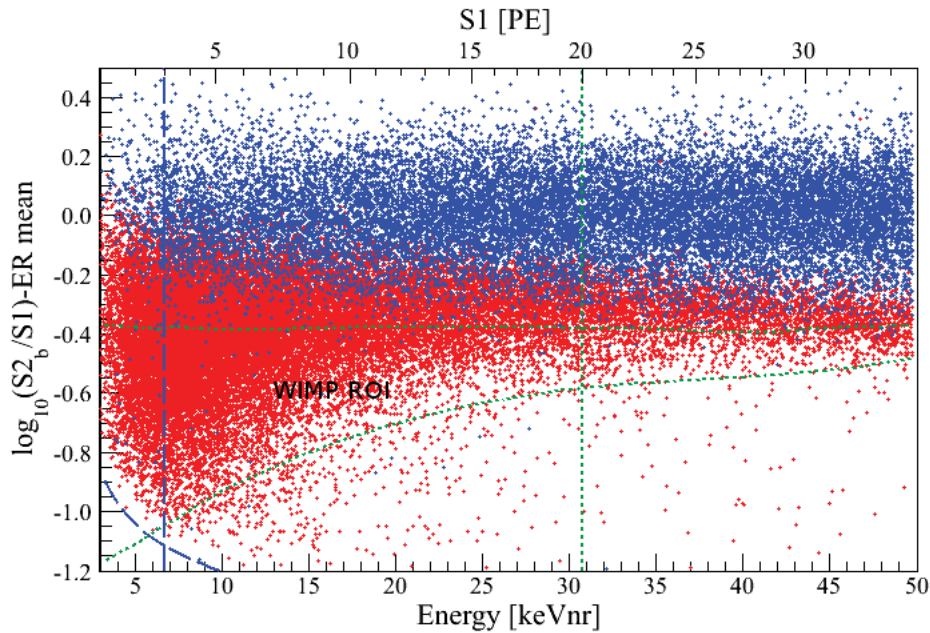


Figure 3.30: WIMP region of interest superimposed with nuclear recoil and electronic recoil calibration data. The top dotted green line corresponds to 99.75% ER rejection, the bottom top dotted green light corresponds to the 97% NR quantile. The left dashed blue line and the right green dotted line correspond to the energy window for WIMP recoil energy. The small blue dashed line in the bottom left corner shows the negligible impact of the  $S2 > 150$  pe threshold cut.

Similarly, if the alpha comes from outside the detector, it will have already lost most of its energy on the way and if it reaches the detector, it will surely interact on the edges of the detector and will then be cut off during fiducialization. Because of this, alphas do not represent any background for the XENON100 experiment which is thus alpha-free.

### Betas

Only one natural existing isotope of xenon is radioactive and could be a source of beta emission.  $^{136}\text{Xe}$ , indeed, undergoes a double  $\beta^-$  decay with a half-life of  $2.165 \cdot 10^{21} \text{ yrs}$  [84]. However both  $^{85}\text{Kr}$  and radon daughters are also beta emitters and will not be taken out of the xenon target by the getter (see section 3.3.4). While XENON10 was not sensitive enough and had a too high background to even care about betas, this is not the case for XENON100, and will be even worse for XENON1T where betas will become the dominant background. Indeed because betas are charged particles they have a very small interaction length in the xenon and cannot be avoided, especially in the fiducial volume. However, they constitute an electronic recoil and can thus be discriminated against. In XENON100, the background consists of about 50% betas.

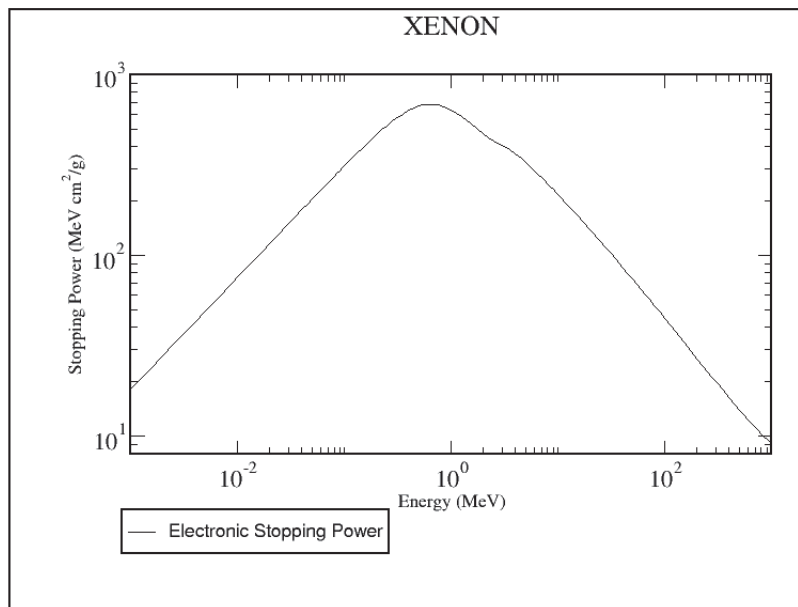


Figure 3.31: Stopping power for alpha particles in  $^{131}\text{Xe}$  [20].

## 3.6 Data Analysis

Once the data has been acquired, it needs of course to be carefully analyzed. The details of this lengthy procedure can be found in [94]. However, a few key features will be discussed here.

### 3.6.1 Position Correction

As explained in section 3.1.5, one of the priorities is to be able to determine where in the detector did an interaction happened and so be able to reconstruct the position of an event.

However, the x-y-z position reconstruction is not as trivial as it seems. Indeed the two PMT arrays light collection is non-uniform due to geometrical effects, dead PMTs and different PMT behavior. Additionally depending on where the interaction took place the scintillation light and more importantly the ionization signal must travel more or less distance and are more or less attenuated by residual impurities. Because of this, the detector's response to S1 and S2 signals is position dependent. Consequently, before being able to reconstruct an event, the detector's response to S1 and S2 and consequently the signals themselves must be corrected. This is done for S1 by mapping the light yield throughout the detector, a procedure which will be the main focus of the next chapter. For S2, this is done by correcting for the electron lifetime.

### 3.6.2 Data Quality Cuts

Once the position of the data has been reconstructed, the first step of the analysis is to discard those events who are obviously not coming from a WIMP-interaction and only select the most likely candidates. For this purpose, many data quality cuts are applied to the data. As a rule, any event which fails more than three cuts is immediately discarded.

For an S1 signal to be considered, it must be seen by at least two PMTs and be larger than 0.35 pe to be clearly visible above electronic noise [94].

Because WIMPs are expected to scatter only once in the detector, any multiple scatter event is rejected by simply looking at its spatial reconstruction. Any scattering which happens with greater than 3 mm separation in  $z$  can be easily identified and is systematically rejected, because two distinct S2 peaks can be identified.

To make sure that no noise might be mistaken for a real interaction, each event must have a signal to noise ratio above a certain threshold. Too noisy events are also removed.

Of course, for each S1 signal, there must at be at least one coincident S2 signal and no other coincident S1 in either the TPC or the active veto.

For an event to be considered valid, the biggest S2 peak must be bigger than the trigger threshold, cannot be too wide or too asymmetric.

Finally, to be considered, an event must of course be in the right calibration band and in the pre-defined fiducial volume (the region of interest of figure 3.30).

### 3.6.3 Profile Likelihood Analysis

After the analysis and the event selection has been done, the remaining few events are all possible dark matter candidates. To be able to tell if they are indeed a dark matter candidate, which would lead to a discovery, or if they are simple background fluctuations (which then places a limit on the WIMP-nucleon cross section), these events must be run through a statistical model. In XENON100, the method used is the profile likelihood (PL) analysis [22].

The full likelihood function for a given WIMP mass  $m_\chi$  and a given cross section  $\sigma$  is the product of the likelihoods of all the measurements done to constrain the nuisance parameters. It is given by equation 3.7, where  $\mathcal{L}_1$  is the main measurement from the detector,  $\mathcal{L}_2$  is the nuclear recoil band measurement,  $\mathcal{L}_3$  is the electron recoil band measurement,  $\mathcal{L}_4$  is the  $L_{eff}$  measurement and  $\mathcal{L}_5$  is the measurement of the galactic escape velocity. The main advantage of using the PL analysis over other statistical methods is that it takes into account both calibration and dark matter data

as parameters as well as the systematic uncertainties due to  $L_{eff}$  and  $v_{esc}$ , which are treated with their own likelihood functions  $\mathcal{L}_4(L_{eff})$  and  $\mathcal{L}_5(v_{esc})$  and are multiplied to the normal likelihood  $\mathcal{L}_1(\sigma, N_b, \epsilon_s, \epsilon_b, \mathcal{L}_{eff}, v_{esc}; m_\chi)$ .

$$\mathcal{L} = \mathcal{L}_1(\sigma, N_b, \epsilon_s, \epsilon_b, \mathcal{L}_{eff}, v_{esc}; m_\chi) \times \mathcal{L}_2(\epsilon_s) \times \mathcal{L}_3(\epsilon_b) \times \mathcal{L}_4(L_{eff}) \times \mathcal{L}_5(v_{esc}) \quad (3.7)$$

To calculate this likelihood, the nuclear recoil calibration is divided into bands containing the same amount of data. The electron recoil calibration data is then superimposed on these bands and the amount of electronic recoils is calculated for each band, thus giving a background distribution function. This is shown on figure 3.32.

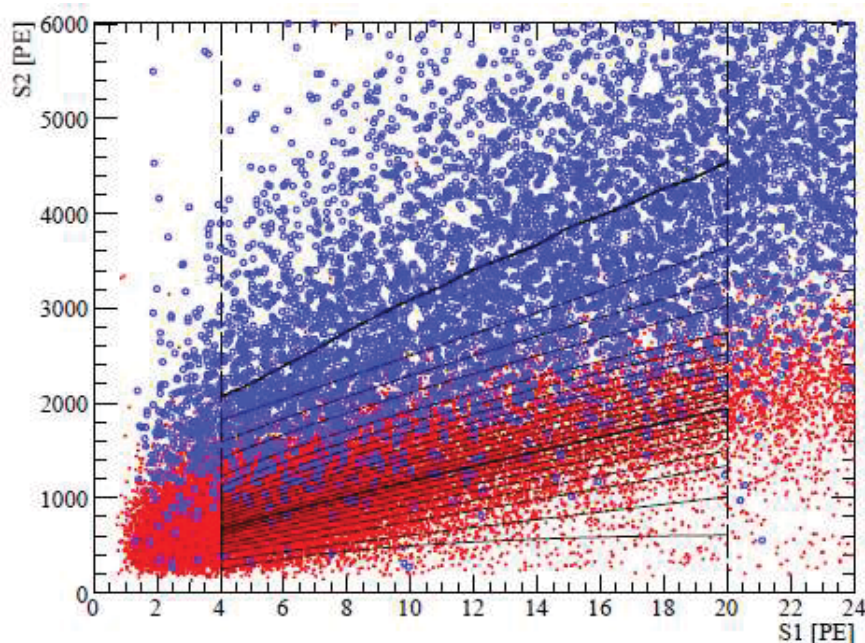


Figure 3.32: Profile likelihood analysis. The blue dots are the electronic recoils from a  $^{60}\text{Co}$  calibration source. The red dots are the nuclear recoils from an  $^{241}\text{AmBe}$  calibration source. The thin lines represent the  $j$  bands of the analysis, while the two thick lines are the median of the nuclear recoil and electronic recoil bands. The dashed vertical lines represent the relevant S1 parameter range [22].

It is noteworthy to mention that the profile likelihood analysis is performed over all parameters, including all calibration and WIMP search data, in order to define the maximum possible likelihood. Moreover, it is always performed to check for two hypotheses, that is whether the residual events after a dark matter search are consistent with background only or with background plus signal.

### 3.7 Dark Matter Search Results

After 225 live days of data taking, the results of the dark matter search were disclosed. To ensure that the data was not biased, a blind analysis was performed, using only calibration and side bands data. Because the data from the WIMP ROI is never looked at, the analysis is referred to as a blinded analysis. Once the analysis package was done and completed, the ROI was unblinded and the analysis package run over it. There was no post-analysis of the data, except to identify the remaining events.

Within the defined ROI, only two events remained as shown on figure 3.33 when only one was expected from the background.

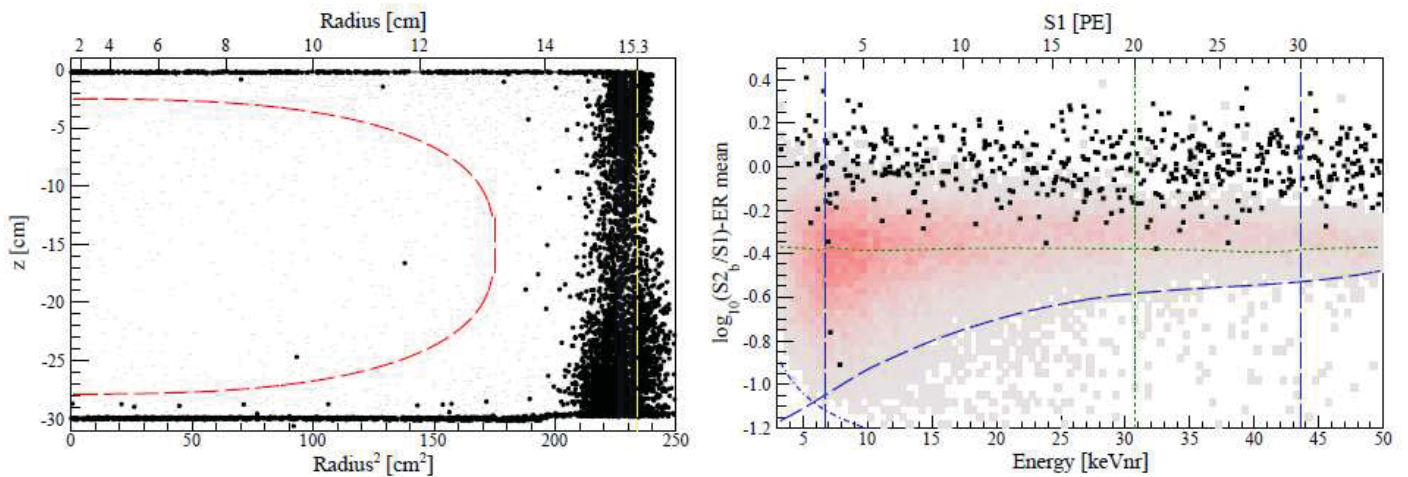


Figure 3.33: The two events from the XENON100 225 live days results. Right: as seen in the WIMP ROI with the calibration bands. Left: as seen on the physical detector

Running the PL analysis on these two events revealed that there was a 26.4% probability that they were due to background fluctuation. Because the PL analysis could not reject entirely the fact that these could only be background events, no claim of discovery was made and only a new limit in sensitivity was obtained, albeit, the best in the world at the time, reaching to cross-sections up to  $2.0 \cdot 10^{-45} \text{cm}^2$  (figure 3.34).

Note that in late 2013, the LUX experiment, which operates a dual phase xenon TPC almost identical in design to XENON100, released results on a dark matter search. With an increased mass of 250 kg and a fiducial volume of 118 kg, combined with a low energy threshold of 3 keVnr due to a high light yield and careful efficiency modeling, LUX placed a limit on the WIMP-nucleon cross section at  $\sigma_{SI} < 7.6 \cdot 10^{-46} \text{cm}^2$  for a  $33 \text{ GeV}/c^2$  WIMP [75]. This independent search and analysis provides a powerful confirmation of the XENON100 results.

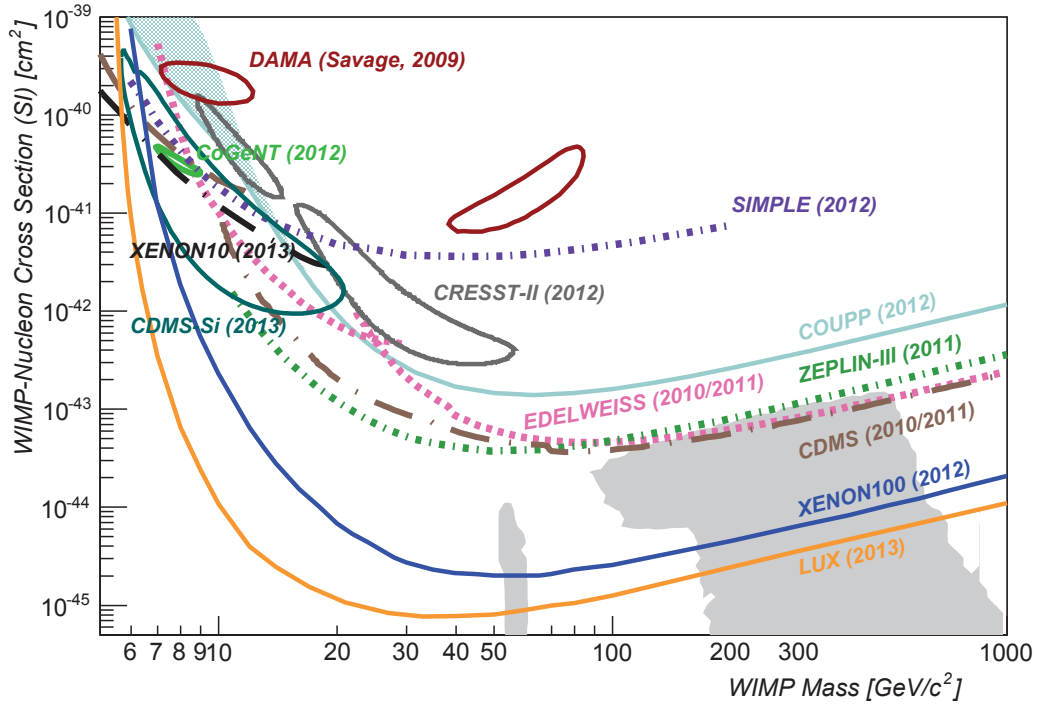
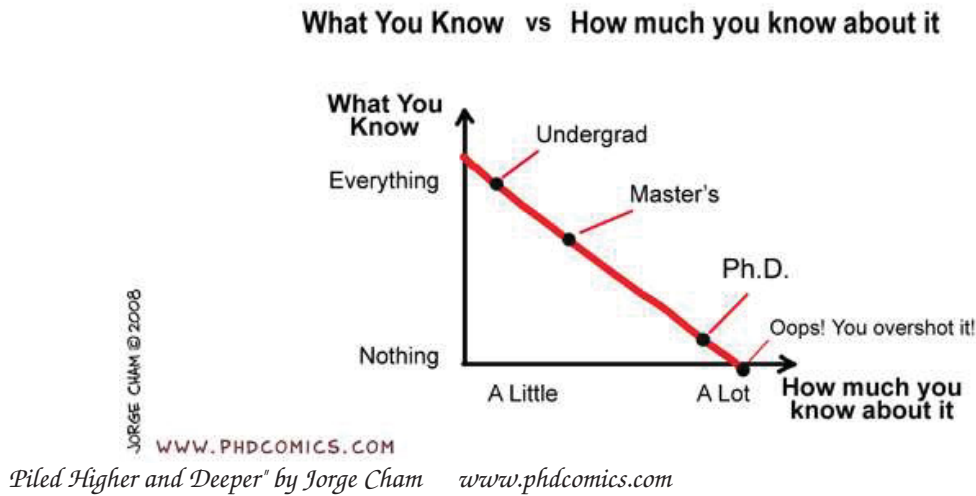


Figure 3.34: Results on spin-independent scattering from 225 live days of data by XENON100 [23]

Since the release of the XENON100 spin independent results, other analyses have been performed on the data such as a spin dependent search which also led to new improved sensitivities [95] and an inelastic dark matter search [76], which looks for interactions due to DM particles which can upscatter to an excited state in the collision process. The main result from the inelastic DM search was that it ruled out the claim that the DAMA/LIBRA data could be due to inelastic dark matter.



# Chapter 4. LIGHT YIELD STUDIES FOR THE XENON100 EXPERIMENT



## 4.1 Introduction to Light Yield

As explained in the previous chapter, the XENON100 experiment detects scintillation light from interaction of particles with a liquid xenon target to look for dark matter interactions. The detection of this light is thus one of the most important components of the experiment. In addition to the amount of light liberated in the interaction, which is dependent on the recoil energy, the efficiency of the light collection must be known. This is a dominantly geometrical effect and highly depends on the interaction position in the detector. The two quantities of interest related to these effects are the light yield (LY), which is the number of photoelectrons detected by the PMTs per keV recoil energy (pe/keV), and the light collection efficiency (LCE), which is a dimensionless quantity defined as the local light yield divided by the average light yield in the detector.

To be able to measure the energy spectra of the background and a possible dark matter signal above this background, the energy resolution must be as small as possible. The dominant contribution to the energy resolution is the variation in light collection efficiency as a function of the position in the detector. The bigger the variations, the worse the energy resolution. Consequently, these variations in the detector's response to light must be corrected for. This means that for a given recoil energy,

the S1 signal should be corrected to account for the position dependent light collection efficiency. For example, this means that for the same energy recoil, the corrected S1 signal should be the same whether the interaction happened at the top or at the bottom of the TPC. Consequently, the S1 light collection efficiency is mapped out throughout the detector and used to apply a correction to the raw S1 signal.

In addition, because the detector is cylindrical, the LCE should be axially symmetric to lowest order, which means that the correction maps need in principle only be done in  $r$  and  $z$ . Figure 4.1 shows the 2D correction map which was used up to the 100 live days dark matter search (run 8) in 2011 [19]. The correction map shows the relative light collection efficiency, which is given by the ratio of the local light yield to the average light yield in the detector.

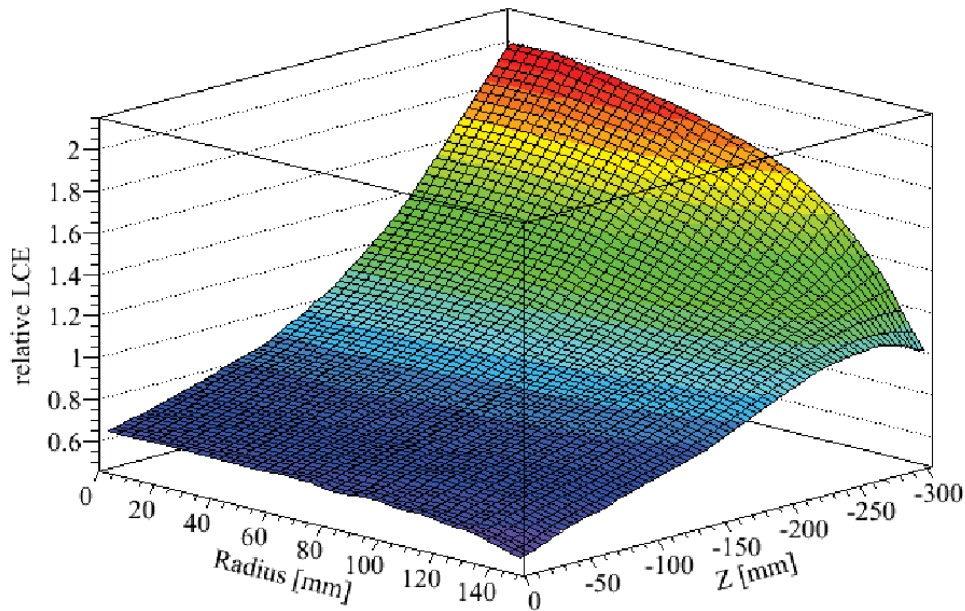


Figure 4.1: The 2D light collection efficiency map for the XENON100 detector [15].

For run 10 of XENON100, which comprised 225 live days of data taken in 2011 and 2012 [23], the LCE maps had to be checked to ensure that the behavior of the detector had not changed. Additionally, to facilitate analysis, there was a need to convert these 2D  $LCE(r,z)$  maps into 3D  $LCE(x,y,z)$  maps. While no deviation from axial symmetry was expected, the first very coarse  $LCE(x,y,z)$  map made revealed an axial asymmetry in the bottom part of the TPC as shown on figure 4.2.

This finding was unexpected and gave rise to the concern that the assumption that the LCE was axially symmetric was wrong, thus requiring a detailed study to be made on the matter. This eventually led to the creation of 3D  $LCE(r,\theta,z)$  maps and a 3D correction function which was used

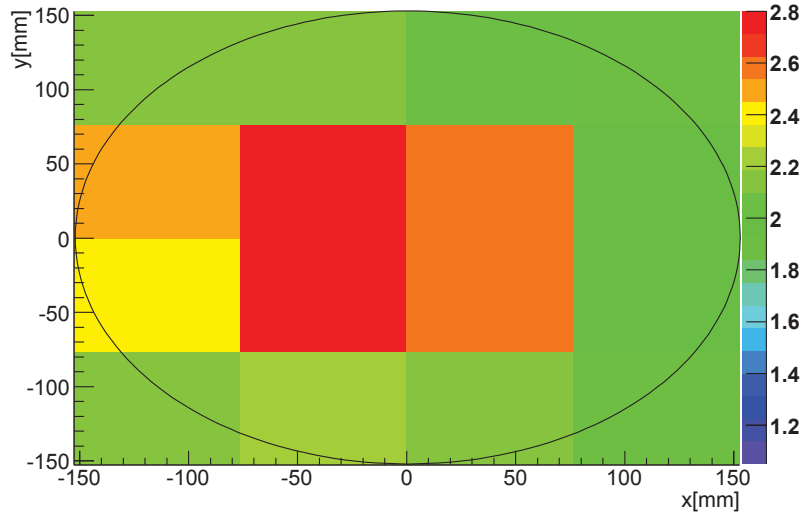


Figure 4.2: Coarse LCE( $x,y,z$ ) map for the bottom part of the TPC. The black circle represents the edge of TPC.

in the run 10 analysis and published results [23]. This particular study is the object of this chapter.

## 4.2 Measuring the Light Collection Efficiency and Light Yield

To measure the LCE, the detector is exposed to a mono-energetic gamma source. Events where the full gamma energy has been deposited in a single scattering site in the detector have a known recoil energy which is equal to the incident gamma energy. By carefully selecting these events, the local light yield can be obtained by measuring the S1 signal in number of photoelectrons detected by the PMTs and normalizing this by the known incident gamma energy. By measuring the LY throughout the detector, and normalizing by the average LY of the detector, the energy dependence cancels out and the position dependent LCE is obtained.

### 4.2.1 Choosing a Calibration Source

In order to choose an adequate mono-energetic source, some considerations have to be taken into account. Because of the high  $Z$  value of xenon, gamma radiation has generally a short attenuation length. It is hence difficult to have sufficient statistics throughout the detector. In particular, at lower gamma energies, the attenuation length is shorter than at higher energies. Because of this, a source, such as  $^{137}\text{Cs}$ , which emits high energy gammas should be chosen. Indeed,  $^{137}\text{Cs}$  decays via  $\beta^-$  into a metastable state of  $^{137}\text{Ba}$  which then in turn emits a 662 keV gamma when transitioning to the ground state. This energy is high enough to penetrate to the center of the detector, and by

positioning this source at three points about the axis of the detector one ensures that the sides of the detector are illuminated more uniformly.

One shortcoming of using a high energy gamma source like  $^{137}\text{Cs}$  is that XENON100 was designed to detect low energy recoils. The S2 signals from such high energy recoils saturate the most brightly illuminated PMTs, thus affecting the position reconstruction which would in turn affect the position dependent LY and LCE. To avoid this problem, data was taken using a reduced voltage on the anode, which in turn reduces the production of the proportional scintillation light of the S2 and prevents PMT saturation.

### 4.2.2 Gamma Interactions

In general, gamma radiation can interact in the detector by three processes, photoelectric effect, Compton scattering, and pair production. Since the 662 keV gamma from  $^{137}\text{Cs}$  is less than twice the electron mass, pair production is forbidden. Of the remaining two processes, the photoelectric effect happens about 10% of the time and Compton scattering has the dominant cross section for this energy as previously shown on figure 3.28.

#### *Photoelectric Effect*

The photoelectric effect is the absorption of a photon by an electron where the entire energy from the photon goes into the ionization and recoil of the electron. The recoil energy  $E_{rec}$  is less than the energy of the incident photon  $E_\gamma$  because of the binding energy of the atom  $E_B$ , and is related by  $E_{rec} = E_\gamma - E_B$ . However, due to transitions of the ionized xenon atom such as x-ray emission and Auger electrons, the binding energy of the ionized electron is released into the xenon medium as well. Thus, the sum of the energy from the recoiling electron and the decay products from the excited xenon atom gives the full incident photon energy. In the case of  $^{137}\text{Cs}$  this translates into a full absorption peak at 662 keV on an S1 spectrum.

#### *Compton Scattering*

Compton scattering is the scattering of a photon off of an electron. The photon deposits some of its energy to the electron which recoils while an outgoing photon of longer wavelength is emitted.

Because the local light yield calculation requires a full energy deposition in a single site, it is crucial to understand how and where in the detector does Compton scattering happen. There are three possibilities for the outgoing gamma. First, there are events where after the first Compton scatter,

the lower energy outgoing gamma can Compton scatter again, then the still lower energy outgoing gamma of the second Compton scatter can also interact, ending in absorption by the photoelectric effect, thereby depositing the full energy of the initial incident gamma in the detector. Due to the spatial resolution of the detector mentioned in section 3.6.2, if these multiple scatters happen within 3 mm in  $z$ , the detector cannot resolve them as separate scatters and they are interpreted as a single interaction where the energy of the incident gamma has been fully absorbed by the electron, akin to the photoelectric effect. These events are considered good calibration events and are the events selected to calculate the light yield.

Second, some gammas undergo exactly the same process except for the fact that it happens on distances higher than 3 mm. Again, as explained in section 3.6.2, these events are considered to be multiple scatters, that is, separate events with two distinctly identifiable S2 signals. These events are thus simply discarded.

Finally, some gammas after one or several scatters leave the detector. These events will thus not contribute to the full absorption peak but will exhibit a separate feature in the spectrum.

That said, because the first category of events contributes to the full absorption peak and can be used to determine the LY, it is important to be able to determine what percentage of the total events will scatter within 3 mm. This is shown in equation 4.1 where the probability  $P_{scatter}$  of a second interaction happening within a distance  $d$  of the initial scatter is given by:

$$P_{scatter} = \frac{1}{l} \int_0^d e^{-\frac{x}{l}} dx, \quad (4.1)$$

However, equation 4.1 depends on the mean free path  $l$  of the outgoing gamma after the first scatter. This mean free path can be calculated from the attenuation coefficient shown on figure 3.28 which itself depends on the energy of the outgoing photon  $E'_\gamma$ .

This outgoing photon energy is linked, via equation 4.2 to the wavelength of the outgoing photon  $\lambda'$ , which itself depends on the initial wavelength of the photon  $\lambda$  according to the Compton scattering formula in equation 4.3 where  $h$  is the Planck constant,  $m_e$  is the electron rest mass,  $c$  is the speed of light and  $\theta$  is the scattering angle.

$$E'_\gamma = \frac{hc}{\lambda'} \quad (4.2)$$

$$\lambda' - \lambda = \frac{h(1 - \cos\theta)}{m_e c} \quad (4.3)$$

In addition, the fraction of incident gammas that undergo multiple scattering in the detector can be understood by looking at the differential cross section for Compton scattering, given by the Klein-Nishina formula :

$$\frac{d\sigma}{d\Omega} = \alpha^2 r_e^2 P^2(E_\gamma, \theta) [P(E_\gamma, \theta) + P^{-1}(E_\gamma, \theta) - 1 + \cos^2(\theta)]/2, \quad (4.4)$$

where  $\alpha$  is the fine structure constant,  $r_e = \hbar/m_e c$  is the reduced Compton wavelength of the electron,  $m_e$  is the electron mass, and  $P(E_\gamma, \theta)$  is the ratio of photon energy  $E_\gamma$  after and before scattering, derived from equations 4.2 and 4.3 and given by:

$$P(E_\gamma, \theta) = \frac{E'_\gamma}{E_\gamma} = \frac{1}{1 + (E_\gamma/m_e c^2)(1 - \cos(\theta))}. \quad (4.5)$$

Averaging equation 4.4 over all scattering angles allows to derive the average energy of a photon that has undergone a single Compton scatter. This average energy of the outgoing photon is then given by:

$$P(E_\gamma) = \frac{\pi \sqrt{m_e c^2}}{\sqrt{2E_\gamma + m_e c^2}}. \quad (4.6)$$

Applying equation 4.6 for a 662 keV gamma, the average energy of the outgoing photon after one Compton scatter is 398 keV. Looking at figure 3.28, the mean free path at this energy is 3.3 cm. Using this number in equation 4.1 and integrating from 0 to 3 mm, one can finally answer that the probability  $P_{scatter}$  of a second interaction happening within 3 mm in z of the initial scatter for a 662 keV photon is 9% which means that the remaining 91% of incident photons that undergo Compton scattering either multiple scatter and are thus discarded or leave the detector.

### 4.2.3 S1 Spectrum

Now that the proportions of events which can be used in the calibration have been calculated, the last point is to establish what the S1 spectrum should look like.

In gamma spectroscopy, there is typically a Compton edge with a gap between the maximum energy deposition due to Compton scattering (see equation 4.3 for  $\theta = 180^\circ$ ) and the full absorption peak. This is what should be expected in this case. However, some photons lose energy by scattering in the cryostat and other materials before they enter the detector. These photons will then be more easily fully absorbed. However this full absorption will happen at lower energy, thus smearing the full absorption peak towards lower energies. Similarly, events who leave the detector may have scattered multiple times before leaving the detector, losing energy in the process. By doing so the Compton

edge is smeared into a peak (hereafter called the Compton peak). Finally, the combination of these two effects bridges the gap between the Compton edge and the full absorption peak so there is no visible Compton edge.

Additionally, since the energy of forward and backward scattered photons is different, as shown in equation 4.3, the location of the Compton peak depends on the event position relative to the source. This is represented on figure 4.3.

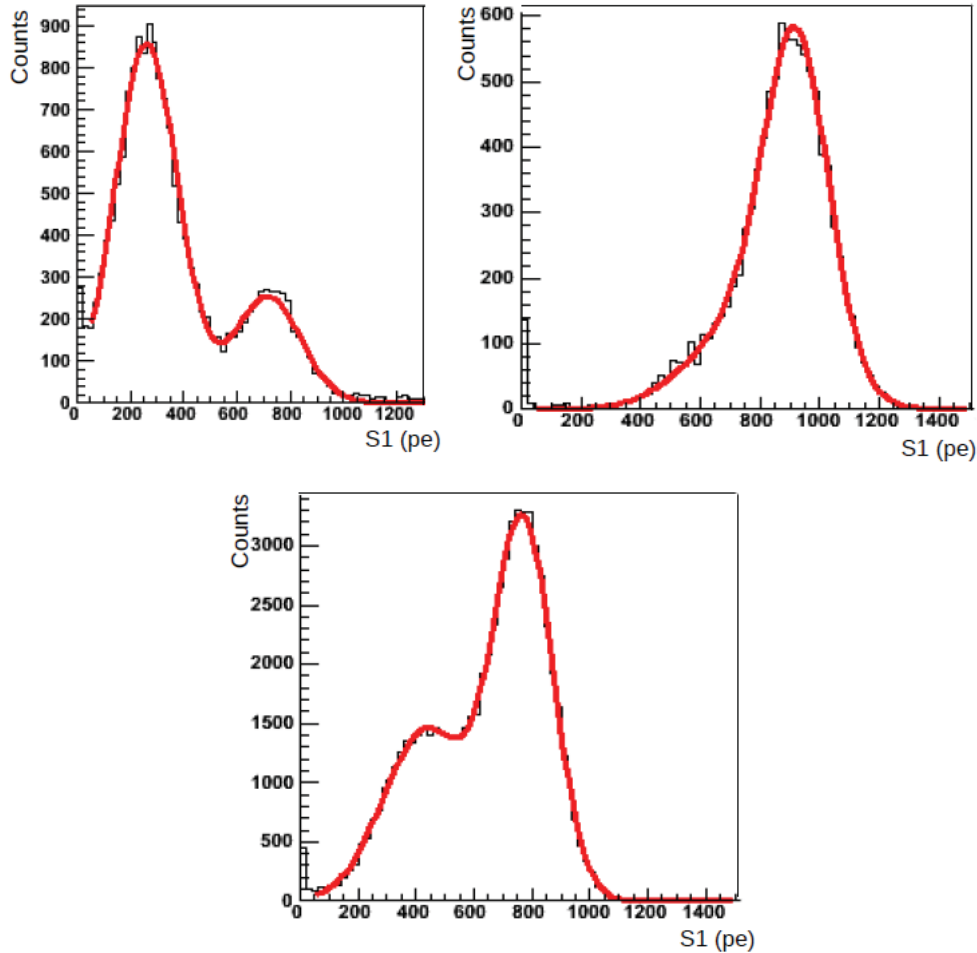


Figure 4.3: Spectra of the S1 light (pe) in the detector from a  $^{137}\text{Cs}$  calibration for initial scatters opposite the source position (top left), in the center of the TPC (top right) and next to the source position (bottom).

For events with an initial scatter near the source, forward scattering higher energy gammas have a large volume of xenon to traverse before leaving the detector, and thus there are few forward scattering gammas that leave the detector. However, for backward scattering photons, there is a high probability to leave the detector, thus giving rise to a high energy Compton peak. This is shown on figure 4.3 (bottom) where the Compton peak is clearly dominated by backscattered photons.

At the opposite side of the detector from the source, the converse is true. Forward scattering

high energy gammas have a high probability to leave the detector as they have already traversed most of the detector without interacting, thus giving rise to a lower Compton peak, while backward scattering gammas have to traverse again the whole detector to leave and so have a low probability to escape. This is shown on figure 4.3 (top left) where the dominant contribution of single scatter events is due to photons that undergo a single Compton scatter in the forward direction and then escape the detector.

For initial scatters in the center of the detector, there is a low probability for the gamma to leave in any direction. This is shown on figure 4.3 (top right) where the Compton peak is negligible and the only visible feature is the full absorption peak.

Note that to plot the S1 spectrum for  $^{137}\text{Cs}$  calibration data, a minimal set of data quality cuts is applied. The cuts used are a signal to noise cut that ensures the S1 signal is clearly visible above any noise present on the waveform, a veto cut which ensures that events have not triggered in the veto before triggering in the TPC, a single S1 selection cut that discards waveforms with multiple S1 signals, and a single scatter cut that removes events with multiple S2s coming from multiple scatters farther apart than the 3 mm necessary to resolve these events in XENON100. The events that pass these selection criteria should consist predominantly of single site events due to full absorption from the photoelectric effect or Compton scattering. Note that while extensive data quality cuts were defined for the dark matter search analysis, a minimum set were used here to minimize the bias on the light yield measurement.

Finally, to fit the data, a two Gaussian fit function is used, which matches the full absorption peak and Compton peak well. The light yield is calculated from the fit function according to equation 5.1 where LY is the light yield in pe/keV, and  $\langle S1_{fap} \rangle$  the S1 signal associated to the mean of the full absorption peak.

$$LY = \frac{\langle S1_{fap} \rangle}{662\text{keV}} \quad (4.7)$$

### 4.3 3D $r\theta z$ Maps of the Light Yield

Now that the procedure to calculate the local light yield has been laid out, 3D position dependent maps of the light yield can be produced.

For these maps,  $^{137}\text{Cs}$  data from both run 8 and run 10, which was taken at all three source locations, were combined.

The detector is divided in 1450 bins, 10 bins in  $z$ , making each slab 3 cm thick, 5 bins in  $r$  and respectively 10, 15, 20, 40 or 60 bins in  $\theta$  for increasing  $r$ . The detector should indeed be divided in as many bins as possible so as to be able to calculate the most precise ly maps later on. This number was found as the maximum possible number of bins which would all have sufficient statistics.

Following the method described in the previous section, for each of these 1450 bins, the S1 spectra have been plotted and fitted and the corresponding light yield calculated. Because of the big amount of data required not all fits are presented here but only a small subset of them are shown on figure 4.4 as an example.

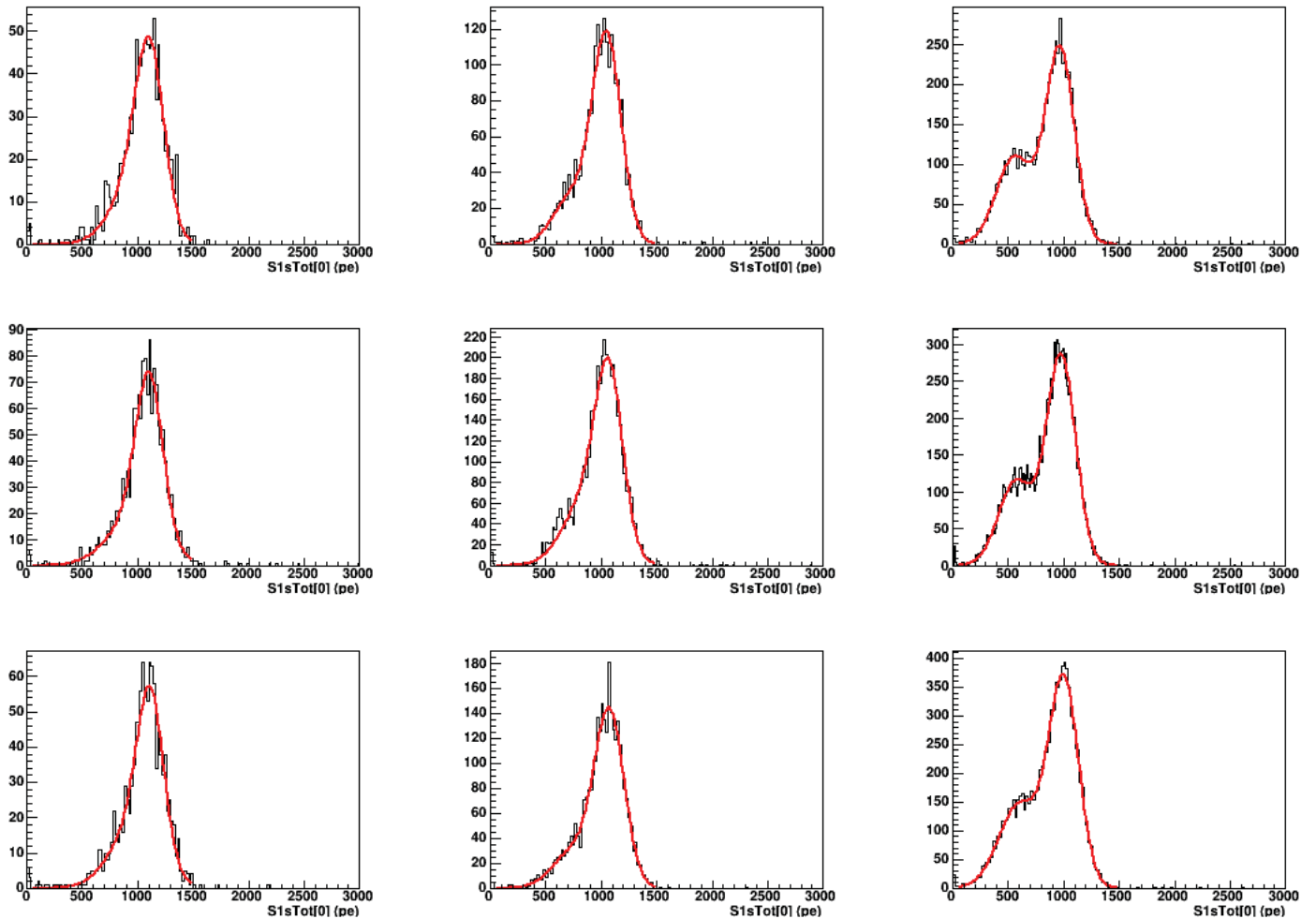


Figure 4.4: Example of S1 spectra with associated fits used to calculate and make the light yield map.

The corresponding light yield maps are shown on figure 4.5. The asymmetry is once again extremely clear in the lowest two slabs of the TPC, so within 6 cm of the bottom.

These maps give an average light yield on the whole TPC of 1.6 pe/keV with a minimum light yield of 0.9 pe/keV at the top of the TPC and a maximum light yield of 3.3 pe/keV at the bottom of the TPC.

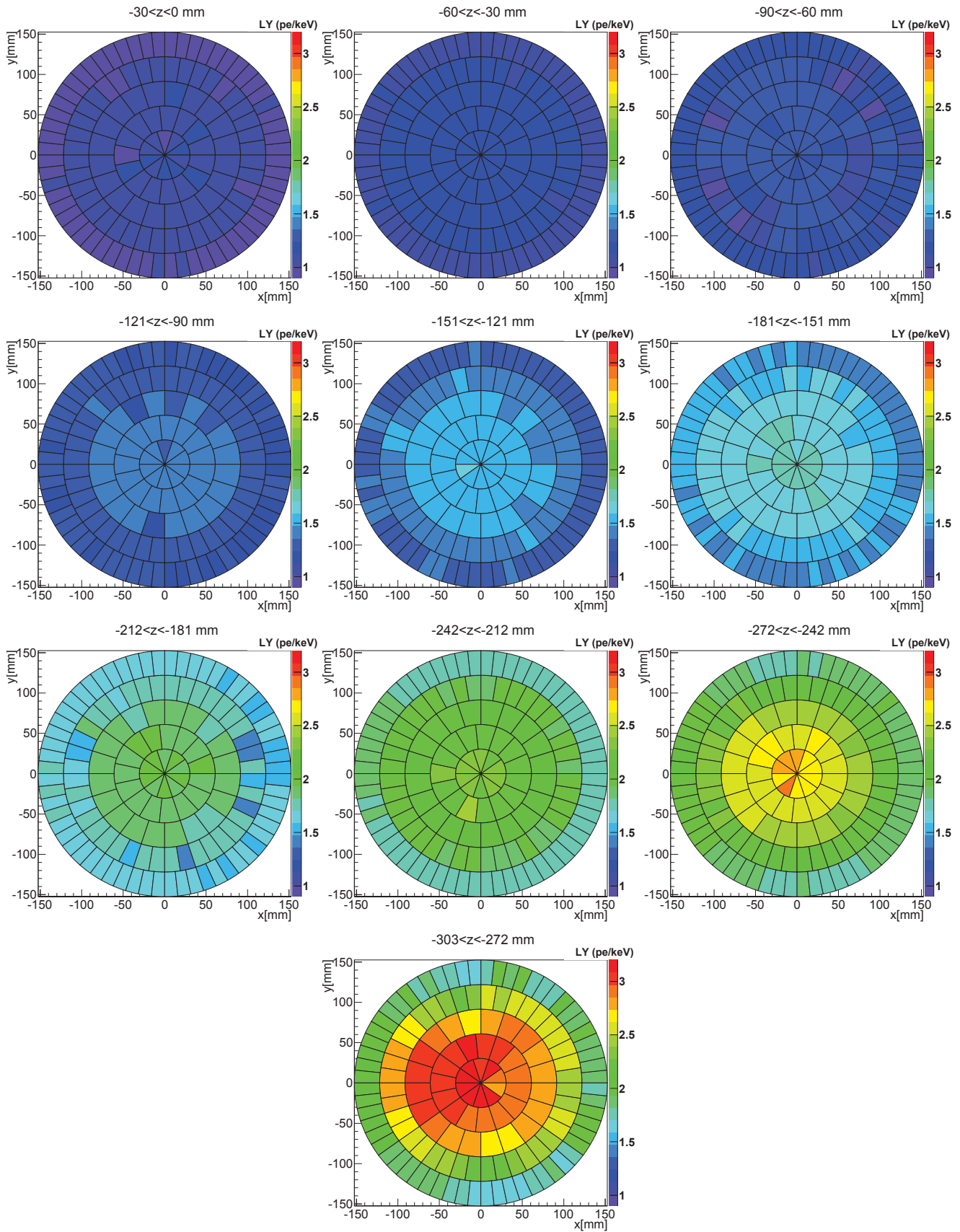


Figure 4.5: Light yield maps for the 9 z slabs of the TPC from top to bottom (z ranges from 0 to -303 mm)

## 4.4 Evolution of the LY over Time

As mentioned in the previous section, data from run 8 and run 10 have been combined to give out the most statistics especially at the center of the TPC. However these two runs happened 1.5 years apart from one another and the light yield in the TPC could very well have changed in that amount of time. It was thus necessary to check that the light yield was indeed the same for these two runs. This was done by generating ly maps for both runs and dividing the maps from run 10 by the maps from run 8. The results is shown on figure 4.6. There is effectively no difference between in light yield between the two datasets, except for a few localized discrepancies due to differently functioning PMTs, thus making the combined use of run 8 and run 10 appropriate.

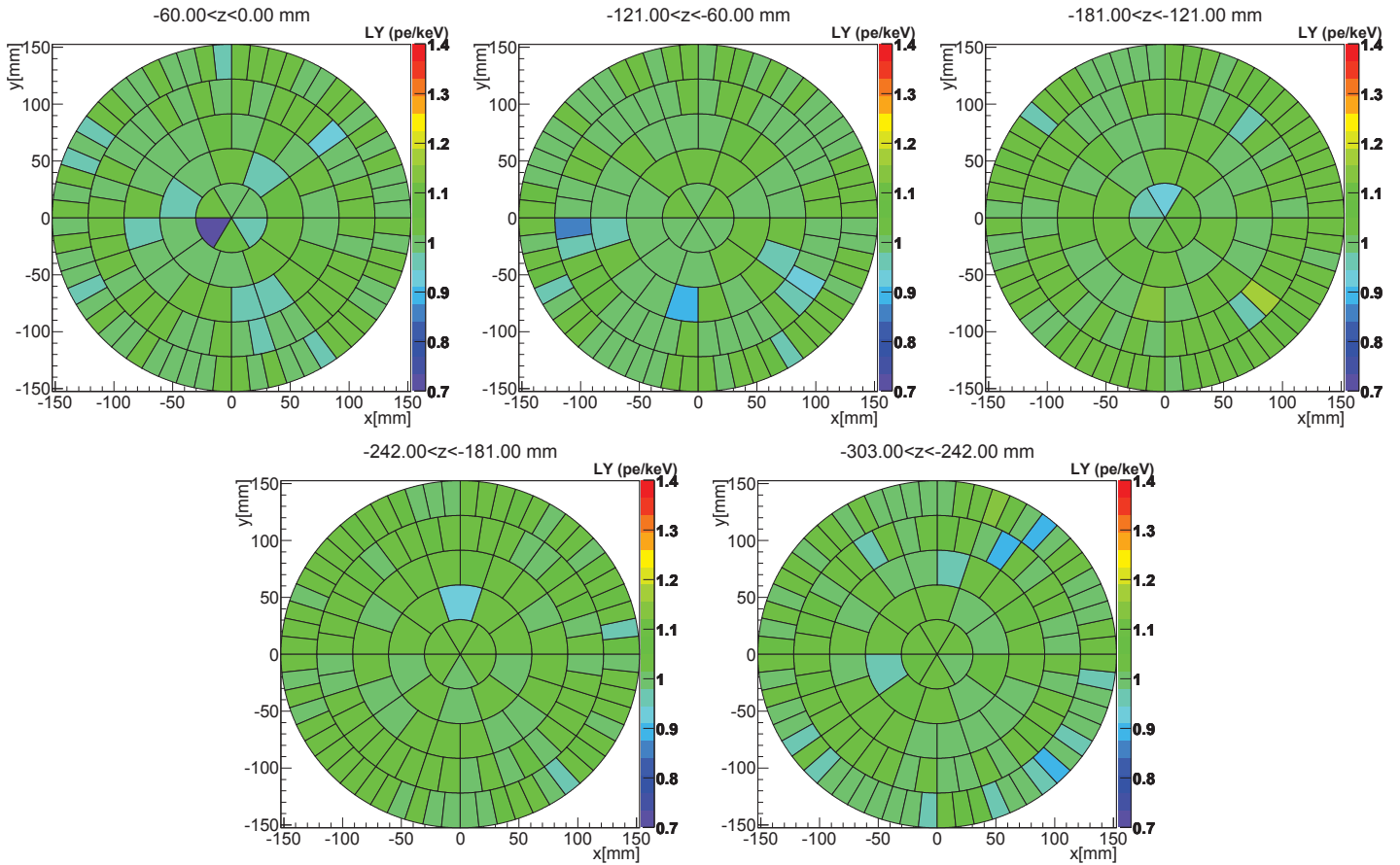


Figure 4.6: Ratio of the light yield maps of run 10 over those of run 8 from top to bottom of the TPC.

## 4.5 Quantifying the Asymmetry

To quantify the asymmetry, the light yield is plotted as a function of  $\theta$  and compared for all vertical z slabs at different radial positions  $r$ . This is shown on figure 4.7.

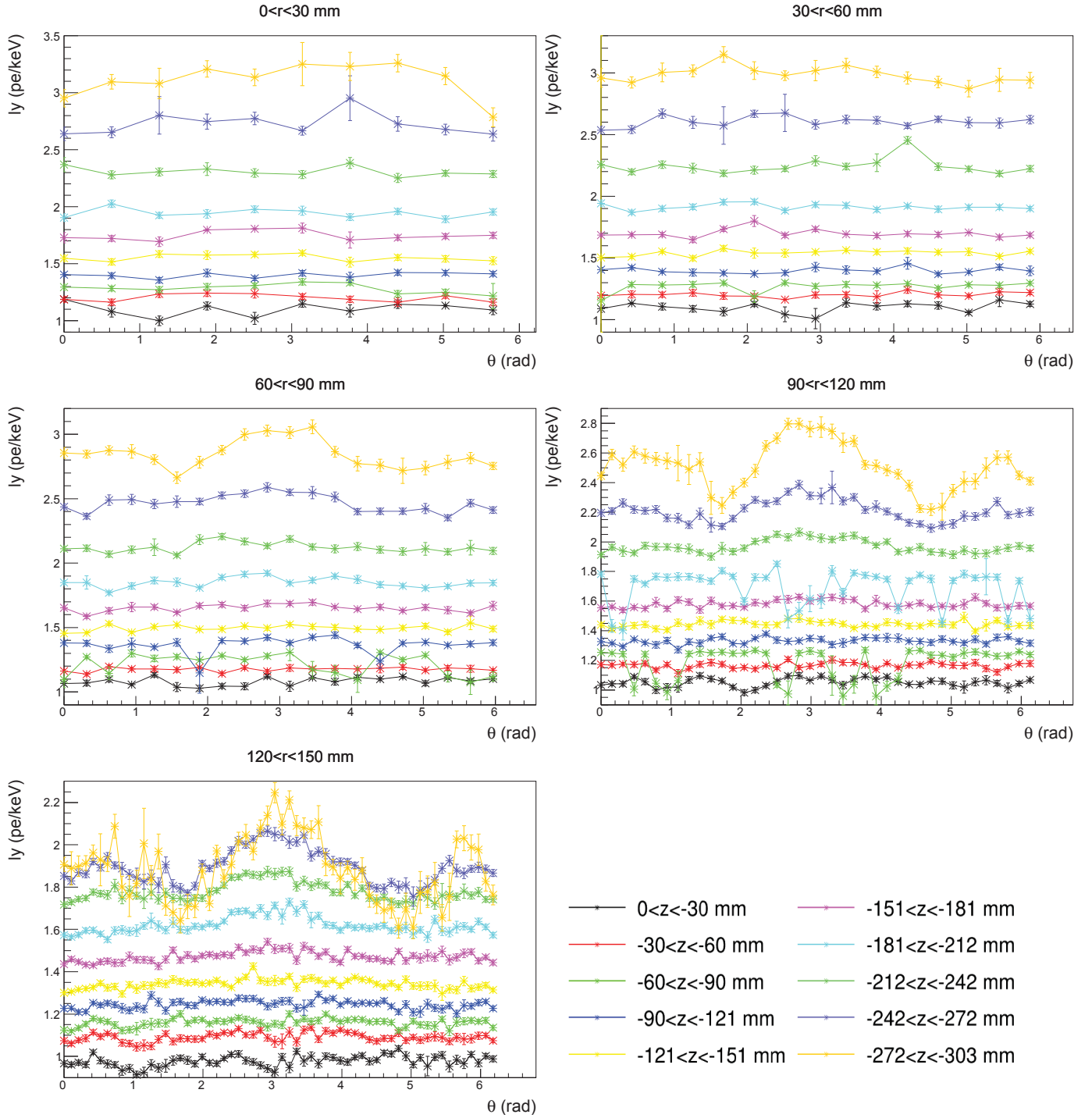


Figure 4.7: Light yield as a function of the azimuthal angle  $\theta$  for different vertical slabs  $z$  of the TPC and radial rings  $r$ .

Once again, the same two obvious features are observed however perhaps even more evidently. First the light yield increases from top to bottom of the TPC and second, the light yield axially fluctuates much more at the bottom of the TPC especially for radii superior to 60 mm.

To quantify these azimuthal fluctuations, order 0 polynomial fits are done to each plot of figure 4.7 and the corresponding reduced  $\chi^2$  is computed. In this case the reduced  $\chi^2$  is a measure of how

flat in light yield each ring is and gives thus an idea of how big an asymmetry there is. This is shown on figure 4.8. For most of the detector, the reduced  $\chi^2$  is around 2, which corresponds to a rather flat distribution. The reason the reduced  $\chi^2$  is greater than 1 is that there are additional systematics that are difficult to quantify in the error treatment, such as the finite bin sizes for the LY measurements. However, the reduced  $\chi^2$  goes up to 14 in the outer rings of the bottom part of the TPC which means that these azimuthal fluctuations are indeed a real asymmetry and not just some random fluctuations.

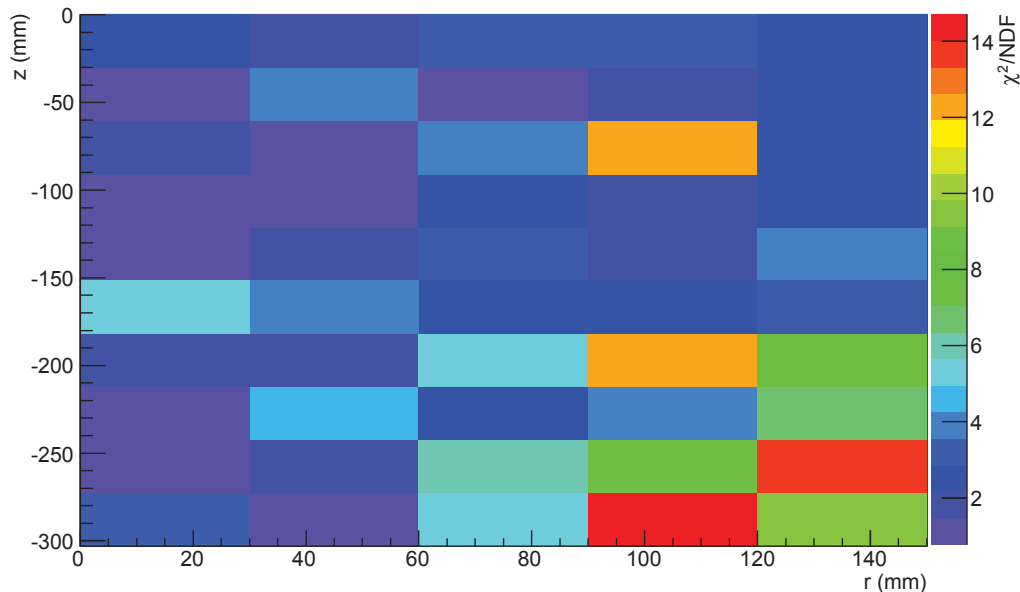


Figure 4.8: Reduced  $\chi^2$  for each z,r ring of the TPC

## 4.6 Cause of the Asymmetry

Unfortunately the cause of the asymmetry is still as of today, unknown. Several hypotheses have indeed been put forward however they are all extremely difficult or impossible to test until the detector is emptied or that dedicated experiment be built to answer those questions. Amongst these hypotheses, four are the most likely. First, some PMTs have different quantum efficiencies and thus lead a different amount of lights than other. This however is difficult to test without a dedicated experiment. Second, this could come from the meshes. Either there are some inequalities in their transparencies, or they could also have distorted or eroded with time. This is unfortunately impossible to check until the detector is emptied and the meshes checked. Third, the teflon holding the PMTs could have shrunk or deformed and thus shifted the PMT arrays. However, once again,

this is impossible to check without opening the detector. Finally, the obvious hypothesis was that broken PMTs could produce this problem. However this was easily checked by superimposing the light yield map to the PMT map as shown on figure 4.9. However because no broken PMTs were nowhere near the asymmetry, this was discarded as the cause of it.

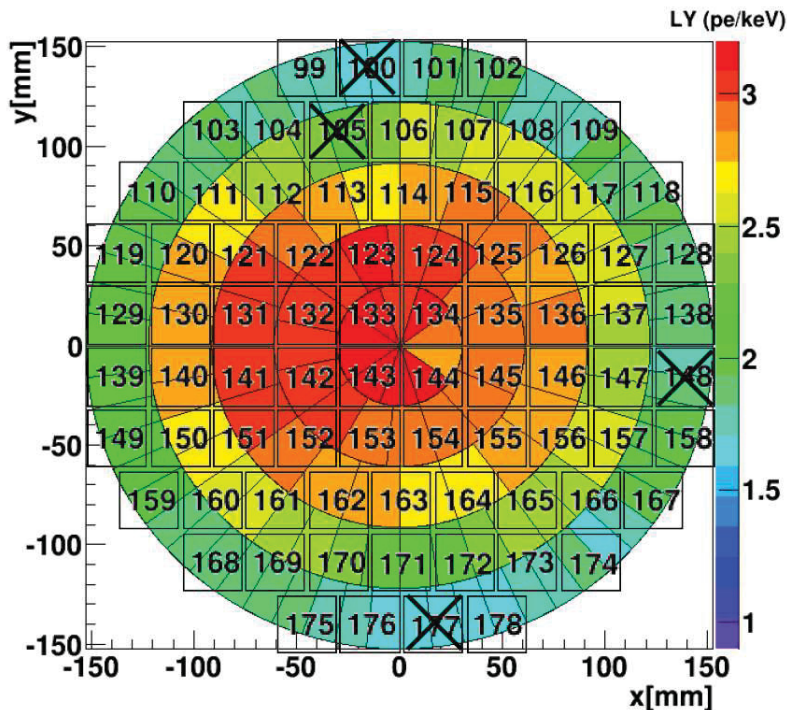


Figure 4.9: Superposition of the light map with the PMT array. PMTs marked with a cross are broken.

## 4.7 3D Correction Function

Once the asymmetry has been confirmed, the raw S1 data needs to be corrected to account for the light yield non-uniformity over the whole TPC. For this purpose, a correction function has to be implemented. Such a correction is simply a number which varies depending on the position in the TPC. This number has to be multiplied accordingly to each S1 signal in order to create a uniform variable throughout the TPC and must be available for any possible point in the TPC, thus making a 3D correction function. The process which allows to establish such a correction is the object of the following sections.

### 4.7.1 Method

As a reminder, to map out the light yield, the TPC was divided in 1450 volumes, 10 vertically in  $z$ , thus effectively cutting the TPC in 10 equal slabs, 5 radially in  $r$ , thus cutting each  $z$  slab into 5

rings, and 10, 15, 20, 40 or 60 azimuthally in  $\theta$  depending on increasing  $r$ , thus cutting each  $r$  ring of each  $z$  slab into 10, 15, 20, 40 or 60  $\theta$  slices. The light yield was calculated and is thus known in each of these 1450 volumes.

Using the light yield maps above (figure 4.5), the 1450 volumes are used to create 1450 lattice points, which will serve as a basis for the correction function. These lattice points are located at the center of each of the corresponding 1450 volumes and have a known light yield.

The light yield at any random position in the detector is calculated by performing a 3D linear interpolation between the 8 closest lattice points, 2 in  $r$ , 2 in  $\theta$ , 2 in  $z$ . The average light yield in the detector is then divided by the local light yield to give out the correction factor, which is the number that will be multiplied to the S1 signal. The process to find the local light yield is intuitively described in 2D on figure 4.10.

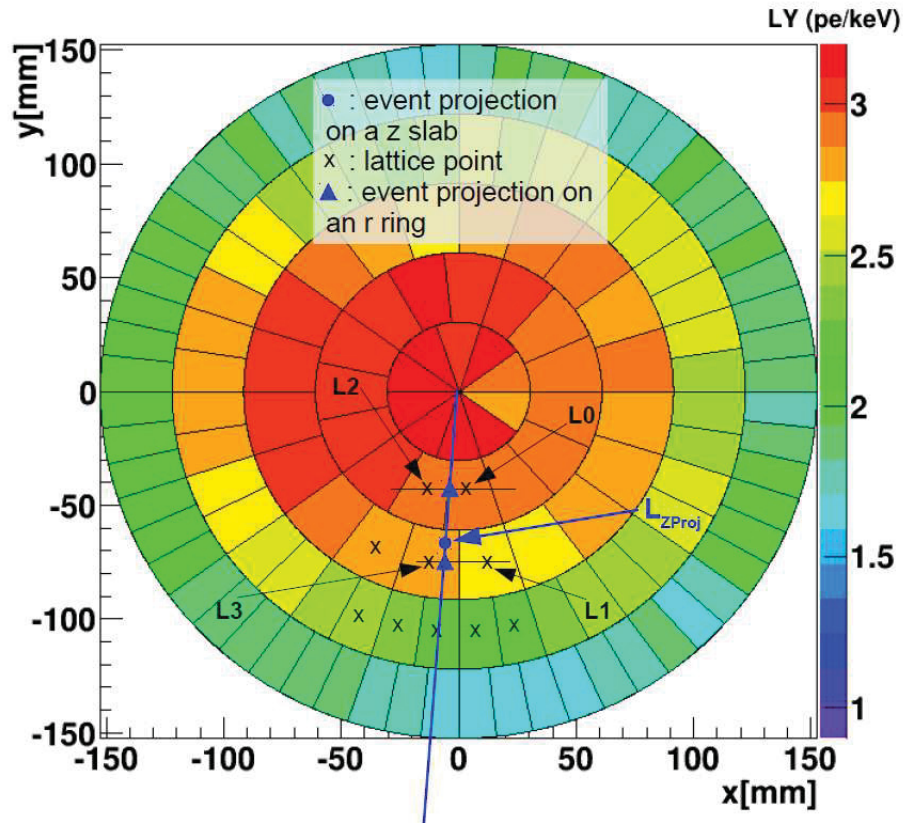


Figure 4.10: Intuitive description of the correction function for one  $z$  slab.

In more details, for each event, the correction function first finds between which  $z$  slices the event lays and then projects the event onto these two  $z$  slices. Figure 4.10 shows this process in 2D for one  $z$  slab but the process is the same for the other slab. For each  $z$  slab, the function then finds the 4 nearest neighboring lattice points (L0,L1,L2,L3). It then draws a line between the two pairs of same  $r$  and calculates the light yield at the position of the projection of the event onto these

two lines (purple triangles). These two points are again interpolated between to find the light yield at the positions of the projections of the event on each of the two  $z$  slabs ( $L_{ZProj}$ ). Finally a last interpolation, not shown on figure 4.10, is done between the two  $z$  projections to find the proper light yield for the event at its original position.

In only two special cases will this function be slightly modified. For the edges, top and bottom of the detector, the event does not lay between two  $r$  rings. The 3D linear interpolation is still used but the lattice points used are the ones of the 2 preceding  $r$  rings resulting in an extrapolation to larger  $r$  rather than an interpolation.

For the center, something similar is done. The event is situated between the very center of the  $z$  slabs and the first  $r$  rings. The 3D linear interpolation is thus calculated between the center of the  $z$  slab and all 10 surrounding lattice points corresponding to the first  $r$  ring. As for the light yield at the very center of the  $z$  slab, it is simply calculated as the average of every lattice points on the first  $r$  ring.

### 4.7.2 Quality Checks

#### *Using a Random Function*

The first check to prove that the correction is behaving properly is to make a small MC using a random function for the light yield, generate lattice points and then apply the correction function to random events. If the correction is working properly, the distribution should narrow considerably and be made uniform. This is used to ensure that the algorithm functions correctly. Equation 4.8 represents the random function chosen for this MC where  $z$ ,  $\theta$  and  $r$  are the vertical, azimuthal and radial position of an event. This function was chosen because it is smooth in all three variables and is periodic in  $\theta$ .

$$ly = -2z + 15\sin(\theta) + 5r \quad (4.8)$$

Figure 4.11 shows the results on the distribution after applying the correction function. As expected, the distribution has been drastically narrowed with a diminution factor of 22.5, found by taking the ratio of the RMSs. This is the first proof that the correction function fulfills its requirements.

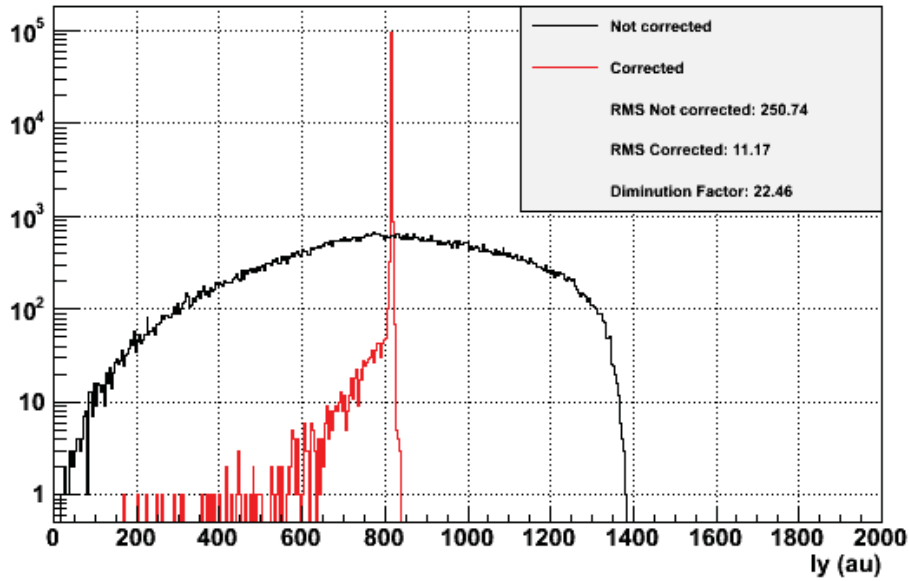


Figure 4.11: Check of the validity of the correction function for a random test function.

### Comparison with the 2D Correction Function

To check the performance of the correction function, it has to be compared to the actual 2D correction function which was used until run 10. This old correction function was done not using data from  $^{137}\text{Cs}$  but using the 40 keV line from AmBe calibration data. The principle was the same, the detector was separated in volumes and lattice points where found. However no interpolation was done, instead a smoothing function was drawn over these lattice points.

*Comparison of the Light Yield at the Lattice Points* The first element to compare is the initial behavior of the light yield at the lattice points used by both functions. To do this, the 3D light yield was recalculated in 2D by adding up the histograms over the azimuthal angles  $\theta$  and redoing the fitting. In addition, the light yield is normalized with  $z$  as the lattice points in the new and the old corrections are not at exactly the same  $z$  positions, due to the detector being divided into 12  $z$  slabs in the case of the 2D correction but in only 10  $z$  slabs for the 3D correction. The expectation from this comparison is that if the 3D correction works, then it should, once brought back to 2D, give the same results as the 2D correction.

An example of such a comparison is shown on figure 4.12 where the relative light yield is plotted as a function of the radial distance  $r$  for both the new and the existing correction function. The smoothing function for the old correction is also shown. It is very clear that the general trend is the same and that these two corrections seem to agree with one another, as was expected.

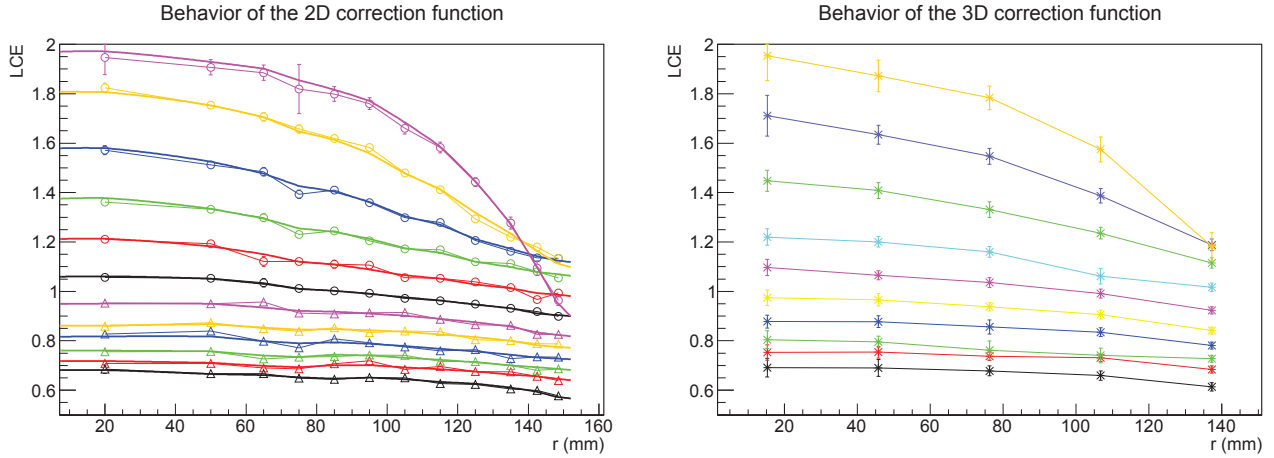


Figure 4.12: Comparison of the old (run 8) 2D correction function using AmBe (left) with the new 3D correction function using  $^{137}\text{Cs}$ . The 3D function has been brought back to 2D (right). The ordering of the curves from top to bottom corresponds to positions in the detector (z slabs) from bottom ( $z=-303$  mm) to top ( $z=0$  mm).

*Comparison of the Correction Factors* As a second step the behavior of the correction function itself must be checked at different  $z$ ,  $r$  and  $\theta$  positions. For this the correction factor itself is plotted as a function of  $r$ ,  $\theta$  and  $z$  for respectively different  $\theta$  and  $z$ ,  $r$  and  $z$ , and  $\theta$  and  $r$ . Again, the new 3D correction, averaged over  $\theta$  should match the old 2D correction, while it should be very different when looking at the correction factor as a function of  $\theta$ . Figures 4.13 show the correction factor as a function of  $r$  (top) and  $z$  (bottom) at the top (top left) and bottom (top right) of the TPC and in the center (bottom left) and on the edges (bottom right) of the TPC for all the different  $\theta$  slices. When averaging over  $\theta$ , the correction factors for both 2D and 3D correction agree with one another, thus once again proving that the 3D correction works and when averaged over  $\theta$  gives the same results as the 2D correction.

In addition figure 4.14 show the correction factor as a function of  $\theta$  for the bottom (right) and top (left) of the TPC for all  $r$  rings. The 2D correction, which of course doesn't change with  $\theta$ , is represented for each  $r$  ring by the dashed straight lines. Once again, it is very clear that while at the top of the TPC, the 3D correction simply fluctuates around a median value corresponding to the 2D correction, at the bottom of the TPC the 3D correction has a much bigger impact. The straight line from the 2D correction does not match the median of the curves corresponding to the 3D correction anymore, thus indicating a real correcting effect from the 3D correction, especially for the middle  $r$  rings of the TPC. This is proof that the 3D correction really improves the existing correction over the azimuthal angle, and that this correction is indeed needed.

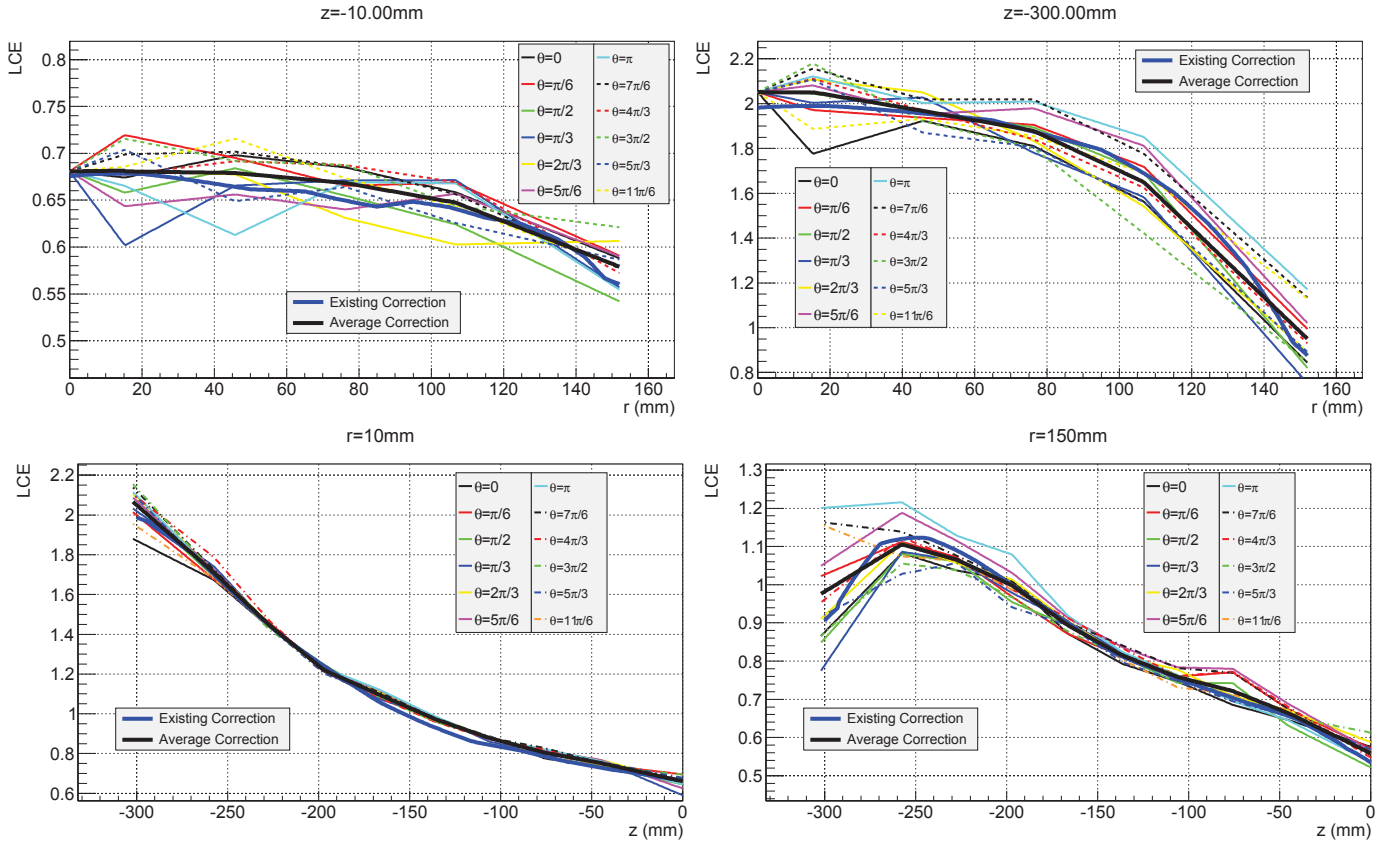


Figure 4.13: Behavior of the correction factor. Top Left: at the top of the TPC. Top Right: at the bottom of the TPC. Bottom Left: in the center region of the TPC. Bottom Right: at the edges of the TPC.

## Conclusions

In conclusion, using the  $^{137}\text{Cs}$  data to calculate the light yield leads to similar results to using AmBe data. In addition, with the new 3D correction function and unlike the old correction, smoothing is unnecessary. Because both corrections match sufficiently, a 2nd order correction to the 3D correction function is also unnecessary. By the same argument, the current binning is sufficient and re-binning is thus unnecessary. Finally, the two correction functions behave the same in 2D, thus validating the 3D correction, but they differ greatly in 3D, only due to the  $\theta$  component, which was indeed what was desired and required as to be able to address the azimuthal asymmetry of the light yield in the TPC.

## 4.8 Applying the Correction Function to the Data

Now that the 3D correction function seems to be working, it needs to be applied to different calibration data, not just  $^{137}\text{Cs}$  data. If it successfully flattens the ly distribution through the detector, no

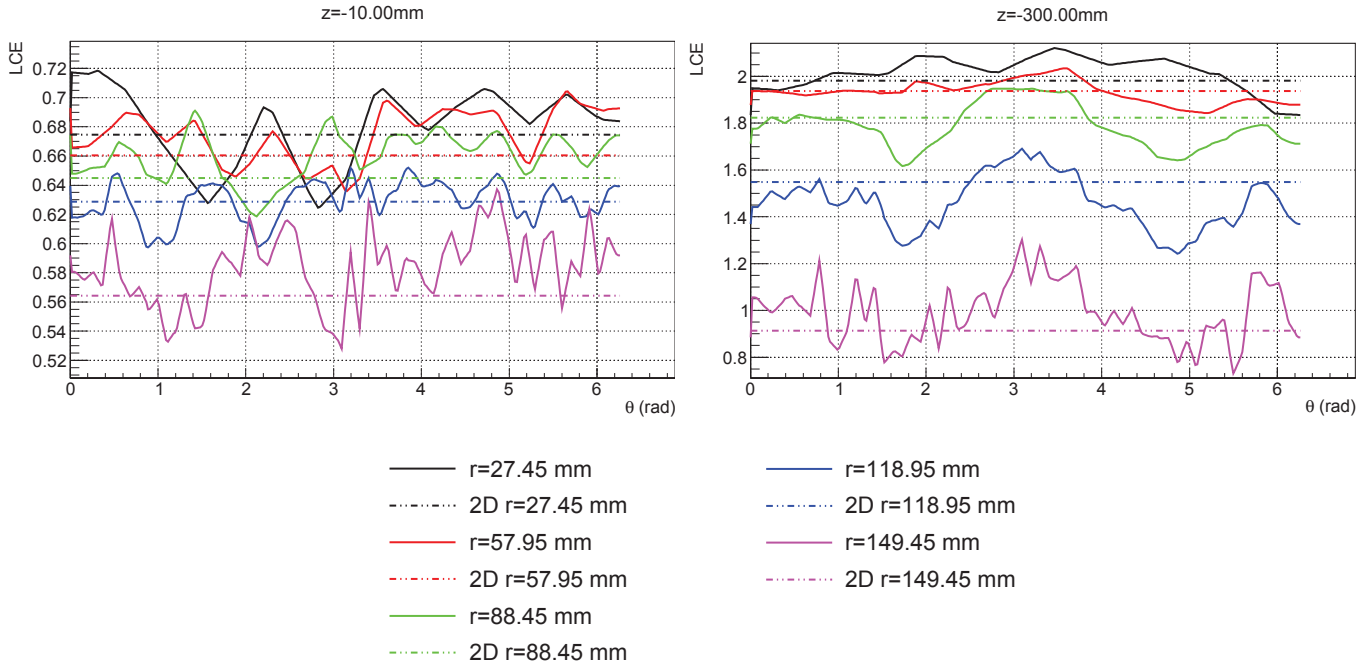


Figure 4.14: Behavior of the 3D correction factor as a function of  $\theta$ . Left: at the top of the TPC. Right: at the bottom of the TPC.

matter the data it is used on, this will be the ultimate proof that it works as intended and can be used as the standard correction for all data.

For completion, the correction function is applied first to  $^{137}\text{Cs}$  data, where it should obviously perform best. It will then be applied to the 40 keV AmBe data, and to the 164 keV xenon activated lines. Moreover, the 2D correction is also applied to the same data with the calculation of the light yield done using the same 3D binning as for the 3D correction. This will allow to see the variations over theta from both the 3D and the 2D corrections.

For the following, in order to have ample statistics everywhere, the detector is divided into 240 volumes. The correction function, however, is still obviously using 1450 lattice points to calculate the corrected light yield. The TPC is thus divided into 8 vertical  $z$ -slabs, 5 radial  $r$ -rings and 6 azimuthal  $\theta$ -slices.

#### 4.8.1 $^{137}\text{Cs}$ Data

A comparison of 2D and 3D corrected light yield maps applied to  $^{137}\text{Cs}$  data are shown on figure 4.15 on a scale of 1.45 to 1.74 pe/keV.

As expected, it is very clear that the 3D correction performs much better especially at the bottom of the detector where it smooths out the very obvious left-right asymmetry. To quantify the

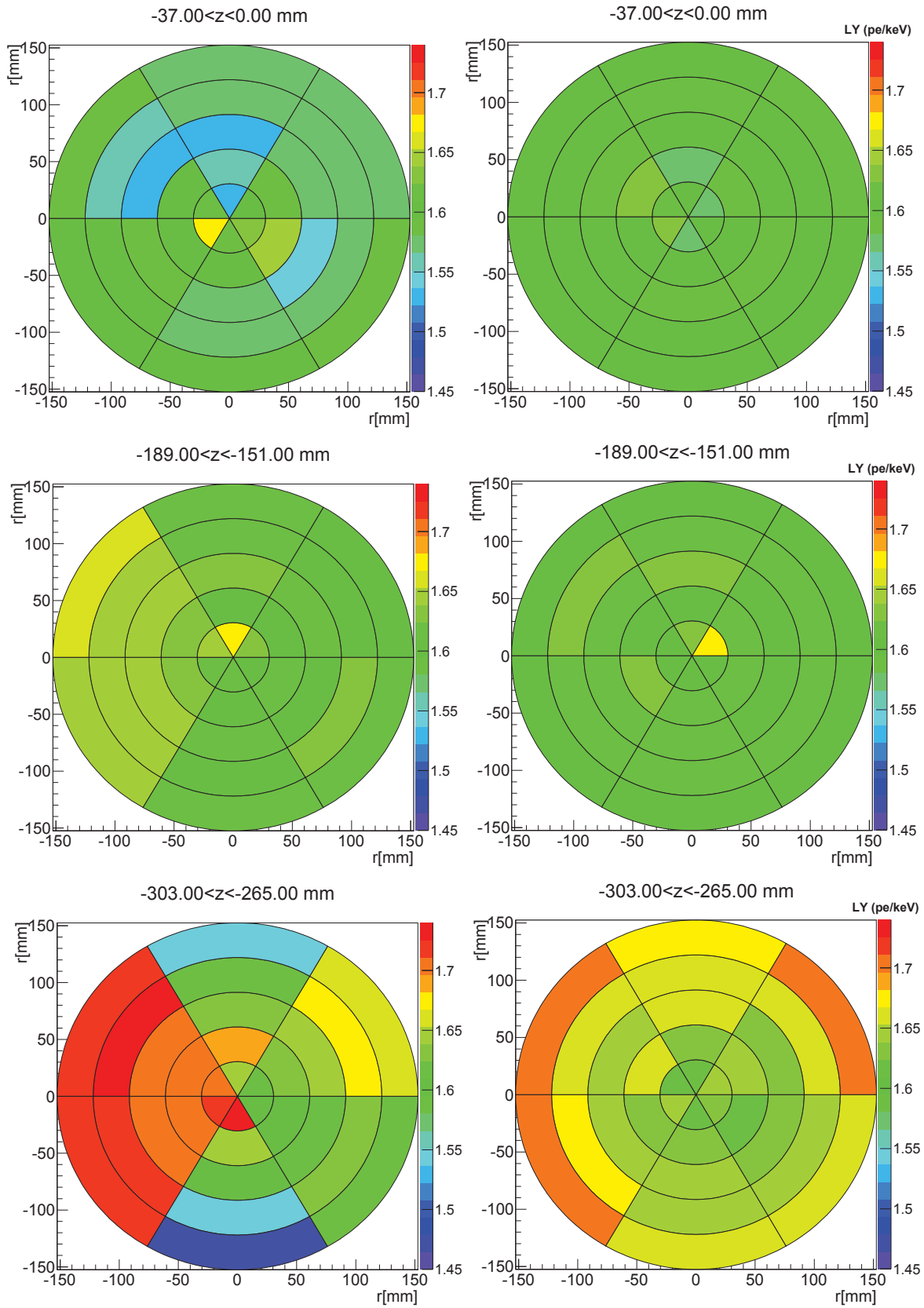


Figure 4.15: Corrected light yield maps from top ( $z=0$  mm) to bottom ( $z=-303$  mm) of the TPC. Left: 2D correction. Right: 3D correction

improvement a bit better, the angular dependence of the maps of figure 4.15 are shown on figure 4.16 for the bottom part of the detector.

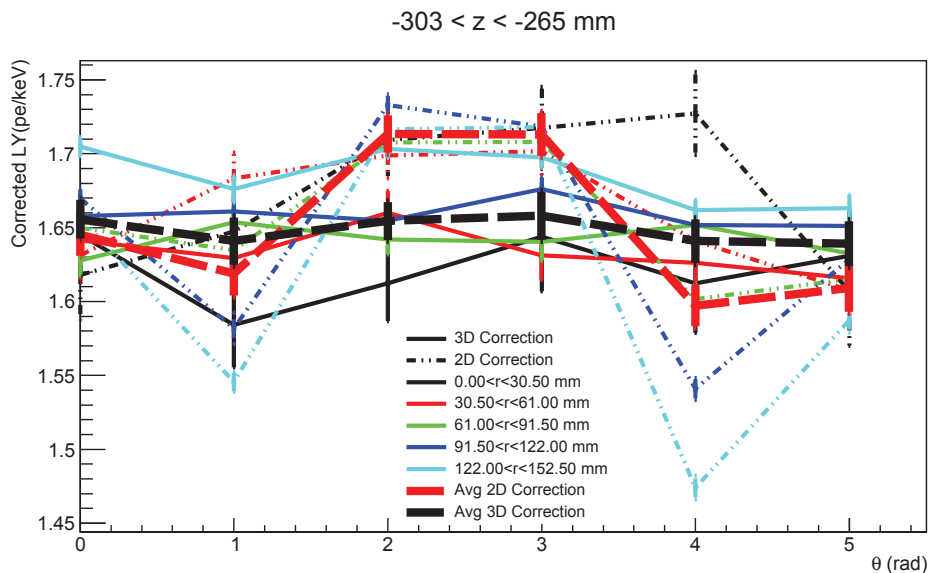


Figure 4.16: Corrected light yield as a function of  $\theta$  for the bottom of the TPC.

From figure 4.16, the new 3D correction gives maximum light yield fluctuations of the order of 1% while the 2D correction gave maximum light yield fluctuations of the order of 4%. The 3D correction thus gives a factor 4 improvement on the light yield uniformity of the detector. This is best seen by looking at the RMS of the light yield distribution for the non corrected data, the 3D and the 2D correction as shown on figure 4.17 for the overall TPC and for the bottom part. The RMS of the different distributions can thus be used as a quality factor for the correction, the smaller the RMS, the better the correction. While overall the 3D correction is not a significant improvement over the existing correction, on the bottom part of the TPC, the factor 4 improvement due to the 3D correction is very obvious.

Finally, the direct impact of the new 3D correction function is investigated on  $^{137}\text{Cs}$  spectra randomly selected amongst the many  $^{137}\text{Cs}$  datasets taken over the course of the run and not used to make the original 3D light yield maps. Once again, spectra for the overall TPC and for the bottom part are compared. Results are shown on figure 4.18.

Once again as already confirmed by the other figures, there is no difference at all in the full spectra. The energy resolution improvement is not visible on this scale. This is once again expected as the difference between the 2D and 3D corrections is mostly localized at the bottom of the detector and is only at the level of a few percents. And indeed, when looking at the bottom of the detector, there is a slight difference between 2D and 3D corrections. The sigma of the gaussian fit corresponding

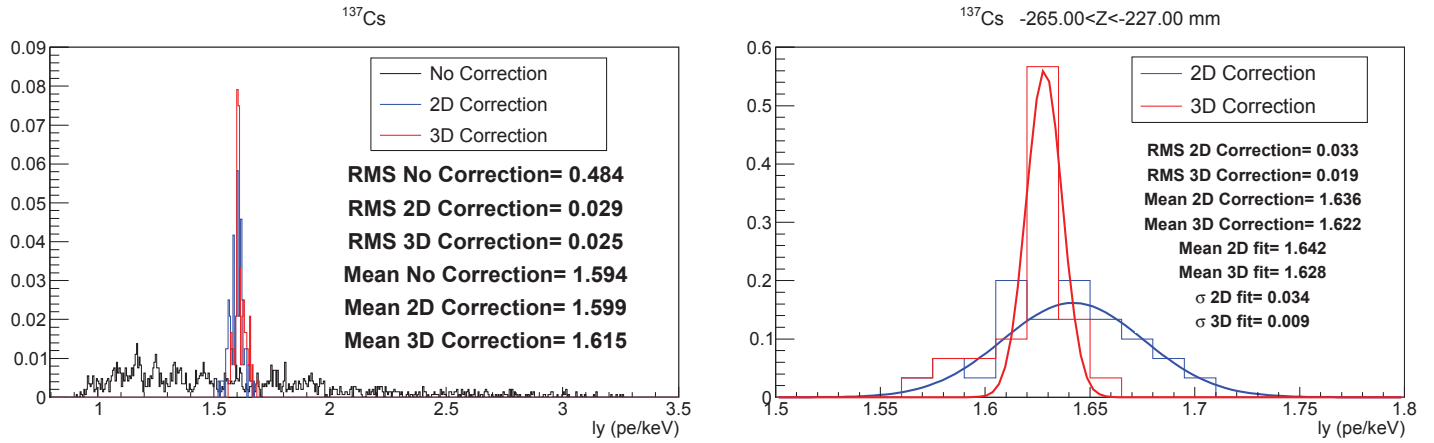


Figure 4.17: Quality factor of the light yield for no correction, the 2D correction function and the 3D correction function. Left: Overall TPC. Right: Bottom of the TPC.

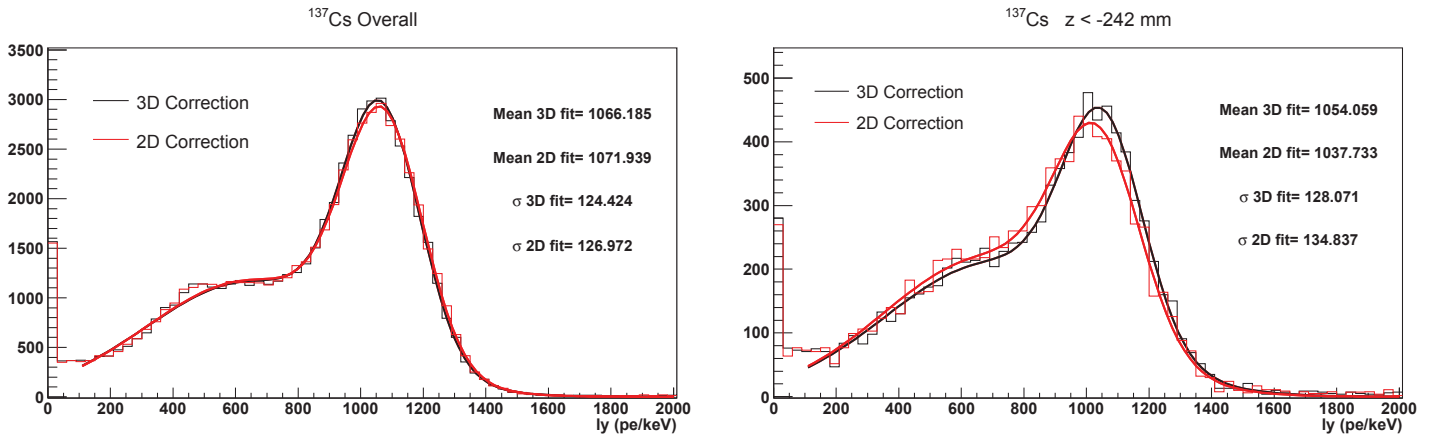


Figure 4.18: Effect of the correction function on the  $^{137}\text{Cs}$  spectra for random datasets, for the overall detector (left) and the bottom part of the TPC (right)

to the 662 keV peak is better for the 3D correction by 3%, thus confirming the statements made in previous sections. In addition, the 3D correction seems to have a slight impact on the spectrum at the bottom of the TPC and shifts the light yield higher by 1.8%.

## 4.8.2 40 keV Lines from AmBe Data

### Parameter Space and Line Selection

This whole process is repeated for the AmBe neutron calibration source. When a neutron hits a  $^{129}\text{Xe}$  atom depositing more than 40 keV of energy, the nucleus can be excited. When this  $^{129}\text{Xe}^*$  goes back to its ground state with a half life of 0.97 ns, it emits a 40 keV gamma which is then used for light yield calculations. This gamma emission is what is hereafter referred to as the 40 keV line from AmBe. Because the half life of the 40 keV state is very short relative to the digitization rate, the electron recoil from the 40 keV gamma cannot be resolved from the nuclear recoil of the inelastic

scatter. Additionally, the 40 keV line is not spatially uniform because it follows the same spatial distribution as the nuclear recoils, and is thus localized near the AmBe source position. This limits the statistics available for light yield uniformity measurements with this line.

The only difference is in the way data is chosen. Indeed, it is not sufficient anymore to take all data from the calibration but some cuts need to be applied to determine which of the AmBe data corresponds to such a line. Thus, a new parameter space has to be chosen, which is based on the 3D correction, where the 40 keV line will be clearly separable from other events. In this case the logarithm of the ratio of the total S2 signal on the bottom PMTs over the corrected total S1 signal is plotted as a function of the 3D corrected total S1 signal. Because this parameter space is used to distinguish electronic and nuclear recoils (see section 3.5.3), it gives a good way to separate the 40 keV recoils from the background of nuclear recoil events in the AmBe calibration. In this parameter space, the AmBe calibration gives very obvious regions depending on energy. Figure 4.19 shows the AmBe data in such a parameter space. A 2D gaussian fit is applied to the region of interest corresponding to the 40 keV line and the  $2\sigma$  contour is extracted from this fit. This is represented by the red ellipse on the plots, whose contour clearly maps well the region of interest.

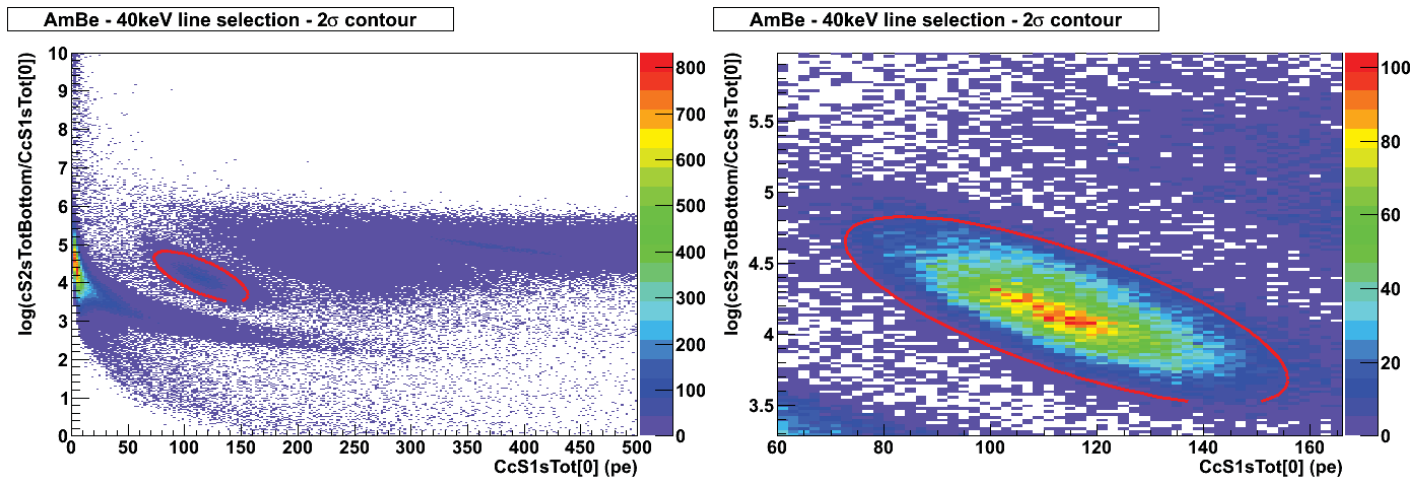


Figure 4.19: Spectra from AmBe. Left: the whole spectrum. Right: zoom on the region of interest corresponding to the 40 keV line

The bulk of the events follows very nicely a 2D gaussian fit. The non gaussian visible tail in the lower right of the zoomed figure 4.19-right, is due to events where more than 40 keV are deposited in the neutron scattering process thus adding a small nuclear recoil component seen simultaneously with the electronic recoil from the 40 keV gamma. This tail does not fall within the fit range contrarily to selection methods previously used by the collaboration, where the line selection cut just drew a rectangular box around the region of interest and did contain parts of this tail. Because of this more

precise definition of the parameter space which does not include any part of the tail, the light yield is expected to be a bit lower than what was found in the past, but with reduced systematic uncertainty.

Finally, as before, to calculate the light yield, the S1 distribution corresponding to the selected data is plotted and the peak fit as shown on figure 4.20.

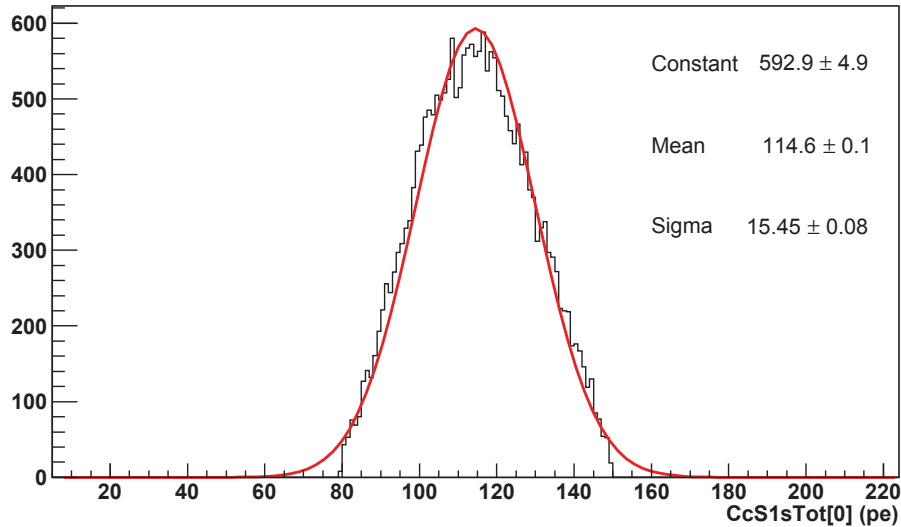


Figure 4.20: S1 distribution and fit for the 40 keV line from AmBe data

### Comparison between 2D and 3D Corrections

As for  $^{137}\text{Cs}$ , the detector is divided in 240 volumes. The corrected light yield maps using both 2D and 3D corrections are shown on figure 4.21 at the bottom and at the top of the detector.

Figure 4.22 shows the quality factor for both corrections at the top and bottom of the TPC. The 3D correction function performs once more much better than the 2D correction at the bottom of the detector, as can be seen by the narrower width of the light yield distribution. The performance at the top is similar between 2D and 3D correction, but for a slight lower shift in light yield for the 3D correction, thus showing the impact of removing the non-gaussian tail in the line selection.

#### 4.8.3 Xenon Activated Lines - 164 keV

##### Parameter Space and Line Selection

The same as for the 40 keV line, during a neutron calibration, the  $^{131}\text{Xe}$  isotope in the xenon gets excited into a metastable state  $^{131m}\text{Xe}$  which has a half-life of 11.9 days and an energy of 164 keV above the ground state. When this metastable state decays, it thus emits a 164 keV gamma.

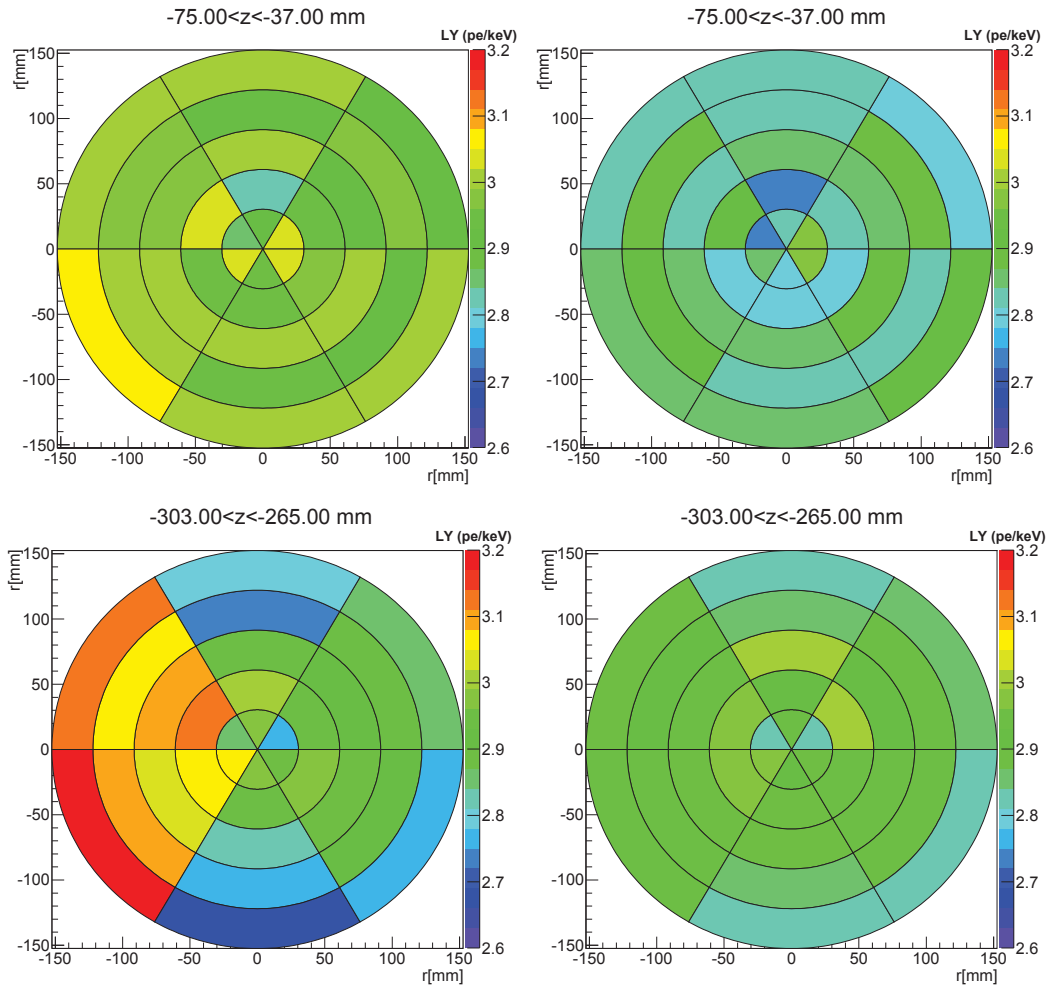


Figure 4.21: Corrected light yield maps using the 2D (left) and 3D (right) correction function for top and bottom of the detector for the 40 keV line from AmBe.

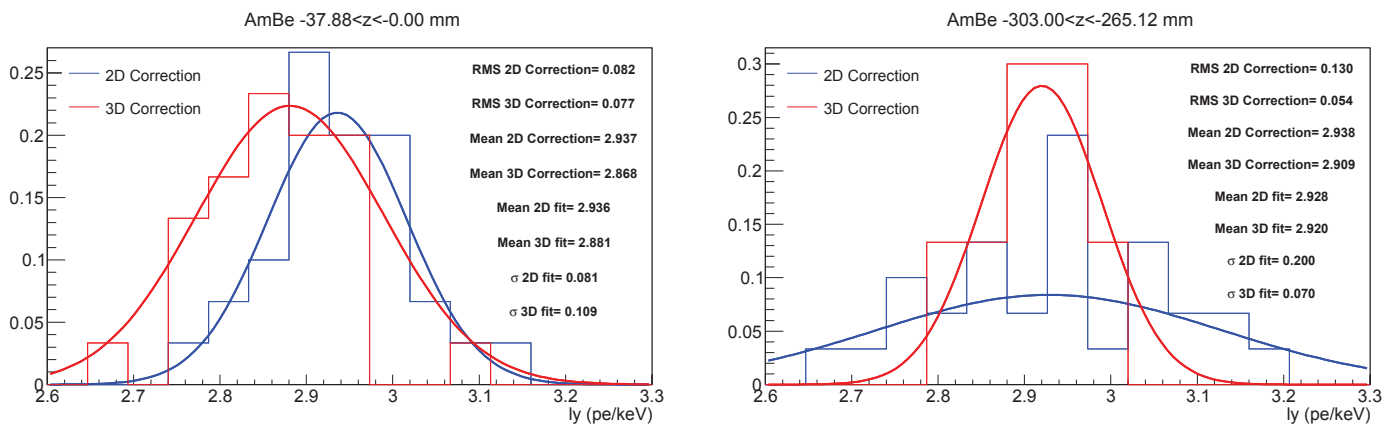


Figure 4.22: Quality factor for the 2D and 3D correction applied to the same AmBe data at the top of the detector (left) and the bottom of the detector (right)

Consequently, this 164 keV line requires a neutron calibration to exist and is available for data acquisition for only about two weeks after this neutron AmBe calibration.

As for the 40 keV line, this decay is not visible on a simple S1 spectra but yet another parameter

space has to be found to be able to make it out. This new parameter space consists of the ratio of the total S2 signal on the bottom PMTs (cS2sTotBottom) over the corrected total S1 signal (CcS1). Once again, note that to find the corrected S1 signal, the 3D correction is used.

The 164 keV line selection in this new parameter space is shown on figure 4.23. Again the 164 keV region is fitted with a 2D gaussian and the  $2\sigma$  contour of the fit is plotted as the red ellipse. These contours seem to match the data very well as can be clearly seen on the zoomed figure.

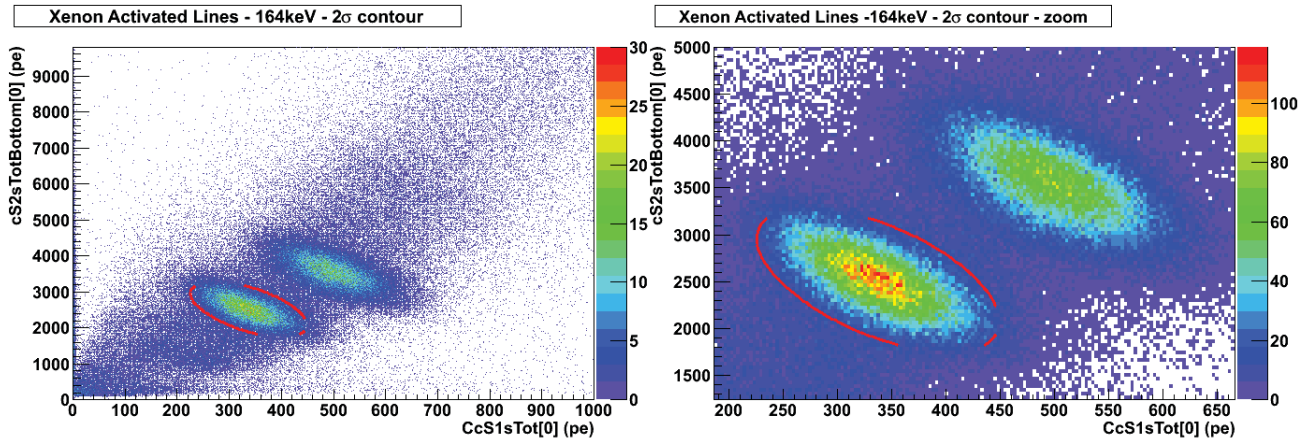


Figure 4.23: Parameter space and line selection for the 164 keV activated line from AmBe calibration

Note that on figure 4.23 there are two well defined distributions. The first one corresponds to the 164 keV activated xenon line as explained above. The second one however, corresponds to another xenon activated line with an energy of 236 keV from  $^{129m}\text{Xe}$ . This line was not used in the study as it is not a one step decay but rather a two steps decay (a 196 keV gamma followed by a 40 keV gamma) so it does not correspond to a one gamma emission but to two gammas emitted in delayed coincidence, thus making the light yield calculation more complicated due to the non-linearity of the light yield as a function of energy which is known to be different for two gammas than for a known single 236 keV gamma ( $ly_{236keV} \neq ly_{40keV} + ly_{196keV}$ ).

Once again, to calculate the light yield at 164 keV, the 3D corrected S1 distribution is plotted and the corresponding peak fit as shown on figure 4.24.

### Comparison between 2D and 3D Corrections

Once again, when comparing the corrected light yield maps for the 2D and 3D correction, the asymmetry is well visible when the light yield is 2D corrected but disappears when it's 3D corrected as shown on figure 4.25.

As before, the improvement is once more focused at the bottom of the TPC. Using once again

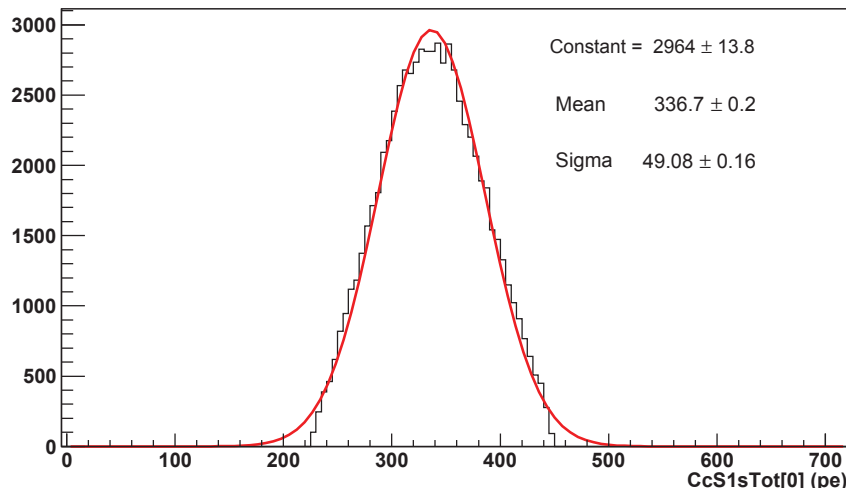


Figure 4.24: S1 distribution and fit for the 164 keV xenon activated line

the quality factor in figure 4.26, the improvement at the bottom of the TPC due to the use of the 3D correction is about 60%.

#### 4.8.4 Comparison of the Effect of the Correction Function on All Three Types of Data

As a final point, the impact of the correction function between the three types of datasets should be quickly investigated. This is done in two ways, first by looking at the residuals between the two corrected light yield, especially at the bottom of the TPC, and second by comparing the RMS of all data over the whole TPC.

Figure 4.27 shows the residuals of the corrected light yield, by subtracting the 2D ly maps from the 3D ly maps. This is shown only for the bottom 4 cm of the detector where the effect of the 3D correction is most prominent.

What figure 4.27 clearly shows is that, as intended, the 3D correction function has a clear impact on the left side of the detector where the asymmetry was first spotted in figure 4.2, while it has a very minimum impact on the rest of the detector where the previous 2D correction was already adequate.

Moreover, looking now at figure 4.28, in all cases, the 3D correction has a much smaller RMS especially at the bottom of the detector than the 2D correction, which confirms that the asymmetry has indeed been corrected. In numbers, at the bottom of the detector, the 3D correction leads a reduction in RMS of 66% for the 40 keV lines from AmBe, of 52% for  $^{137}\text{Cs}$  data and of 32% for the 164 keV line from AmBe.

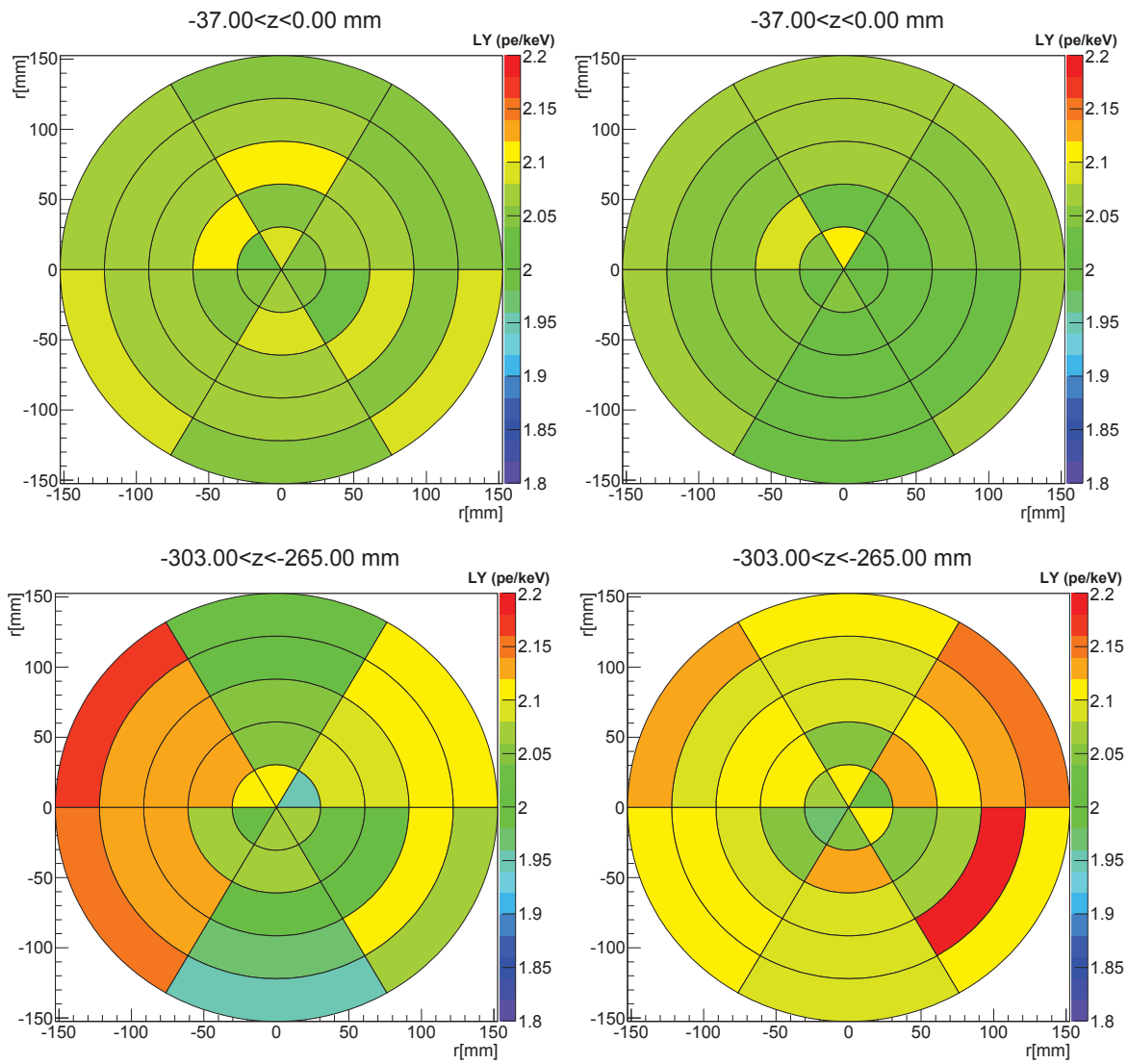


Figure 4.25: Corrected light yield maps using the 2D (left) and 3D (right) correction function for top and bottom of the detector for the 164 keV activated xenon data .

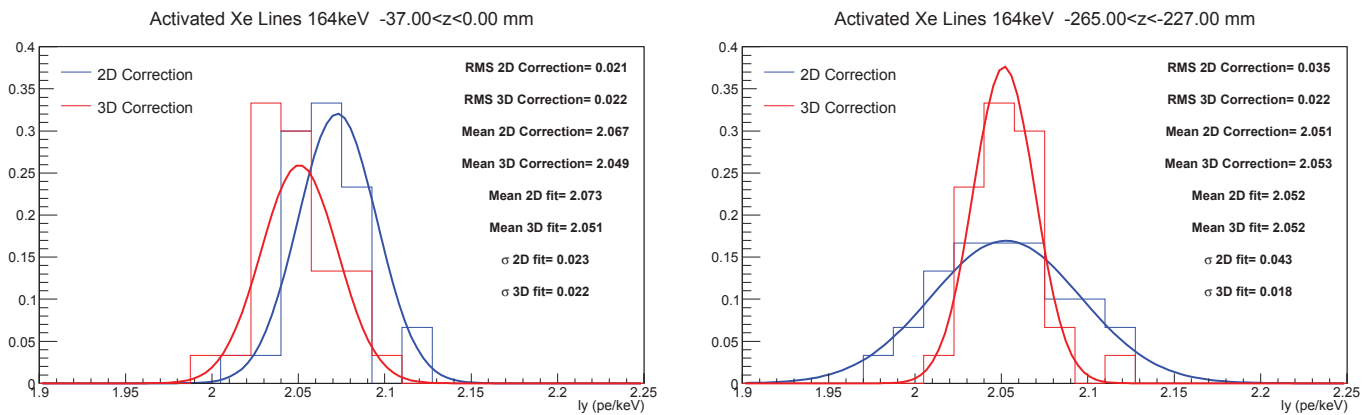


Figure 4.26: Quality factor for the 2D and 3D correction applied to the same 164 keV line from AmBe data at the top of the detector (left) and the bottom of the detector (right)

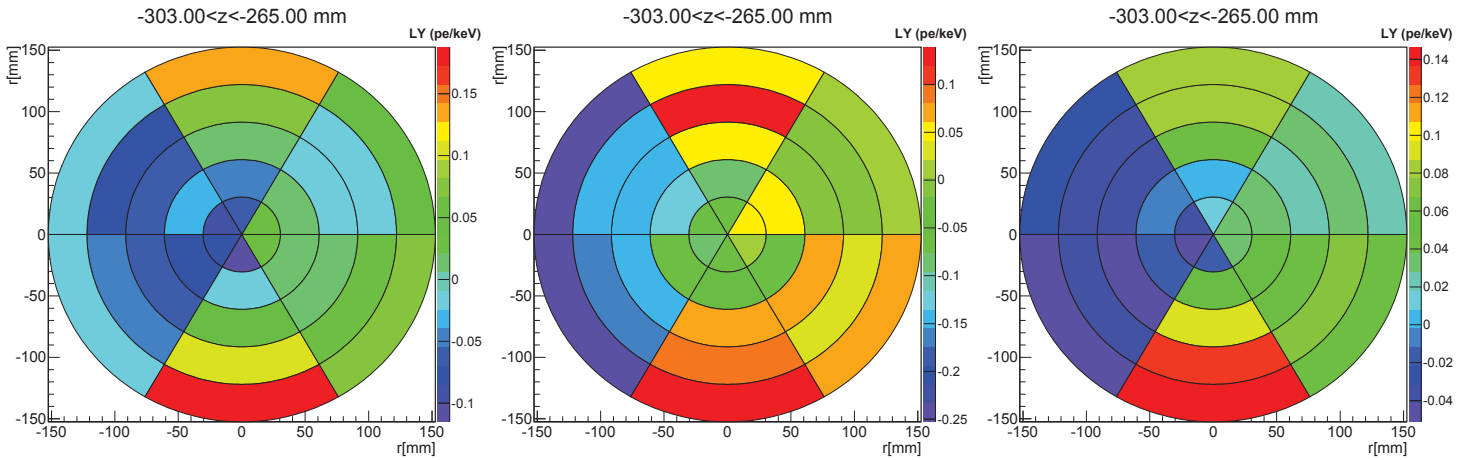


Figure 4.27: Light yield residuals between 3D and 2D correction for  $^{137}\text{Cs}$  data (left), 40 keV AmBe data (middle) and 164 keV AmBe Data (right)

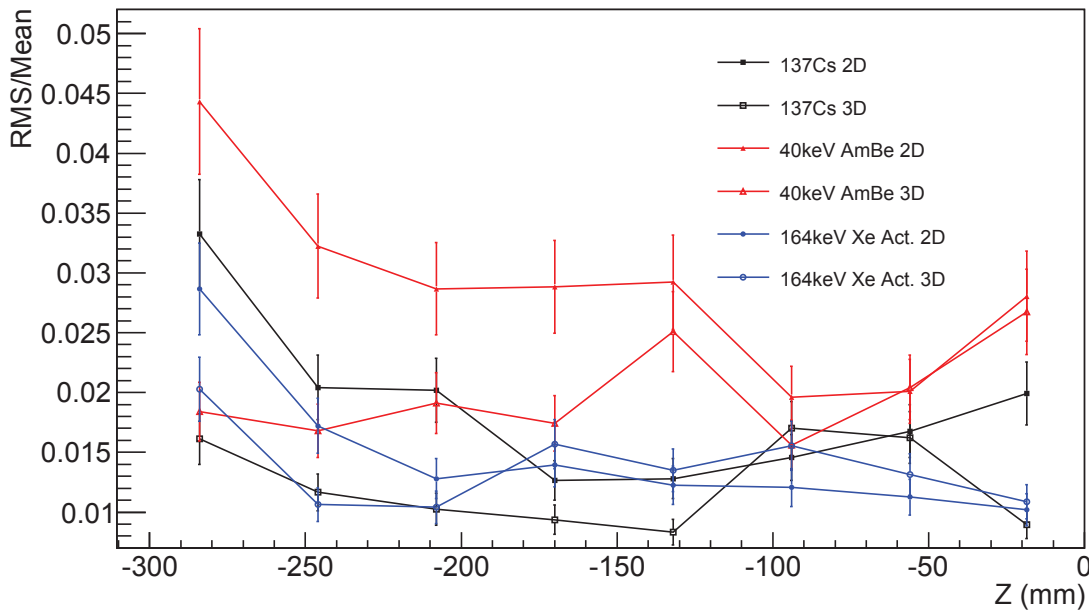


Figure 4.28: Comparison between the RMS of the 2D and 3D corrections applied to all data types.

In conclusion, the 3D light yield correction function fixes the axial asymmetry found at the bottom of the TPC. It allows for more precise light yield calculations everywhere in the detector and works for any type of data. Consequently, this correction function was implemented in the raw data processor and was used in the subsequent analysis which led to the published XENON100 run 10 results [23].

## 4.9 Light Yield at 122keV

Now that the new 3D light yield correction is in place, it must be used to recalculate the light yield at 122 keV.

As mentioned in chapter 3 section 3.4.3, the light yield at 122 keV is of utmost importance as normalization scale, as it is a necessary parameter to calculate the relative scintillation efficiency  $L_{eff}$  (equation 3.5) which in turn is crucial for the determination of the nuclear recoil energy scale.

This value of 122 keV was chosen years ago when the first need to calculate  $L_{eff}$  arose. At that time detectors were small and a very easily recognizable decay was the 122 keV photon from  $^{57}Co$ .

However, the choice of this value is becoming more and more problematic as detectors are becoming bigger and bigger and the 122 keV gammas cannot penetrate them anymore as their mean free path in liquid xenon is 1.6 mm (see figure 3.28), which is too short for meter scale detectors. Consequently, for XENON100 and the next generation of detectors, the light yield at 122 keV has to be found by other methods than using a  $^{57}Co$  calibration source.

As of today, the best way to do this, is to calculate the light yield at other energies and then fit the data points with an appropriate model which will then allow to extract the value of the light yield at 122 keV. The choice of the model is of course a source of disagreement in the field however the most recent one, called the NEST model [24] seems the most appropriate, for now.

Consequently, using the new 3D correction, the light yield is calculated at 662 keV from  $^{137}Cs$ , 164 keV from the xenon activated lines after the AmBe neutron calibration, and for 40 line from the AmBe calibration. Note that the AmBe calibration gives another line at 80 keV, which comes from the excitation of  $^{131}Xe$  and is also used in this study. However, for reasons explained before in section 4.8.3, the 236 keV xenon activated line is not used.

### 4.9.1 Light Yield at 662, 40 and 164 keV

Because this was already extensively explained in the previous sections, the process to calculate the light yield at 662, 40 and 164 keV will not be reexplained here. Only the final light yield values are summarized on table 4.1. Note that the error is the sum of the small statistical error coming from the  $\chi^2$  minimization of the fit function and the dominant systematic errors coming from the choice of the fit range, the parameter space selection and the contour selection.

Source	Energy Line (keV)	Average Light Yield (pe/keV)
$^{137}\text{Cs}$	662	$1.597 \pm 0.0112$
AmBe	164	$2.057 \pm 0.0022$
AmBe	40	$2.932 \pm 0.176$

Table 4.1: Light yield values for the different energy lines

### 4.9.2 Light Yield at 80 keV

As explained in a previous section, when a neutron hits a  $^{131}\text{Xe}$  atom, the atom is excited. While the second excited state is a metastable state with a half life of 11.84 days and gives the so called 164 keV xenon activated line, the first excited state will immediately decay in 0.5 ns by emitting a 80 keV gamma.

As done previously, the parameter space used to select the proper events is the S2 total signal on the bottom PMTs as a function of the 3D corrected S1. This line selection is shown on figure 4.29.

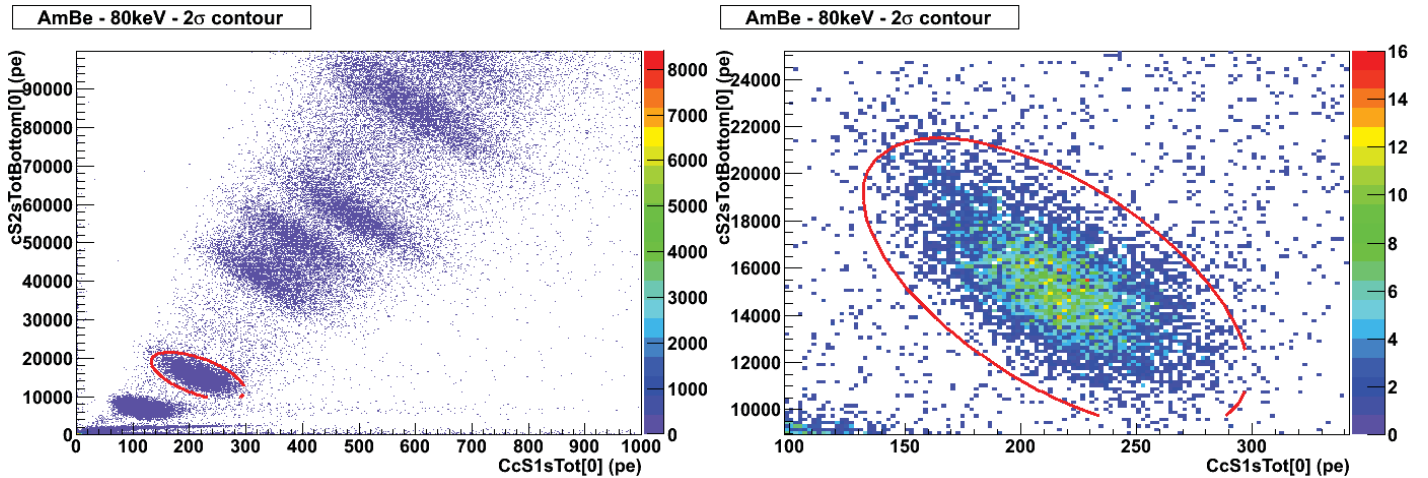


Figure 4.29: Parameter space and line selection for the 80 keV gamma emission from AmBe

The corresponding spectrum to this selection is shown on figure 4.30 which leads to a light yield of  $2.781 \pm 0.115\text{pe/keV}$ .

### 4.9.3 Extracting the Light Yield at 122 keV

Now that the light yields have been calculated at four different energies, the NEST model [24] must be fitted to this data points. However this is a generic model and thus cannot be taken as is but must be adjusted to match XENON100 to account for differences in light collection, electric field or any other parameter which varies from detector to detector.

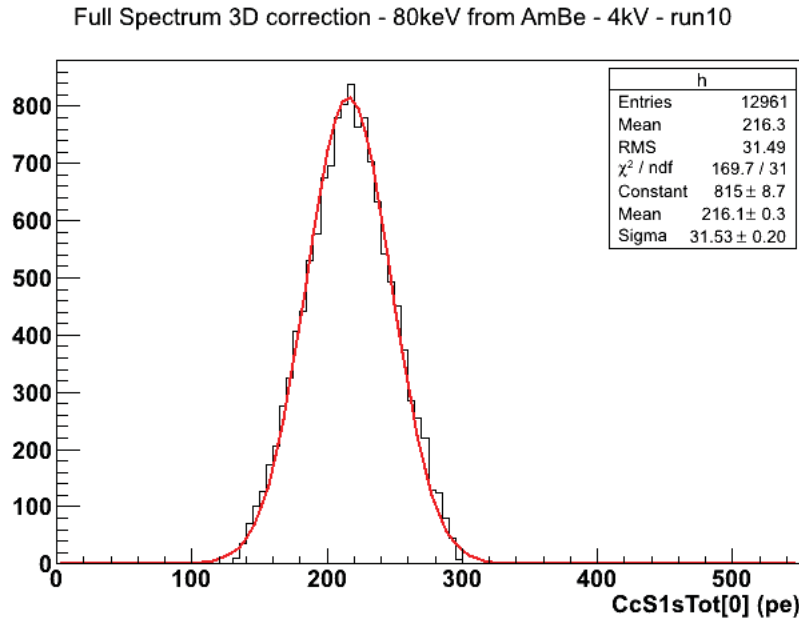


Figure 4.30: Spectrum corresponding to the 80 keV line from AmBe

### *Adjusting the NEST Model*

The NEST model [24], which is a combination of the Doke/Birk model and of the Thomas Imel box model and which accounts for fluctuations in recombination, is the most recent and realistic model of scintillation yield in liquid xenon. Consequently, it is used for this analysis.

This model is presented in figure 4.31 and shows the expected behavior of the absolute yield of scintillation light in liquid xenon at zero field. The absolute yield is the inverse of  $W_{\text{photon}}$ , which is the average energy required to create one scintillation photon, in this case, in liquid xenon. The absolute yield is distinct from the light yield in that it is the number of scintillation photons created and not the number of photoelectrons detected. The two are related by the geometric light collection efficiency and the photon detection efficiency which includes the quantum efficiency of the PMTs.

However, as mentioned before, this does not match the conditions of XENON100 which has a different light collection efficiency and where an electric field of 530V/cm is applied. Consequently, the model of figure 4.31 must be adjusted to match such a field. To do this, the dependence on energy of the field quenching at 530V/cm must be found. Figure 4.32 (left) [25] represents the field quenching at 662 keV, while figure 4.32 (right) [26] shows the same quenching at 9.4, 32 and 122 keV.

Combining the results from figures 4.32 (left and right) and assuming a linear trend of the quenching versus  $\text{Log}_{10}$  of energy over the range of energies where measurements exist, the field quenching at 530V/cm depending on the energy is shown on figure 4.33.

Using the fit from figure 4.33, the NEST model of figure 4.31 can be corrected for the electric

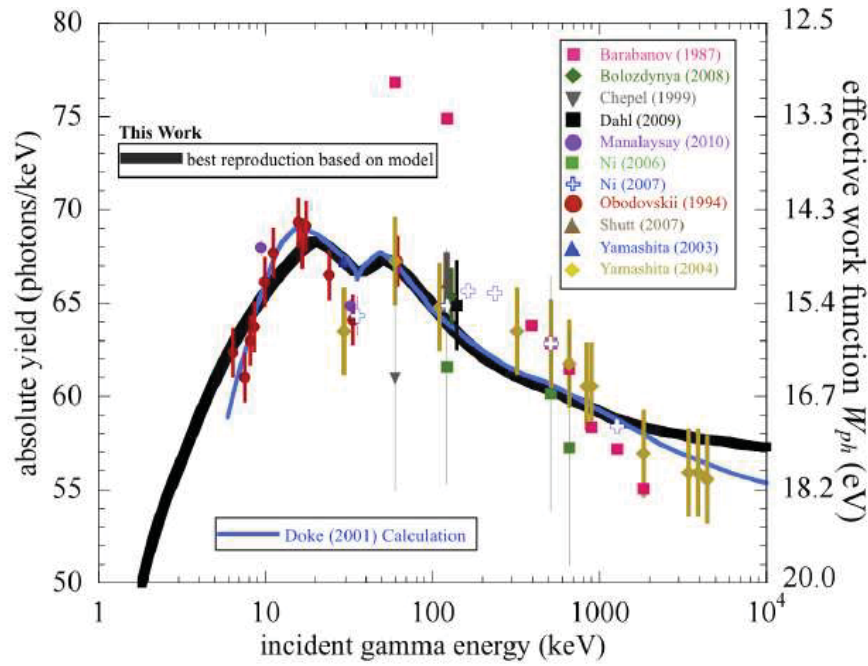


Figure 4.31: NEST model for the scintillation yield in liquid xenon [24]

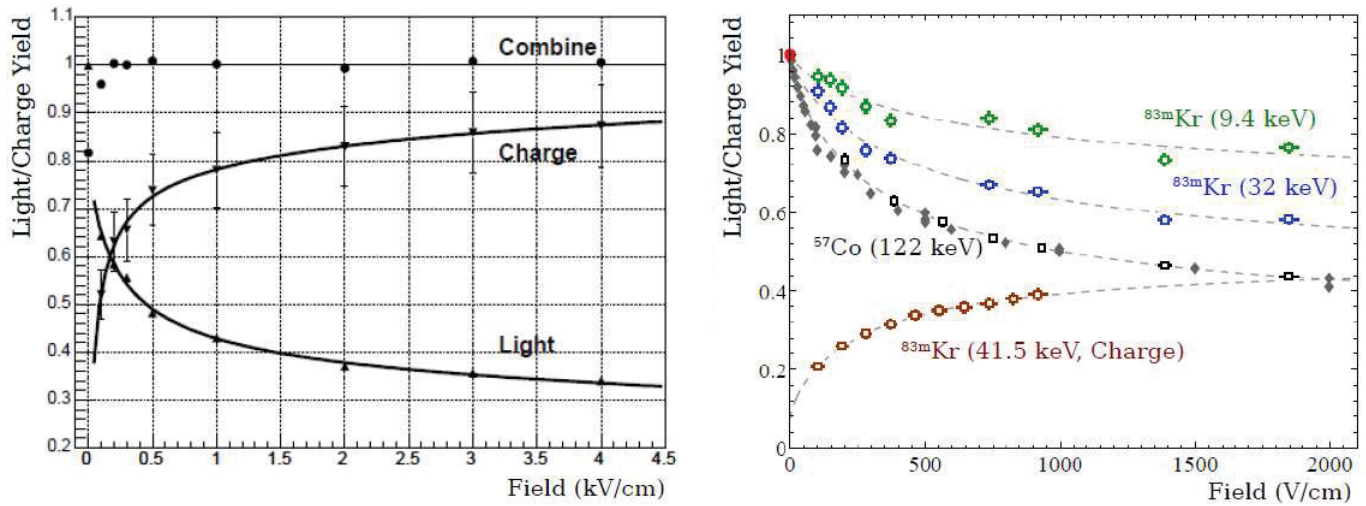


Figure 4.32: Field quenching at 662 keV [25] (left), and at 9.4, 32 and 122 keV [26] (right)

field. The resulting model is shown on figure 4.34.

### Fitting the Data

Finally, to obtain the light yield at 122 keV, the NEST model must be fitted to the light yields found previously. To try and get more agreement, an extra light yield point, calculated using a different method not explained here, from fluorine at 197 keV is added [96]. This particular light yield measurement was taken from an independent study within the XENON100 collaboration and is based on 197 keV gammas coming from neutron activation of fluorine in the PTFE during an AmBe

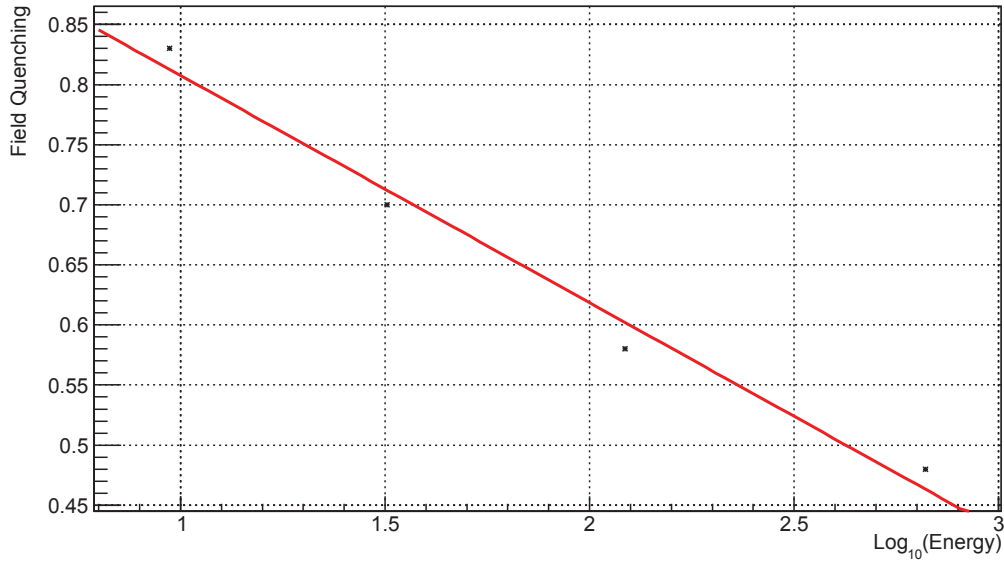


Figure 4.33: Field quenching for a 530V/cm electric field

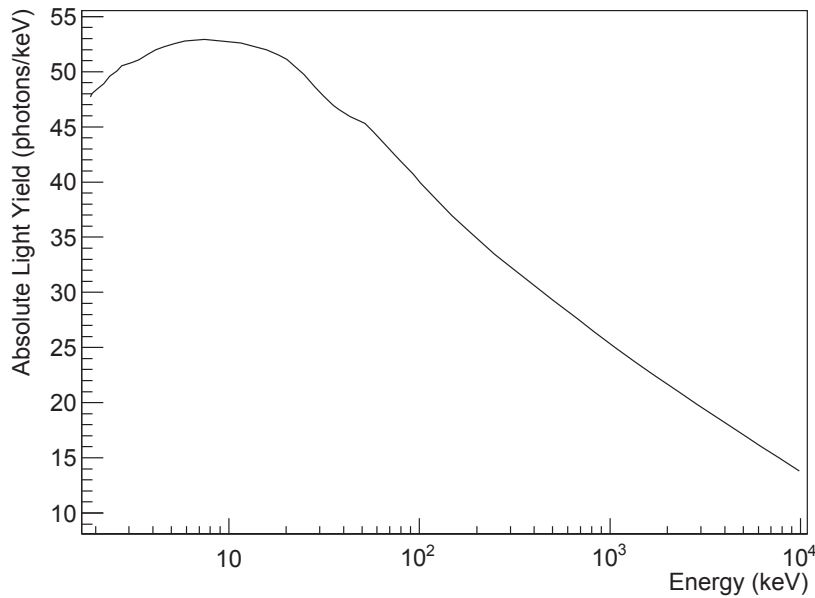


Figure 4.34: The NEST model at 530V/cm in liquid xenon found by applying the correction of figure 4.33 to the NEST model of figure 4.31

neutron calibration. Since it is localized at the edge of the TPC, the analysis is very different from that for the lines presented in this work, and is therefore not presented here. Instead, the light yield from this measurement is used as an additional constraint while extracting the light yield at 122 keV.

To convert figure 4.34 from photons/keV to photoelectrons/keV, the measured data is fitted with the NEST model times a constant which is then the only free parameter of the fit, which represents the average light collection efficiency of the TPC. This constant allows thus to shift and match the

NEST model accordingly with the measured data. The error analysis however is a bit tricky. On one hand, the calculated errors of table 4.1 can be used. When using these errors, the reduced  $\chi^2$  of the fit is about 4, which is too high, while the light yield value obtained at 122 keV is  $2.24 \pm 0.009$  pe/keV, and so has a very small error. However, even at that, this error analysis should not be completely discarded as the error analysis for these light yield measurements is well understood. The problem really comes from the treatment of the systematic errors for the 40 keV and 80 keV AmBe lines which are likely underestimated in the error analysis. The NEST model fit to the data with this error analysis is shown on figure 4.35. From this figure, it is indeed evident that the two AmBe measurements are entirely responsible for the high  $\chi^2$  value of the fit.

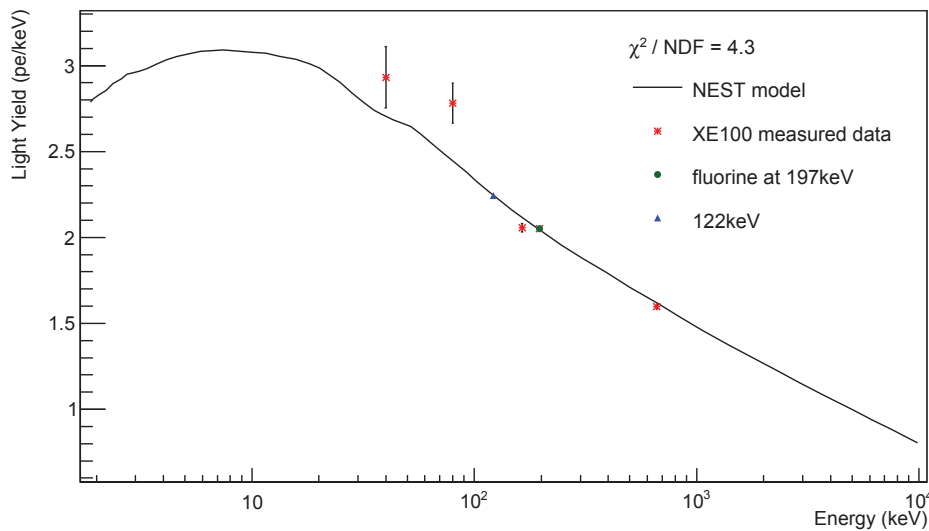


Figure 4.35: Fit of the XENON100 data using the NEST model with an error analysis based on the actual calculated errors

Nonetheless, to try and reduce the  $\chi^2$ , a second error analysis is performed. This time the same relative error is given to all data points and is varied until a reduced  $\chi^2$  of 1 is obtained. This happens with a relative error of 6%. The light yield calculation at 122 keV from this analysis leads to a value of  $2.31 \pm 0.062$  pe/keV. This agrees within errors with the result from the first analysis, but also has a much larger error due to the fact that all data points have a large error for this analysis.

In addition, other different analyses based on MC simulations, also using the NEST model, were performed in parallel to this one by the collaboration and led to a light yield value at 122 keV of  $2.26 \pm 0.04$  [97]. A combination of all of these results was used to obtain the published value [23] for the light yield at 122 keV of  $2.28 \pm 0.04$  pe/keV.

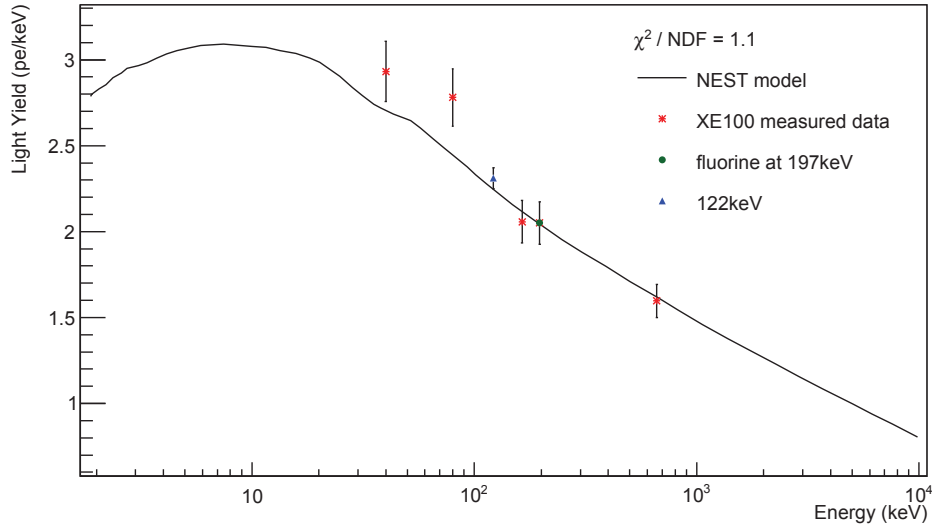


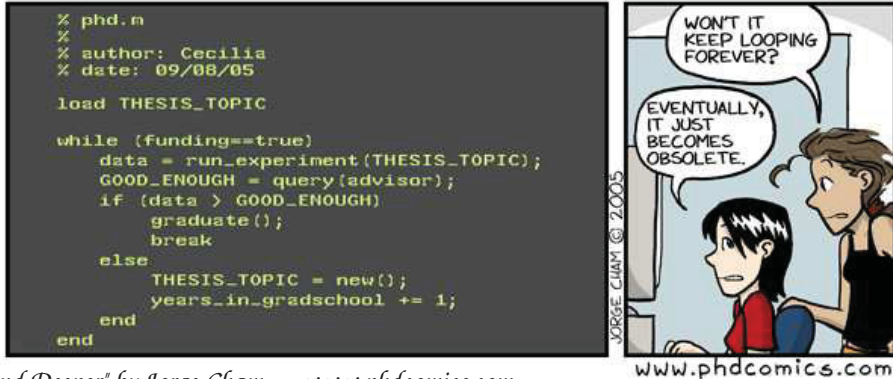
Figure 4.36: Fit of the XENON100 data using the NEST model with an error analysis based on the reduced  $\chi^2$

## 4.10 Conclusion

Studies of the light yield are extremely important and necessary for the proper analysis of the XENON100 data. Improvements were made on the correction function which allows to calculate a uniform light yield throughout the detector. Such a function used to be only in 2D, with only a radial and a vertical component. It was improved to also have an azimuthal component, which lead to significant improvement. Using this new correction, a new value of  $2.28 \pm 0.04$  pe/keV for the light yield at 122 keV was calculated. The light yield studies presented in this chapter had a direct impact on the energy resolution and the determination of the nuclear recoil energy scale necessary to perform a successful dark matter experiment.



# Chapter 5. MONTE-CARLO SIMULATIONS OF THE MUEENSTER TPC



*Piled Higher and Deeper* by Jorge Cham [www.phdcomics.com](http://www.phdcomics.com)

In order to test different systems to be implemented on the XENON1T experiment, the Muenster XENON group has set up a small 3 kg two phase xenon TPC. To understand and characterize this TPC and its properties, Monte-Carlo (MC) simulations are necessary. By comparing these simulations to real data taken with the TPC, the physics behind the detector can be understood.

This chapter presents a MC package that models the geometry of the Muenster TPC and the physical interactions in the xenon target and detector materials.

## 5.1 The Muenster TPC

The TPC was developed and designed at the University of Muenster in 2011 [27]. It is a much smaller detector than XENON100 but with an equivalent operation principle. The TPC itself has a 17 cm drift length, with a 4 cm radius and contains 2.56 kg of xenon in the active volume. It uses 14 1" square PMTs (7 at the bottom in the liquid xenon and 7 at the top in the gas xenon) that monitor the active volume. The TPC is made of a cathode at the bottom, a gate mesh 17 cm above this cathode and an anode another 5 mm above the gate mesh, all of which are constructed of transparent stainless steel meshes. The sides of the TPC consist of copper field shaping electrodes housed in a teflon support structure. A technical drawing of the TPC can be seen in figure 5.1.

Two vessels are used to contain the TPC, an outer one with 133 mm radius and 1.5 m tall for insulation purposes and an inner one with 74 mm radius and 334 mm tall, which will contain

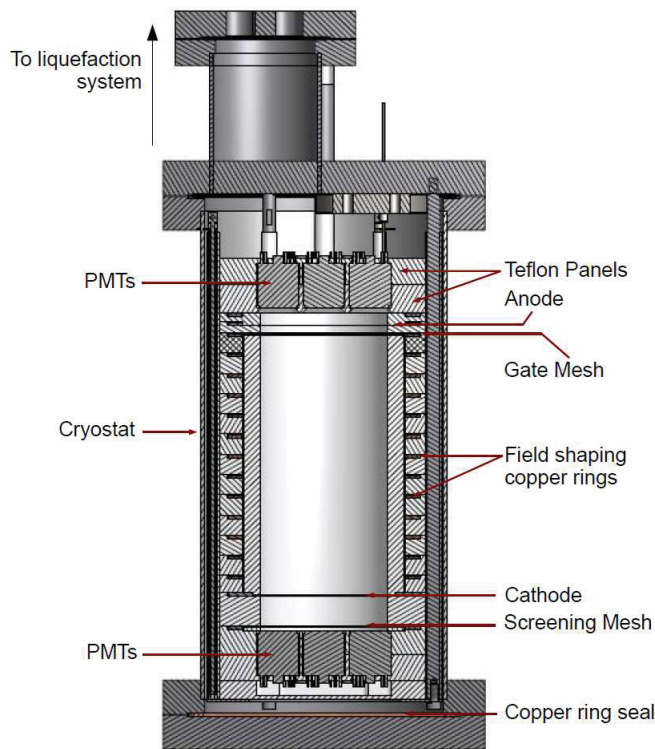


Figure 5.1: Sectional view of the technical drawing of the TPC encased in the inner cryostat.[27]

the xenon and serves as a cryostat. The outer vacuum vessel was designed much taller than the TPC to allow for a future longer TPC, however this does not enter in the scope of this work. As in XENON100, all materials were selected to have a very low radioactivity and all the cooling equipment is located outside, at the top of the outer cryostat so as to avoid contamination from any non-necessary material. A global view of the insulating vacuum chamber, cooling tower and TPC inside the structure is shown on figure 5.2.

## 5.2 A *GEANT4* Simulation of the Muenster TPC

Once the detector is physically built, it is important to be able to characterize it. While this can in principle be exclusively done by taking appropriate data, the time and means to do this are not always available and it is thus often necessary to resort to a MC simulation. A simulation is a more or less precise reproduction on a computer of what has been built in reality, in this particular case a xenon detector. The simulation is not only a virtual copy image of the detector geometry but it also includes all the physical processes that may happen in reality in the detector. This has the obvious advantage to allow any possible change made in the system to be studied and analyzed in a timely manner.

In this case, the simulation is mainly used to study the S1 and S2 response of the detector as well

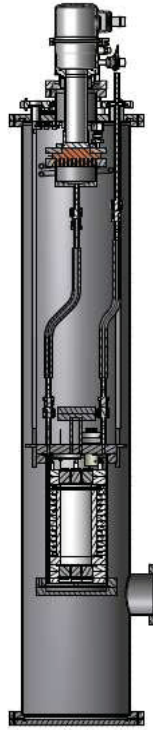


Figure 5.2: Mechanical drawing of the outer vacuum vessel with the TPC encased inside and the cooling tower located outside.[27]

as the detector's response to changes in various parameters such as absorption length of scintillation light in liquid xenon or teflon reflectivity. It is also used to compute virtual gamma and neutron calibrations with different radioactive sources.

The software used to perform these simulation is the CERN-developed GEANT4 (GEometry AND Tracking) software, version 4.9.1, which is broadly used in today's nuclear and particle physics world. The power of GEANT4 is its ability to handle detector geometry as well as particle generation, interactions and tracking using visualization tools and user interface.

Because of the similarities between the Muenster TPC and XENON100, the XENON100 simulation package [18] was used as a starting point and has been adapted to fit the needs of the Muenster TPC.

### 5.2.1 The Detector Geometry

The first step in building a successful simulation is to reproduce the physical layout of the experiment, or detector geometry. This can be done at a more or less detailed level, depending on the need of the user. Because the simulation package will be mostly used for light yield and calibration studies, a high level of details is not immediately necessary. The simulation package thus includes the inner and outer cryostat, the main flanges, the teflon panels, electrodes, field shaping rings and PMTs

in the TPC, as well as the liquid and gaseous xenon. The insulating vacuum chamber and main flanges were necessary elements as calibration sources will be placed outside in the lab and so they constitute the first possible interaction material. The TPC and its housing cryostat is obviously the most important part of the simulation as it is where the interactions of interest happen and where all the studies have to be made. Consequently it was simulated using a high level of detail and is pictured in figure 5.3.

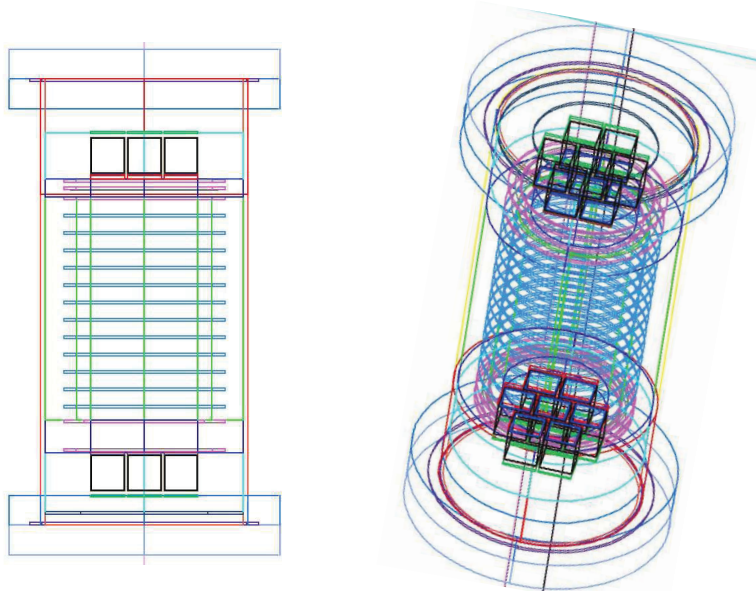


Figure 5.3: The simulated TPC and its cryostat with the major components visible, the pmts, copper rings, meshes and teflon holders.(left) Side view. (right) Perspective view.

It is to be noted that the entire cooling apparatus being located outside and far away from the TPC, has been neglected. Because of their small size or location, the feedthroughs and the inside cabling have also been neglected. The final simulated geometry can be seen in figure 5.4.

### 5.2.2 Particle Tracking and Basic Detector Response

Once the geometry is done, it is necessary to test that every component is placed properly by sending non-interacting particles through the whole system. This is done to check that boundaries between all detector components are properly located and was tested in many positions and directions to ensure that the detector geometry was correctly simulated. An example of this is shown on figure 5.5 where a non-interacting particle is sent upwards from the outside laboratory. The particle crosses all the different layers whose output can be seen in figure 5.5.

Particle interactions in GEANT4 can be divided into two categories. The first is the interaction of radiation in the detector materials and target, and the second is the propagation of the xenon

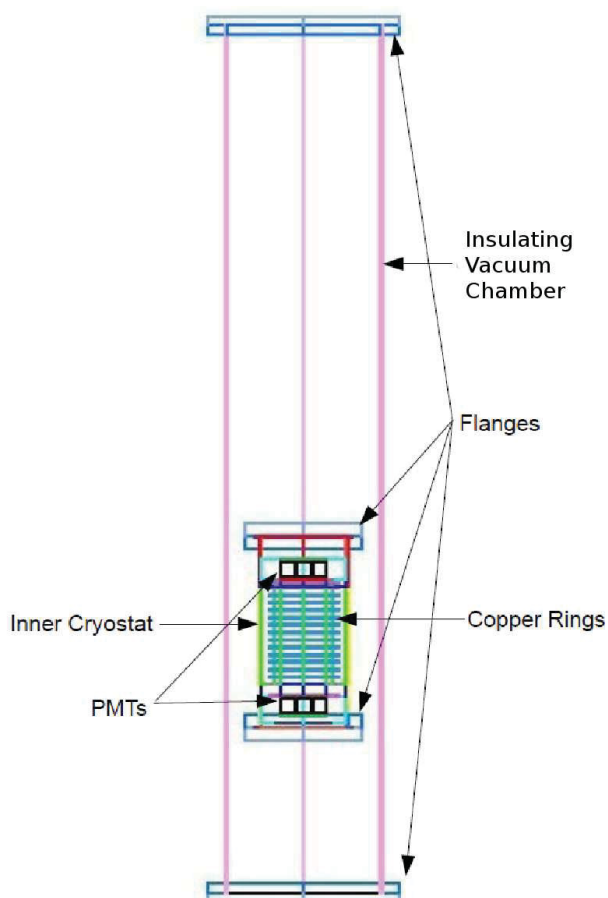


Figure 5.4: Visualization of the final simulated detector geometry

scintillation light.

In the first case, the two types of incident radiation relevant for this work are neutrons and gammas from radioactive sources. For neutrons, elastic and inelastic cross sections are used to describe the interactions of the incident particle. For gammas, different interactions are possible, but for the energy range of interest, the interactions modeled are the photo-electric effect, Compton scattering, and for gamma energies above 1.22 MeV, pair production. Again, GEANT4 uses tabulated cross sections for each of these processes to model interactions.

For the scintillation light, GEANT4 uses particles that follow geometric optics, including reflection and refraction. Additionally, these particles can scatter via Rayleigh scattering, or be absorbed in the liquid xenon. The scattering and absorption are governed by scattering length and absorption length which are user-defined parameters. For liquid xenon, the Rayleigh scattering length is measured to be 30 to 50 cm, and the absorption length is typically varied to account for different electronegative impurity levels in the xenon.

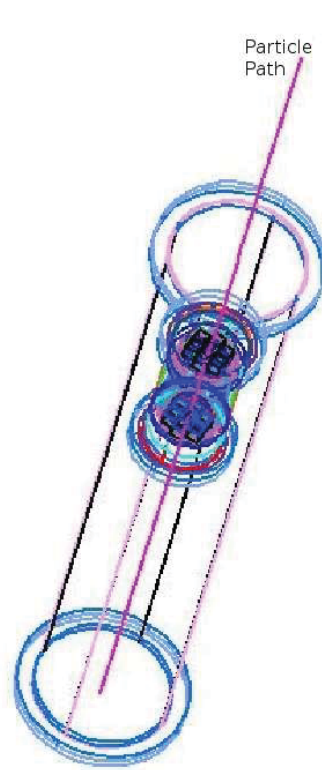


Figure 5.5: Example of the propagation of a non-interacting particle through the whole detector.

### 5.3 Scintillation Light Propagation

Just like for the XENON100 detector, the Muenster TPC's light response must be understood. The scintillation light propagation is simulated by producing isotropic light at 178 nm uniformly throughout the detector, by generating 7 eV photons. The geometric light collection efficiency (LCE) can then be obtained by looking at the fraction of light that hits a PMT.

The first parameter to look at is thus the light yield overall and over different regions of the detector, to ensure that it is behaving in an expected manner. This will also be used as another cross check that the simulation package is working properly. In addition, by varying parameters such as the absorption length in the xenon and the teflon reflectivity, their impact on the light yield can be studied.

#### 5.3.1 2D Light Yield Map

As already explained in section 4.1, the light yield is a measure of how much scintillation light (S1 signal) is seen by the PMTs per keV recoil energy. Closely related to this, is the light collection efficiency (LCE), which is the fraction of light collected by the PMTs. Because the Muenster TPC operates on the same principle as the XENON100 TPC and is also axially symmetric, it is expected

to observe a similar behavior in the light yield. However, the Muenster TPC being an elongated cylinder rather than a circular one, the light yield at the bottom of the TPC is expected to be much higher than at the top while the light yield difference between low and high radii should not be as pronounced as in XENON100. Figure 5.6 shows the LCE of the detector in arbitrary units as a function of the vertical position  $z$  and the radius squared. As expected, the LCE is much higher at the bottom of the TPC while it decreases as  $r$  increases. It is also again higher at the top of the TPC due to the proximity of the PMTs. This expected behavior is yet another cross check that the simulation package is working properly.

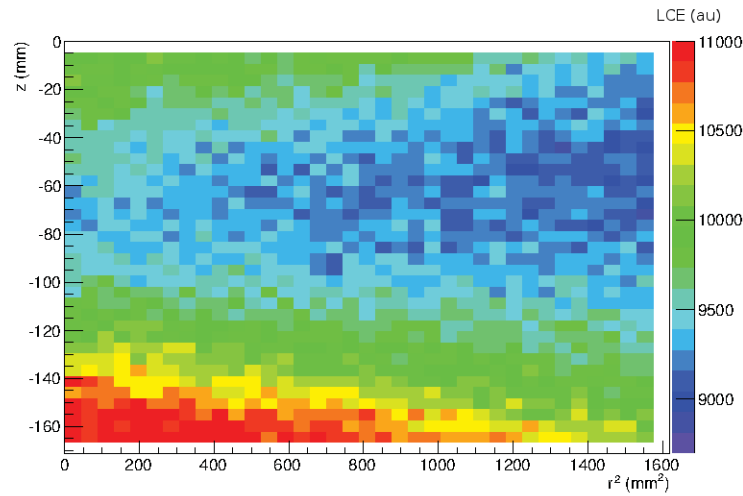


Figure 5.6: Light collection efficiency in the Muenster TPC.

### 5.3.2 3D Maps of the Light Yield

Again, as presented in chapter 4, a 2D LCE map might not be sufficient to precisely describe the TPC. A 3D light yield map of the detector is a more accurate way which could allow to identify smaller scale variations. Because of the very symmetric design of the TPC and considering that the TPC was not modeled in every detail, such variations should not be visible. However, some variation might be visible in theta due to the fact that the PMTs are not assembled in a circular but in a rectangular pattern.

To check this, the detector is divided into 1000 total volumes, 10 in vertical  $z$ , 10 in radial  $r$  and 10 in azimuthal theta. The light yield in each of these volumes, taking into account the detector geometry, scintillation yield and PMT quantum efficiency, is calculated according to equation 5.1 where  $ly_i$  is the light yield in volume  $i$ ,  $N_i$  is the number of PMT hits in each volume  $i$ ,  $NSimu_i$  is the simulated number of photons in each volume  $i$ ,  $NSimu_{tot}$  is the total number of simulated

photons,  $V_i$  is the volume of each individual volume,  $V_{tot}$  the total volume of the detector,  $QE$  is the average quantum efficiency of the PMTs, and  $W$  is the average energy required to produce one scintillation photon in LXe.

$$ly_i = \frac{1}{W} \frac{QE \times N_i}{NSimu_i} \quad (5.1)$$

with  $QE = 0.30$ ,  $W = 20eV$  and  $NSimu_i = NSimu_{tot} V_i / V_{tot}$

The resulting maps are shown on figure 5.7. Again, the light yield is much lower at the top than at the bottom of the TPC as expected with values of  $1.85 \pm 0.1$  pe/keV in the 16 top mm of the TPC and of  $2.16 \pm 0.1$  pe/keV in the 16 bottom mm, thus accounting for an 8 % difference. Moreover and also according to expectations, the light yield is also lower on the edges of each z slab. As can be seen, there is no obvious asymmetry or variation in the detector's behavior which thus implies that the simulation is working properly.

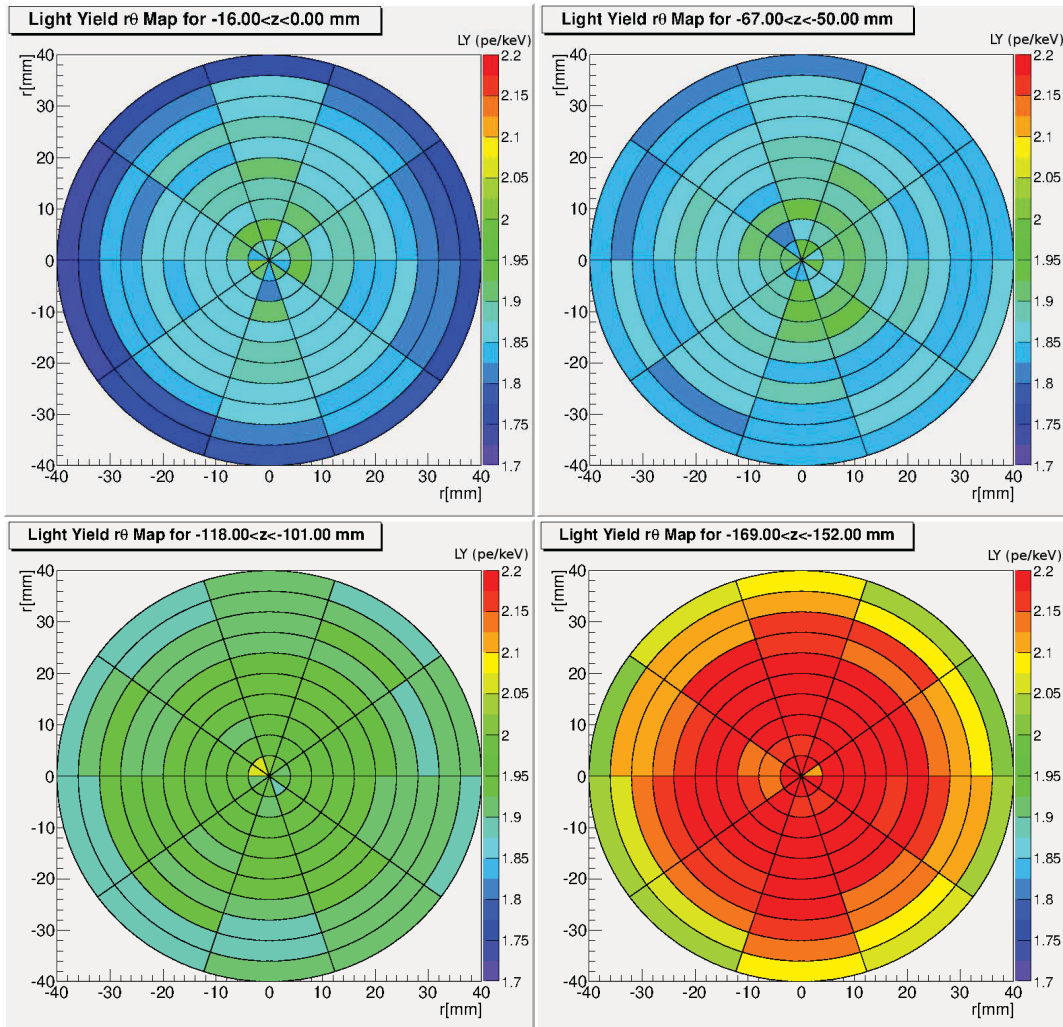


Figure 5.7: Light yield maps in the muenster TPC from top ( $z=0$  mm) to bottom ( $z=-169$  mm) of the TPC

### 5.3.3 Influence of the Absorption Length in Xenon on the Light Yield

Next, the impact of xenon purity on the light yield can be investigated. The absorption length in xenon is particularly interesting to look at, as it varies as a function of xenon purity, the purer the detector the longer the photons can propagate without interaction and so the higher the absorption length. Consequently the absorption length can give important information about how pure the detector is and how pure it should be to reach a maximum light yield.

To test this, different simulations are run with different absorption lengths. The result is plotted and fitted on figure 5.8.

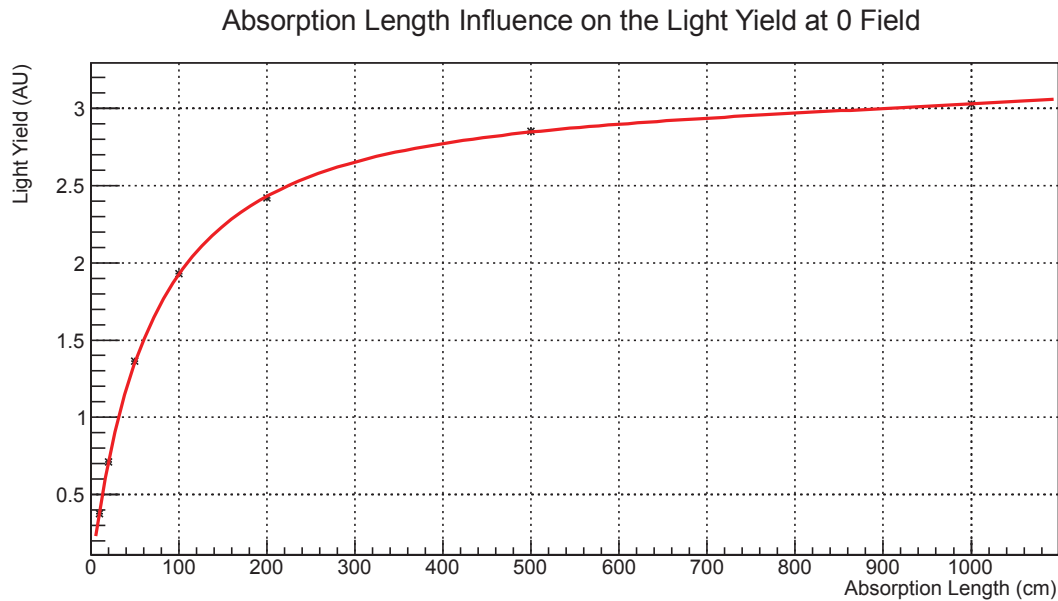


Figure 5.8: Absorption length influence on the average light yield in the detector

According to this simulation, it is very clear that up to 200 cm absorption length, the light yield is strongly dependent on the absorption length. In the range 0 to 200 cm absorption length, the variation are significant enough to be able to probe the purity of the system using the absorption length as parameter. However, at higher absorption lengths, the finite size of the TPC makes it less sensitive to the absorption length, as it is much larger than the detector.

### 5.3.4 Influence of the PTFE reflectivity on the Light Yield

Another crucial parameter which can be tested is the reflectivity of teflon.

As for XENON100, the reflection process is modeled in GEANT4 as follows. The only processes allowed are absorption or reflection, but not refraction. What is called reflectivity in GEANT4 is the probability of reflection and is input by the user. In addition the reflected light is split between a

Lambertian component which follows a cosine distribution given by Lambert's law of reflection and a mirror-like specular component. The modeling of this reflected light is done by the generic reflectivity model in GEANT4. However since details of the reflective properties of teflon are unknown at the time of this work, the values for the diffuse and specular component are the same as those used in XENON100, of 97% and 3% respectively.

The reflective properties of teflon will be extensively studied and discussed in the next two chapters of this work, but for the purpose of this MC this simplified reflection model is adequate.

The study done here is akin to what is done in XENON100 and in all other LXe detectors. Because, as mentioned, the reflectivity of teflon in liquid xenon is actually unknown, simulations are carried out where only the reflectivity of the teflon is changed and its effect on the light yield is plotted. Once the experiment itself works and the light yield can actually be physically measured, the teflon reflectivity is deduced by matching it to the appropriate light yield. Figure 5.9 shows such a plot for the Muenster TPC. Unfortunately, because physical data is not yet available, the corresponding reflectivity cannot be determined yet.

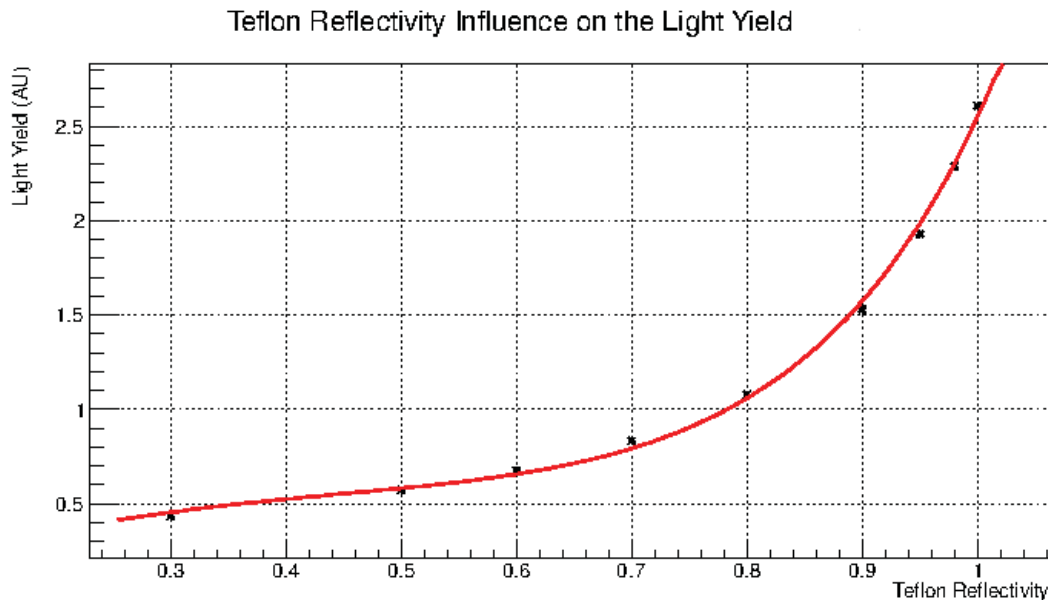


Figure 5.9: Influence of the reflectivity on the light yield

## 5.4 Gamma Simulations

Finally for the scope of this work, gamma calibration sources are simulated. Again, as for XENON100, the use of such sources will be necessary to determine the light yield and the light response of the TPC. However, there are many gamma sources to choose from and simulations can help to select the

appropriate one. In this case, three sources will be tested,  $^{137}\text{Cs}$ ,  $^{57}\text{Co}$  and  $^{60}\text{Co}$  and simulations were carried out with the same number of events and with the sources placed on the center left of the TPC only.

The first thing to check is if the peaks from the different decays are visible in the spectra. Because this is a simulation, the energies are known and so these spectra are plotted as a function of recoil energy  $E_r$  without including detector resolution, making the peak identification much easier. This is done for  $^{137}\text{Cs}$ ,  $^{57}\text{Co}$  and  $^{60}\text{Co}$ . The decay chains from these three sources can be seen in figures 5.10, 5.11 and 5.12.



Figure 5.10: Decay scheme of  $^{137}\text{Cs}$  [28].

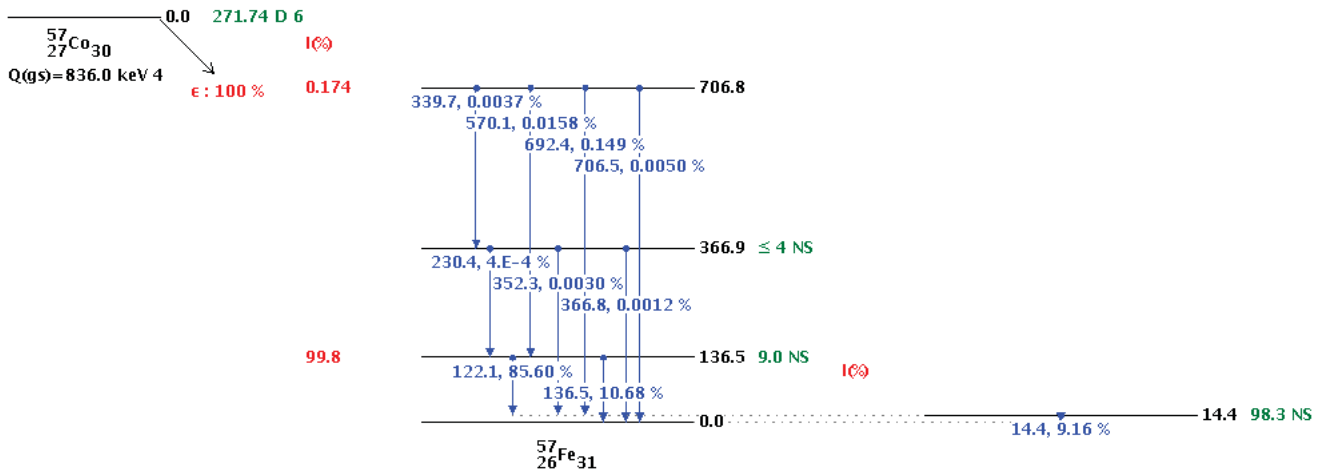


Figure 5.11: Decay scheme  $^{57}\text{Co}$  [28].

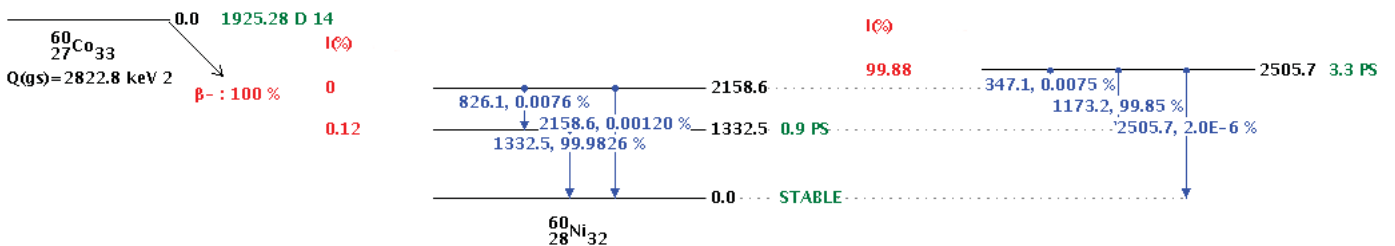


Figure 5.12: Decay scheme of  $^{60}\text{Co}$  [28].

The 662 keV peak from  $^{137}\text{Cs}$  is clearly visible in figure 5.13. The broader part of the spectrum below the full energy peak at 662 keV is due to single and multiple Compton scattering, as was detailed in the previous chapter. This matches very well what is seen in XENON100 and so what is expected. Note, in addition, the absence of a Compton edge and instead, the distribution extends all the way to the full absorption peak. These are gammas which Compton scattered in the stainless steel or the teflon before being fully absorbed in the xenon, and thus have lower energy when they reach the xenon. This effect is visible for all three calibration sources as will be seen hereafter.

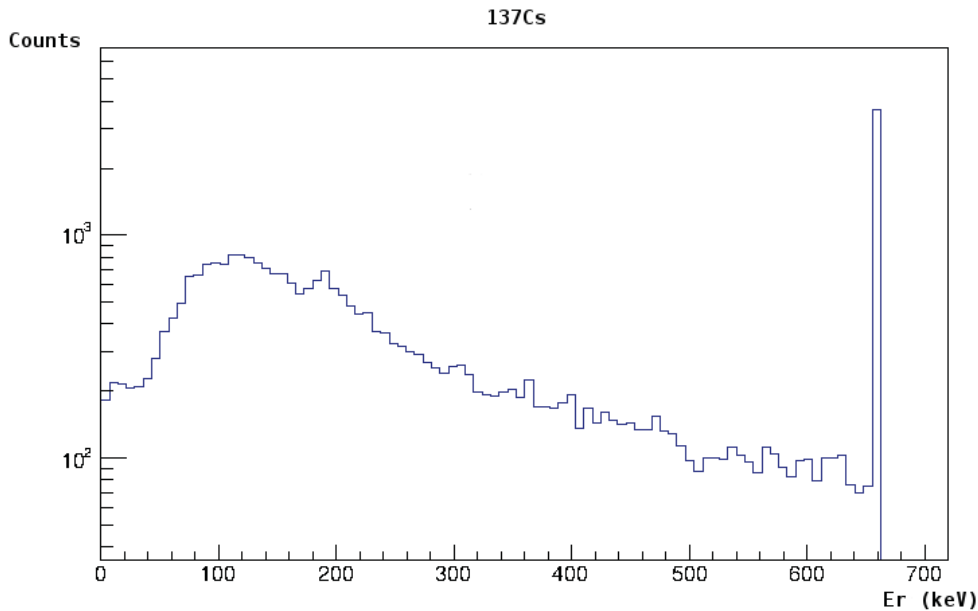


Figure 5.13:  $^{137}\text{Cs}$  spectrum from simulation.

The 122 keV and 136.5 keV peaks for  $^{57}\text{Co}$  are also clearly visible, as well as a much smaller yet still visible peak at 707 keV, which is as expected, as shown on figure 5.14.

Finally, the two high probability 1.17 and 1.33 MeV peaks from  $^{60}\text{Co}$  show particularly well. There is also a small peak at 2.5 MeV, which is the sum line from the 1.17 and 1.33 MeV peak.

Note also that for both cobalt sources, there seems to be a lot of backscatters and Compton scatters at lower energies. Despite this, the spectra are exactly what was expected and are yet again a proof that the simulation package works properly.

Finally an interesting analysis to perform with these sources is to map out the positions of the events in the detector. This is done for the three sources on figure 5.16 which were all placed outside the isolating vacuum chamber at a position  $(x,y,z)=(-150,0,0)$  mm with the  $(0,0,0)$  position as the center of the xenon cryostat. Figure 5.16 shows how deeply each source penetrates into the detector. Ideally a perfect calibration source can pass through the entirety of the detector, and thus give signals

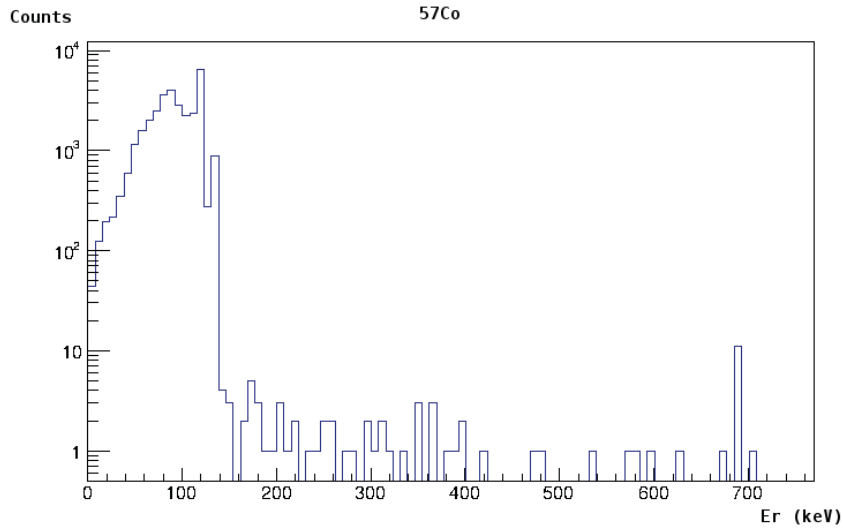


Figure 5.14:  $^{57}\text{Co}$  spectrum from simulation.

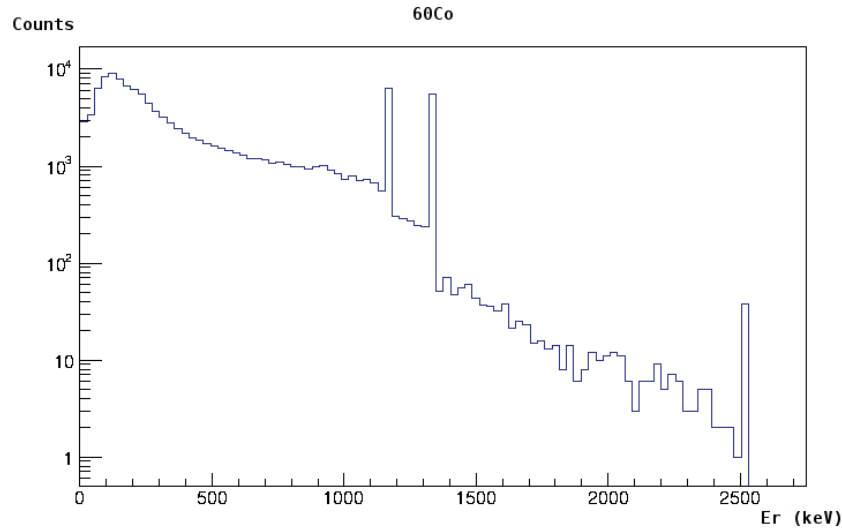


Figure 5.15:  $^{60}\text{Co}$  spectrum from simulation.

everywhere. However this is usually not the case, which is why during a calibration the sources are placed in different spots around the detector, to give out a uniform calibration.

That said, even if the sources can be placed around the detector, they need to be penetrative enough to at least reach the center parts of the detector. From figure 5.16 this is clearly not the case for  $^{57}\text{Co}$  which barely makes it to the edges of the TPC. This was expected of course as the mean free path of 122 keV gammas in liquid xenon is 0.07 cm compared to the 10 cm length scale of the Muenster TPC, however this simulation is a nice confirmation of this effect and discards the use of a  $^{57}\text{Co}$  source for calibration purposes for this TPC.

On the other hand, both  $^{137}\text{Cs}$  and  $^{60}\text{Co}$  sources, with a mean free path of 4 and 5 cm respec-

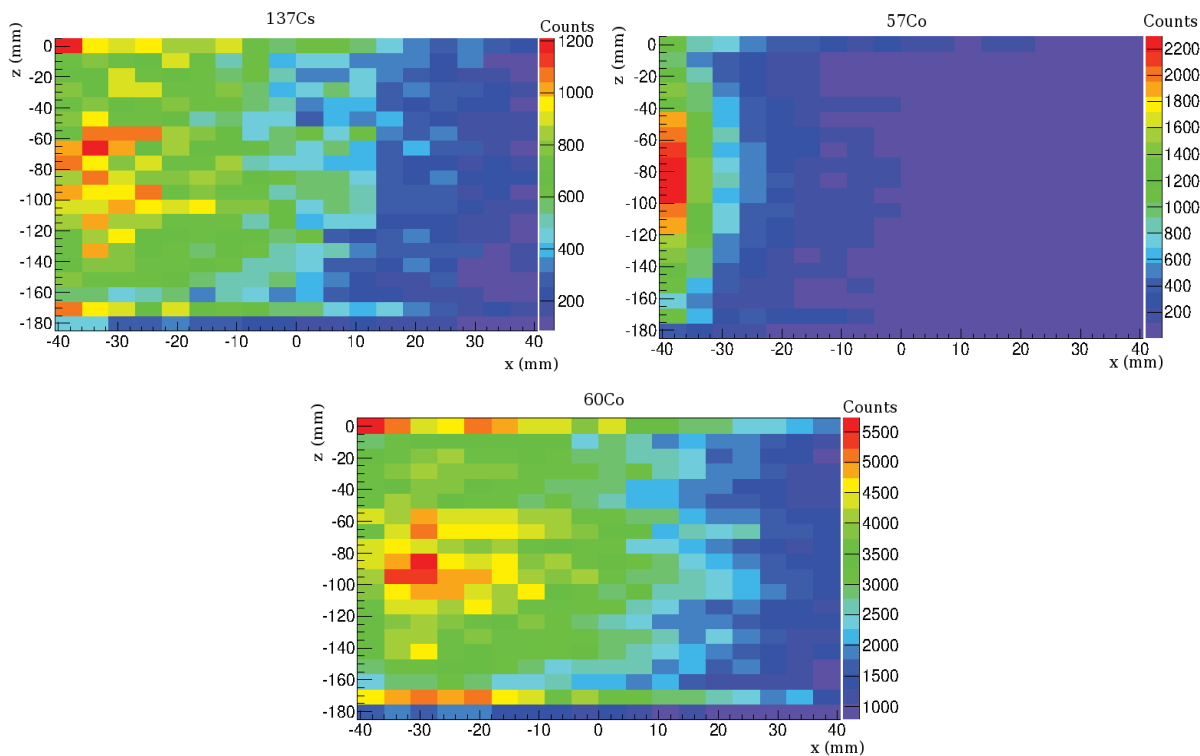


Figure 5.16: Events (first scatter) position in the Muenster TPC for three different gamma sources. Top left:  $^{137}\text{Cs}$  . Top right:  $^{57}\text{Co}$  . Bottom:  $^{60}\text{Co}$

tively, reach the center of the TPC and propagate well enough through it, with just a little better performance from  $^{60}\text{Co}$  . However, neither can reach the full extent of the TPC and thus, as for XENON100, need to be placed in separate positions in order to reach through the whole TPC. In addition, while  $^{60}\text{Co}$  seems to reach the whole TPC in  $z$ , this is not the case for  $^{137}\text{Cs}$  which does not reach the bottom part well. Consequently, while only moving the source around the TPC is enough if using a  $^{60}\text{Co}$  source, it also needs to be moved up and down the TPC if using  $^{137}\text{Cs}$  .

## 5.5 Conclusion

The GEANT4 software was used to create an extensive MC package to simulate the geometry and the different physical processes in the Muenster TPC. This is a necessary and very useful tool to be able to study many effects, phenomena and parameters of the TPC, some of which could not possibly be done otherwise. The light yield of the detector behaves as expected, and gamma source simulations have been used to determine one optimal calibration source and its positioning. While much more work is necessary to fully take advantage of this software package, it has been tested and proved to be in a working condition, allowing anyone who wishes it to use it and perform more studies in order to fully understand the Muenster TPC.





# Chapter 6. TEFLON REFLECTIVITY STUDIES IN VACUUM

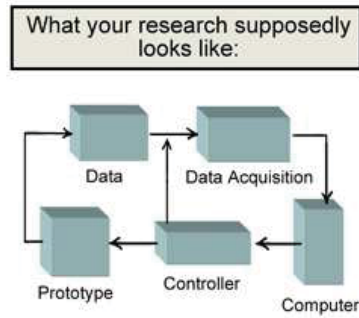


Figure 1. Experimental Diagram

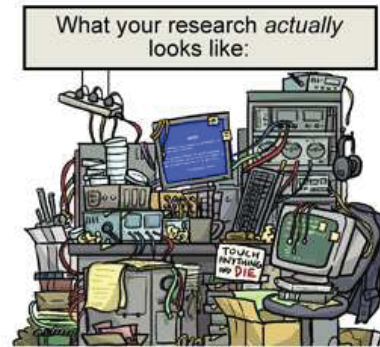


Figure 2. Experimental Mess

WWW.PHDCOMICS.COM JORGE CHAM © 2008

*Piled Higher and Deeper* by Jorge Cham [www.phdcomics.com](http://www.phdcomics.com)

## 6.1 Introduction and Motivation

As presented in chapter 3, in order to maximize light collection in the detector, the XENON100 TPC is made of a highly reflective material, polytetrafluoroethylene  $(C_2F_4)_n$ , commonly known as teflon. Teflon (PTFE) is a hydrophobic fluorocarbon (a material made only of carbon and fluorine) thermoplastic polymer which, amongst many other interesting features, is known to be a good V-UV reflector and is thus well suited for reflecting the 178 nm V-UV scintillation light of xenon. Because teflon is made of a pressed powder, it is constituted of many uneven microsurfaces whose shape and pattern may be altered depending on the shaping technique used on the powder. Indeed, to give the final desired form to the powder, techniques such as pressing, molding or extruding can be applied to the teflon. In addition, many different machining techniques can be used to cut the final material. All of this may have a huge impact on the teflon surface properties, in particular its reflective properties.

Because teflon has proved to work rather well in liquid xenon detectors, it will certainly be used to build the TPC of the upcoming XENON1T experiment. However, the specific teflon which will be used in XENON1T is still unknown. To choose this material accurately, several potential teflon samples have to be tested and their reflective properties investigated so that the optimal material and machining technique can be selected. Consequently a setup dedicated to the measurements of

the reflective properties of teflon was built at Muenster University. Based on a setup constructed by Muenster University and Columbia University [98], an apparatus was designed and built by Karen Bokeloh [99] to measure V-UV reflectivity in vacuum and vacuum measurements were performed in the context of this thesis to measure the reflectivity of a teflon sample, its transparency and the impact of its thickness. These measurements and the subsequent analysis are the subject of this chapter.

In a second step, the setup was upgraded to perform measurements in liquid xenon. This will be thoroughly discussed in chapter 7.

## 6.2 Basic Theory of Reflectivity

The reflectivity of a material is the fraction of incident light that is reflected when interacting with the material. For a homogeneous, flat surface, the expectation is that the reflectivity should have an angular dependence which gives rise to two types of reflection, specular and diffuse reflection, however the amount of specular and diffuse reflection is highly dependent on the material.

Specular reflection is a mirror like reflection where the incident and reflected light are coplanar and make the same angle with respect to the surface normal  $\mathbf{n}$  as shown on figure 6.1. The incident angle  $\theta_I$  is thus related to the reflected angle  $\theta_R$  via

$$\theta_I = \theta_R \quad (6.1)$$

Consequently, in the case of pure specular reflection, reflectivity will be zero except at the reflected angle.

In the case of diffuse reflection, the reflection process is governed by Lambert's cosine law, which states that the light intensity in a solid angle element  $d\Omega$  is directly proportional to the cosine of the reflected angle  $\theta_R$  with respect to the surface normal, with the proportionality factor  $I_0$  being the initial intensity.

$$\frac{dI(\theta_R)}{d\Omega} \propto I_0 \cos(\theta_R) \quad (6.2)$$

Consequently, the light will be reflected at many angles rather than just one like for the specular reflection as shown on figure 6.1.

Modeling the reflectivity process in reality is of course different than from the ideal case and, mostly due to the uneven and amorphous teflon surface, is far from a trivial process. This will be

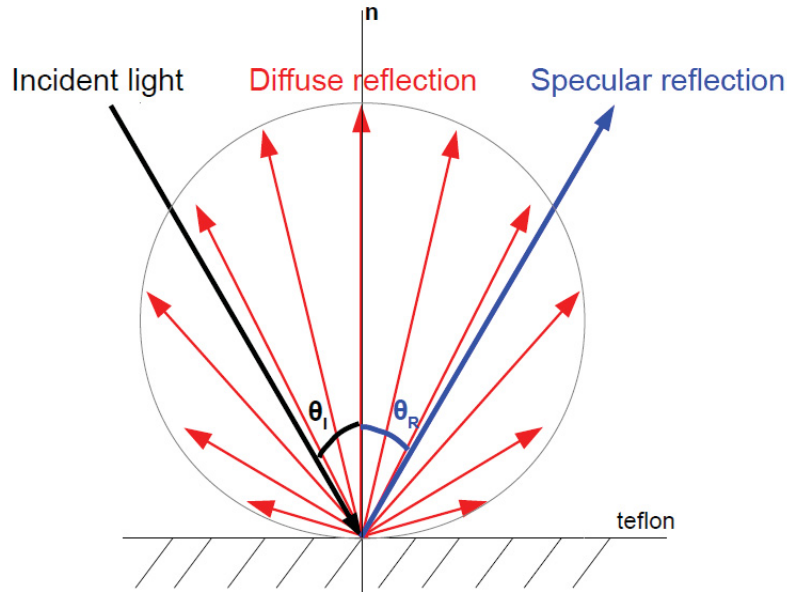


Figure 6.1: Schematic of specular (blue) and diffuse (red) reflection processes.

extensively reviewed and explained in section 6.4.5. However, the main feature of the reflectivity remains that there is typically both a specular and diffuse component. Moreover, the specular component is smeared in two dimensions about the direction of perfect specular reflection, such as with a 2D gaussian.

### 6.3 The Setup

The full description of the vacuum measurement system can be found in Karen Bokeloh's thesis [99]. Only a summary of the most essential features will be given in this section.

The setup can be summarized as follows. A spectrum of UV light is generated in a deuterium lamp and passed through a monochromator which consists of a series of mirrors and gratings used to select a specific wavelength. The monochromator is set to transmit 178 nm light to match the scintillation light of LXe. The light then passes through a converging lens and a collimator to finally reach a sample of teflon, placed in a vacuum vessel, of which it reflects off. The light is then detected at different angles by a PMT that can rotate about the reflection point. This is schematized on figure 6.2.

The setup can thus be separated in two main parts, the light assembly containing a monochromator and a deuterium light and responsible for the light emission and the main vacuum chamber which is the vessel containing the PMT and the teflon and isolates the system from the outside. These two vacuum chambers are physically isolated from one another by a  $MgF_2$  window, which is

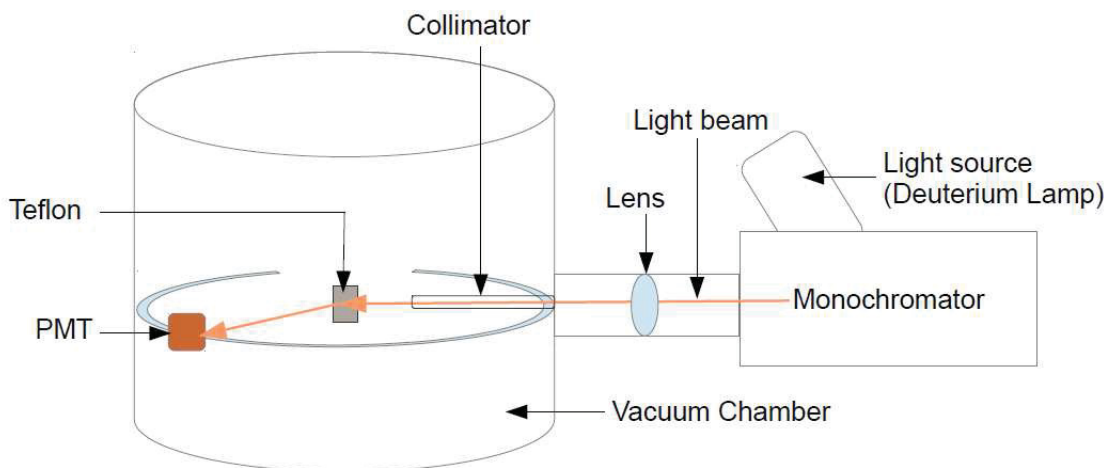


Figure 6.2: Schematic view of the reflectivity setup under vacuum.

transparent to UV light.

### 6.3.1 The Light Assembly

To generate the proper light, a McPherson deuterium lamp model 632 is attached to a McPherson .3m scanning monochromator model 218 set to select light at 178 nm. The monochromator itself has to be under vacuum to transmit light efficiently, as vacuum ultraviolet (VUV) light of 178 nm is attenuated when traveling through air. The proper vacuum of  $2.5 \times 10^{-5}$  mabr is achieved by a Pfeiffer turbo molecular pump TMH 071. The light assembly with the different components is shown on figure 6.3.

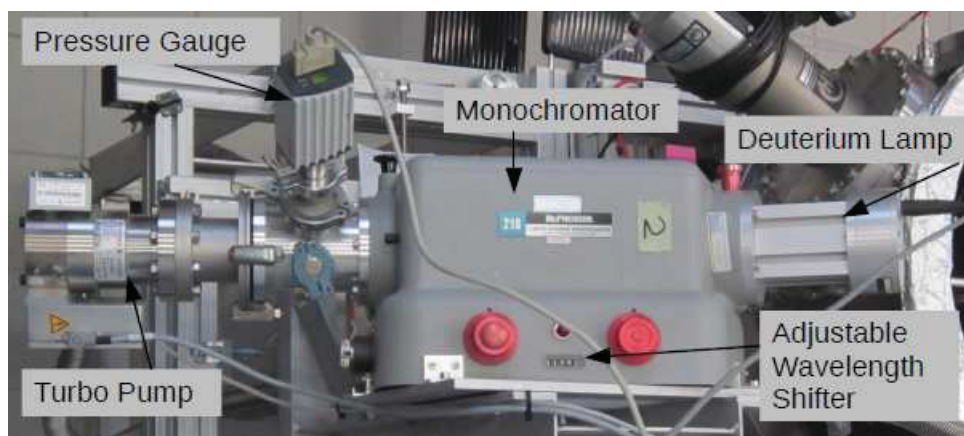


Figure 6.3: The light assembly of the reflectivity setup.

A deuterium lamp is a gas discharge lamp which behaves like an arc lamp. It is constituted of two electrodes, a tungsten filament and an anode separated by a gas, in this case, deuterium. By applying a high voltage (300-500 V) across the lamp, a current is generated between the electrodes,

ionizing the gas in the process and thus creating an arc. Once the arc is created, lower voltages around 100 or 200 V are needed to sustain it. Before an arc can be produced, the filament must be very hot. It is thus heated for about 20 seconds before the lamp itself turns on. Once the arc is stable it ionizes the deuterium which then emits light as it reverts to its ground state, leading to continuous UV radiation. The lamp itself is encased in a magnesium fluoride shell, which can easily sustain the high temperatures caused by the arc and has a high transmission of UV light down to 150 nm. The light produced covers a wide spectrum shown on figure 6.4.

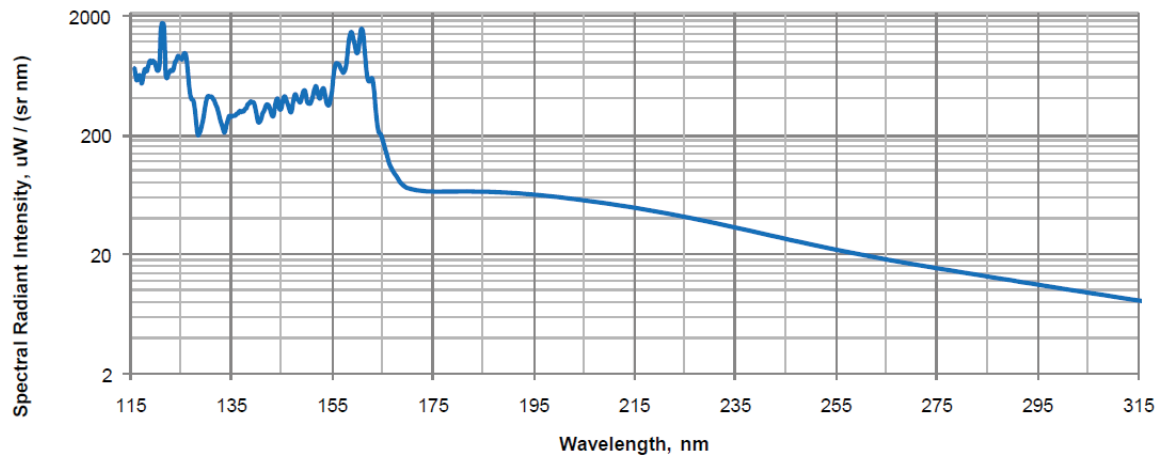


Figure 6.4: Spectrum emitted by the McPherson model 632 deuterium lamp. Courtesy of McPherson.

The monochromator uses a system of a diffraction grating and focusing mirrors to adjust the wavelength. A grating is an optical component which has a periodic structure such as tiny slits. When a beam of light hits a grating it is split in several beams which are diffracted and travel in different directions depending on their wavelength according to equation 6.3.

$$d \sin(\theta_m) = m\lambda \quad (6.3)$$

In equation 6.3,  $d$  is the spacing between two slits,  $\theta_m$  is the angle of maximum diffraction,  $\lambda$  is the wavelength and  $m$  is an integer representing the propagation mode corresponding to the quantized directions of constructive interference, with  $m=0$  corresponding to direct transmission. The explanatory picture of the principle of diffraction through a slit is shown on figure 6.5.

The monochromator used for this setup is composed of two mirrors and one grating arranged as shown on figure 6.6. The grating can be turned such that only the desired wavelength is focused to the exit aperture. For the purpose of this experiment, they are set to select a wavelength of 178 nm.

Finally once the 178 nm light emerges from the monochromator it goes through a UV lens of 80 mm focal distance at 178 nm in order to focus the light beam. The lens is fixed in a CF-40 T-piece

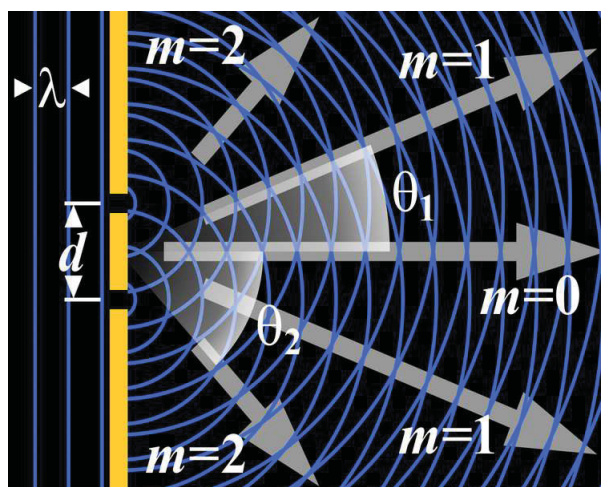


Figure 6.5: Principle of diffraction through two slits showing the relevant parameters of equation 6.3 [29]

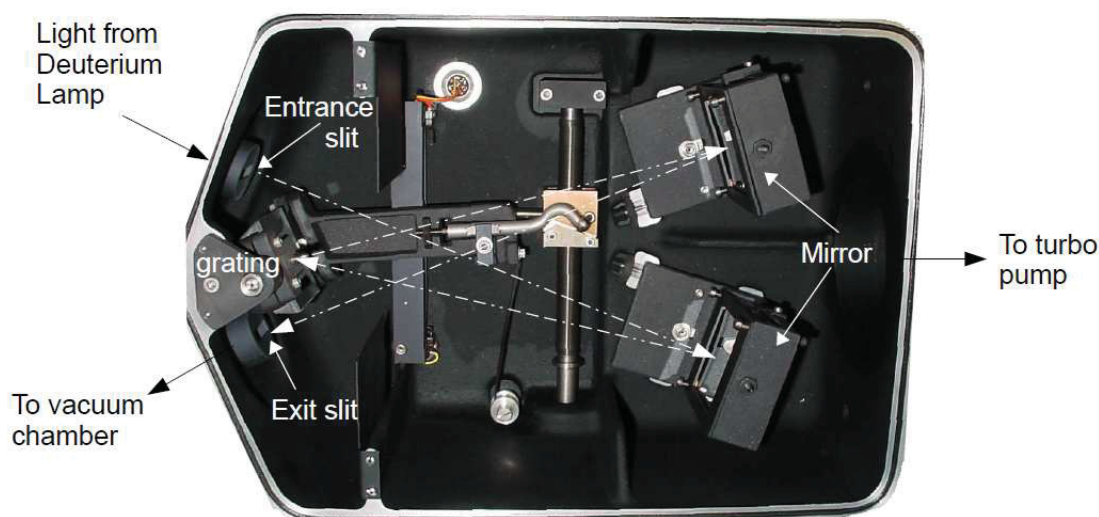


Figure 6.6: The inside of the McPherson model 218 monochromator with the main features and the light path indicated by the dashed lines.

to make sure it doesn't shift out of alignment [99]. The focused beam then passes through a long collimator which has a 1 mm wide aperture before arriving in the main vacuum chamber.

### 6.3.2 The Main Vacuum Chamber

The main chamber is composed of a 65 cm diameter stainless steel cylinder and is connected to the light assembly via the collimator and the T-piece containing the lens. For the light to be transmitted without deflections, the main chamber is maintained under vacuum at about  $1 \times 10^{-6}$  mbar by a Leybold turbo molecular pump TW 300, which is enough to prevent water condensation in the chamber as the vapor pressure of water  $P$  at a temperature  $T$  of  $-100^\circ\text{C}$  is  $1.2 \cdot 10^{-4}$  mbar as defined

by the Clausius-Clapeyron equation 6.4 [100]. The vacuum is then always precisely monitored via an ionivac pressure gauge, except during data acquisition as the gauge produces light when turned on, which would skew the measurements.

$$P = 1.33e^{20.386 - \frac{5132[K]}{T}} \text{ mbar} \quad (6.4)$$

At the center of the chamber, an aluminum holder supports a PMT which can rotate in a plane about the central axis of the chamber. The PMT is encased in a protective copper case and a cover with a 2 mm diameter aperture is placed in front of its quartz window in order to have fine angular resolution. Because PMTs are known to have more dark counts at ambient temperature [101], the chamber and thus the PMT is maintained at low temperature of about  $-100^{\circ}\text{C}$ . This is done by attaching a cold head at the side of the chamber thermally linked to the PMT by a flexible copper thermal link. The cold head also acts as a cryopump where any residual water in the chamber can condense without hindering data taking. In addition, to maintain the whole chamber cold, two cold shields are installed inside the chamber. In order to avoid unwanted reflections from these cold shields, the inner one is anodized with a black color. The inside of the vacuum chamber with the cold shields, collimator, the aluminum holder and PMT is shown on figure 6.7.

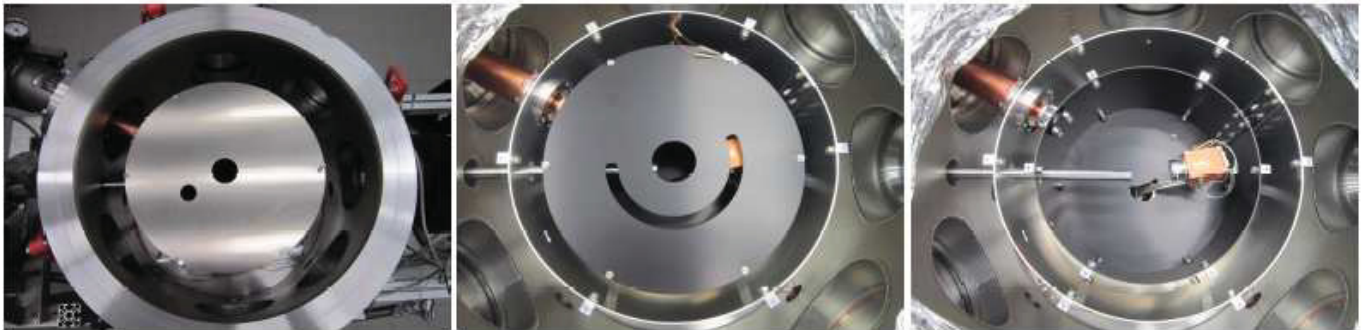


*Figure 6.7:* The inside of the vacuum chamber. Left: once the top flange has been removed, the outer cold shield is visible. Middle: When the lid of the outer cold shield is removed, the anodized inner cold shield remains. Right: After removing the lid of the inner cold shield, the rotatable PMT in its copper case and the collimator are clearly visible.

The aluminum rod supporting the PMT is attached to the bottom of the chamber via a rotational and translational feedthrough. The translational feedthrough allows to adjust the x, y and z position of the PMT and ensures that the center of rotation is in the middle of the chamber. The rotational feedthrough is linked to a stepper motor which can be controlled remotely and allows for the rotational movement of the PMT around the chamber. The feedthrough is shown on figure 6.8.

Finally, hanging from the top flange of the vacuum chamber, an anodized holder holds the teflon

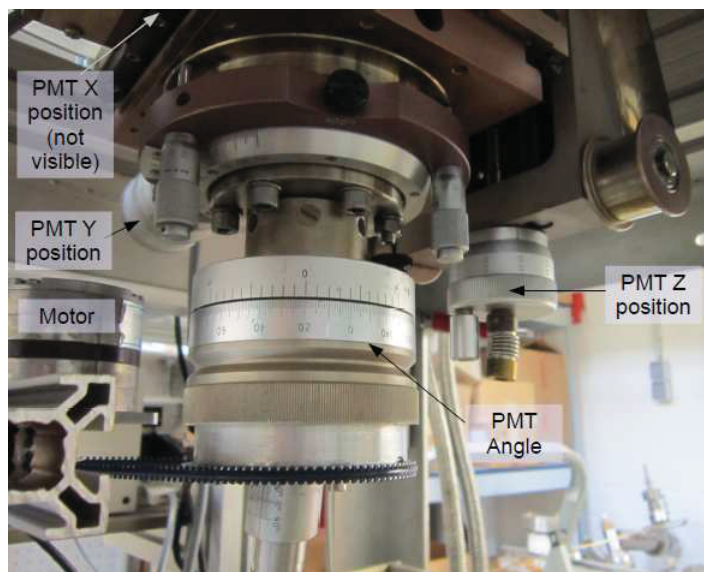


Figure 6.8: The central bottom feedthrough allowing rotational movement of the PMT around the chamber.

sample straight in the center of the chamber, between the PMT and the light path. The holder itself is attached to a rotational and translational feedthrough on top of the main flange which allows the teflon to be rotated  $360^\circ$  and translated in x, y or z, as shown on figure 6.9. While not used for the measurements of this work, the teflon can also be attached to the holder so that it does not hang straight in the chamber but rather at a tilt angle, although always at the center of the chamber. By doing so, the PMT is no longer in the plane of reflection and can thus measure reflected light outside that plane. This was done in [99].

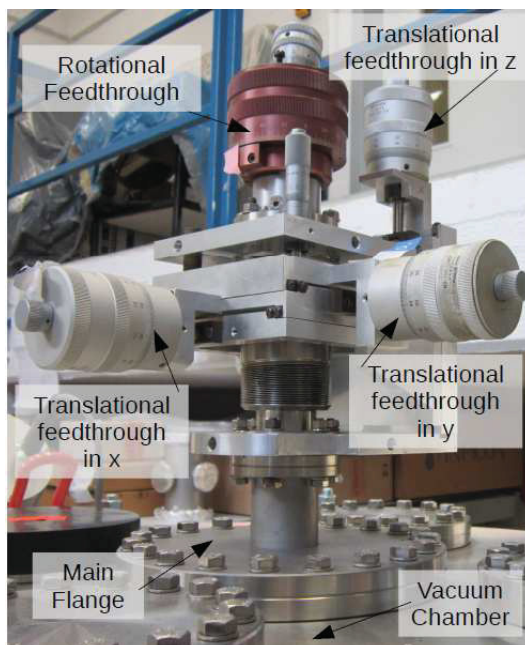


Figure 6.9: The central top feedthrough allowing rotational and translational movement of the teflon in the vacuum chamber.

Figure 6.10 shows a schematic view of the inside of the vacuum chamber, illustrating the points aforementioned.

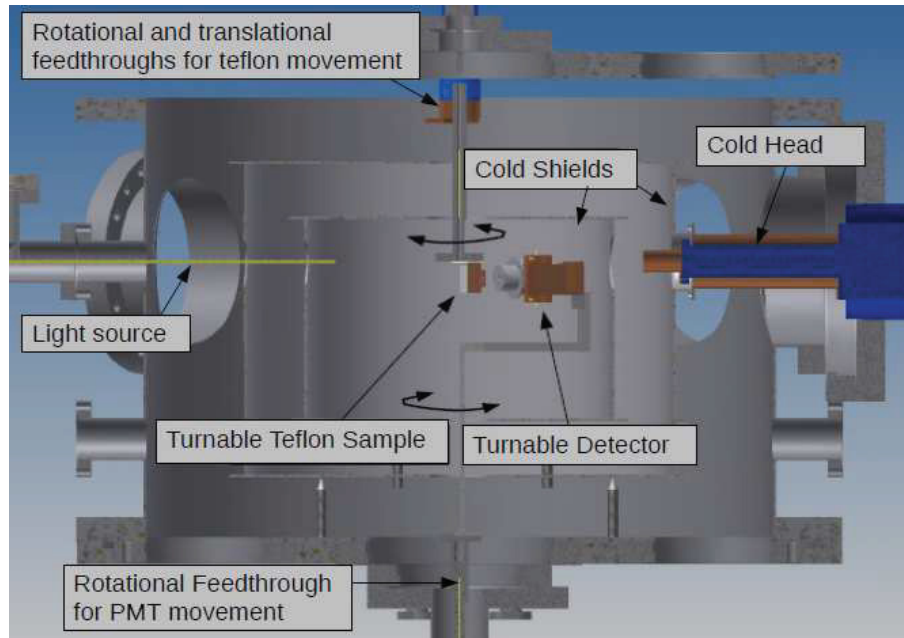


Figure 6.10: Diagram showing the inside of the main vacuum chamber of the reflectivity setup at Muenster university.

Finally, to help for future reference, figure 6.11 shows the setup with x, y and z positions labeled, as they will be used throughout this chapter.

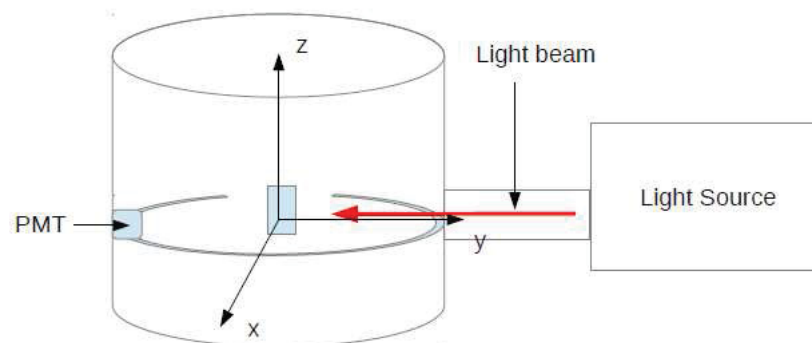


Figure 6.11: Orientation of the setup

## 6.4 XENON100 Teflon Sample Cut in Steps

In order to decide what type of teflon is going to be used for XENON1T, it is important to first investigate the reflectivity of the PTFE currently used in XENON100.

### 6.4.1 The Sample

A teflon sample taken from the same block of teflon used in XENON100 was milled at Muenster, in steps of different thickness. A photograph of this sample can be seen on figure 6.12. The sample is cut in five different steps with thicknesses of 9.5, 5, 3, 2 and 1 mm.

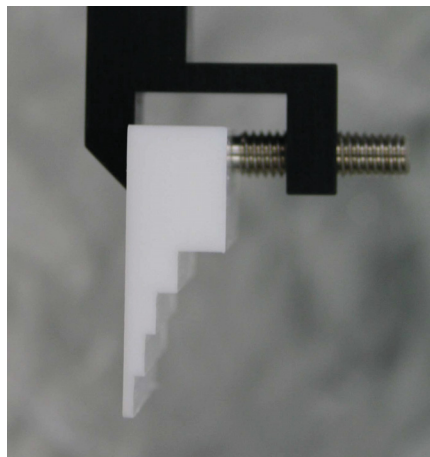


Figure 6.12: Photo of the XENON100 teflon sample cut in steps which is used in the reflectivity setup

### 6.4.2 Calibration

As always when taking measurements with an experimental setup, precise calibration of the system is necessary. In this section, the calibration of the geometric alignment of the setup is described.

#### *Beam Spot*

The first calibration, called beam spot, is carried out to determine at what PMT angle is the beam intensity maximum, so in which position is the beam directly aligned with the PMT. For this purpose, the teflon is put completely out of the way of the beam, as shown on figure 6.13 by moving it in the z or x direction and only the PMT angle is varied. As can be seen on figure 6.14, the beam is aligned with the PMT when the PMT is at an angle of  $7^\circ$  on the scale, value which was determined by taking the center of the plateau. This angle thus corresponds to the reference alignment between beam and PMT.

#### *Teflon Angle Alignment*

The teflon angle alignment (the angle at which the teflon is aligned with the beam) is known with some accuracy, as it was measured when the teflon was inserted in the setup. In this case, it was

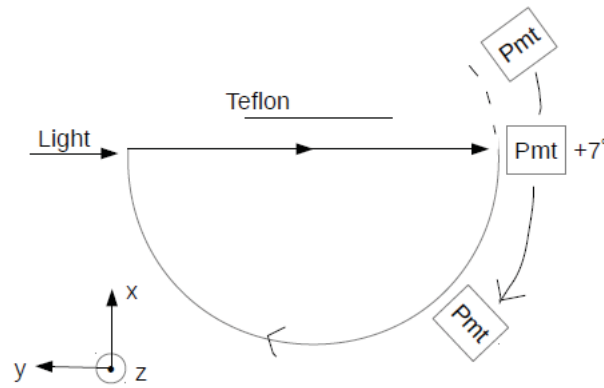


Figure 6.13: Setup position to perform the beam spot measurement.

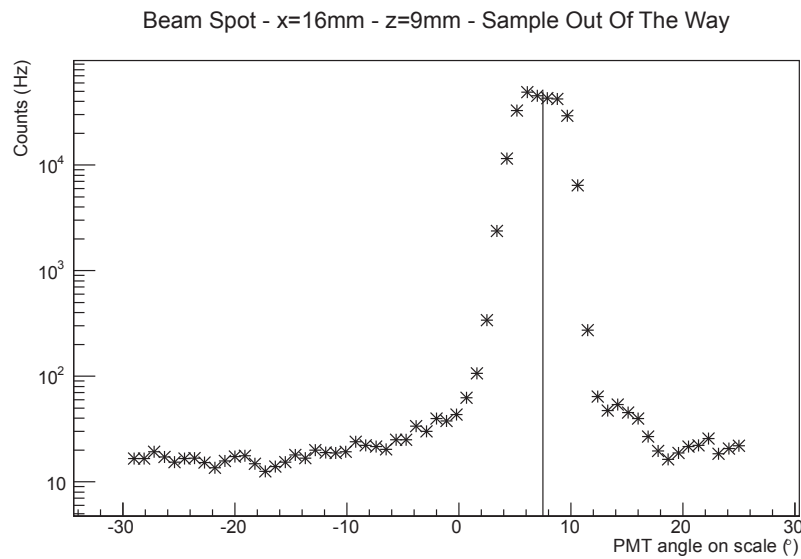


Figure 6.14: Beam spot calibration

measured to be around  $155^\circ$  on the teflon scale but this needs to be determined more precisely. For this, the teflon must be positioned in a manner that the beam grazes its surface and the PMT is fixed at  $7^\circ$  in alignment with the beam. By then varying the angle of the teflon, the point of maximum intensity can be inferred, which will then correspond to the alignment angle between beam and teflon.

However to do this angle alignment calibration, a rough x calibration must be done to know more or less the x position at which the beam grazes the teflon. This is quickly done by aligning the PMT with the beam, varying the x position of the teflon and recording the measured counts on a scaler. Figure 6.15 represents such a setup.

The x grazing distance was found to be around 13.5 mm as shown on figure 6.16.

Knowing this, the teflon is then placed accordingly and its angle varied. At that optimal teflon angle, the teflon will block half of the beam, but it will block more of the beam as it is rotated away

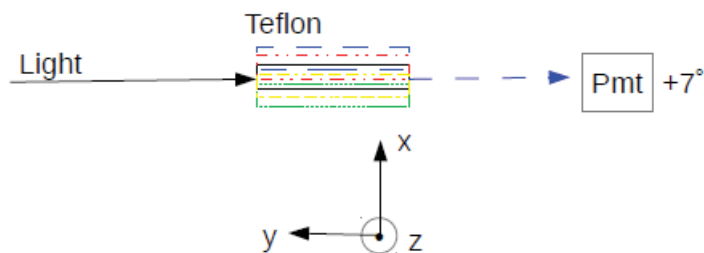


Figure 6.15: Setup for the rough x calibration.

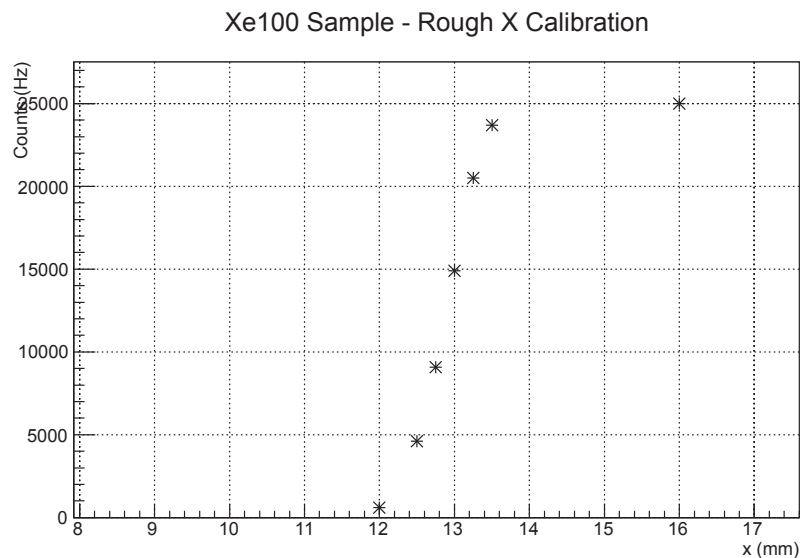


Figure 6.16: Rough X calibration

from this position. Thus, by locating the position of the maximum light, the proper alignment angle can be found. Indeed, it was found, as shown on figure 6.17, that the optimum alignment angle between beam and teflon happens at an angle of  $156^\circ$  on the scale since at this angle the minimum amount of light is blocked by the teflon.

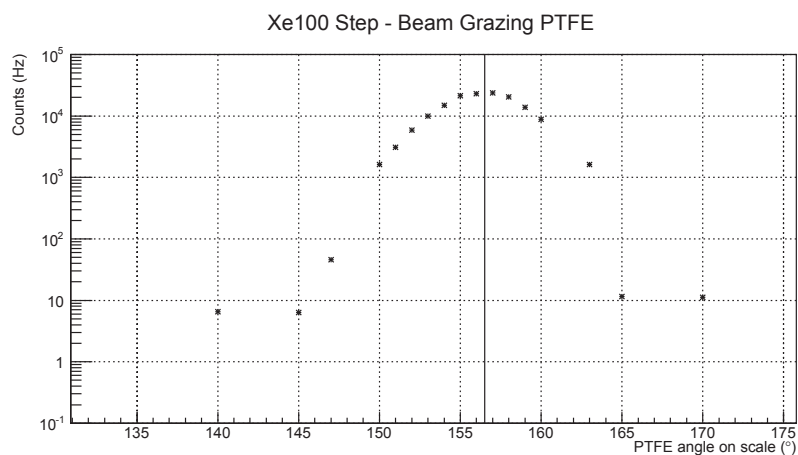


Figure 6.17: Angle Alignment

### Z Calibration

The next step is to figure out exactly where the teflon, and especially each step of different teflon thickness (see figure 6.12), is located on the z axis. This is shown on figure 6.18. The PMT is aligned with the beam and the teflon sample is put on the path of the beam so that it fully blocks the light. It is then lifted up until finally it reaches the point where it is above the beam and where all light shines directly into the PMT. The result is that at  $z=24$  mm the teflon is completely out of the way while at  $z=23$  mm where half intensity is observed, the teflon blocks half of the beam. Consequently, knowing the size of each step, the z positions corresponding to the different steps can be determined and are summarized on table 6.1.

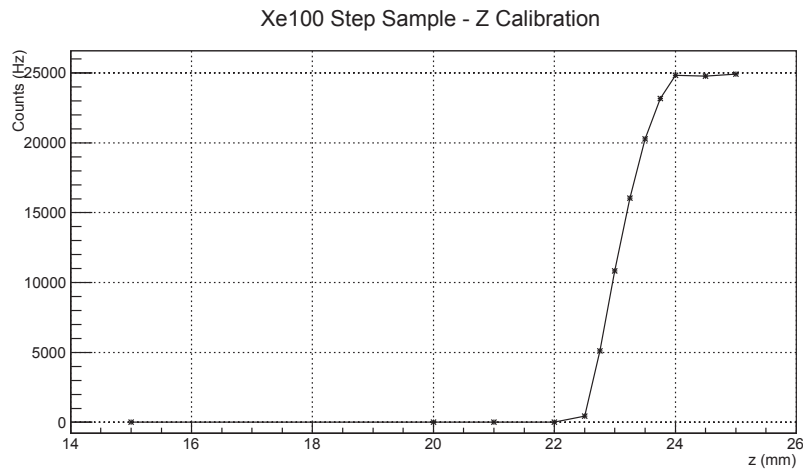


Figure 6.18: Z Calibration

### Precise X Calibration

Now that all the optimal PMT and teflon angles are known, the x axis can be recalibrated more precisely. The teflon is placed with its surface parallel to the beam at a z position where the sample is 3 mm thick. Varying the PMT angle for different x position leads to figure 6.19. It shows that above  $x=13$  mm, the intensity of the reflection is the highest and stays constant, thus indicating that the teflon is out of the way for x higher than 13 mm.  $X=13$  mm is thus the proper grazing distance and will then be used for all following measurements.

Note also that this a confirmation of the Z calibration as it can be seen that the teflon at this z position is in fact 3 mm thick. Indeed at  $x=11$  mm the beam is completely blocked while at  $x=10$  mm and 12 mm some light starts leaking on the side of the teflon with similar intensity. This places  $x=11$  mm as the middle of the step where the beam is completely blocked by the teflon. Considering

Z position on scale (mm)	Position on the teflon sample	Thickness of the step (mm)
$\leq 2$	holder	
5	center	9.5
7	step interface	
9	center	5
11	step interface	
13	center	3
15	step interface	
17	center	2
19	step interface	
21	center	1
23	lower edge	
$\geq 24$	below sample	

Table 6.1: Z positions corresponding to the different sample steps

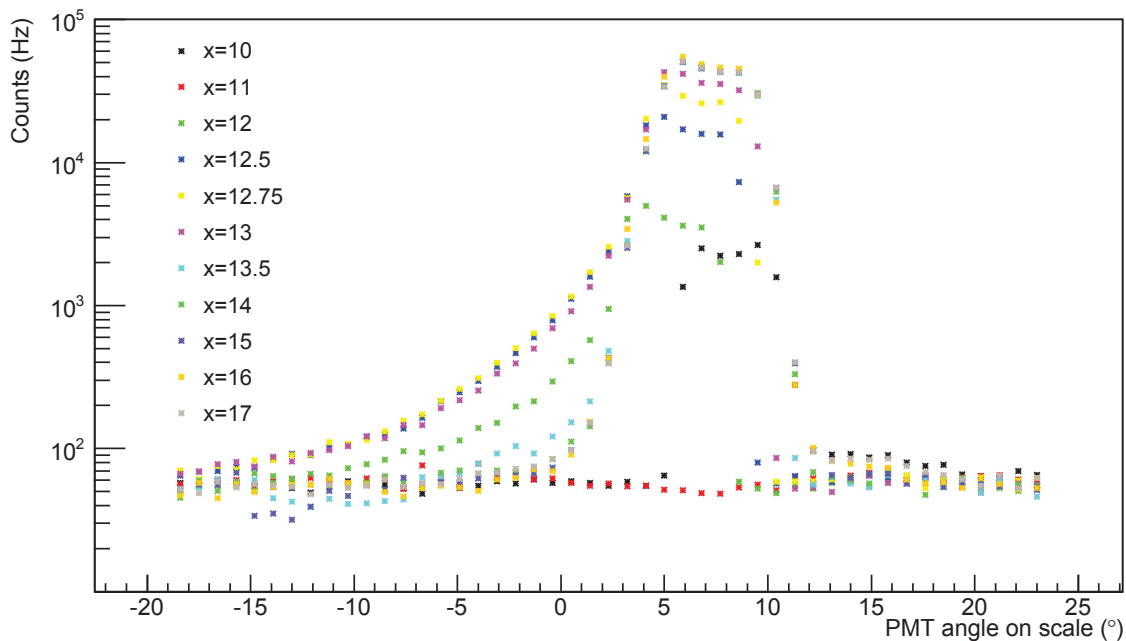


Figure 6.19: X Calibration

that at  $x=12.5$  mm, the intensity is half the maximum intensity and that the beam itself has a 1 mm diameter, it can be inferred that at  $x=12.5$  mm the center of the beam is aligned with the edge of the teflon, thus letting half the beam go through while the other half is blocked. Consequently, knowing that the center of the step is at  $x=11$  mm and the edge of the step is at  $x=12.5$  mm, the

half length of the step is 1.5 mm, making its full length 3 mm thick as expected. This is represented schematically on figure 6.20.

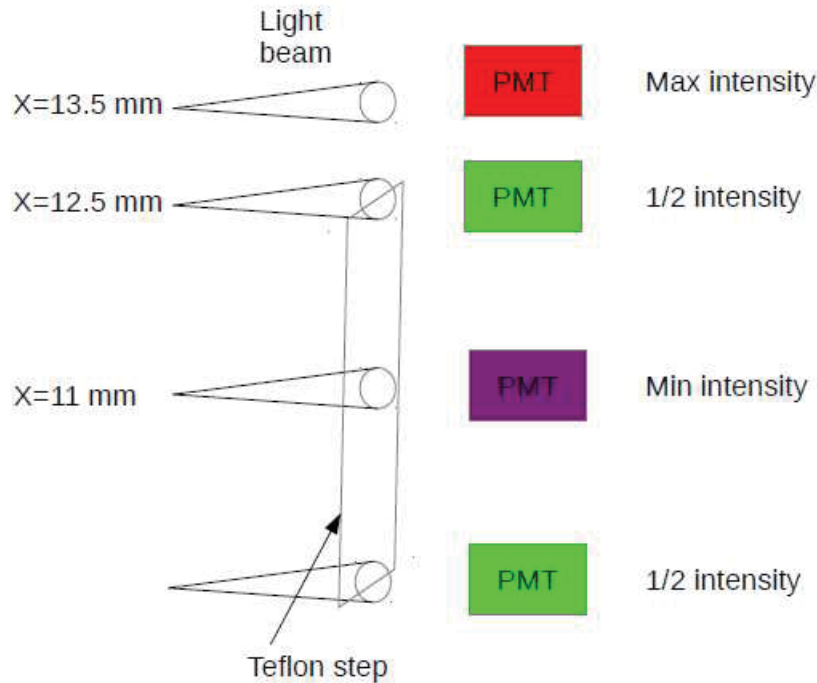


Figure 6.20: Verification of the  $z$  calibration using the  $x$  calibration. Note that in reality the teflon moves, not the beam. Due to the diameter of the beam, depending on where the beam shines on the teflon, the intensity read by the PMT will differ.

### *Y Calibration*

At this point it is needed to strictly define the incident angle and the angle of reflection which will be used in the remaining of this chapter. The incident angle  $\theta_i$  is defined as in optics and refers to the angle between the normal to the teflon  $\mathbf{n}$  and the incident light, while the angle of reflection  $\theta_r$  is the angle between the normal to the teflon surface and the reflected light. Both angles are defined here in the scattering plane, as shown on figure 6.21. Scattering out of the plane is not considered here yet.

The last necessary calibration is of course the  $y$  axis. Indeed if the center of the teflon is not placed in the center of the chamber, the PMT and teflon have a different center of rotation thus making the reflection angles inaccurate. To do this, the teflon is positioned at an incident angle  $\theta_i$  of  $80^\circ$ . If it is indeed in the middle of the chamber and if the  $y$  axis is calibrated properly, the maximum reflection should be at a PMT angle  $\theta_{PMTmax}$  of  $20^\circ$  with respect to the beam direction according to equation 6.5. This is represented on figure 6.22.

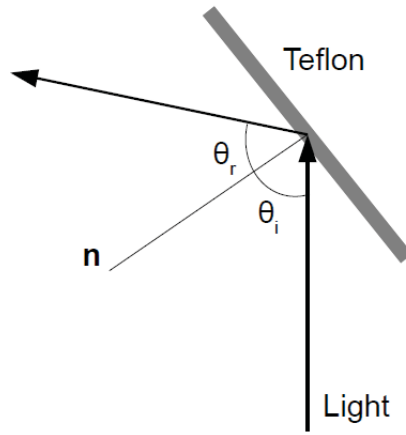


Figure 6.21: Definition of the incident angle  $\theta_i$

$$\theta_{PMTmax} = 2(90 - \theta_i) \quad (6.5)$$

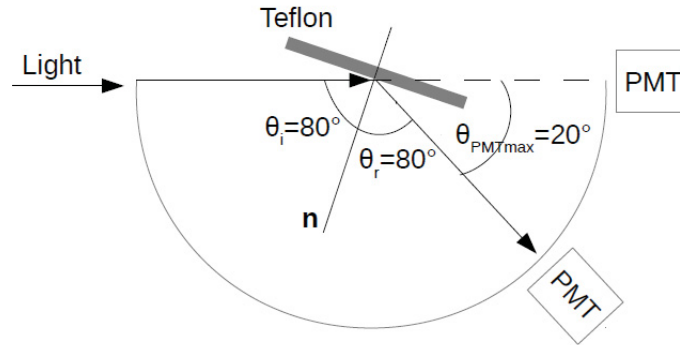


Figure 6.22: Setup position to perform the Y Calibration

Consequently, when varying the PMT angle for different values of  $y$ , the curve whose peak will be at  $20^\circ$  will give the adequate  $y$  position. This is done in figure 6.23. From this same figure, it is found that the proper  $y$  value to be used is 20.5 mm.

Now that the setup is calibrated, science measurements can be taken. Three types of information need to be deduced from this analysis. First the influence of the teflon thickness on the reflectivity, second the reflectivity of the sample for each thickness and third the full transparency of the sample.

### 6.4.3 Influence of the thickness on the reflectivity

As mentioned before, understanding the influence of the teflon thickness on the reflectivity is crucial for the determination of the material thickness for the XENON1T TPC, as it has to be ensured that the TPC will be as reflective as possible. To look for the influence of the teflon thickness on

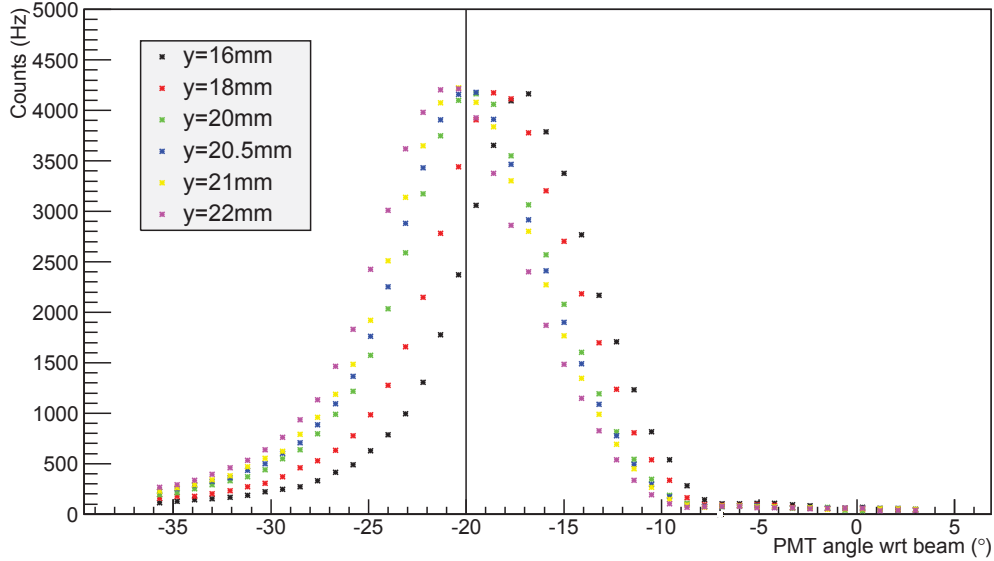


Figure 6.23: Y Calibration

the reflectivity, data with clear features are needed. Consequently, the specular component of the reflected light is investigated. However this effect can only be studied where the specular component is clearly visible, which is only the case at an incident angle of  $80$  or  $70^\circ$  which corresponds to a teflon angle relative to the beam of  $10$  or  $20^\circ$ .

### ***80° Incident Angle***

Data are taken at  $80^\circ$  incident angle for every millimeter over the height of the teflon. Raw data are shown on figure 6.24 on a linear scale and figure 6.25 on a logarithmic scale.

Several features can be inferred from this plot. First, x and y calibrations were done properly as the peaks are centered at a PMT angle  $\theta_{PMTmax}$  of  $20^\circ$  with respect to the beam, which is exactly where it should be for an incident angle  $\theta_i$  of  $80^\circ$  as calculated by equation 6.5.

Second, the z calibration is confirmed to be accurate. At  $z=2$  mm, the reflectivity drops drastically as the beam reached the black holder holding the teflon. At  $z=23$  mm, the reflectivity drops and the onset of the unreflected light shining directly through the chamber unimpeded can be seen, especially on figure 6.25, indicating that the bottom part of the teflon has been reached and some of the beam is now passing under the teflon localized around a PMT angle of  $0^\circ$ . At  $z=24$  mm, no more reflection at a PMT angle of  $20^\circ$  can be seen as the beam is now totally under the teflon and thus is not reflected. The corresponding curve of figure 6.25 actually corresponds to the beam spot measurement of figure 6.14, as should be the case.

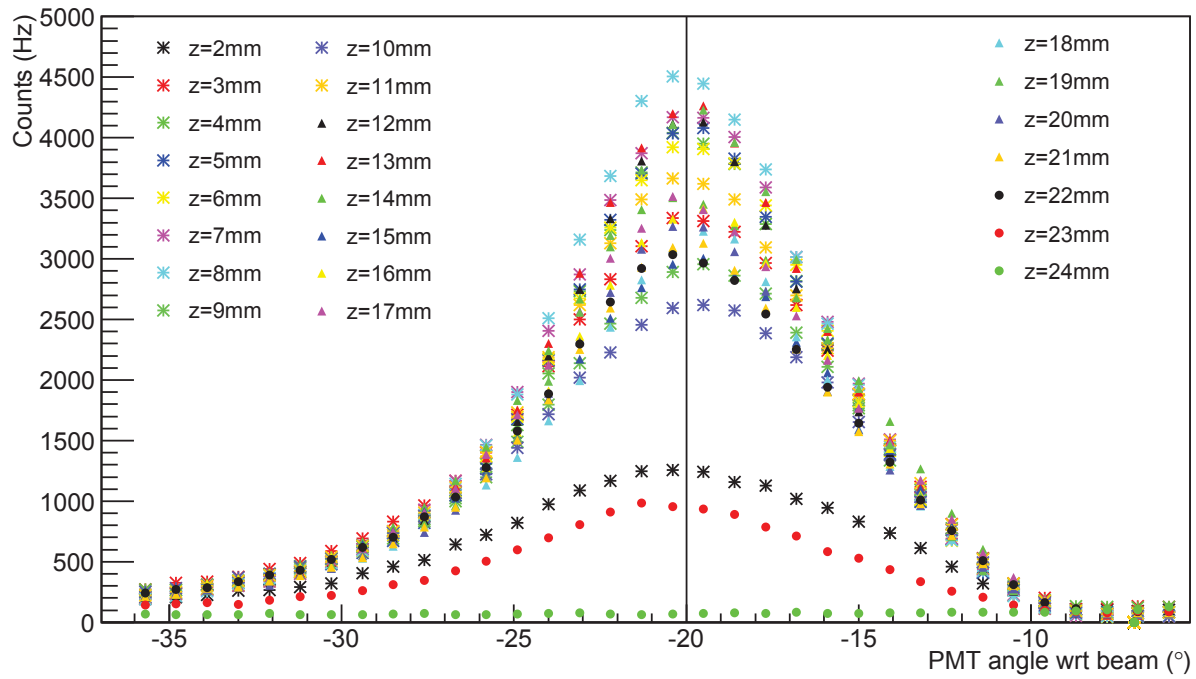


Figure 6.24: Raw data from the teflon positioned at  $80^\circ$  incident angle over the entire height of the teflon. Linear scale.

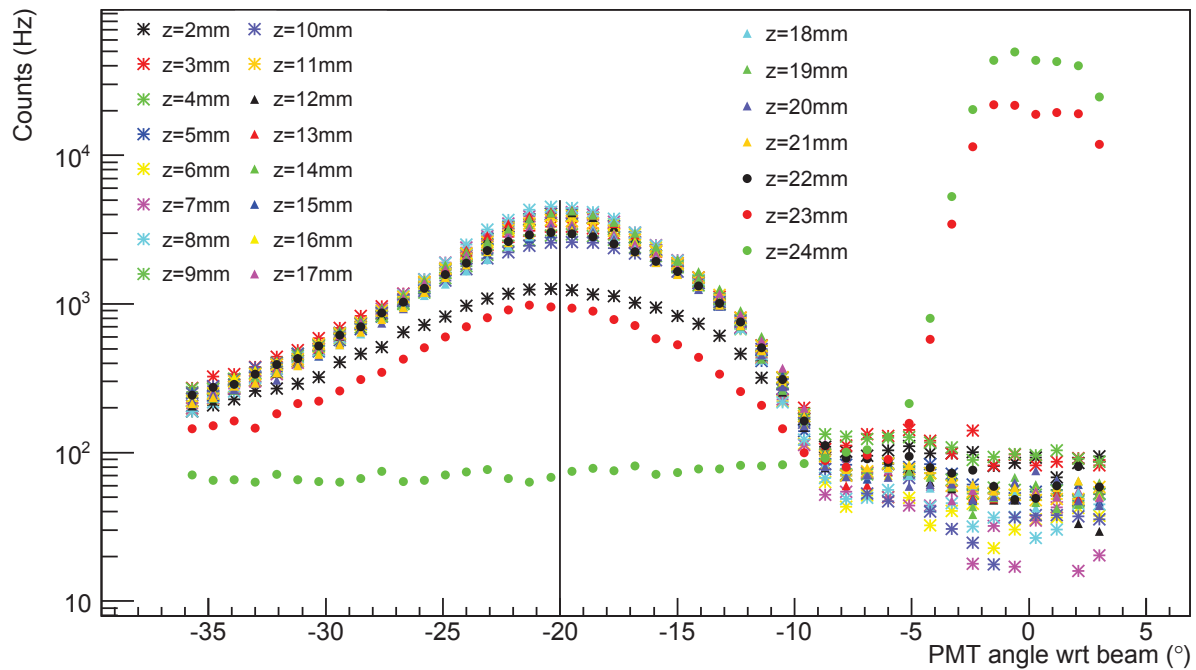


Figure 6.25: Raw data from the teflon positioned at  $80^\circ$  incident angle over the entire height of the teflon. Logarithmic scale.

Finally, as scanning the whole sample is scanning over five different thicknesses, it can be inferred that there is no clear pattern of a dependence of the specular reflectivity on the thickness, at least not at such scales. Further analysis is thus required.

To do so, figure 6.24 is plotted again but in a different set of coordinates. Each one of the curves in figure 6.24 is fitted by a gaussian and their maximum amplitude is plotted as a function of  $z$ . The result is shown in figure 6.26.

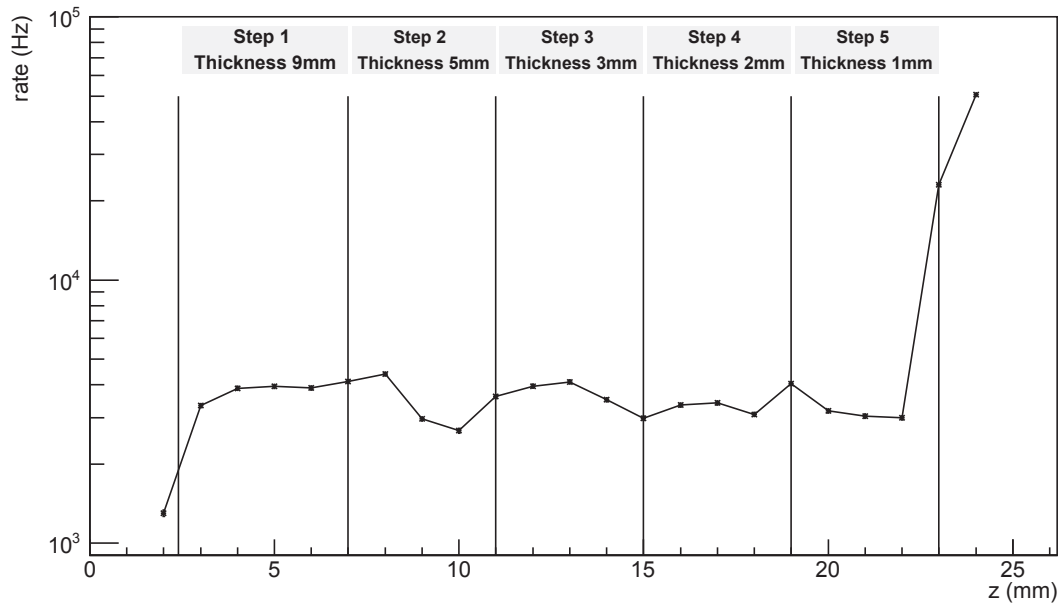


Figure 6.26: Rate of the specular component as a function of the vertical position of the sample for an  $80^\circ$  incident angle.

At  $z=2$  mm, the beam is starting to hit the black holder thus explaining the onset of a decrease in rate. On the contrary, at  $z=23$  mm half of the beam is now passing below the teflon and is not blocked anymore leading to a drastic rate increase. Following this logically, at  $z=24$  mm the full beam is unblocked by the teflon leading to a maximum rate where the PMT is aligned with the beam, which is completely compatible with the results found in section 6.4.2. Between  $z=2$  and  $z=23$  mm, the rate distribution is essentially flat thus meaning that there is no drastic intensity change when changing the teflon thickness. To try and quantize the amount of change, if any, a zoom between  $z=4$  and  $z=22$  mm is performed as shown on figure 6.27, which allows to note a few interesting features.

First there is a general trend where the intensity decreases as  $z$  increases, so with decreasing teflon thicknesses. Second, the points lying on the vertical lines should not be considered as they lay right at the intersection of two steps, thus making the reflection process unreliable. In addition, the machining of the teflon steps occurred around these points which might have induced some stress on

the teflon, thus further changing its reflectivity. Third, while the three central values of step 1, step 4 and step 5 are rather constant it is not the case for step 2 and 3. Step 2 especially is a puzzling case, as there is a big intensity drop visible above 8.5 mm. This effect has no physical explanation and so has to be due to an artifact of the teflon, either the sample is dirty in this place, or it is bumped or damaged. Step 3 doesn't show such a drastic drop but its behavior is also not as constant as the others, however this could simply be due to rather large statistical fluctuations.

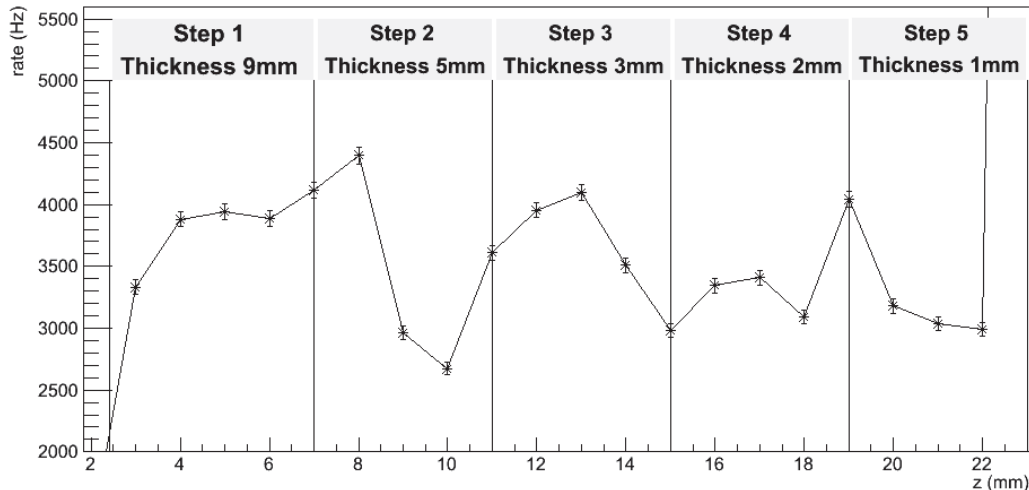


Figure 6.27: Zoom of figure 6.26

Assuming that the teflon presents no defect, the three center values of each step would be expected to yield equal intensity. As was shown, this is not the case so a more precise analysis of this has to be conducted to come to a conclusion which would assign one rate value to one thickness.

For this purpose, the intersection points between two adjacent thicknesses are neglected for the reasons mentioned above. Additionally, the average rate of all the points in a step is calculated, as well as the uncertainty  $\Delta$ , which is related to the standard deviation  $\sigma$  by  $\Delta = \sigma/\sqrt{n-1}$ , with  $n$  the number of points. The result can be seen in figure 6.28. Clearly, there is an increase of rate as the thickness of the teflon increases. Between 1 mm and 9 mm thickness, the rate increases by roughly 26%. However, because of the big uncertainty for steps 2 and 3, precise modeling proves to be rather difficult.

To try to now characterize a bit more the shape of the distribution, the data is fitted with a saturation curve according to equation 6.6 where  $A$  is the saturated rate at largest thickness and  $l$  is the thickness scale of the plateau.

$$f(x) = A(1 - e^{-x/l}) \quad (6.6)$$

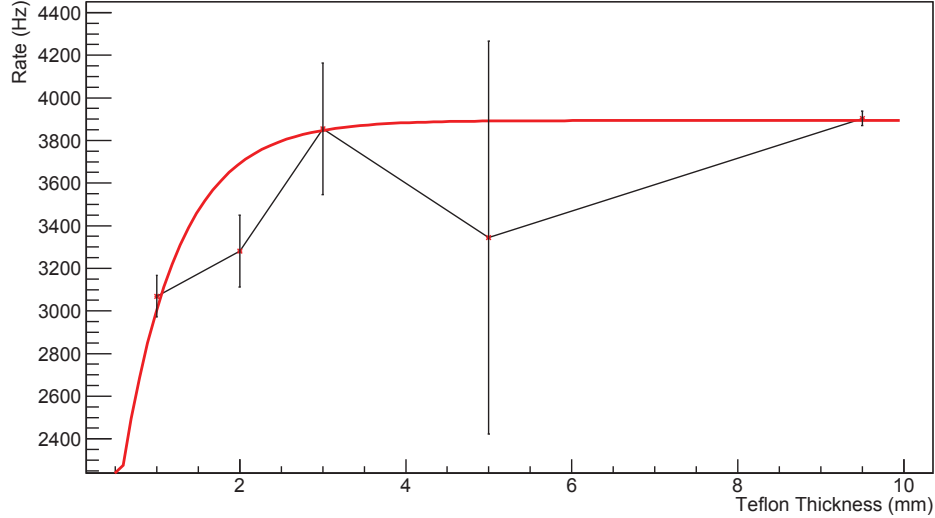


Figure 6.28: Rate versus thickness of the sample for  $80^\circ$  incident angle.

The fit gave results of  $A = 3893 \pm 33$  Hz and  $l = 0.675 \pm 0.053$  mm, with a reduced  $\chi^2$  of 2.25. While the fit is rather poor, it is possible to determine, at least roughly, the impact of the thickness on the specular reflection at  $80^\circ$  incident angle. From figure 6.28 it is clear that for a thickness greater than 3 mm, there is no visible change in the specular reflectivity. When using this value of 3 mm in equation 6.6, a 1% rate loss is expected. As comparison, a thickness of 2 mm would mean a rate loss of 5% from the rate saturation value. Because of the big uncertainties which are superior to 5% and the lack of more data points, a 2 mm thickness could be considered having no impact on the specular reflection at  $80^\circ$  incident angle, however, in order to be conservative, no thickness below 3 mm will be recommended for the thickness of the XENON1T TPC.

### ***70° incident angle***

To try and confirm the conclusions of the above section, the same analysis is redone for an incident angle of  $70^\circ$  as shown on figure 6.29.

This time, data is not taken at each z position but only once per step, at the centermost z position of each step. This is the case except for step 2, where the center position would put us in the dip where the teflon has a problem. So the data are taken at  $z=8.5$  instead of  $z=9$  mm. Following the same argument, data are taken at  $z=14$  mm instead of  $z=13$  mm for step 3. As for the error, the relative errors found in the above section which takes into account the spread of the points distribution over the whole width of each step, are simply applied to each point.

The resulting plot and a fit using equation 6.6 can be seen on figure 6.30.

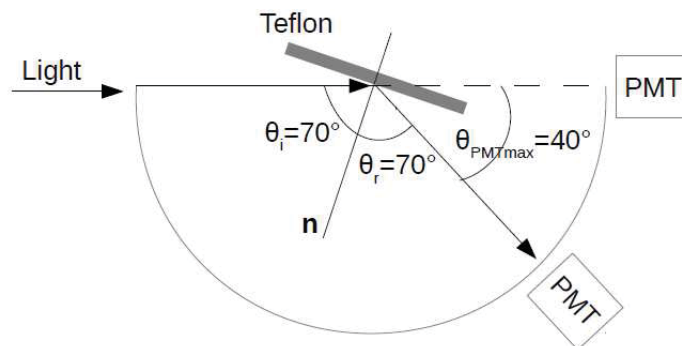


Figure 6.29: Sample position and specular reflection for  $70^\circ$  incident angle.

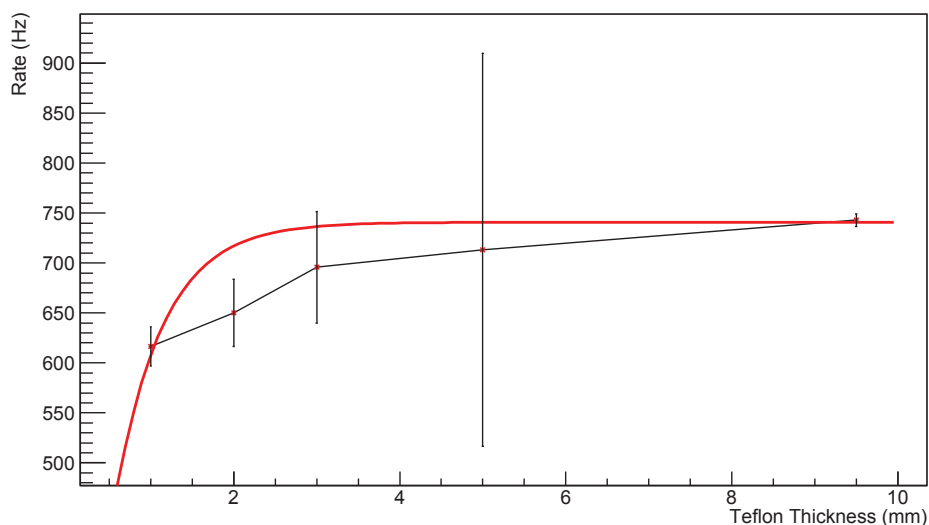


Figure 6.30: Rate versus thickness of the sample for a  $70^\circ$  incident angle

The fit gives values of  $A = 741 \pm 6$  Hz and  $l = 0.582 \pm 0.052$  mm, with a reduced  $\chi^2$  of 1.61. While this is a better fit than for the  $80^\circ$  incident angle, it is still not an excellent description of the data. However, once again, the figure shows an increase of about 20% in the rate between a thickness of 1 and 9.5 mm, and the length scales from the two fits agree within the errors, thus confirming the choice of 3 mm thickness for the XENON1T TPC.

### Conclusion

The large error on the specular reflection amplitude, and the limited amount of data do not allow for a precise model of the influence of the teflon thickness on the reflectivity. However, there is a clear indication that the teflon thickness has an influence on the specular component of the reflectivity. This can be further seen by the 20% difference in rate between a thickness of 1 mm and a thickness of 9.5 mm of teflon for both  $80^\circ$  and  $70^\circ$  incident angles. However, based on the relatively flat behavior

of the specular reflection for thicknesses above 3 mm, and the fit values for the length scale from equation 6.6 of  $l = 0.675$  mm and  $l = 0.582$  mm, it is clear that a teflon thickness of at least 3 mm is necessary to avoid losses of specular reflection. Consequently, it is advised to use a teflon thickness certainly no less than 3 mm for the XENON1T TPC.

Another important piece of information which can be inferred from this study is that even small deformities in the teflon can lead to big effects on the reflectivity, sometimes even bigger than the ones due to a change of thickness in the teflon. Consequently, very special care and attention should be given to the machining of the teflon rather than solely focusing on the teflon thickness.

#### 6.4.4 Full Transparency of the teflon

While it has been shown that the thickness of the teflon impacts the specular reflectivity, whether this is due to a full transparency of the teflon needs to be investigated. For this purpose, a very simple test is performed. The teflon is positioned as shown on figure 6.31, perpendicular to the beam and in a way that the beam is completely blocked in order to see if any light passes through the teflon. Results are shown in figure 6.32. There are no visible features but only a flat background at a level of  $16 \pm 3$  Hz. However to fully conclude on the transparency of the teflon, this number must be compared to the background level taken when no teflon is present. Indeed, there still may be some uniform isotropic transmission of light through the teflon which would lead to a still flat but higher background level. The unbiased background level had already been measured during the beam spot calibration where data was taken with the sample completely out of the way of the beam. Figure 6.14 indeed showed that the background level was around 17 Hz. This value is completely compatible with the results from the transparency measurement, thus indicating that no sizable amount of light was transmitted through the teflon even at a thickness of 1 mm. Thus, there is no clear indication that there is a full transparency of the teflon, at least for light passing directly through the teflon along the incoming beam direction. To fully investigate this, it would be necessary to look for light coming out in a diffuse pattern in the full solid angle behind the teflon, but this would require a much lower background to make a quantitative statement.

#### 6.4.5 Reflectivity of the teflon

A full reflectivity model of teflon is now investigated. For this purpose, data is taken at each step of different teflon thickness for different incident angles. Unfortunately, because the PMT does not run all around the chamber and stops at an angle of  $150^\circ$  from its alignment position with the beam,

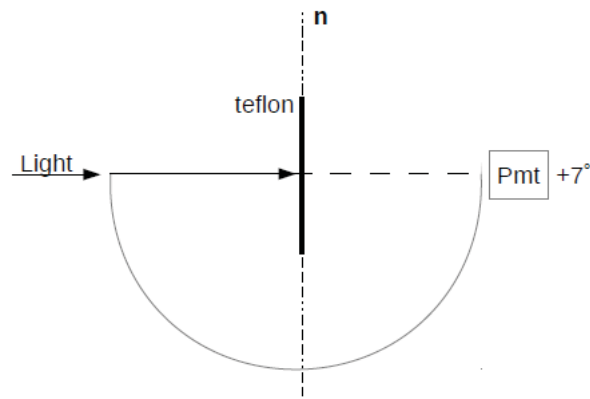


Figure 6.31: Diagram of the setup for full transparency measurements

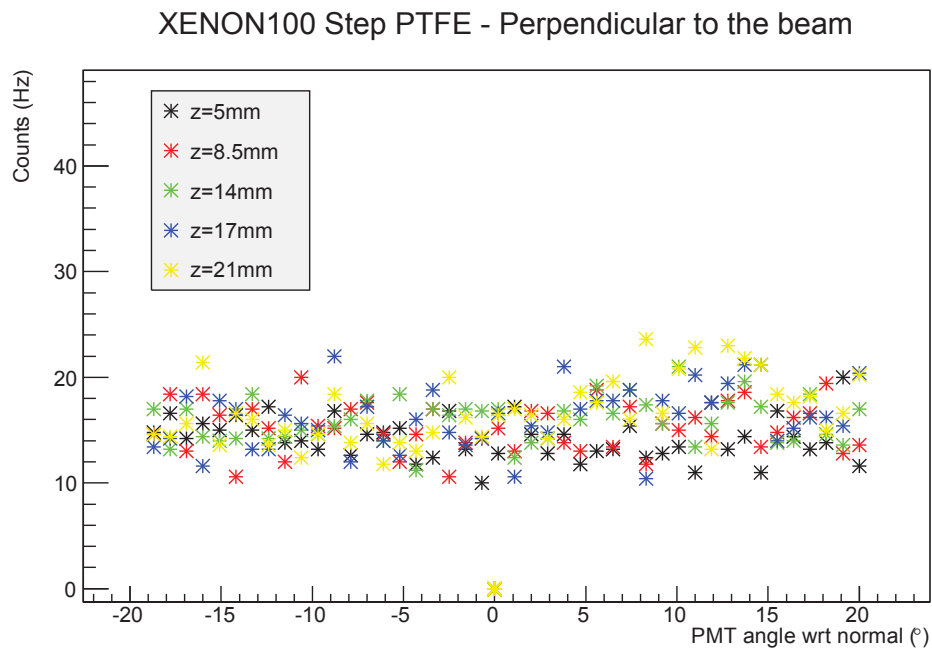


Figure 6.32: Full transparency

only incident angles  $\theta_i$  higher than  $20^\circ$  can be probed, since the specular peak must lie within the scanning range.

### *Analysis Method*

*Fitting the Data* The first step to fully analyzing the data is to be able to fit it. For this purpose, a model must be constructed which will describe the data appropriately. This model must have two components, one for the specular reflection and one for the diffuse reflection. The goal is thus to find a function of the type of equation 6.7 which will depend on four variables only, two incident angles  $\theta_i$  and  $\phi_i$  and two reflection angles  $\theta_r$  and  $\phi_r$ . Although, as already mentioned, the measurements presented here do not utilize a tilt angle, thereby restricting measurements to the plane of reflection

where  $\phi_i = \phi_r = 0$ , the model is developed to account for these angles should such measurements be made. In this equation,  $F_1$  and  $F_2$  are two independent functions describing the specular and diffuse components respectively.

$$F(\theta_i, \phi_i, \theta_r, \phi_r) = F_1(\theta_i, \phi_i, \theta_r, \phi_r) + F_2(\theta_i, \phi_i, \theta_r, \phi_r) \quad (6.7)$$

A more intuitive description of these angles is shown on figure 6.33. Also note that the x, y and z coordinate are not the same as in the previous section but are now the reference coordinates of the teflon with the teflon normal on the z-axis as represented on figure 6.33.

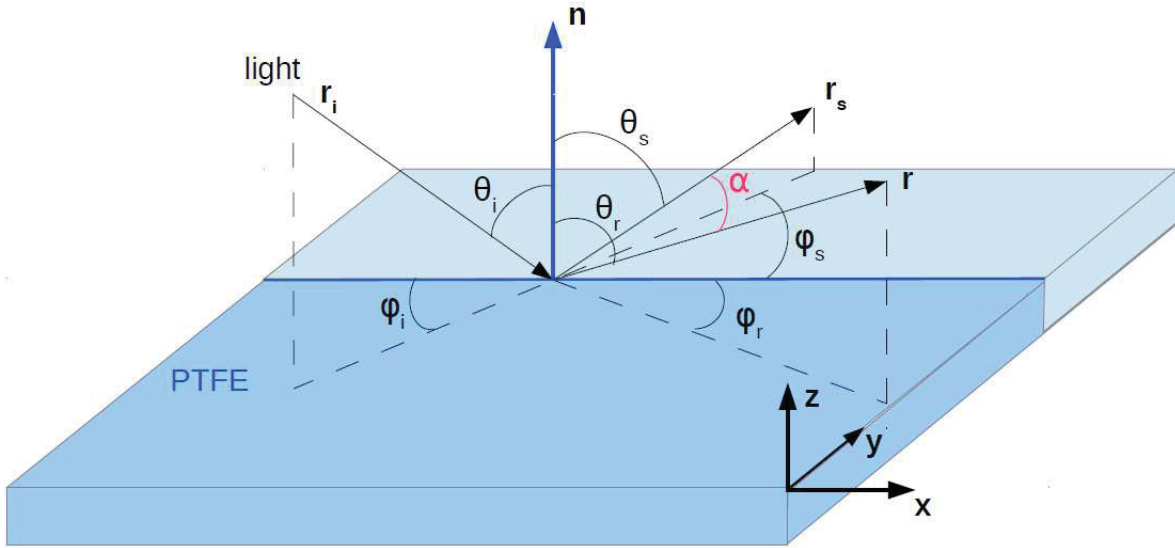


Figure 6.33: Diagram showing the important scattering angles in the reflectivity process.  $\mathbf{r}_i$  represents the incident beam,  $\mathbf{r}$  the direction of the reflected beam,  $\mathbf{r}_s$  the direction of perfect specular reflection and  $\alpha$  the spread angle between  $\mathbf{r}_s$  and  $\mathbf{r}$ .

With this in mind, the functions  $F_1$  and  $F_2$  must now be described, starting with the diffuse function  $F_2$ .

According to Lambert's cosine law, the diffuse component of a reflection is directly proportional to the cosine of the angle between the observer's line of sight and the surface normal, in this case  $\theta_r$ . Lambertian diffuse reflection is independent of both  $\theta_i$ ,  $\phi_i$  and  $\phi_r$ , but since the data show a dependence of the amplitude of the diffuse reflection on the incident angle, as will be shown later, the model is modified to account for this and  $F_2$  can thus be rewritten as:

$$F_2(\theta_i, \phi_i, \theta_r, \phi_r) = R_2(\theta_i) \cos(\theta_r) \quad (6.8)$$

where  $R_2(\theta_i)$  describes the intensity of the diffuse component as a function of incident angle.

The case of the specular component is a bit more complicated. The first step is to find out the shape of the function  $F_1$ . A realistic specular reflection is usually described by a peak with a finite width about the direction of perfect mirror-like specular reflection, such as a two dimensional gaussian distribution. It becomes then logical that  $F_1$  should also follow a gaussian distribution.

Indeed, because the beam is not point like [99] but is spread out, it gives a spread in specular reflected angle distributed as a gaussian. Additionally, the microspheres mentioned in section 6.1 give rise to an additional smearing of the specularly reflected beam. These effects need to be taken into account. Calling this new spread angle  $\alpha$  (see figure 6.33), the function  $F_1$  describing the specular component of a reflection becomes:

$$F_1(\theta_i, \phi_i, \theta_r, \phi_r) = R_1(\theta_i)e^{(-\frac{\alpha^2}{2\sigma^2})} \quad (6.9)$$

where  $\alpha$  is the angle with respect to the direction of perfect specular reflection and is function of  $\theta_i$ ,  $\phi_i$ ,  $\theta_r$  and  $\phi_r$ .  $\alpha$  should then follow a two dimensional gaussian with a mean of zero and a width of  $\sigma$ , where the assumption of symmetry in the two dimensions around the direction of perfect specular reflection has been made.

The angle  $\alpha$  now needs to be derived as a function of  $\theta_i$ ,  $\phi_i$ ,  $\theta_r$  and  $\phi_r$ . Figure 6.33 shows how  $\alpha$  is related to the incident beam described by the vector  $\mathbf{r}_i$ , the direction of reflection described by the vector  $\mathbf{r}$ , and the direction of perfect specular reflection described by the vector  $\mathbf{r}_s$ . Here  $\alpha$  is the angle between  $\mathbf{r}$  and  $\mathbf{r}_s$ .

The parameterization of  $\alpha$  can be done in the reference frame of the teflon, where the z axis is on the normal of the teflon, but to analyze the data it must be parameterized in terms of the actual measurable angles given in a laboratory coordinate system. These angles are  $\theta_{tilt}$ , which is the angle of the teflon relative to the plane of the incident beam and the PMT,  $\theta_{PMT}$ , which is the rotation angle of the PMT around the vacuum chamber, and  $\theta_{rot}$ , which represents the rotation of the teflon so the angle of the teflon normal relative to the incident beam. An intuitive description of these three angles can be seen on figure 6.34.

The conversion is handled by a rotation matrix, which is derived in the appendix. The result of this is an expression for alpha in terms of  $\theta_{rot}$ ,  $\theta_{tilt}$ , and  $\theta_{PMT}$ .

$$\alpha = \arccos( \sin(\theta_s)\cos(\phi_s)\sin(\theta_{PMT}) + \cos(\theta_{PMT})[\sin(\theta_{tilt})\sin(\theta_s)\sin(\phi_s) + \cos(\theta_{tilt})\cos(\theta_s)] ) \quad (6.10)$$

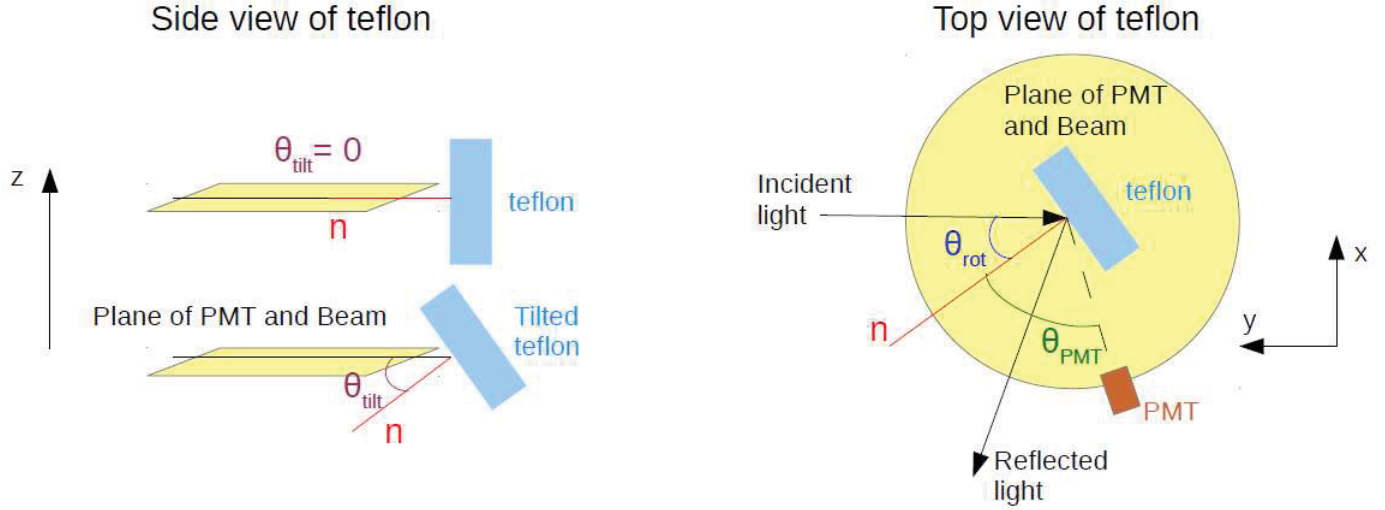


Figure 6.34: Diagram showing the three observable angles in the laboratory coordinates

with  $\theta_s$  and  $\phi_s$  given by,

$$\theta_s = \arccos[\cos(\theta_{tilt})\cos(\theta_{rot})] \quad (6.11)$$

$$\phi_s = \arctan\left(\frac{\sin(\theta_{tilt})\cos(\theta_{rot})}{\sin(\theta_{rot})}\right) \quad (6.12)$$

For the data presented here, another simplification can be made. Since no tilt angle was used,  $\theta_{tilt} = 0$ ,  $\theta_s = \theta_{rot}$ ,  $\phi_s = 0$ , and

$$\alpha = \arccos(\sin(\theta_{rot})\sin(\theta_{PMT}) + \cos(\theta_{rot})\cos(\theta_{PMT})) \quad (6.13)$$

Similarly, to be able to express  $F$ ,  $F_1$  and  $F_2$  as a function of these measurable angles, the incident angle  $\theta_i$  and the angle of observed reflection relative to the normal of the teflon sample  $\theta_r$  in equations 6.8 and 6.9 must be written in terms of laboratory variables.

According to the law of reflection from geometrical optics (mirror-like reflection),  $\theta_i = \theta_s$ . In addition, and as mentioned before, because  $\theta_{tilt}=0$ ,  $\theta_s = \theta_{rot}$ . Consequently:

$$\theta_i = \theta_s = \theta_{rot} \quad (6.14)$$

As for  $\theta_r$ , its derivation follows from the same coordinate transformations used for  $\alpha$  and is described in the appendix. The result is

$$\theta_r = \arccos(\cos(\theta_{tilt})\cos(\theta_{PMT})) \quad (6.15)$$

Again, since all measurements here have  $\theta_{tilt} = 0$ , this reduces to

$$\theta_r = \theta_{PMT} \quad (6.16)$$

Going back to the primary goal of establishing a function  $F$  describing the reflectivity of the teflon for the measurements presented here as a function of measurable angles, with  $\theta_{tilt} = 0$  and  $\alpha$  from equation 6.13, it can now be written that:

$$F(\theta_{rot}, \theta_{PMT}, \theta_{tilt}) = R_1(\theta_{rot})e^{(-\frac{\alpha^2}{2\sigma^2})} + R_2(\theta_{rot})\cos(\theta_{PMT}) \quad (6.17)$$

The model described by equation 6.17 is thus a 3D model of the reflection of light, and will be shown to be well suited to match the data.

In this function,  $\theta_{PMT}$  is the only variable (as the PMT moves constantly around the chamber) while  $R_1$  and  $R_2$ , which represent the intensity of the specular and diffuse component respectively, as well as the incident angle  $\theta_{rot}$  and of course the width of the specular distribution  $\sigma$ , are left as free parameters.

*Calculating the Reflectivity* The total reflectivity  $R_{Tot}$  of the sample can be calculated according to equation 6.18 where  $R_s(\theta_i)$  is the total intensity of the reflected light and  $R_0$  is the total intensity of the incident light, which can be measured by moving the teflon sample out of the way.

$$R_{Tot}(\theta_i) = \frac{R_s(\theta_i)}{R_0} \quad (6.18)$$

Calculating  $R_s$  requires to integrate the fit obtained from function 6.17 over a solid angle, while  $R_0$  requires the integration of the incident beam over a solid angle. However the spherical coordinate system needs to be taken into account. Following the notation of figure 6.33, the total light intensity  $R_s$  is thus

$$R_s = \int_0^{2\pi} \int_0^{\frac{\pi}{2}} (R_1 e^{(-\frac{\alpha^2}{2\sigma^2})} + R_2 \cos(\theta_r)) \sin(\theta_r) d\theta_r d\phi_r \quad (6.19)$$

In the case of a well localized specular peak, the dominant contribution to the specular term comes from a small solid angle about the peak. Thus, the contribution from the bottom hemisphere is negligible, and one can perform the integral in a rotated coordinate system with  $\hat{\mathbf{r}}_s$ , the direction

of perfect specular reflection, on the  $z$  axis.

$$R_s = 2\pi R_1 \int_0^\pi e^{-\frac{\theta''^2}{2\sigma^2}} \sin(\theta'') d\theta'' + 2\pi R_2 \int_0^{\frac{\pi}{2}} \cos(\theta_r) \sin(\theta_r) d\theta_r \quad (6.20)$$

where the double prime system is simply a change of coordinate where  $\hat{\mathbf{z}}'' = \hat{\mathbf{r}}_s$  on figure 6.33.

The solution to equation 6.19 is then

$$R_s = -\frac{\pi\sqrt{\pi}}{\sqrt{2}} R_1 \sigma e^{-\frac{\sigma^2}{2}} \left[ \operatorname{erfi}\left(\frac{\sigma^2 + i\pi}{\sigma\sqrt{2}}\right) + \operatorname{erfi}\left(\frac{\sigma^2 - i\pi}{\sigma\sqrt{2}}\right) - 2\operatorname{erfi}\frac{\sigma}{\sqrt{2}} \right] + \pi R_2 \quad (6.21)$$

where  $R_1$ ,  $R_2$  and  $\sigma$  are the parameters obtained from fitting F to the data and where for any complex number  $z$ , the complex error function  $\operatorname{erfi}$  is defined as:

$$\operatorname{erfi}(z) = -i\operatorname{erf}(iz) \quad (6.22)$$

Because the first two  $\operatorname{erfi}$  terms of equation 6.21 are much smaller than the third one, they can be neglected. Furthermore, to simplify equation 6.21, the Taylor series approximation to the error function can be used:

$$\operatorname{erf}(z) = \frac{2}{\sqrt{\pi}} z \quad (6.23)$$

This leads to the final solution to equation 6.19 :

$$R_s = 2\pi R_1 \sigma^2 e^{-\frac{\sigma^2}{2}} + \pi R_2 \quad (6.24)$$

Now that the analysis method has been layed out, the fitting function 6.17 can be applied to the data and the reflectivity can be calculated using equation 6.24.

### Raw Data

Measurements were taken with the light incident on the five different teflon steps at incident angles of 80, 70, 60, 50, 45, 40 and 30° from the normal of the teflon.

The raw data of the rate as a function of the PMT angle for the 5 mm thick step are shown on figures 6.35. The raw data for the other thicknesses look about the same and are consequently not shown here.

The peak due to the specular component seems to appear correctly at every angle, thus confirming that the data was taken with no major problem. The main feature from these plots is that the specular

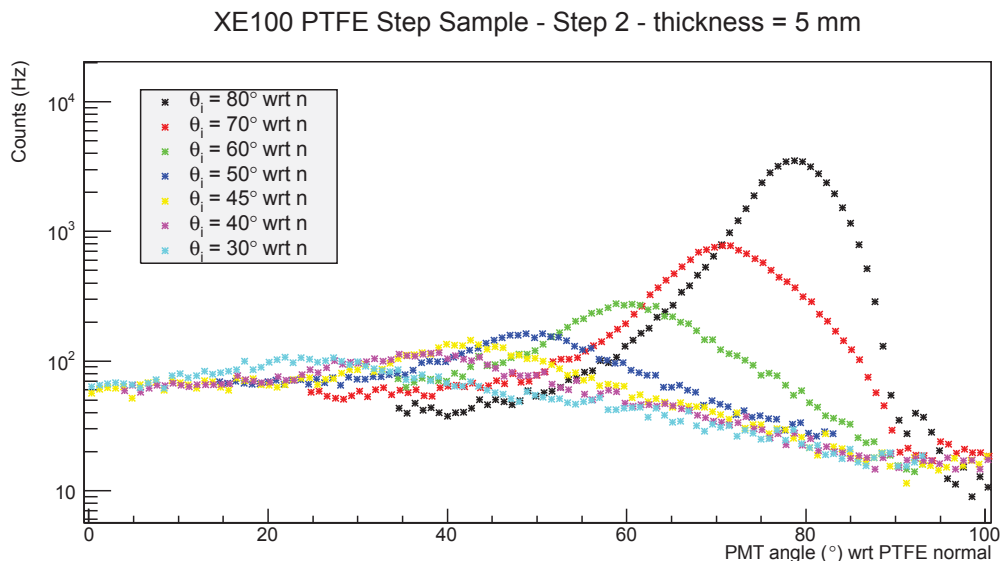


Figure 6.35: Raw data - Beam incident on the second (5 mm) teflon step.

component decreases with decreasing incident angle. The diffuse component decreases at the largest incident angles, as shown in the black and red curves. Note that it was not possible to take data beyond certain reflection angles due to restrictions with the setup, which is why all curves are not present near  $\theta_{PMT} = 0$ .

*Fit to the Data* Each curve of figure 6.35 are fitted independently with the function described by equation 6.17. In addition, the beam spot measurement with the teflon out of the beam (hence no reflection) is also fitted as, being a measure of the incident light intensity, it is used as normalization. The resulting fits can be seen on figure 6.36, with the fit parameters listed in table 6.2.

The errors on each data point of figure 6.36 come from the statistical uncertainty on the total number of counts for each data point, given by  $\Delta n = \sqrt{n}$ .

The reduced  $\chi^2$  values in table 6.2 show good agreement of the fits to the data for small incident angles. At the largest incident angles, the reduced  $\chi^2$  is much higher, mostly due to a non-gaussian tail in the specular peak. While this could be modeled by introducing an additional term in the fit function, the fact that the function describes the data very well at other incident angles led to the choice of keeping it as is.

For the normalization measurement, the reduced  $\chi^2$  of 683 shows the poor fit to a gaussian. This is due to the flattened top on the peak, more clearly visible on figure 6.14. This plateau is likely due to a saturation effect coming from the trigger logic used for the data which was not optimized to account for dead time. This issue will be addressed in the next chapter.

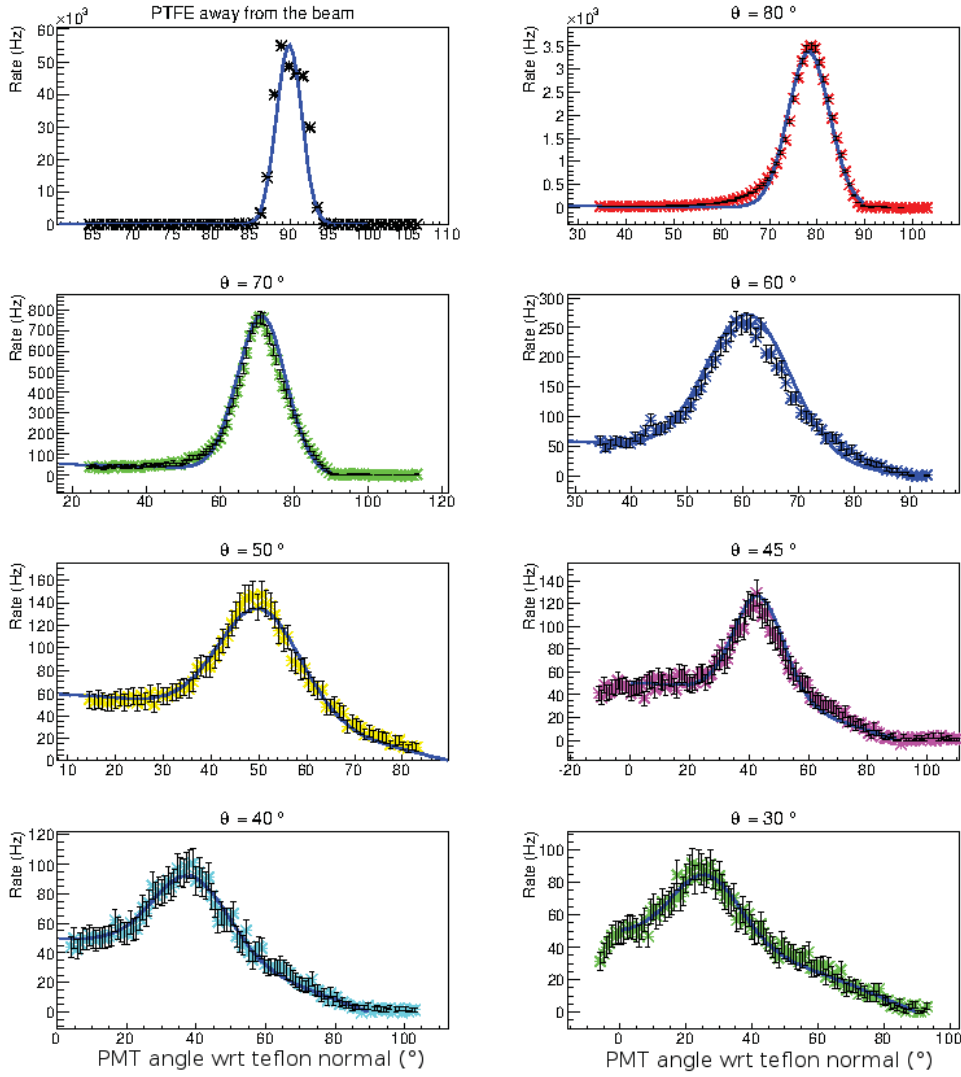


Figure 6.36: Fits on the background subtracted data - Beam incident on the 5 mm thick teflon step. From left to right, top to bottom: normalization,  $\theta_i=80, 70, 60, 50, 45, 40, 30^\circ$

$\theta_i$ ( $^\circ$ )	R1	R2	$\sigma$	Reduced $\chi^2$
	$5.5 \cdot 10^4 \pm 1.428$		$-0.02804 \pm 2.453 \cdot 10^{-5}$	683
80	$3365 \pm 21.84$	$40 \pm 0.07429$	$0.07599 \pm 0.0003343$	38
70	$750 \pm 0.3828$	$57.54 \pm 1.538$	$0.1139 \pm 0.0007701$	5
60	$240 \pm 0.2845$	$66.51 \pm 3.84$	$0.1314 \pm 0.003067$	1.7
50	$96.55 \pm 3.431$	$59.39 \pm 2.05$	$-0.1508 \pm 0.006268$	1.05
45	$90 \pm 0.3002$	$50.18 \pm 1.483$	$-0.1469 \pm 0.006123$	0.85
40	$53.34 \pm 2.664$	$49.48 \pm 2.228$	$0.188 \pm 0.0136$	0.74
30	$40.59 \pm 2.711$	$48.99 \pm 2.067$	$0.1768 \pm 0.01768$	1.05

Table 6.2: Parameters values of the fits corresponding to figure 6.36 (5 mm thick step). The top line is for the normalization measurement of the incident light with the teflon sample out of the way.

Again, while only shown for one thickness, this procedure is applied to all measurements for all different teflon thicknesses.

*Reflectivity* According to [30], the predicted model for teflon reflectivity at 175 nm is as shown on figure 6.37. While this particular model works at 175 nm, it should in principle be close enough to allow for comparison with data at 178 nm.

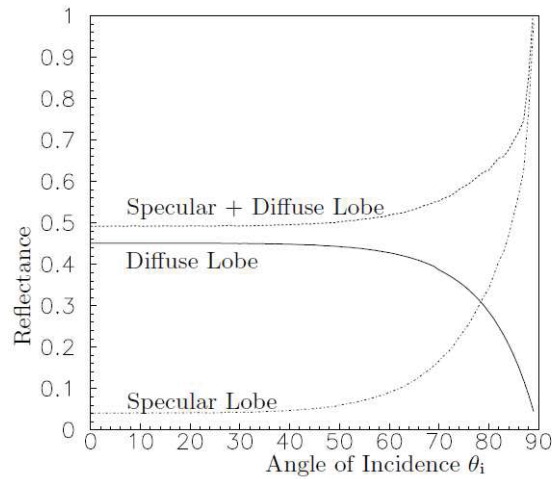


Figure 6.37: Reflectivity model on unpolished molded teflon at 175 nm [30].

Using the fit parameters corresponding to all the fits to the data from all teflon thicknesses, amongst which figure 6.36 and table 6.2 are an example, and applying equation 6.24, the total, specular and diffuse reflectivities for each incident angles and for each teflon thickness can be computed. The resulting total reflectivity as well as specular and diffuse components are shown on figures 6.38, 6.39, 6.40, 6.41 and 6.42.

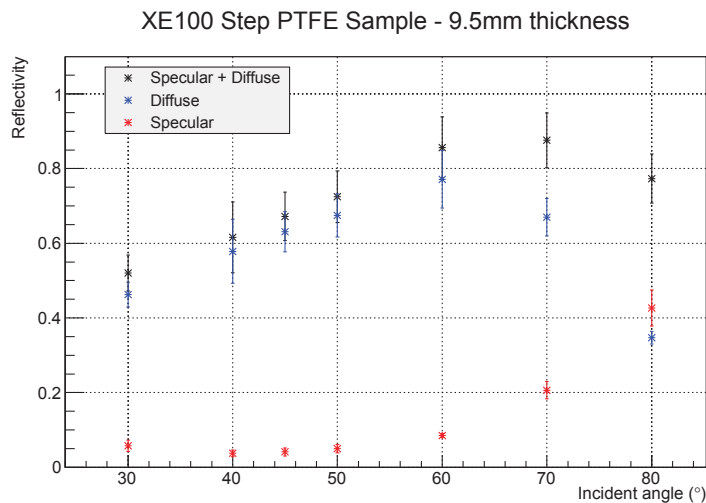


Figure 6.38: Total, specular and diffuse reflectivities of the 9.5 mm thick teflon.

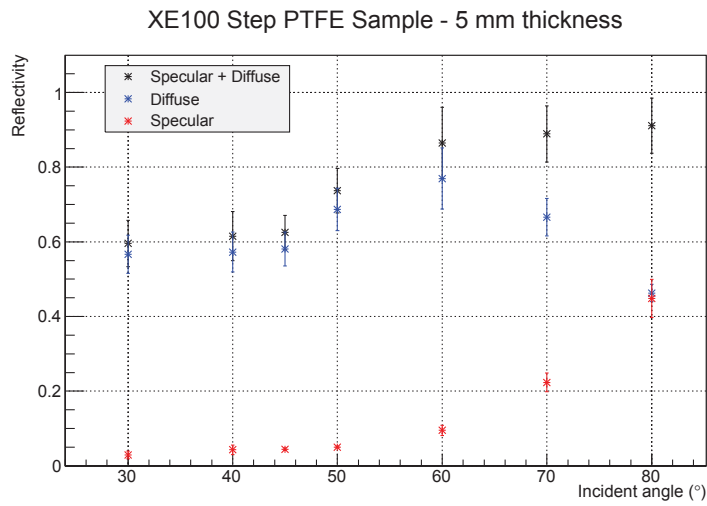


Figure 6.39: Total, specular and diffuse reflectivities of the 5 mm thick teflon.

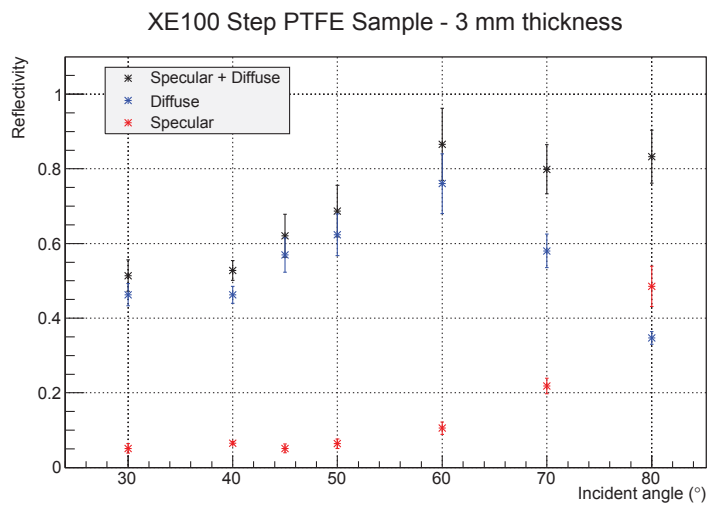


Figure 6.40: Total, specular and diffuse reflectivities of the 3 mm thick teflon.

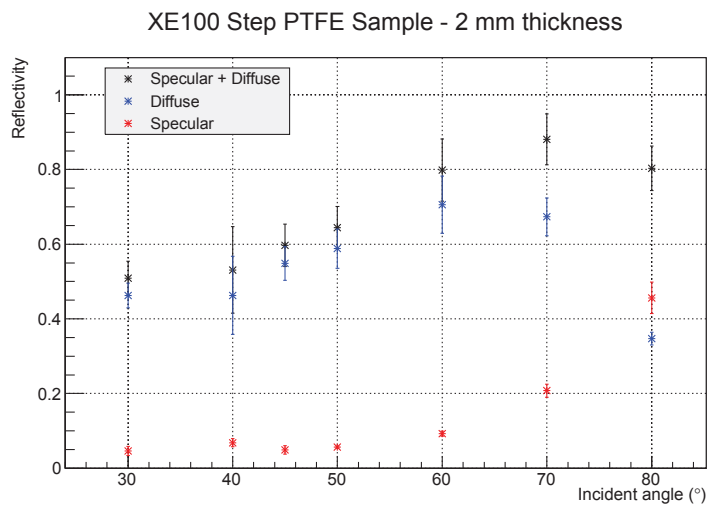


Figure 6.41: Total, specular and diffuse reflectivities of the 2 mm thick teflon.

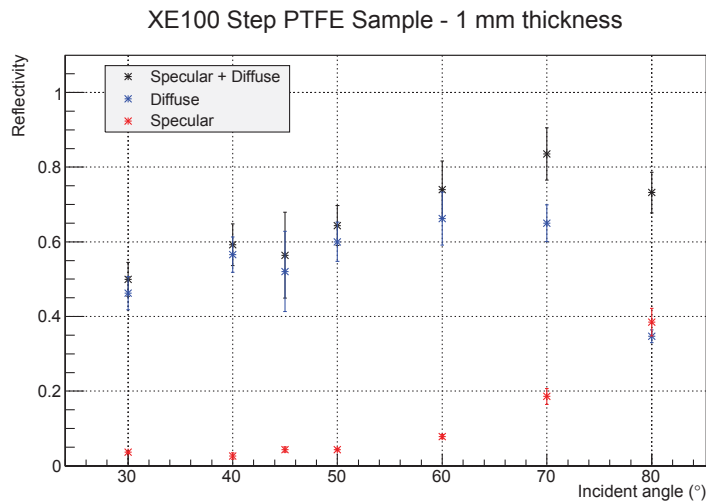


Figure 6.42: Total, specular and diffuse reflectivities of the 1 mm thick teflon.

In all figures 6.38, 6.39, 6.40, 6.41, 6.42 the specular component follows the predicted model from figure 6.37. However, the diffuse component varies slightly as a function of incident angle. Indeed there seems to be a peak in the reflectivity at a  $60^\circ$  angle. The reason for this behavior is uncertain. The fact that it happens at the same point for all teflon thicknesses maybe points to a teflon machining issue, however this is hard to ascertain considering that the exact machining conditions of the sample are unknown.

Finally, integrating over the solid angle to find the average reflectivity for each thickness, figure 6.43 is obtained.

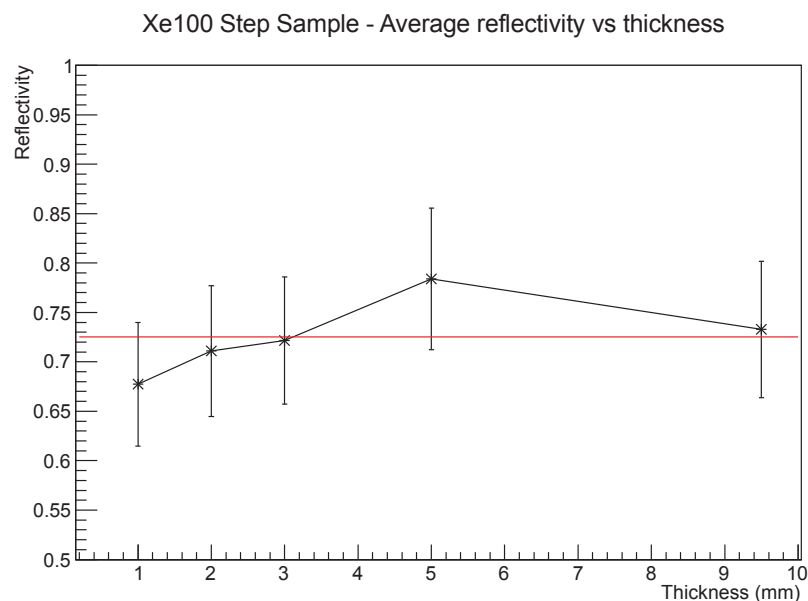


Figure 6.43: Average reflectivity of the Xe100 step sample as a function of the thickness of the sample.

The red line is not a fit but a simple average of the data leading to a total average reflectivity of  $73 \pm 7\%$ . While there seem to be an increase as the thickness increases, the error bars are too large to make such a statement and allow only to say that changing the thickness of the teflon does not affect the reflectivity by more than 10%. Comparing figure 6.43 and figure 6.30, the same trend is observed with the reflectivity dropping slightly below 3 mm thickness, making both analyses consistent with one another.

*Comparison with Monte-Carlo based Analysis Method* In [99], a completely different analysis method was used to obtain the reflectivity of teflon in vacuum. This analysis method, based on MC and whose complete description can be found in [99], was applied to the data of this study in order to compare the results and check that both analyses yield the same result, as should be the case.

Both reflectivities are shown on figure 6.44. Note that this MC based analysis was not optimally tuned to this data but to first order, it can be seen that both analyses are completely consistent with one another, thus making the results of this study robust.

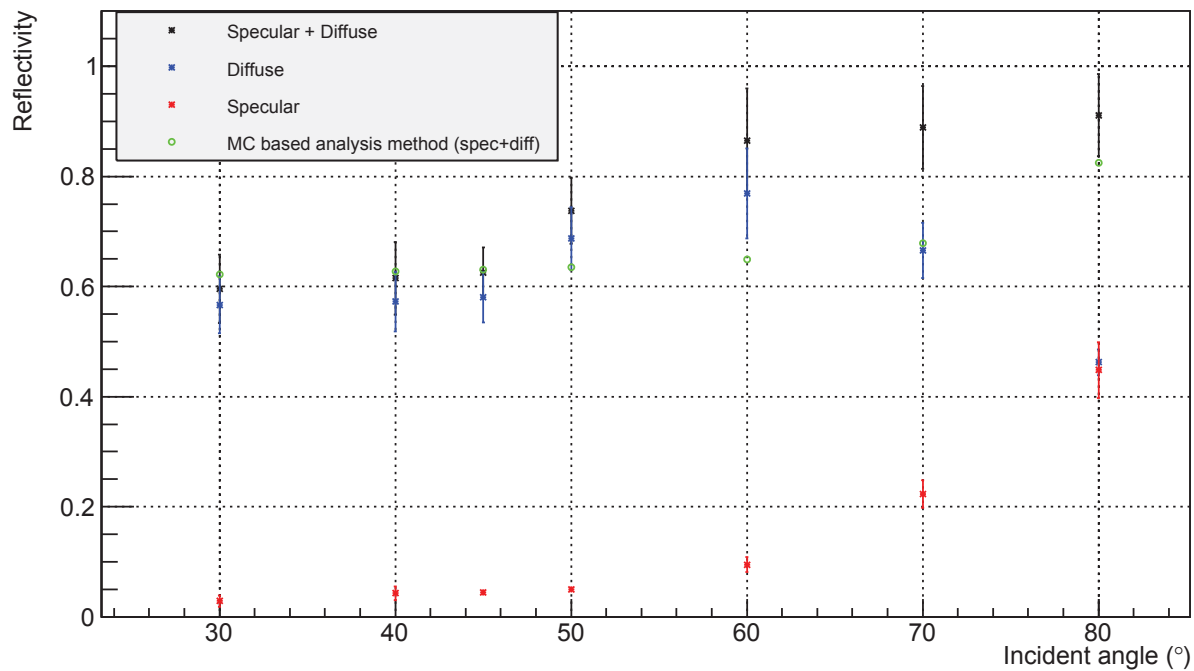


Figure 6.44: Comparison of the output of both analysis methods to the data

### 6.4.6 Conclusion

The reflective properties of VUV light off of a teflon sample taken directly from the batch used for the XENON100 experiment have been investigated. The overall reflectivity of the teflon has been estimated to be  $73 \pm 7\%$  and is completely compatible with the results found in [99]. This number seems to depend only relatively weakly on the thickness of the sample with a maximum change of 26% for an 8.5 mm difference in thickness. To come to a conclusion an analysis based on the amplitude of the specular reflection at  $80^\circ$  and  $70^\circ$  incident angles was performed. It resulted in a reduction of 20% for a 1 mm thickness compared to a 9.5 mm teflon thickness, however it did not take into account the diffuse component of the reflectivity, which could have an impact on the result. Fits to the amplitude as a function of thickness were used to determine that a teflon thickness of 3 mm is necessary to avoid losses in specular reflection at high incident angles. This led to the conclusion that for XENON1T, the teflon to be used in the TPC should have a thickness greater than 3 mm.

Additionally the transparency of the teflon was investigated, and no indication of transparency was seen by looking for light that shines directly through the sample in the direction of the incident beam. This conclusion holds even for a sample with thicknesses as low as 1 mm, but this measurement was background limited. A full study that would account for the transmitted light following a diffuse pattern would not be possible with this setup.

One last important feature to remember is that the reflectivity seems to vary substantially with any type of impurities, damage or non-uniformity within the teflon and that very special care should be taken when machining the teflon. This was shown by the reduction in reflectivity that was seen at particular locations on the teflon sample.





# Chapter 7. TEFLON REFLECTIVITY STUDIES IN LIQUID XENON



*Piled Higher and Deeper* by Jorge Cham [www.phdcomics.com](http://www.phdcomics.com)

## 7.1 Introduction and Motivation

As already introduced in the previous chapter, it is necessary for the XENON1T experiment to study the reflectivity of teflon. While in the previous chapter conclusions on the necessary thickness and on the reflectivity of teflon in vacuum were obtained, this is not enough for the needs of the experiment. Indeed, like for XENON100, in XENON1T the whole reflection process will happen in liquid xenon where it could be very different than in vacuum for several reasons. First, xenon is known to be a good detergent, and the liquid xenon can fill the holes of the porous structure of the teflon surface and dissolve impurities from the surface. Second, liquid xenon has a high index of refraction of  $n = 1.69$ , which closely matches the index of refraction of teflon. This should also have an impact on the way light travels at the uneven surface of the teflon, and likely has an impact on the reflectivity. Consequently, to investigate this, the vacuum reflectivity setup has been adapted to perform the same reflectivity measurements but this time, in liquid xenon (LXe).

## 7.2 The Setup in Liquid Xenon

The setup principle remains almost entirely the same. A deuterium lamp attached to a monochromator is set to emit 178 nm UV light. The light then passes through a converging lens and a collimator

to finally reach a sample of teflon and reflect off of it while a PMT turns around the teflon to detect the reflected light at different angles. However, now the teflon is not held by an anodized holder (see section 6.3) but is instead placed in a quartz tube filled with LXe. This is schematized in figure 7.1.

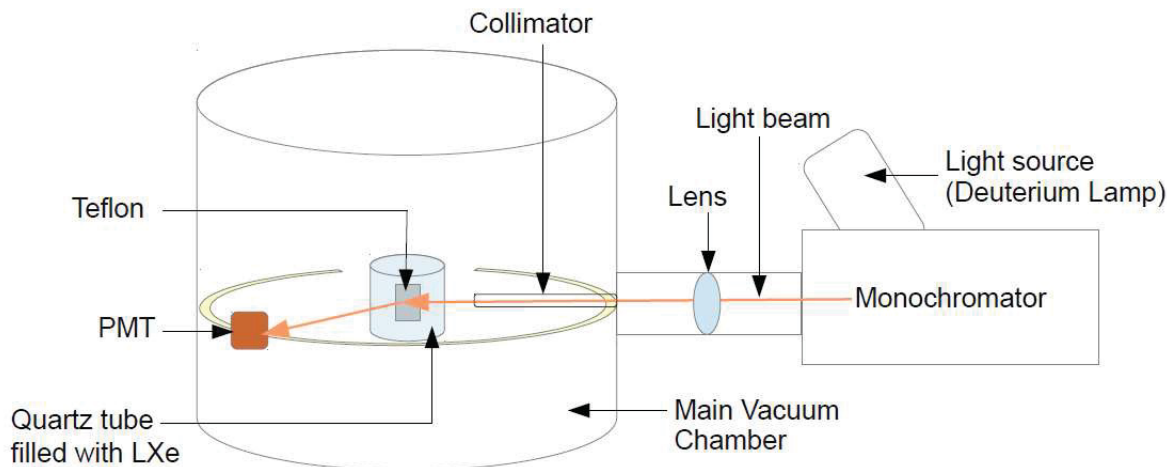


Figure 7.1: Principle of the reflectivity setup

The quartz tube itself is positioned between the PMT and the collimator, just like the teflon was for the setup under vacuum. And just like the teflon used to be, the quartz tube is movable in the vertical direction  $z$  in order to be able to put the teflon in or out of the path of the light and measure the incident beam intensity. The quartz tube is attached to a liquefaction assembly and gas system which allow to fill it with gas xenon and then liquefy this gas into LXe. The liquefaction assembly itself is attached to the top flange and takes the place of the previous rotational and translational feedthrough of the teflon. It is connected to the flange by a custom made rotational feedthrough which allows the whole liquefaction assembly to be turned. By turning the liquefaction assembly, the quartz tube and the teflon also turn, thus allowing to scan several incidence angles, just like the setup in vacuum. However, it was not possible to maintain the  $x$ - $y$  translational motion on this feedthrough, thus making the tube and teflon alignment a fixed position by design.

Both the teflon and the liquefaction assemblies are far from trivial and required inventive designing and extended testing, from choosing an optically flat and polished quartz tube, sealing it and filling it with LXe to being able to rotate and lift it all. Each of these steps will be carefully and extensively explained in the next sections.

However, before diving into more technical details, a few changes made to the vacuum chamber must be described. While, the vacuum chamber stays mostly the same, due to space restrictions, only one cold shield, the largest one which has now been blackened, is used instead of two. In addition,

a hole is drilled in the cold shield to coincide with one of the side flanges of the vacuum chamber. That side flange is blinded with a window which thus allows to see everything that happens inside the chamber, especially the quartz tube and the liquefaction process. When data taking is ongoing, to ensure that no external light is leaking to the setup, this window is capped with an opaque cover and a black blanket. Another small feature is the addition of two stoppers at the bottom of the cold shield. Their role is to prevent the PMT from ever hitting the collimator or the cold head when turning, as could happen before. Although small, this is a rather important feature as in the vacuum setup, the problem occurred that the PMT was turned too far, hitting and displacing the collimator in the process. With this small addition, this is no longer an issue. Finally, two temperature sensors PT100 are attached inside the chamber, one to the black shield and one to the PMT in order to constantly be able to monitor the internal temperatures of the setup.

The inside of the main chamber with these new features is shown on figure 7.2.

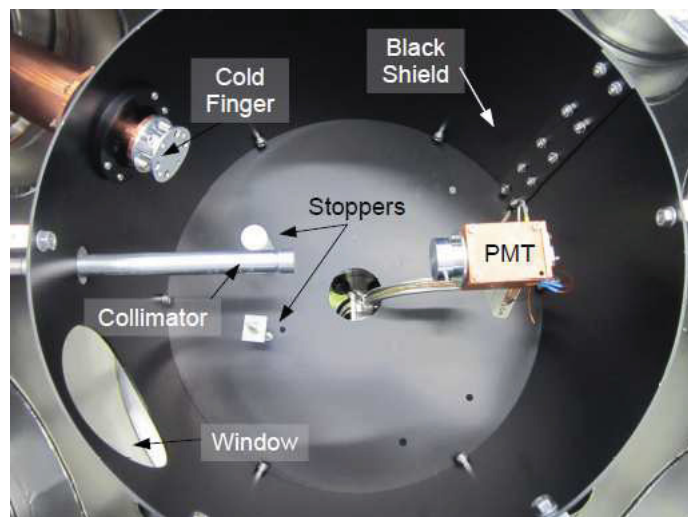


Figure 7.2: Inside the main chamber

As for the light assembly described in section 6.3.1, it stays exactly the same and thus will not be redescribed here.

### 7.2.1 The Tube in Liquid Xenon

As mentioned before, to take measurements in liquid xenon, the teflon is placed into a quartz tube which is sealed and filled with gas xenon which is then liquefied. To achieve this, a complex design was necessary as the tube must be completely isolated from the main chamber which is under vacuum, to be able to contain liquid xenon at pressures superior to 2 bar. In addition, the tube must be linked to a gas system to be able to receive and recuperate xenon gas and must also have its own

refrigeration system to cool down the xenon and liquefy it.

### Choice of the Tube

The selection of the material for the tube is of great importance. Indeed, the tube needs to be maximally transparent to UV light especially at 178 nm. It also needs to be thick enough and capable of withstanding several bars overpressure. Additionally, it has to be of excellent optical quality and polished. Consequently, to meet all these requirements, a synthetic quartz glass made of UV-grade fused silica purchased from QGH (Aachener Quarz Glass Technologie Heinrich) has been chosen. This special type of quartz is specified to have a very high transmission at 178 nm, of about 80% for 10 mm thickness as shown on figure 7.3.

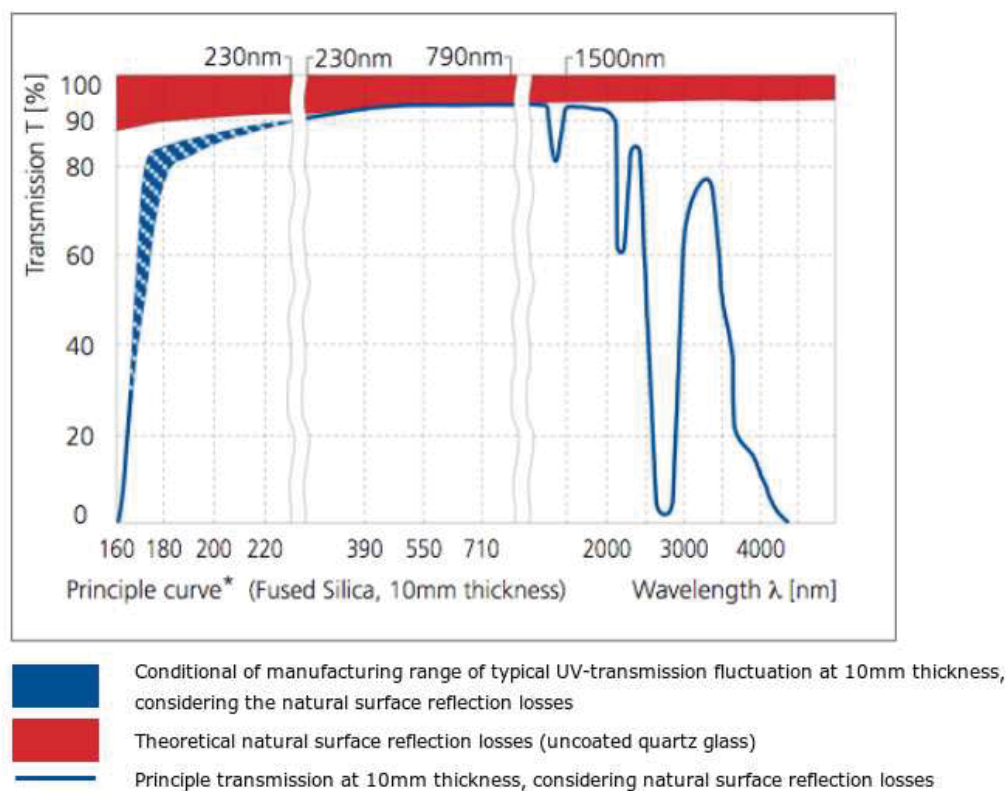


Figure 7.3: Light transmission for synthetic quartz glass made with UV-grade fused silica [31]

The quartz tube specification were tested by placing the quartz tube in the chamber, both chamber and tube under vacuum, and taking data by turning the PMT around the chamber with the light shining through the tube and below the tube. Note that this was done when the setup was not optimized yet, however for the purpose of this quick test, high precision calibration was not needed and this data will thus not be used anywhere else in this work. The result of such a test is shown on figure 7.4.

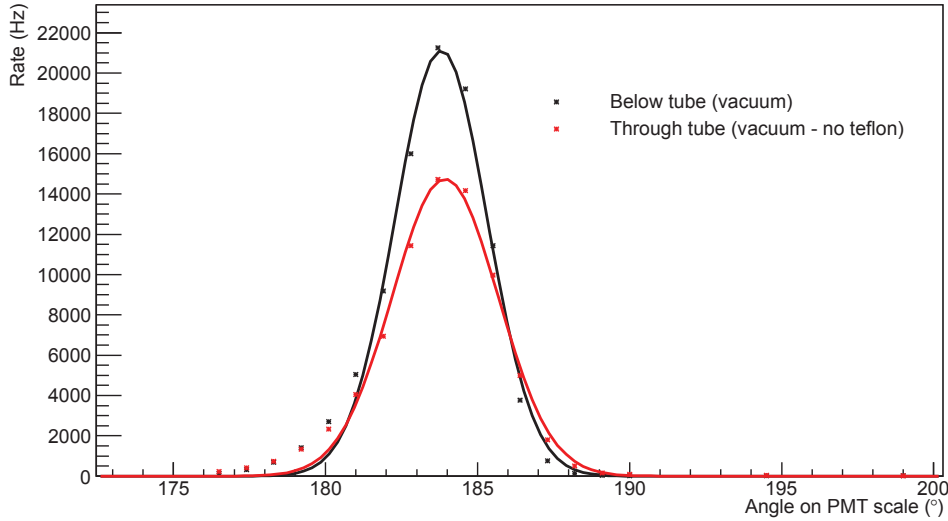


Figure 7.4: Effect of the quartz tube on the incident light

By integrating the gaussian fits of figure 7.4, it results that a 20% light loss occurs when shining the light through the tube, which is indeed what was specified from the company.

In addition, from a physics point of view, this light loss mostly comes reflection in the quartz and can be also calculated through Fresnel formula 7.1.

$$R = \left( \frac{n - 1}{n + 1} \right)^2 \quad (7.1)$$

Applying equation 7.1 and knowing that quartz has an index of refraction at VUV wavelengths of  $n = 1.6$ , the amount of light that reflects at one surface is  $R = 0.053$ , thus meaning that about 95% of the light is transmitted. Since the light crosses four surfaces, its intensity is decreased by a factor of about 0.80 when passing through the tube. Again, this is in perfect agreement with both the company specifications and the measurements.

### *Sealing of the Quartz Tube*

To seal the tube properly, it is inserted between two stainless steel flanges which are held with three rods evenly spaced by  $120^\circ$ . The leak tightness between the tube and the flanges is ensured by two viton o-rings. Additionally, the use of spring washers on the bottom flange allows for the system to remain leak tight even when the steel contracts from the cold during the xenon liquefaction process. The bottom flange is always tightened using a torque wrench with a torque of  $7N \cdot m$ . This sealing method was extensively tested and proven to be sufficiently leak tight by using a common glass tube

submerged in liquid nitrogen.

As for the teflon in the tube, it is held from the bottom edge by a set screw to an anodized black aluminum holder in order to avoid undesirable reflections. The holder is itself screwed at the bottom flange of the sealing assembly and was designed to avoid air pockets that could contaminate the xenon or serve as bubble nucleation sites.

The top and bottom flange as well as the final assembly are shown on figure 7.5.



Figure 7.5: The sealing of the quartz tube. Left: the top flange with the xenon supply and return lines welded to it. Middle: the bottom flange, with the holes to screw the teflon holder in place. Right: the final assembly with the tube sealed and the teflon and teflon holder inside

### *Xenon Filling and Liquefaction*

As can be seen on figure 7.5, the top flange of the tube has two lines welded to it. These two lines are used to fill or empty the tube with xenon gas. Attached to these lines, two 1/4 inch flexible lines connect to a feedthrough in a CF100 flange. On the other side of this feedthrough, two 1/2 inch flexible lines are linked to a gas system allowing the supply or recuperation of gas xenon. This gas system is not described in this work but can be found in [102].

To liquefy xenon, the gas must be brought to a temperature around  $-100^{\circ}\text{C}$ . The exact liquefaction point depends on the equilibrium xenon pressure but this is of no importance for these measurements. This liquefaction is achieved by connecting the tube to a cold head. The cold head used is a CRYOMINI Iwatani model PDC08 which has a cooling power of approximately 20 W at  $-100^{\circ}$ . The cold head is itself connected to a hollow copper tube which is in turn connected to the top flange of the tube sealing assembly which has a large hole in the center to allow xenon to pass between the quartz tube and the copper tube. Because of copper's extremely good thermal conduction, the liquefaction process happens when the xenon gas touches the walls of the now cold

copper tube. The temperature of the copper tube is constantly monitored by a lakeshore DT-670 silicon diode and read out by a lakeshore 336 temperature controller.

In addition, great care must be taken in this process as the tube cannot get too cold otherwise the xenon will solidify as shown on figure 7.6 which represents the phase diagram for xenon at the pressures and temperatures of interest.

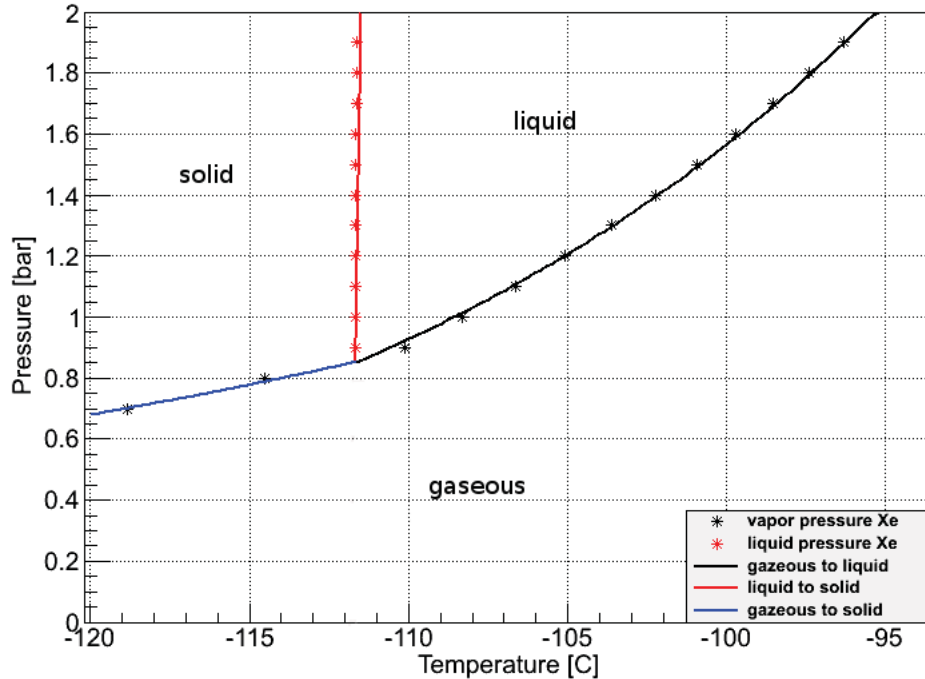


Figure 7.6: Xenon phase diagram [32]

Consequently the temperature of the xenon must be maintained stable. This is done by adding a 25 W heater into the side of the copper tube. The heater is then remotely and automatically controlled by the lakeshore 336 unit and is set to give more or less power depending on the temperature fluctuations, to keep the overall temperature stable within  $0.1^{\circ}\text{C}$ .

Figure 7.7 shows a photograph of the tube and liquid xenon assembly with all the relevant aforementioned features.

The xenon assembly which consists of the xenon lines, the hollow copper cold finger and the quartz tube, is filled by opening a valve to a xenon gas source at constant pressure. Once the xenon assembly is full of xenon gas, it is cooled down to start the liquefaction process. As the gas cools down and liquefies, the xenon density decreases and more gas enters the xenon assembly thus maintaining a constant pressure. Once the whole xenon assembly is homogeneously cooled down to a temperature around  $-100^{\circ}\text{C}$ , liquid xenon drops into the quartz tube where it accumulates until the tube is full of liquid xenon. At that point, the xenon supply is closed and the system is held in equilibrium for

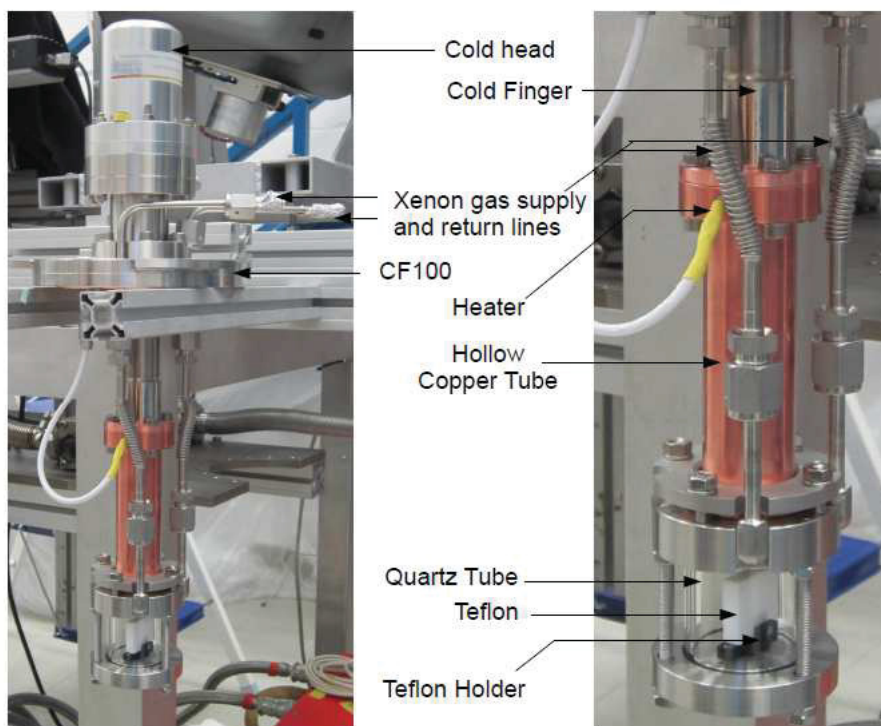


Figure 7.7: The tube and xenon liquefaction assembly.

the measurements.

One last noteworthy point is the presence of a burst disc directly linked to the xenon lines. In case the temperature of the xenon would start increasing drastically the disc would break thus releasing the xenon into the air rather than have the quartz tube explode from the pressure. The disc is rated to burst between 3.2 and 3.8 bar gauge.

### 7.2.2 Movement and Degrees of Freedom

The quartz tube containing the teflon must have two degrees of freedom. It must be rotatable in order to be able to scan different incident angles and it also must be vertically movable so that the beam can shine either below the whole assembly, through the tube and off the teflon, or through the tube but above the teflon. This must be done inside the main chamber without breaking the vacuum and of course with liquid xenon still in the quartz tube. This puts on serious constraints on the design and it results that to obtain such degrees of freedom, not only the quartz tube but the whole liquefaction assembly, shown on figure 7.7 must be rotatable and vertically movable. While both motions will be described in details, for better comprehension it is necessary to start by giving a quick idea of what the system looks like. A simplified picture of the system is shown on figure 7.8.

The liquefaction assembly is mounted on a hollow stainless steel tube and is attached to it via

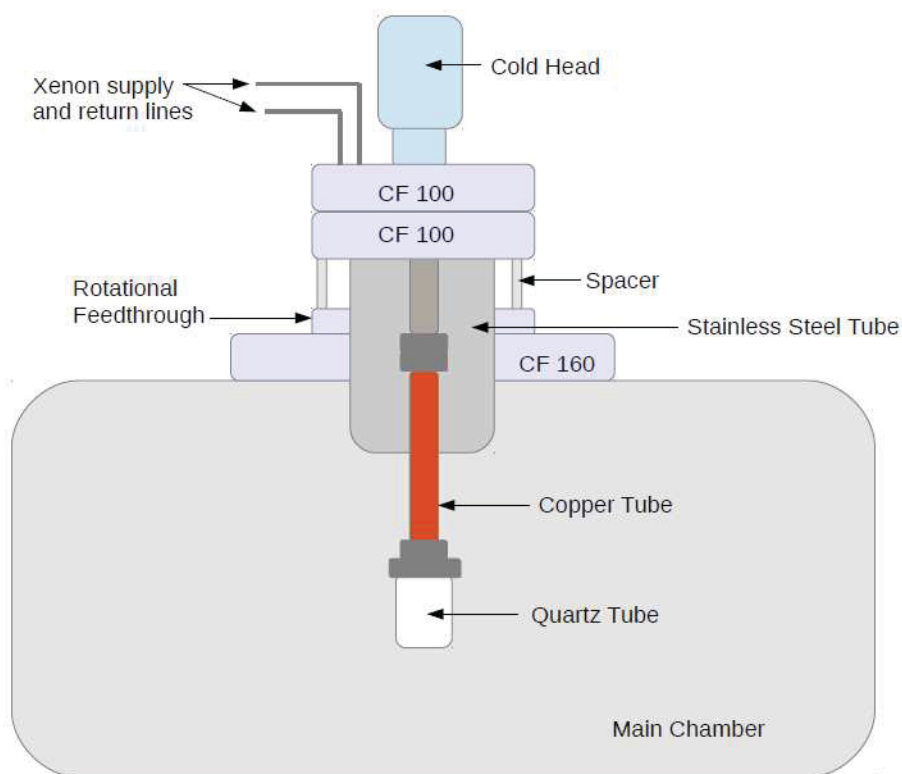


Figure 7.8: Simplified picture of the motion assembly.

CF100 flanges. The stainless steel tube (and so the attached liquefaction assembly) is itself mounted at the center of the main chamber through a custom CF160 flange. The stainless steel tube is shown on figure 7.9.



Figure 7.9: The stainless steel tube which allows the chamber to be maintained under vacuum while moving the quartz tube assembly.

The stainless steel tube is sealed to the main chamber via a viton o-ring, which seals against the outer surface of the tube and the inner surface of the custom CF160 flange, thus keeping the inside of the chamber and everything under this viton ring, under vacuum. By covering the stainless steel

tube in vacuum grease, it can slide up and down relative to the main chamber and still be vacuum sealed via the viton ring. Because the stainless steel tube is connected to the liquefaction assembly, it is therefore connected to the quartz tube and thus lifting the stainless steel tube up and down also lifts the quartz tube up and down, thus achieving the desired vertical motion. Because of the weight of the liquefaction assembly, the stainless steel tube is prone to fall down to the level of the main flange so in order to leave it at whatever vertical position is desirable, spacers of various heights can be put between the main flange (CF160) and the connecting flanges (CF100) between liquefaction assembly and stainless steel tube, thus holding the system into place.

In addition a system of pulleys was set in place to help for the up and down motion for two reasons. First, once the system is under vacuum the force required to lift the whole assembly is increased by about 0.8 kN due to the vacuum pressure over the stainless steel tube hole and is such that lifting is not possible manually. Second, the vertical motion must happen in a very controlled way to avoid two problems, first that the assembly be pulled too far up and thus that the stainless steel tube pop out of the viton ring and break the vacuum, and second so that when lowering the assembly it doesn't drop suddenly over several centimeters and break the quartz tube. A winch and two pulleys have thus been attached to the cold head flange allowing to lift the tube up and down in the most controlled way.

Just like for the quartz tube translation, the whole assembly must be manually rotated from outside to be able to rotate the quartz tube and teflon inside. To achieve this the main flange had to be redesigned with several particular features. The support of the flange is a typical CF160 flange which is screwed to the main chamber, however, rotational bearings are added to it to allow for a rotational motion as shown on figure 7.10. Additionally, a groove was cut at the inside of the opening to house the viton o-ring to form the seal between the flange and the stainless steel tube.

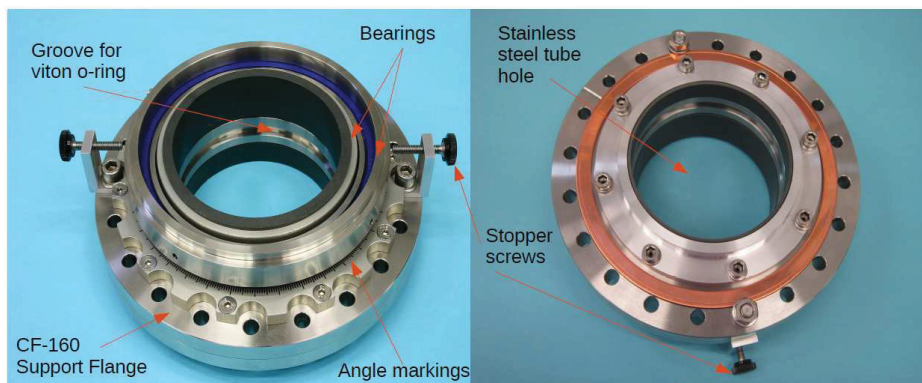


Figure 7.10: The flange allowing the rotational motion of the xenon assembly. Left: top part, outside the main vacuum chamber. Right: bottom part, inside the main vacuum chamber.

In reality two parts must be rotated separately but simultaneously, namely the stainless steel tube and the part of the flange which supports the tube and where the spacers are placed. This motion is achieved through the use of bearings, which in this case are made of two stainless steel rings around a plastic guard ring. In figure 7.10, both bearings are visible. The outer one with the blue guard ring, supports the spacers and the stainless steel tube and the inner one with the black guard ring allows the stainless steel tube to rotate without breaking the vacuum. In addition, screws are added to the outer bearing to serve as stoppers and maintain the assembly motionless thus avoiding unwanted rotation. The groove where the viton ring which allows the sealing of the setup is placed, is also visible. Additionally to be able to record the angle of rotation the flange is marked with a 360° scale. An angle marker is also attached to the stainless steel tube flange for the reading of the angle. Finally, the xenon lines are connected to the gas system with flexible lines to allow the motion of the whole assembly.

Figure 7.11 shows a picture of the whole motion assembly.

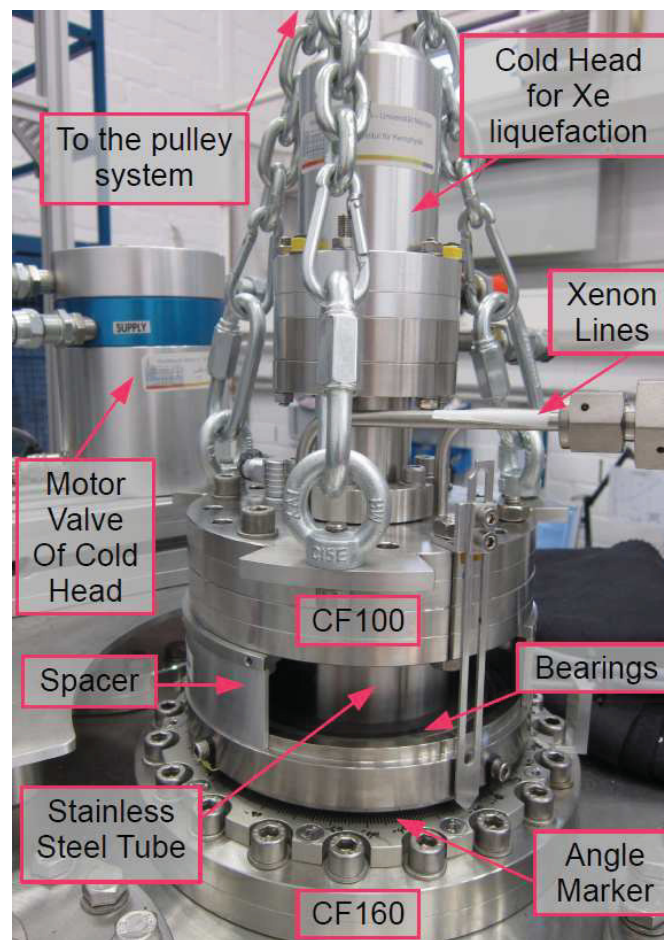


Figure 7.11: A photo of the motion assembly with the bearings, spacers and angle marker clearly visible. The motor valve is also visible in the back as well as the chains linked to the pulley for the lifting movement and the xenon supply lines.

While in principle the rotation motion can happen over  $360^\circ$ , in practice it can only be done by  $100^\circ$  or so. This is because of the flexible xenon lines which of course also move with the liquefaction assembly, but have a limited range. In addition, the motor valve of the cold head also has to be moved as it is attached to the cold head via a high pressure copper line. The motor valve cannot be attached to the assembly however because its weight would tip the quartz tube. Consequently it is just simply placed on a platform on top of the main chamber and must be turned or adjusted manually when necessary as shown on figure 7.11.

A view of the whole setup from the outside recapitulating all the main features described in the previous sections is shown on figure 7.12.

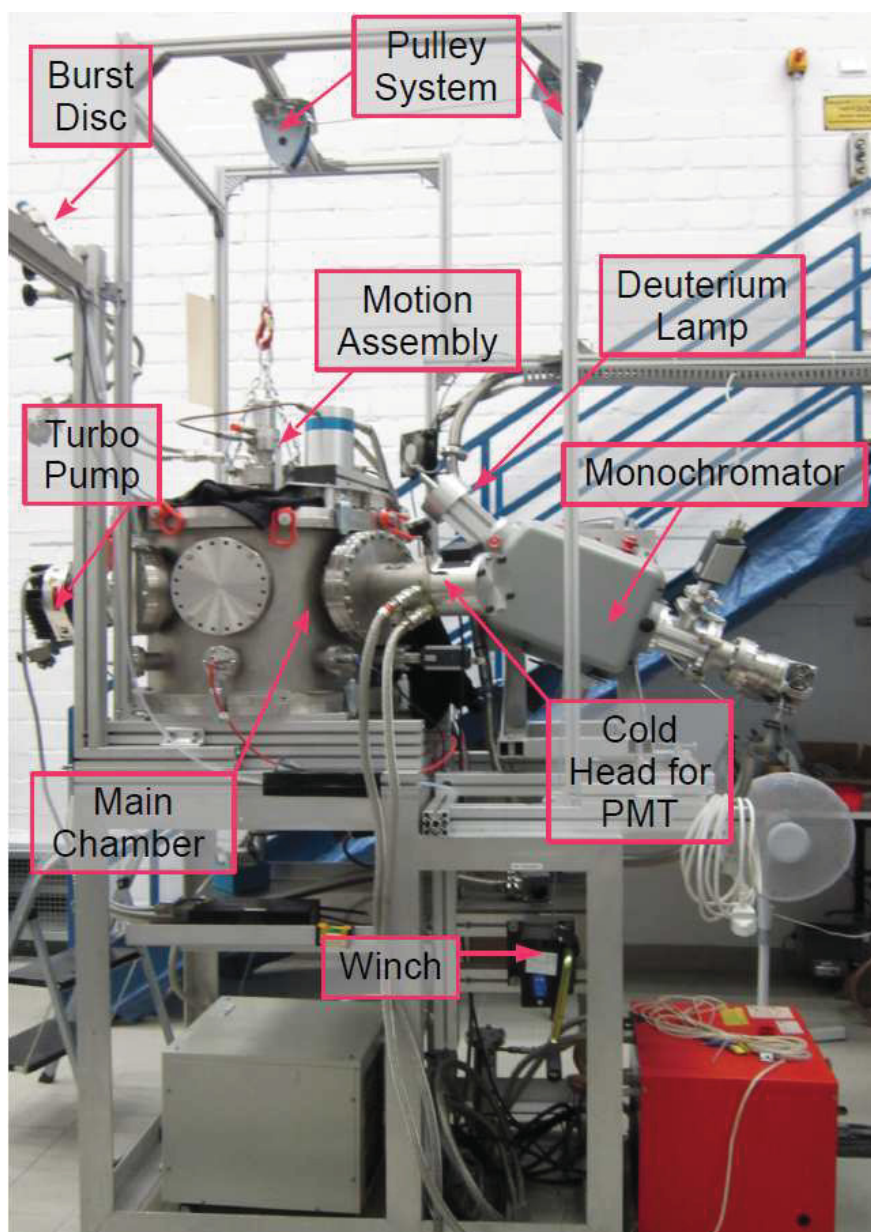


Figure 7.12: The full reflectivity setup as viewed from the outside.

### 7.2.3 Data Acquisition

The PMT is powered by +800 V using a CAEN N470 power supply. The PMT signal is amplified by a factor 10 using a CAEN N979 fast amplifier. A CAEN N840 leading edge discriminator (LED) is then used to create a digital pulse when the amplified PMT signal crosses a certain threshold. This threshold was selected just above the electronic noise level to maximize signal to background ratio, and set to 100 mV. This discriminator value as well as the optimal operating voltage have been selected based on studies performed in [32]. The LED signal is then sent to a NI USB6008 interface which is configured to count these digital pulses in LABVIEW. Additionally, the LED signals can be counted externally with a CAEN N145 counter timer for debugging purposes.

Figure 7.13 shows the power supply and trigger system. A typical PMT signal and the digital pulse from the LED are shown on figure 7.14.



Figure 7.13: A photo of the trigger logic for data acquisition. From left to right, the high voltage supply, the LED, the counter timer and the fast amplifier.

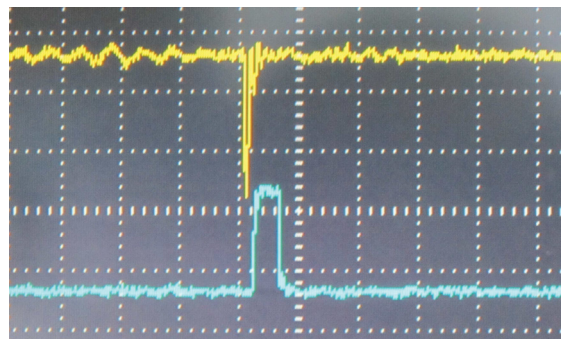


Figure 7.14: A typical PMT signal; in yellow, the signal once amplified; in blue, the yellow signal once inverted and digitized. The amplitude scale is for yellow: 100 mV/div and for blue: 500 mV/div. The time scale is 100 ns/division.

With such a trigger logic, a signal to background ratio of over 1000 is reached with the dominant background coming from dark counts from the PMT.

### 7.3 Measurements and Analysis

Now that the setup has been thoroughly explained, measurements were made using the step teflon sample shown on figure 6.12. While the same sample is used for comparison and consistency purposes, the analysis on the impact of thickness which was carried out in the previous chapter will not be repeated here. Instead the focus will be on the reflectivity of teflon in different media.

Three sets of measurements were carried out. The first one is made in vacuum to be compared to the results of the previous chapter to serve as cross check and reference point. A second set of measurements is made in GXe. Finally the most interesting set of measurements for the XENON collaboration is made under LXe.

#### 7.3.1 Calibration of the PMT

One big difference between this setup and its predecessor is that the collimator, quartz tube and teflon are by definition aligned. The teflon, tube and collimator cannot be translated or moved and are thus in a fixed position. Only the PMT can be moved in x, y and z until it is properly aligned with the beam. Indeed if the PMT were to be misaligned in either x or y, its center of rotation would be different from the center of rotation of the teflon, leading to incorrect angles. Here, the alignment is much more important than in the vacuum setup, because once the quartz tube is filled with liquid xenon, the tube and xenon will act as a lens as soon as the light is not pointed directly to and from the center. In addition, because the PMT is never touched, it's enough to calibrate its position once and for all. Note that these calibrations were done with LXe in the quartz tube.

To make the following sections more understandable, figure 7.15 shows the orientation of the setup and PMT.

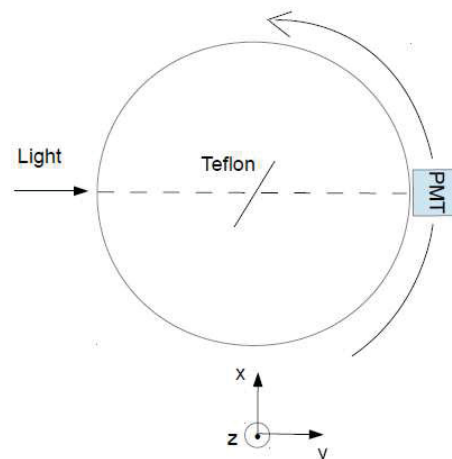


Figure 7.15: The orientation of the PMT. Top view.

### 7.3.2 X Calibration

The x position of the PMT is the first calibration to be done. Indeed a misalignment in x will have the biggest impact on the data. Additionally both y and z calibration depend on the x calibration, while the latter is independent of the rest.

To perform the x calibration, the light is shone above the teflon, directly into the PMT which is then rotated around its central position. This is done for several x positions of the PMT and is schematically drawn in figure 7.16.

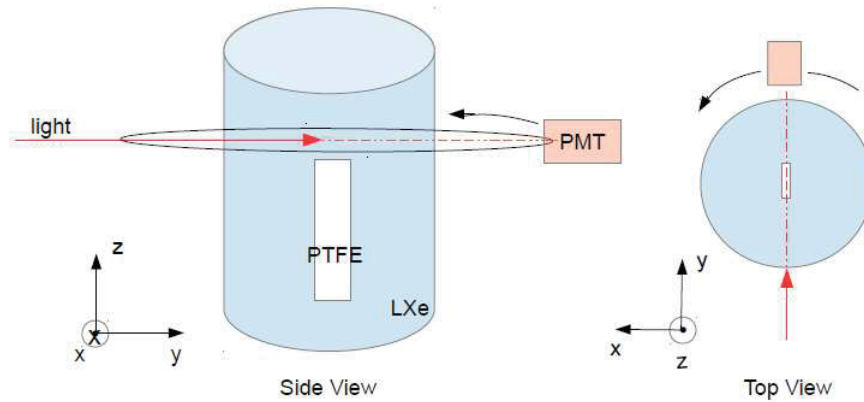


Figure 7.16: Setup to perform the PMT calibration in the X direction.

Figure 7.17 shows the data for such a calibration.

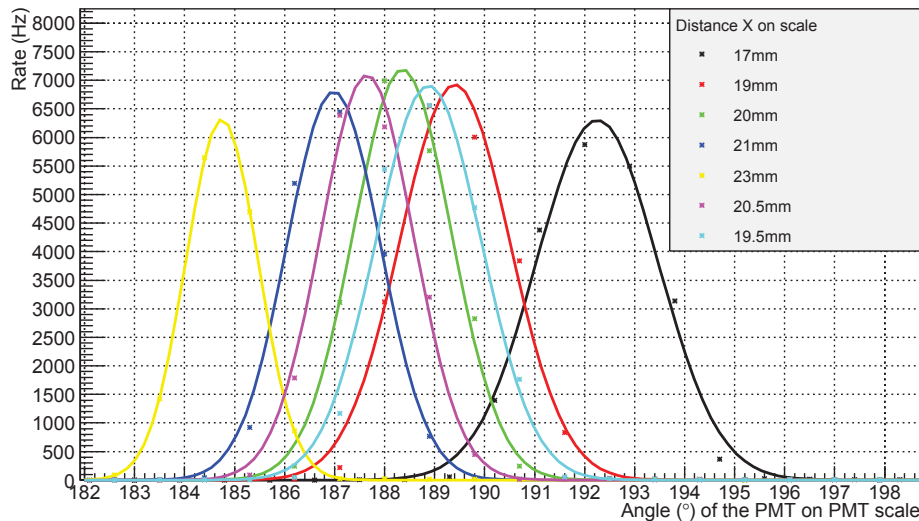


Figure 7.17: X calibration of the PMT

The correct x position for the PMT is found to be 20 mm, as it is the maximum intensity curve but also corresponds to the average value between each pair of curves with the same intensity as

one another. And indeed, the correct x alignment should yield the curve with maximum intensity, because this is where the normal to the aperture in front of the PMT is aligned with the beam at its center. When x is misaligned, the effective area of the aperture decreases, leading to a lower maximum intensity.

### 7.3.3 Y Calibration

The second calibration has to be done in the y direction. Calibrating the y position is however rather tricky because it needs to be done while shining the light off of the teflon and without any assumptions about the absolute PTFE alignment or angle position. This is done using an artifact of the setup, namely the rods. As mentioned in the setup description above, the tube is held into place by three rods whose positions are fixed relative to the teflon. Out of the three rods only one is in front of the teflon, thus blocking the light at a fixed angle. When the PMT passes behind this rod, no light can get through thus creating a very recognizable dip in the data. This can be used as a very powerful calibration tool.

The light is shone off of the teflon at two different angles spaced  $10^\circ$  apart by rotating the teflon and the quartz tube by exactly  $10^\circ$ . Instead of looking at a reflection peak, the emphasis is put on the position of the rod. There should then be exactly a  $10^\circ$  difference between the dips of each data set. A schematic view of the setup to perform this measurement is shown on figure 7.18.

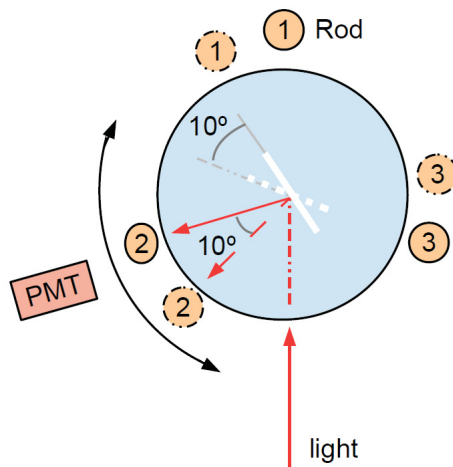


Figure 7.18: Setup for the y calibration

However, because the rods are not point like, and the dip in the data has a certain width, it's hard to assess precisely the angle difference. Consequently the data are superimposed to one another with an offset of exactly  $10^\circ$  for one of them. This is done for several y positions of the PMT and is

shown on figure 7.19. The rod position aligns best for the datasets taken at a position  $y=0.4$  mm, making this value the proper choice for the  $y$  calibration.

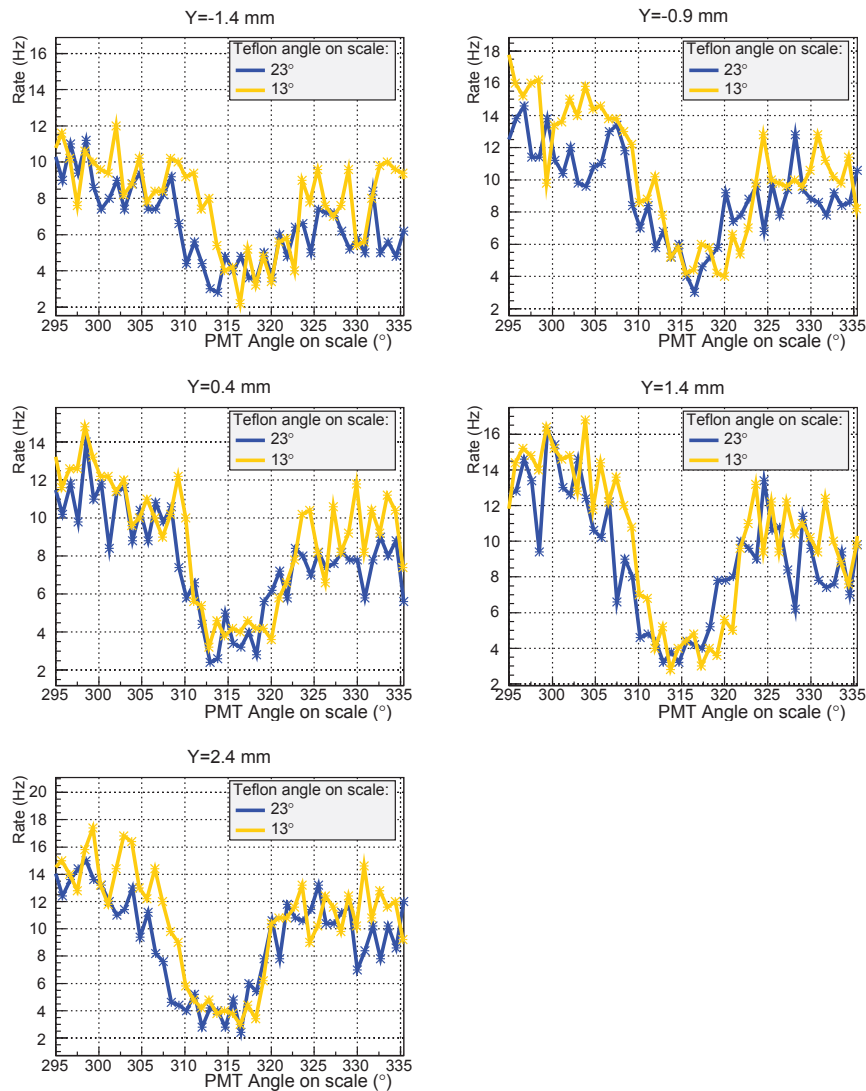


Figure 7.19: Y calibration of the PMT using the rod as a point of reference

### 7.3.4 Z Calibration

The last necessary calibration is the PMT position in  $z$ . This is rather straight forward. The tube is lowered so that the teflon is out of the way of the light and the light is shone directly into the PMT which is moved exactly as done before for the X calibration (figure 7.16). This time however, this is done for different values of  $z$ . When  $z$  is aligned the maximum intensity is at its highest. The results from this calibration are shown on figure 7.20. The maximum intensity occurs at  $z=1.85$  mm, which is thus the value that is used hereafter.

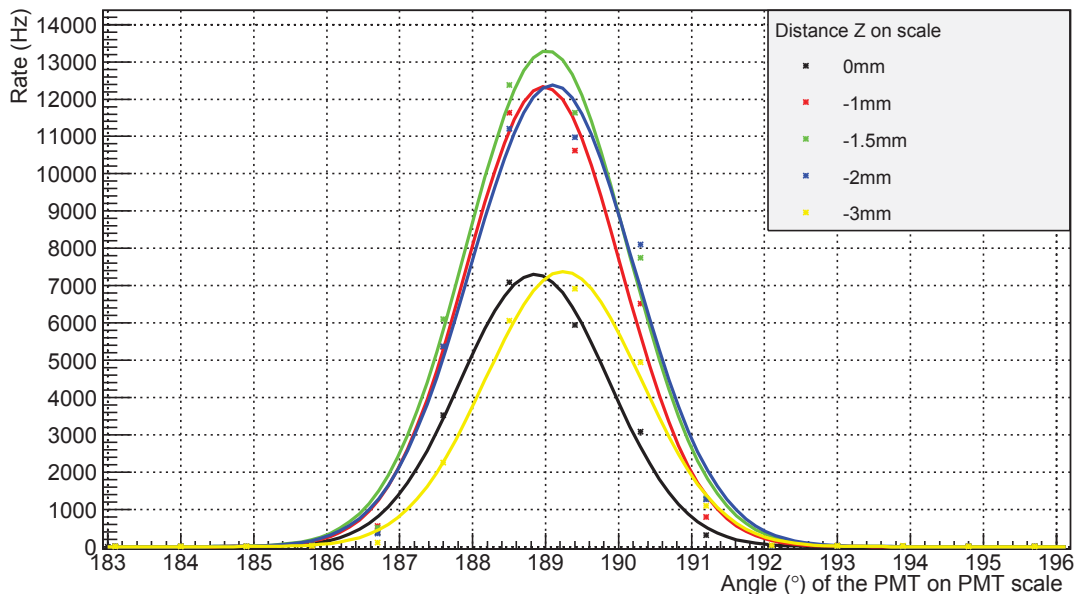


Figure 7.20: Z calibration of the PMT

### 7.3.5 Vacuum Measurements

Now that the setup is properly calibrated, measurements can be taken. The first step is to repeat the measurements of the previous chapter but this time with the quartz tube under vacuum at room temperature. This should allow to identify any potential effect of the tube on the data, such as reflective light loss or attenuation in the quartz.

Just like in the previous chapter, before getting to a reflectivity result, two final calibrations are necessary. First, the point on the PMT scale where the PMT is aligned with the beam has to be known. This will also give the normalization data used to calculate the reflectivity. Second, the PTFE angle at which the teflon is aligned with the beam must be also known in order to be able to define the angle of incidence. Unlike the calibrations of the PMT position, these calibrations must be performed every time a new sample is installed.

#### *Normalization*

As mentioned above and done in the previous chapter, to have a reference measurement, a normalization measurement must be taken where the light is shone directly onto the PMT with the teflon out of the way. Such a measurement serves two purposes. First, it allows to calibrate the PMT angle on the PMT scale to determine at what angle on that scale is the PMT aligned with the beam. Second, it serves as a measure of the amount of incident light  $R_0$ , accounting for losses in the quartz,

which will then be used to calculate the reflectivity  $R_{Tot}(\theta_i)$  as explained in section 6.4.5.

To do this measurement, the PMT is thus moved around to find the maximum intensity point where it will be aligned with the beam. This arrangement is the same as the one used for the x calibration and shown on figure 7.16.

The actual data is shown on figure 7.21 with a gaussian fitted to it. The alignment angle where the PMT is aligned with the beam is  $\theta_{PMTRef} = 186 \pm 0.3^\circ$ .

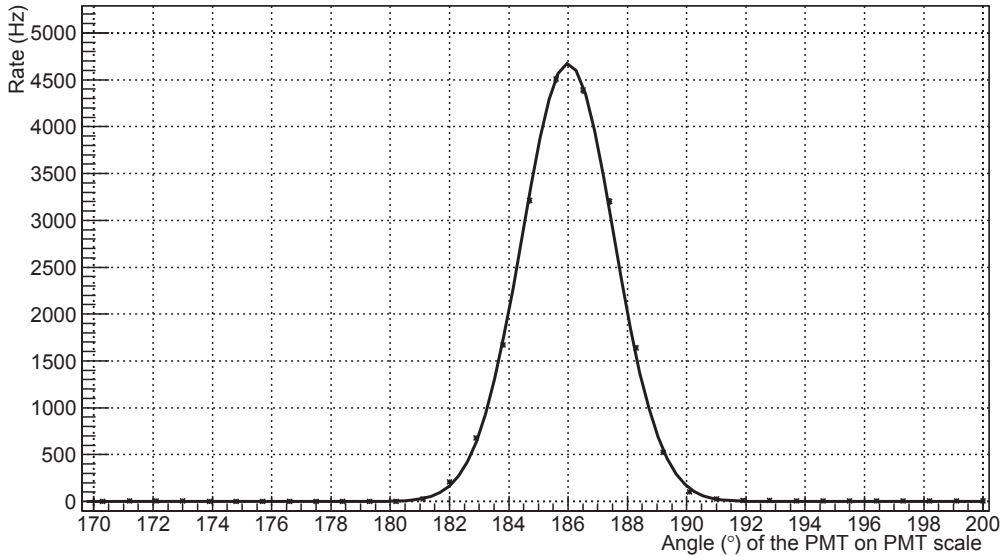


Figure 7.21: Normalization data through the quartz tube in vacuum

### ***PTFE Alignment***

The next step is to find the teflon alignment angle  $\theta_{PTFEref}$  which means the angle on the teflon scale which corresponds to the position where the teflon is aligned with the beam.

This aligned position is known to be around  $60^\circ$  on the teflon scale, simply by looking at it when the setup was assembled, however this should be known more precisely. While in the old setup this alignment was rather easy to do because the teflon could be translated in and out of the beam, in this setup it is a bit trickier to achieve as the teflon can only be rotated. To get the teflon alignment, data is thus taken at several teflon angles around  $60^\circ$  on the scale which should mean that the teflon is only slightly inclined. By localizing the position of the specular peak on the PMT scale  $\theta_{peak}$  and knowing that this peak must be at a position  $180 - 2 \times \theta_i$  with respect to the beam direction and by knowing the PMT reference angle  $\theta_{PMTRef}$  on the PMT scale, the incident angle  $\theta_i$  can be calculated by applying formula 7.2.

$$\theta_i = \frac{180 - \theta_{peak} + \theta_{PMTRef}}{2} \quad (7.2)$$

These angles are shown schematically in figure 7.22.

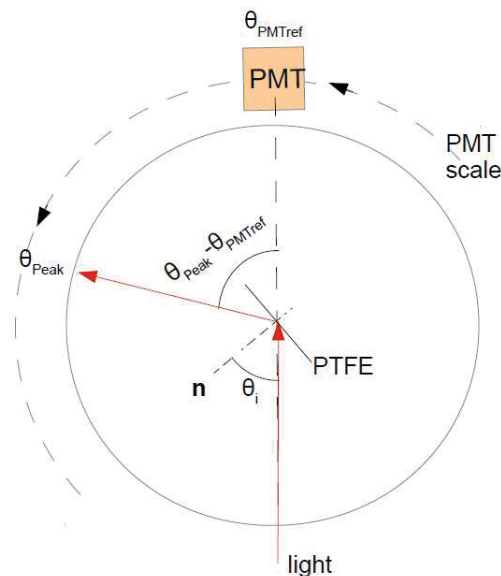


Figure 7.22: Schematic view of the angles needed to calculate the incident angle

Additionally, because of the finite size of the sample, very big incident angles are not accessible as a significant fraction of the light hits the side of the sample. Consequently to find out the biggest incident angle at which data taking is possible, this data taking procedure is repeated for several angles until it is evident that the full specular peak is visible and all the incident light hits the reflecting surface. A schematized view of the setup to take these measurements is shown on figure 7.23.

The data on figure 7.24 shows that at a PTFE scale angle  $\theta_{PTFEscale}$  of  $55^\circ$  not all the light passes through. This means that at this PTFE scale angle, some light is blocked by the side of the teflon and does not reach the PMT. However this doesn't necessarily mean that the teflon is aligned with the beam. While turning the PTFE scale angle to  $48^\circ$  in the direction of decreasing incident angle, the data always increases in intensity. This is evidence of light blockage, as with decreasing incident angle, the specular intensity should decrease. This is the case until the PTFE scale angle  $\theta_{PTFEscale}$  is  $48^\circ$  where no more light is being blocked and the full reflected beam is visible. This is deduced from the fact that the specular peak at an angle of  $47^\circ$  has less intensity than at  $48^\circ$ , as expected. Consequently, only data taken at a PTFE scale angle less than  $48^\circ$  is usable.

The reference alignment angle of the PTFE  $\theta_{PTFEref}$ , which corresponds to the angle on the scale for the PTFE rotation where the sample is aligned with the beam and the incident angle is  $90^\circ$ , is

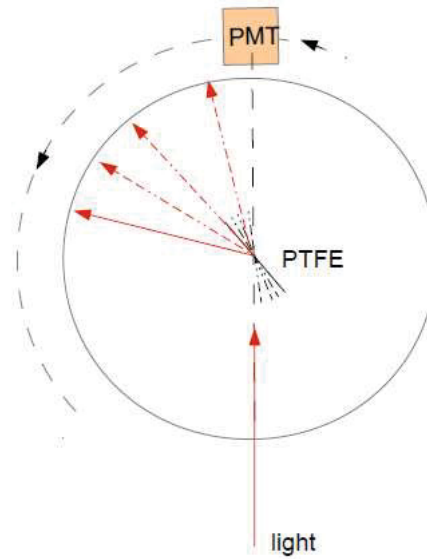


Figure 7.23: Setup for the PTFE alignment data

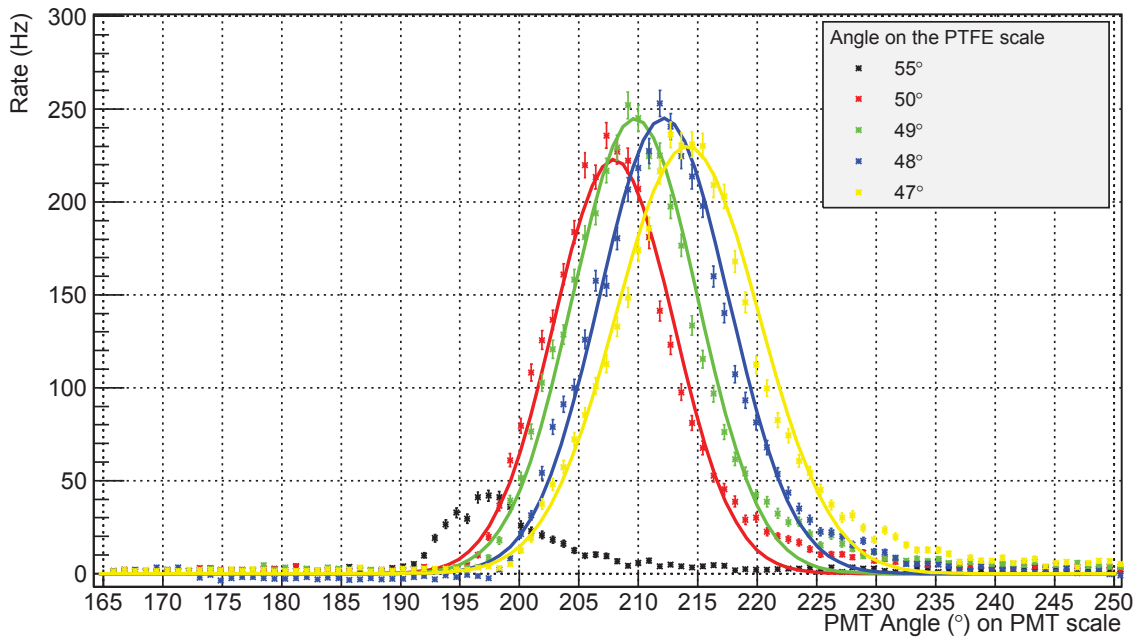


Figure 7.24: PTFE alignment data through the tube under vacuum. Note that a teflon scale angle of  $47^\circ$  corresponds to an incident angle of  $76^\circ$ .

then found by fitting gaussians to both the  $\theta_{PTFEscale} = 48^\circ$  and  $\theta_{PTFEscale} = 47^\circ$  data. From their respective specular peak position and following equation 7.2, the angle of incidence  $\theta_i$  corresponding to these scale angles are calculated to be  $\theta_i = 77^\circ$  and  $\theta_i = 76^\circ$  respectively. The reference alignment angle of the PTFE  $\theta_{PTFEref}$  is then found to be  $61^\circ$  on the scale by using these values for  $\theta_i$  and  $\theta_{PTFEscale}$  in equation 7.3.

$$\theta_{PTFEref} = \theta_{PTFEscale} + 90 - \theta_i \quad (7.3)$$

### Data

The raw data of the reflectivity measurements is shown on figure 7.25 for different incident angles spanning a range of  $40^\circ$ , starting at an incident angle of  $77^\circ$ . The general shape and trend of this data is completely similar to those of the data of the previous chapter (figure 6.35).

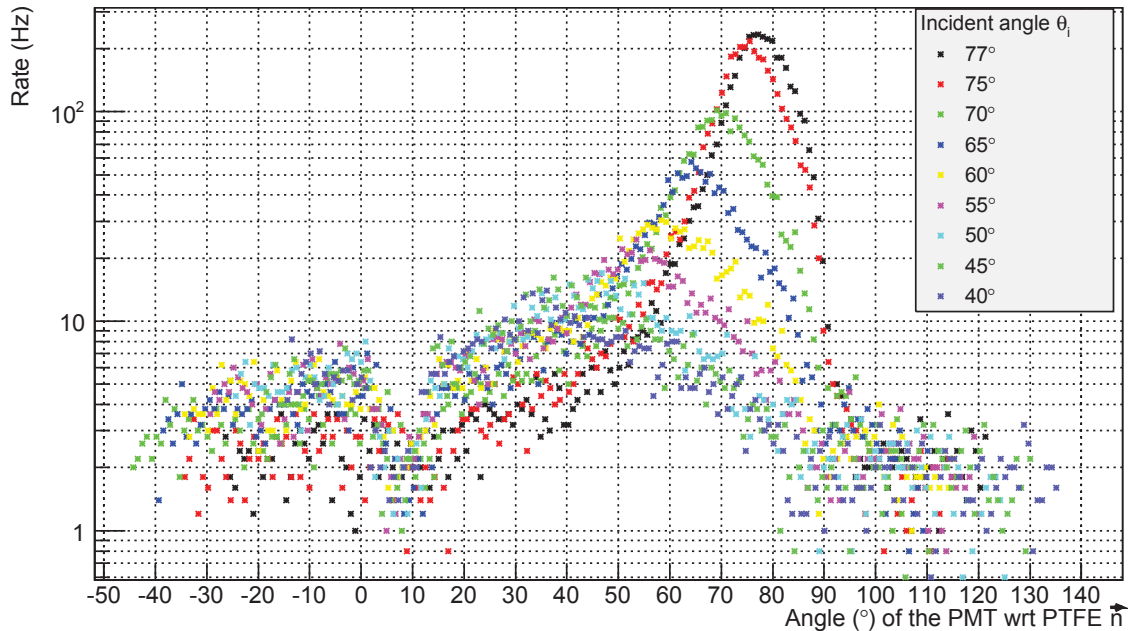


Figure 7.25: Raw Data of the reflection off of the teflon in vacuum. The dip around  $10^\circ$  is due to the rod position around the quartz tube.

Additionally, the raw data can be used to check if the setup alignment is indeed correct or not, by using the rods' position. As mentioned before, out of the three rods, two are behind the teflon and one is in front of it, so there will always be a point in the data where the PMT passes behind the rod in front of the teflon and the rate will drop to zero. The average PMT angle with respect to the teflon normal where this happens  $\theta_{rod}$  can be easily calculated to be at  $10^\circ$  from the basic design of the rod system which is shown on figure 7.26.

Looking at the raw data from figure 7.25, a dip is indeed observed at  $10^\circ$ , thus confirming that the setup is properly aligned.

### Reflectivity

The method used to calculate the reflectivity is exactly the same as the one outlined in the previous chapter and will thus not be repeated here. Note that compared to the previous chapter, the rates are expected to be smaller due to the losses through the quartz described by equation 7.1.

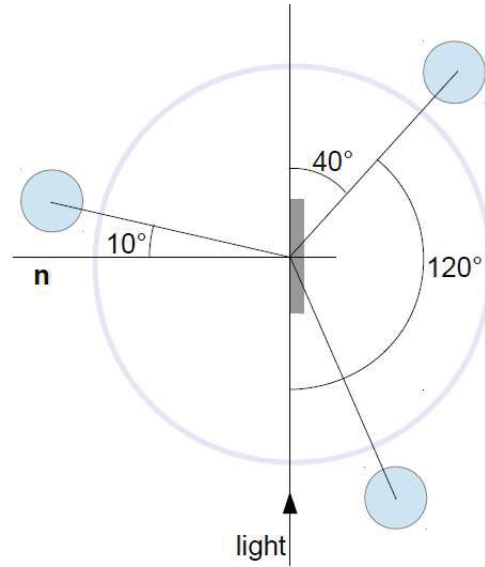


Figure 7.26: Position of the rods around the quartz tube.

Fit function 6.17 is applied to the data resulting in the fits presented in figure 7.27. Note that the error on each measurement is slightly higher in the new setup because the statistics are slightly lower due to reflections at the tube and attenuation in the quartz.

The reduced  $\chi^2$  resulting from the fits of figure 7.27 are shown on table 7.1. As in the previous chapter, while they are good at low incident angles, they get worse at higher incident angles, however, once again, the fits still are not bad and considering the simplicity of the model are still adequate.

Incident angle ( $^{\circ}$ )	Reduced $\chi^2$
	7.65245
77	7.22956
75	5.83319
70	4.02296
60	1.68714
50	1.71855
45	1.86172
40	1.49996

Table 7.1: Reduced  $\chi^2$  for the fits to the vacuum data through the quartz tube. The first reduced  $\chi^2$  value corresponds to the normalization data (no reflection off teflon)

Applying equation 6.24, the reflectivity at different angles for both specular and diffuse components of the light is calculated and shown on figure 7.28. This results in an average reflectivity of  $70\% \pm 10\%$  which is in complete agreement with the results found in the previous chapters which were of  $73\% \pm 7\%$ .

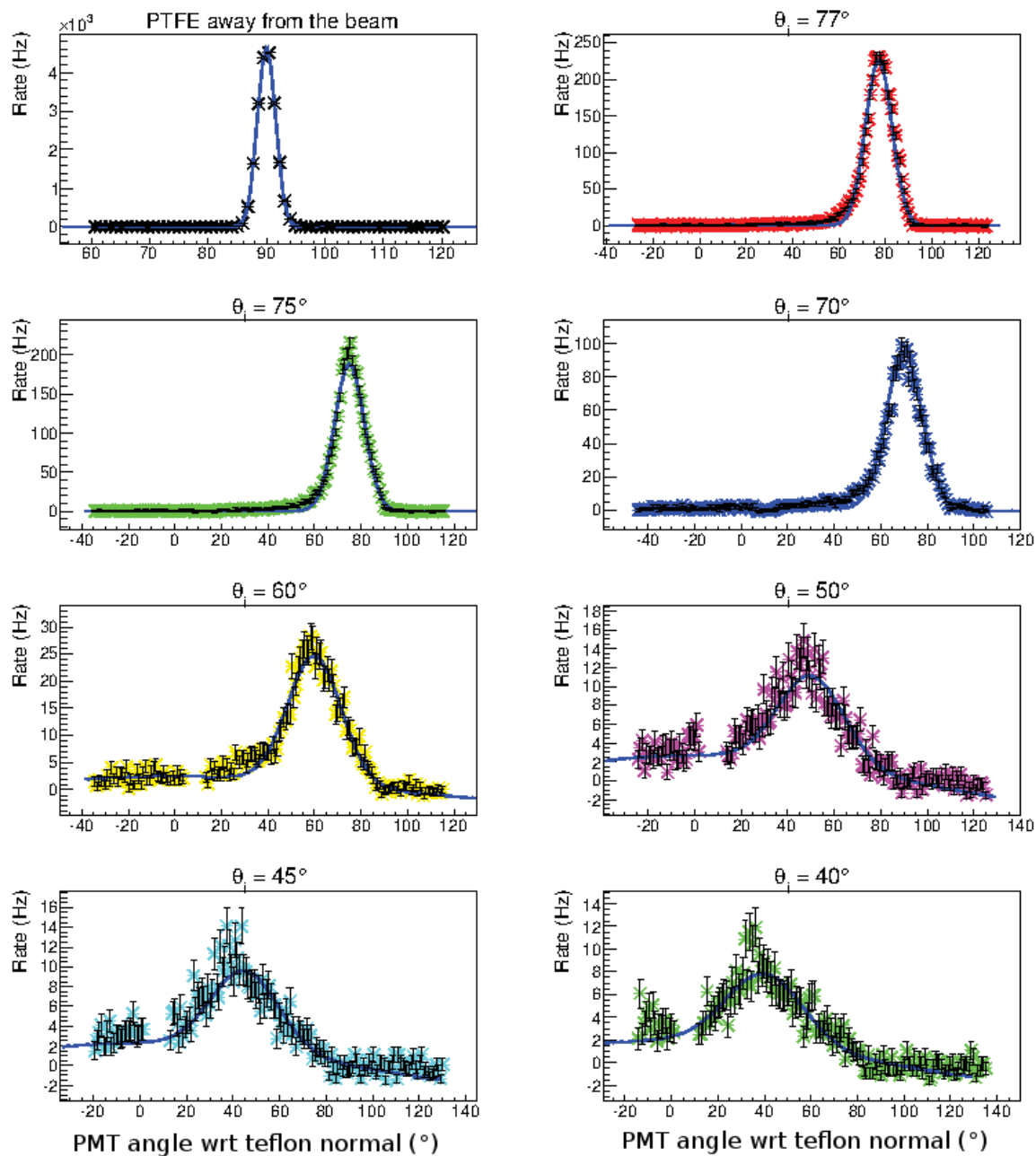


Figure 7.27: Fits to the raw data in vacuum

However, while the average number agrees, when comparing the specular and diffuse components between the two setups, differences arise. As a reminder, the results found in the previous chapter are shown here in figure 7.29.

Comparing figures 7.28 and 7.29, it seems that the effects of the specular and diffuse components are inverted. In the old setup, most of the reflectivity came from diffuse reflection while in this setup much more of the reflectivity seems to come from the specular reflection. While this was not expected it could be explained by a simple fact, namely that for this new data, the teflon had been

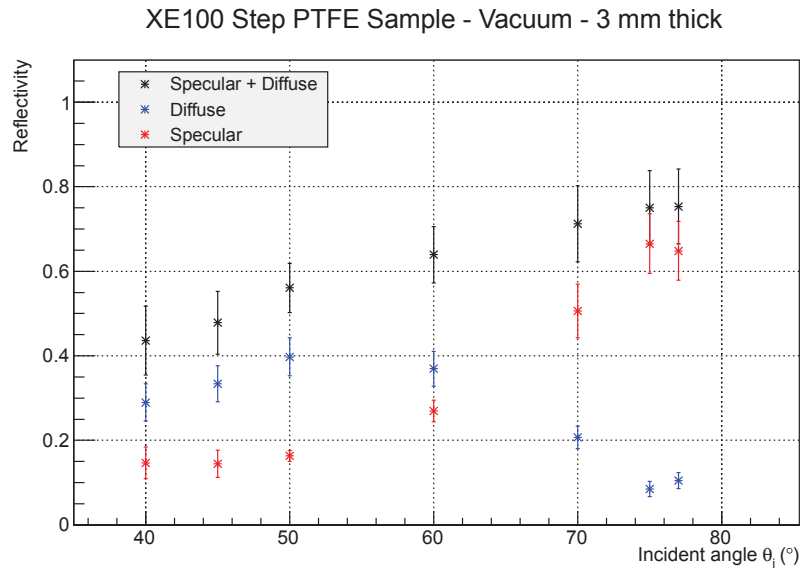


Figure 7.28: Reflectivity in vacuum through quartz tube

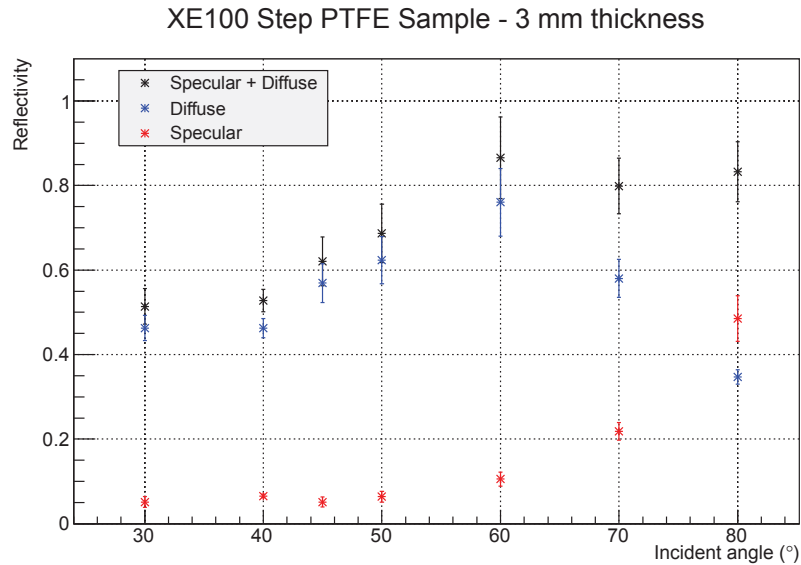


Figure 7.29: Total, specular and diffuse reflectivities of the 3 mm thick teflon in the original vacuum setup. The data for the cold and warm measurements lie on top of one another.

submerged in liquid xenon for a month before the data was taken. This might have for all purposes washed the teflon surface making it more mirror like. This effect, however interesting, will not be investigated further in this work, as its main purpose was to show that the results obtained were compatible with the results of the previous chapter, thus allowing to have a strong basis before going into gas and liquid xenon measurements.

### 7.3.6 Gas Xenon Measurements

The measurements made in vacuum are now repeated in gas xenon (GXe). The main dataset was taken just after recuperating the liquid xenon and maintaining the cold head temperature at  $-90^{\circ}\text{C}$ . This was done in the hope that, because the quartz tube was presumably still cold, the GXe and teflon could also be maintained at a rather cold temperature. However, the lack of a temperature sensor inside the quartz tube did not allow for precise monitoring of the temperature. To see any effect due to temperature changes, and as a crosscheck, a second dataset was taken a day later, after the cold head had been turned off and the GXe and teflon were presumably near room temperature.

#### Normalization

Just as for the vacuum data, the normalization data in GXe at both cold and warm temperatures are shown on figure 7.30. The PMT alignment angle  $\theta_{PMTRef}$  is  $186.5^{\circ} \pm 0.1$  at warm temperatures and  $186.3^{\circ} \pm 0.1$  at cold temperatures. In addition, the intensity at warm temperatures is a bit lower than at colder temperatures. While this disagreement is larger than the statistical error, the decrease could be due to other systematic effects such as the reproducibility of the intensity from the deuterium lamp or changes in the reflective losses at the quartz tube due to thermal expansion.

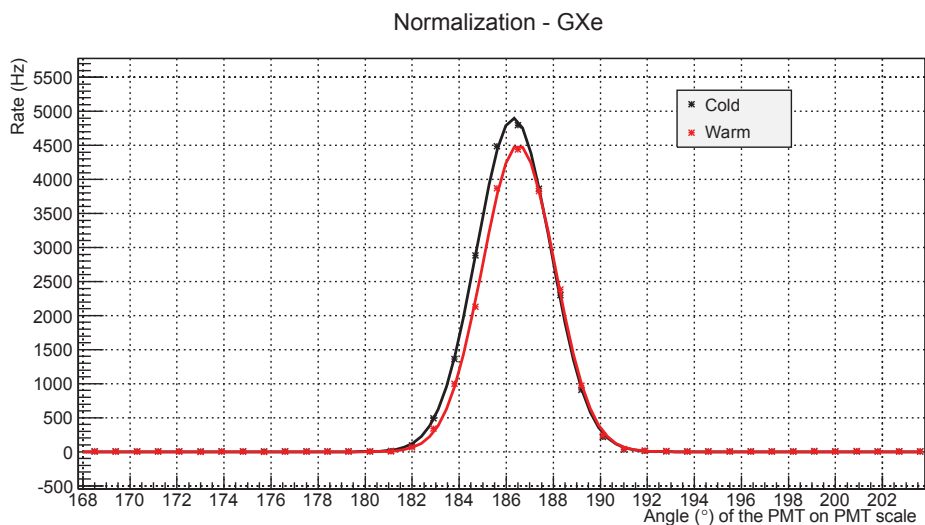


Figure 7.30: Normalization data through the quartz tube in gas xenon

#### PTFE Alignment

Again, as for the vacuum data, the PTFE alignment must be redone. While it shouldn't change a lot, it's always a possibility that a change of state might induce some angle shifts due to lensing, other

optical effects or thermal expansion of the tube or the teflon. Figure 7.31 shows the result of the PTFE alignment in GXe. As before, gaussians are fitted to the 48° and 47° data which again are the largest incident angles at which a full measurement is possible. They correspond again respectively to a 77 and 76° incident angle yielding the same teflon reference angle of 61°.

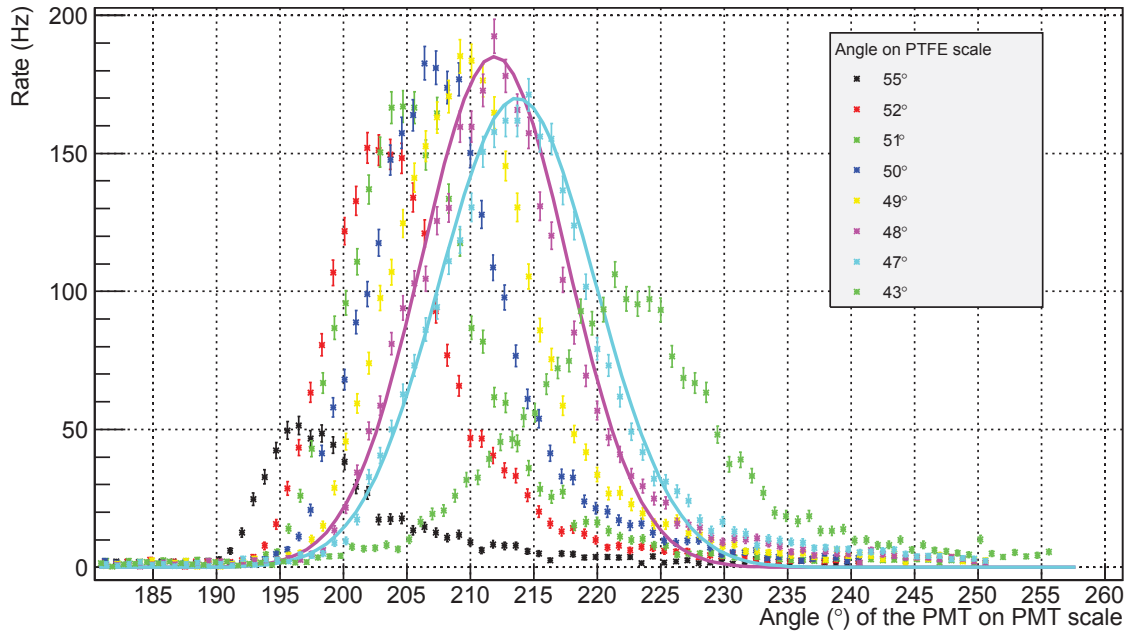


Figure 7.31: PTFE alignment data through the tube under gas xenon

### Data

The data in GXe is shown on figure 7.32. As mentioned before, some measurements were made at warm temperatures and are shown as triangles on the data. There is no major difference between the cold and warm measurements except at high incident angles where the warm measurements have a slightly higher rate. The general trend of the data is the same as in vacuum but with slightly lower intensity.

### Reflectivity

Once again the analysis used to calculate the reflectivity is the same as described in the previous chapter. The fits corresponding to the data of figure 7.32 are shown in figure 7.33 with the reduced  $\chi^2$  shown on table 7.2. When presenting the data in this manner an unexpected feature arises, namely a small bump around 100° from the incident angle, which explains why the reduced  $\chi^2$  are a bit worse than for the vacuum data (but still acceptable). The reason for this small peak is unknown but may

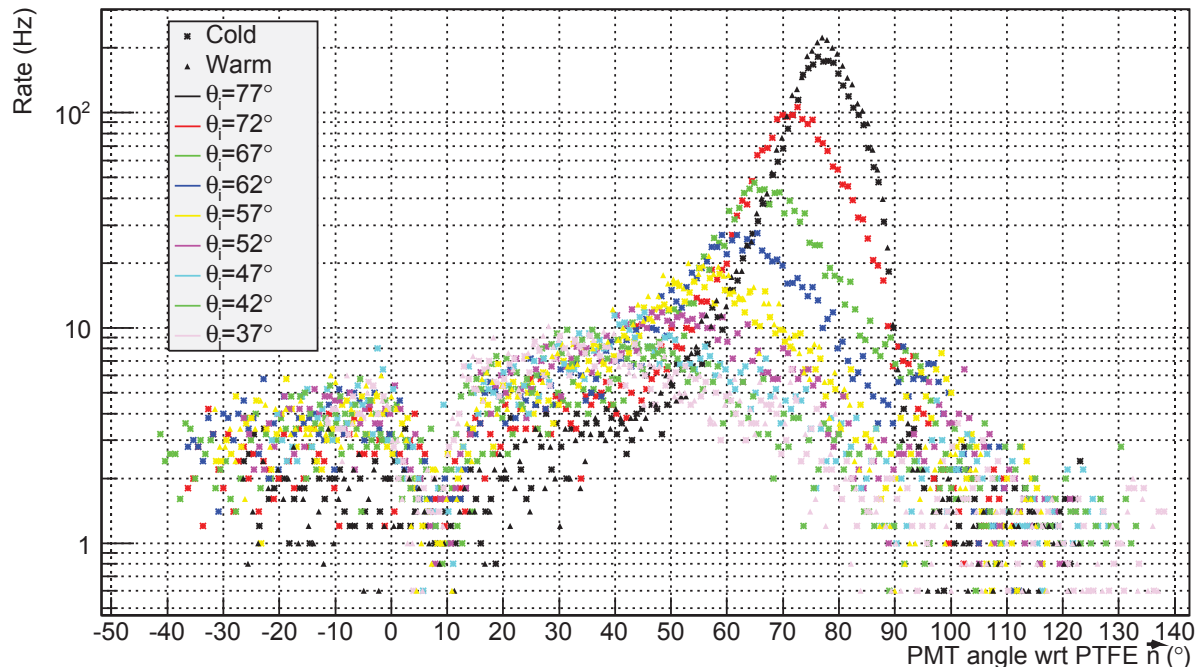


Figure 7.32: Raw Data of the reflection off of the teflon in both cold and warm gas xenon

simply be due to impurities in the gas or an extra reflection. However this effect being tiny will simply be ignored.

Incident angle (°)	Reduced $\chi^2$
	31.7045
77	5.57227
72	3.07063
62	2.32266
52	2.12511
47	1.85764
42	1.73335
37	1.40652

Table 7.2: Reduced  $\chi^2$  for the fits to the GXe data. The first reduced  $\chi^2$  value corresponds to the normalization data (no reflection off teflon)

The reflectivity in GXe for both warm (triangle) and cold (stars) data is shown on figure 7.34. As can be seen, the aforementioned slight differences in intensity between warm and cold data have a negligible impact on the reflectivity which has an average value of  $56\% \pm 7\%$ . This value while lower than the reflectivity in vacuum is not significant enough within the errors to be conclusive.

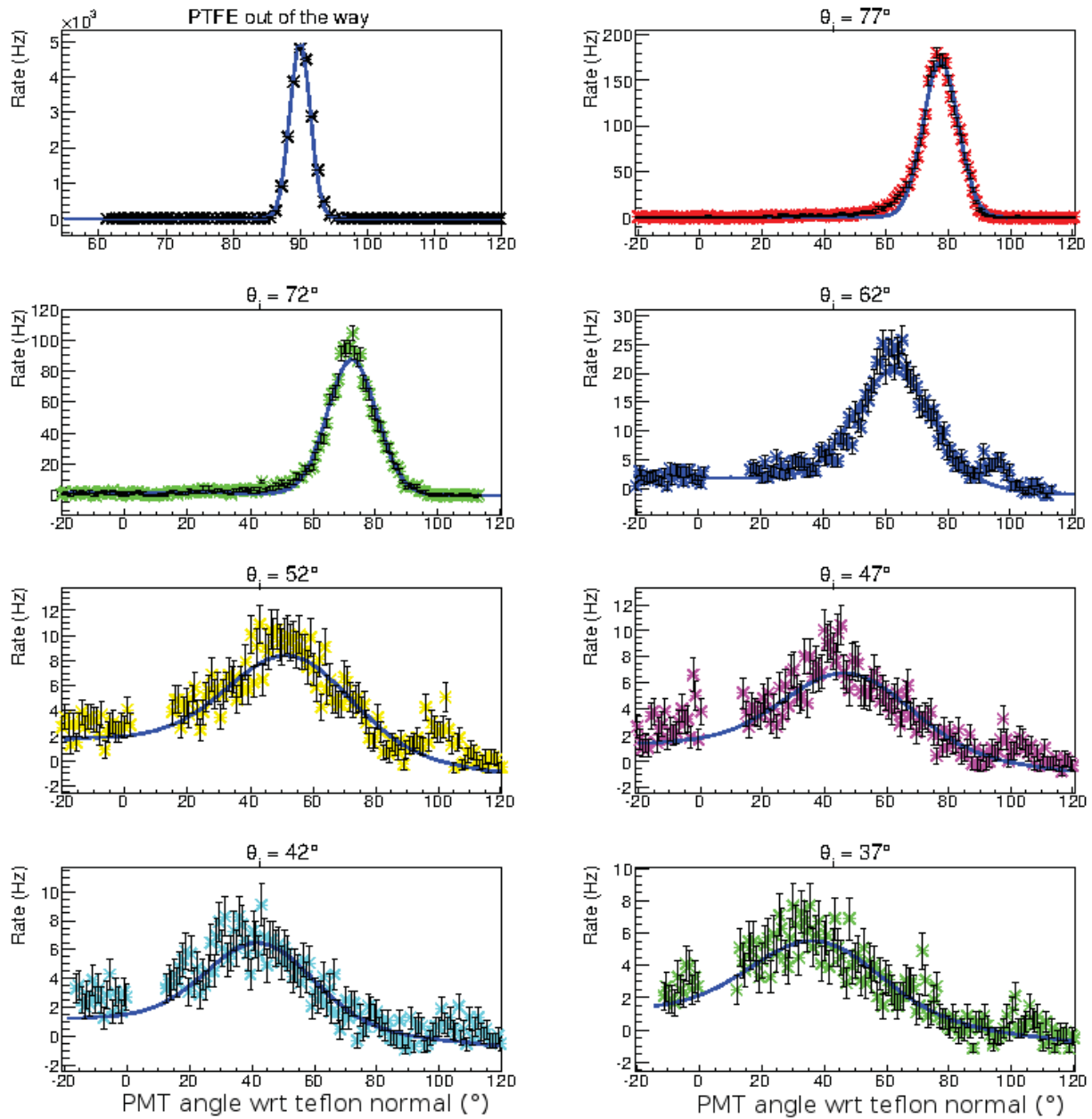


Figure 7.33: Fits to the data in cold GXe

### 7.3.7 Liquid Xenon Measurements

The last and most important set of measurements is done with the quartz filled with liquid xenon (LXe) and maintained at a pressure and temperature of 1.5 bars and  $-102^{\circ}\text{C}$ . Other than a visible convective motion, the LXe is stable and homogeneous with no bubbles or obvious artifacts which could prevent data taking.

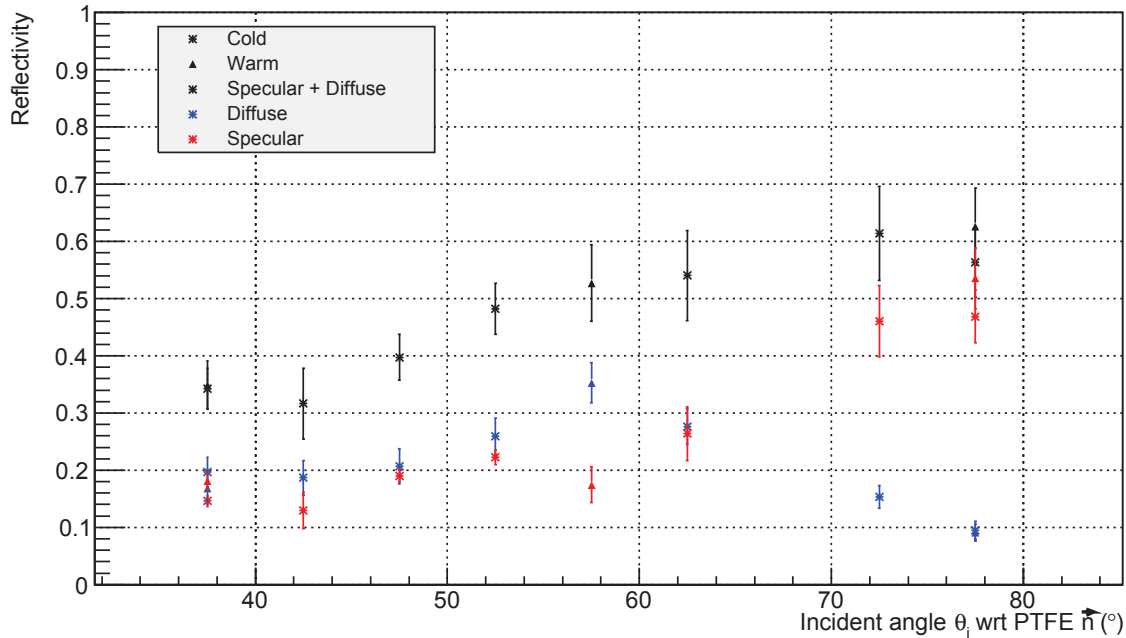


Figure 7.34: Total, specular and diffuse reflectivities of the 3 mm thick teflon under both cold and warm gas xenon.

### Normalization

As previously done in both vacuum and GXe, normalization data are necessary to identify the alignment angle of the PMT with the beam and measure the incident intensity. Here, the normalization measurement also accounts for light loss in the liquid xenon, as well as in the tube as in the previous measurements. The results are shown on figure 7.35.

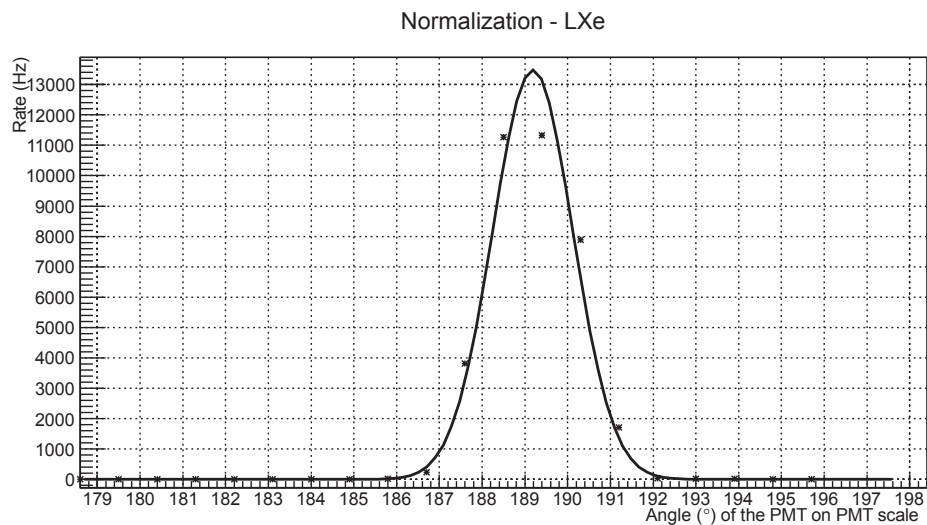


Figure 7.35: Normalization data through the quartz tube in liquid xenon

The peak intensity has gone drastically up by almost a factor 3 compared to the measurements in gaseous xenon and vacuum, shown on figures 7.30 and 7.21 respectively, but the width of the beam is much smaller. The total intensity can be compared by the integral, which gives a factor 1.1 higher for the liquid xenon measurement than the vacuum measurement. The increase in the integrated intensity can be described by the fact that there are fewer reflective losses at the surfaces of the quartz tube when it is filled with liquid xenon. Since the index of refraction of liquid xenon closely matches that of quartz, the reflective losses at the inner surfaces are negligible, and there are only two surfaces with large reflective losses compared to four when the tube was under vacuum. Using equation 7.1 again, and applying it at two surfaces compared to four, the losses from reflections should be only about 10% of the incident light as opposed to about 20% in the vacuum case, which entirely explains the increased intensity.

The fact that the beam is higher and narrower in liquid xenon than in vacuum can be explained by the fact that the xenon acts as a lens. It effectively focuses the beam to a smaller width at the location of the PMT.

In addition the PMT alignment angle with the beam is found to be  $189.2^\circ \pm 0.1$  which is  $3^\circ$  off compared to vacuum and GXe. This should not happen if the system were perfectly aligned. To investigate this issue simulations of the light path were performed. Because the PMT has been calibrated, and assuming that the design is correct and the quartz tube and teflon are centered in the chamber, the only likely explanation is that the light beam itself is tilted. This is highly possible as there is some slack in the viton rings which hold the light assembly to the main chamber and getting the two aligned was non-trivial. Consequently, the simulations were carried out with a tilted light source and resulted that a  $0.3^\circ$  tilt would cause the  $3^\circ$  difference seen between vacuum and LXe. This is a negligible misalignment and much lower than the resolution with which the setup was aligned. Moreover, because the normalization and alignment calibrations are redone in LXe and used to calculate the reflectivity, this  $3^\circ$  difference is thus taken into account and will have a negligible impact on the following results.

### ***PTFE Alignment***

Because of the change of state to liquid, this step is even more important than before as there is the distinct possibility that the LXe acts as a lens due to its high index of refraction  $n=1.69$ , which would have an effect on the angle. The data is shown on figure 7.36. Unlike before, only from a PTFE scale angle of  $46^\circ$  on, can the full measurements be made. Again applying formula 7.2, a  $45^\circ$  angle on

the PTFE scale corresponds in reality to a  $77^\circ$  incident angle, which gives a teflon reference angle of  $58^\circ$  on the scale which as expected from the previous section is  $3^\circ$  off compared to the data in vacuum and GXe, thus also confirming that the xenon acts as lens. Because the sample was not changed and nothing was touched on the system, the data was taken in exactly the same conditions which means that this is definitely an artifact of light propagation through LXe and not due to any change on the setup.

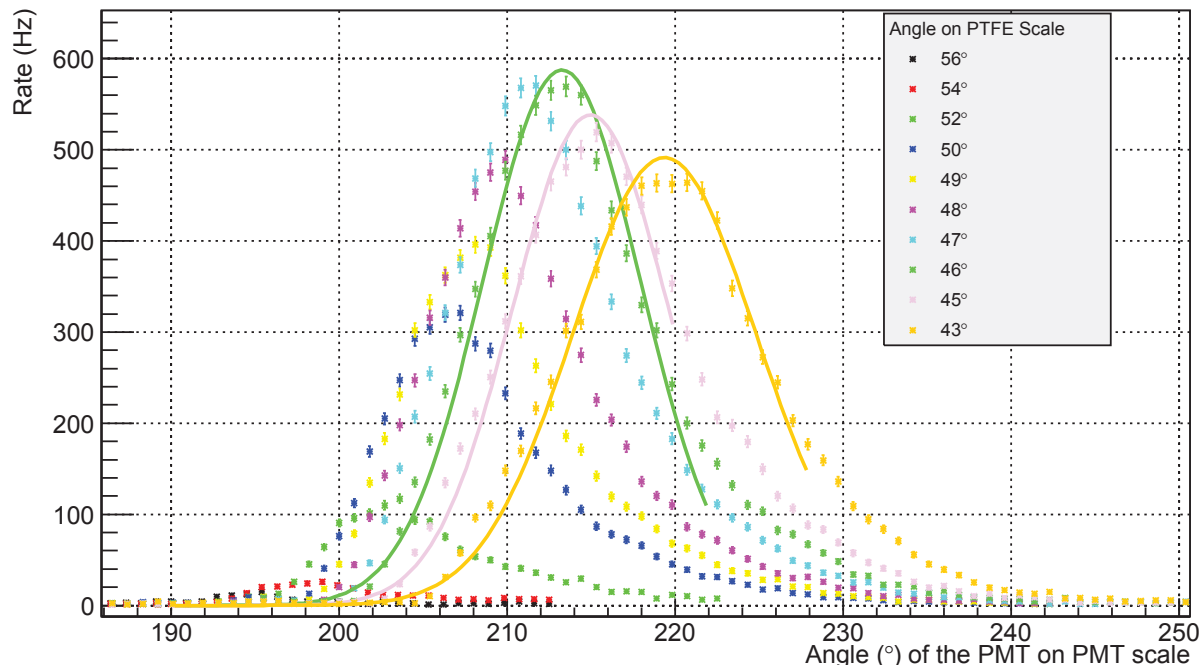


Figure 7.36: PTFE alignment data through the tube under liquid xenon

### Data

The reflectivity data taken in LXe is shown on figure 7.37. Again, the data intensity is about three times bigger than the data under vacuum or GXe, however the main surprise comes from the shape of the data. At large incident angles, the specular peak is observed as expected where  $\theta_r = \theta_i$ . However, as the incident angle decreases, the specular intensity is attenuated asymmetrically. Indeed, the center of the peak is no longer where it is expected and the distribution is more asymmetric.

A comparison of this data with the same data in vacuum for selected angles is shown on figure 7.38. This shows very explicitly that the specular component in LXe is cut off asymmetrically for incident angles around  $70^\circ$  until it is completely gone at low incident angles inferior to  $40^\circ$ .

This clearly was not what was expected. Indeed it was always assumed that reflections in LXe

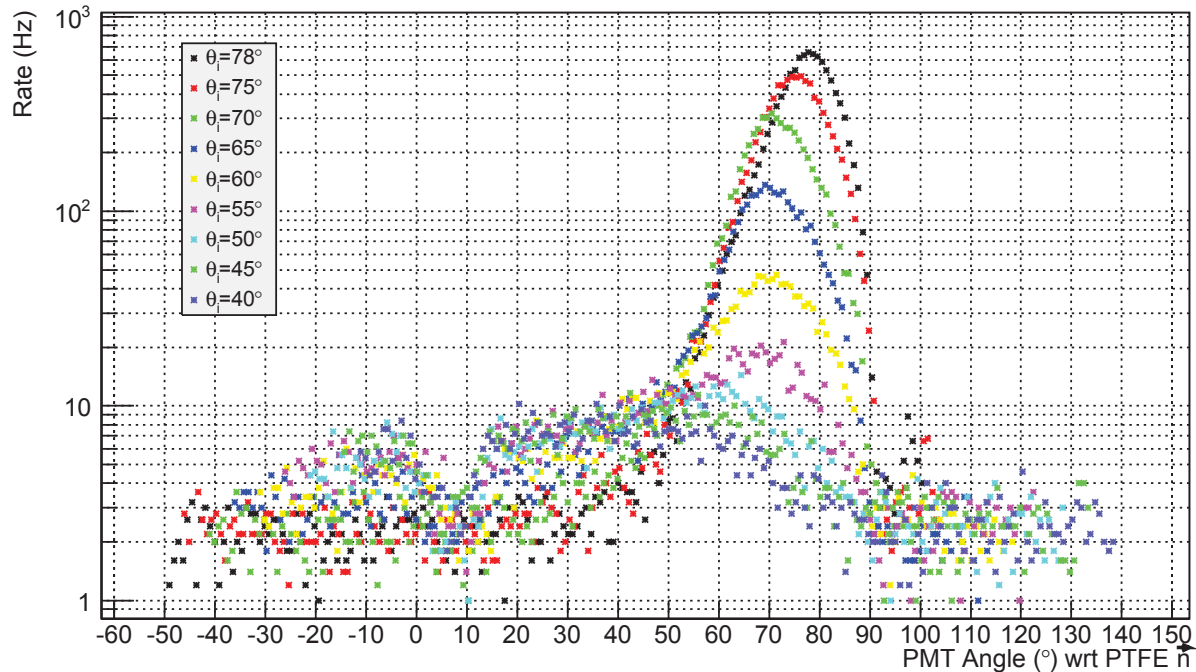


Figure 7.37: Raw Data of the reflection off of the teflon in liquid xenon

would behave exactly the same as in vacuum but with simply a different intensity, since xenon is a known detergent and thus cleans surfaces. While figure 7.38 really hints that this effect is real, it must be investigated to make sure that it cannot be an artifact of the setup. In addition, if this trend is found to be a real effect, the analysis should be modified and a new fitting function should be implemented. This will be answered in the following sections.

### *Explaining the Data*

There are two possible explanations for the data. On one hand, there might be a systematic problem with the setup which induces such a behavior. On the other hand, it might be that the assumption that light behaves the same way in LXe as in vacuum is simply wrong and the observed behavior is truly what is happening. The first step in clearing up this matter is to try to eliminate any possible cause of systematic error from the setup.

The first reason that could come to mind as to why the data is so different is an alignment problem from the setup. This hypothesis can however be easily discarded as precise calibrations in all directions have been carried out to make sure the setup was properly aligned as explained earlier on. In addition, again the fact that the rod always shows up at the same spot on figure 7.37 is another argument that shows that the setup is properly aligned. On top of this, this hypothesis can

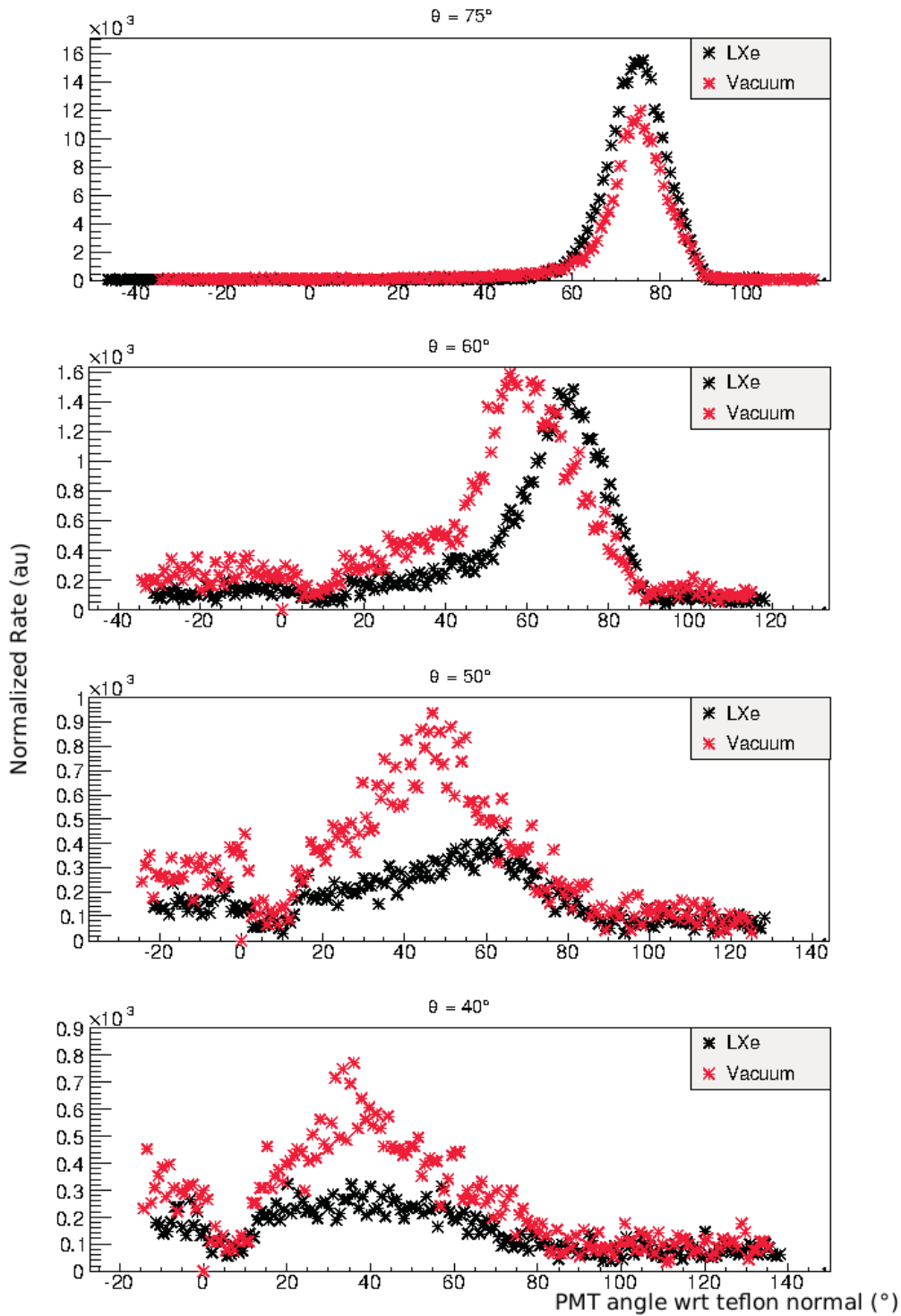


Figure 7.38: Comparison between data in LXe and in vacuum for selected angles

be fully discarded thanks to rather trivial geometrical arguments which show that misalignment in  $x$ ,  $y$  or  $z$  could not be the cause of such a trend in the data. The same holds for a misalignment of the tube or the light beam.

However, there is the possibility that the light assembly itself is slightly tilted, thus tilting the

quartz tube which could induce potentially big changes in the reflection process. While when filling the tube with LXe, the LXe level rose steadily and equally on all sides, making this explanation rather unlikely, this is still worth investigating. To do so, the tube is tilted artificially by attaching a rope to the cold head and pulling on it. Due to the flexible nature of the viton o-ring on the stainless steel tube, this created a very visible artificial tilt of the tube. Data was taken with the tube tilted (from the rope in two orthogonal directions) and with the tube hanging naturally. The result can be seen on figure 7.39 where it is clear that a tilt of the tube would not account for the effect in the LXe data.

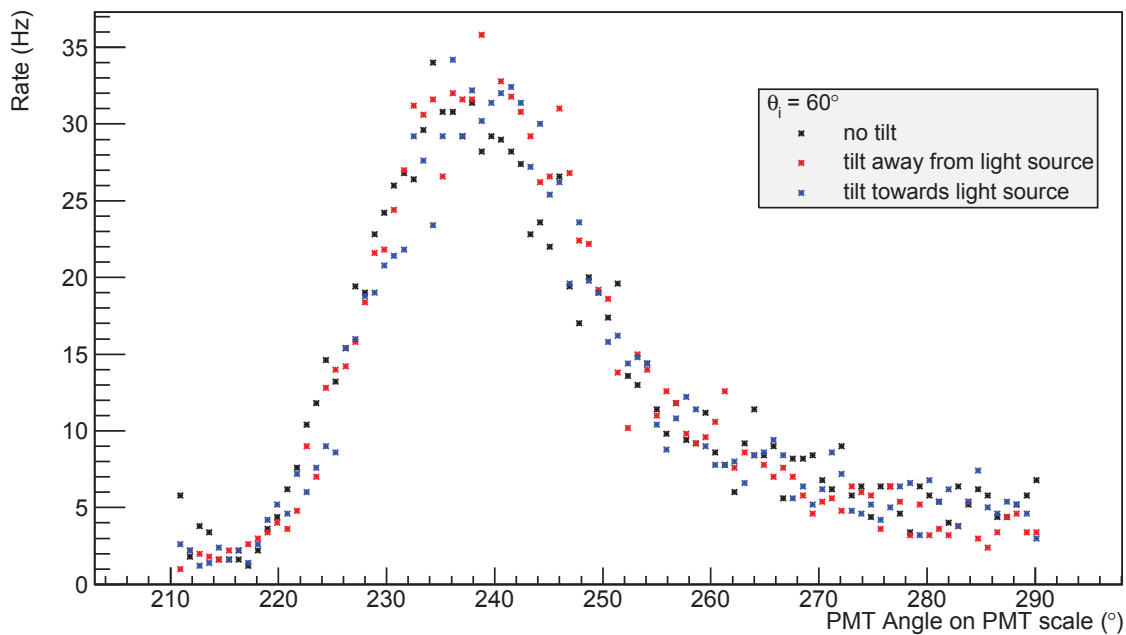


Figure 7.39: Effect of an artificial tilt on the quartz tube

Another possibility would be simply that this is a problem with the teflon and that the data happened to be taken at a bad spot on the teflon. To check that, the data is retaken at different positions on the teflon as shown on figure 7.40. Again, there is no difference in shape between the data at three different teflon spots each spaced 5 mm apart and it can then be concluded that the trend in the data does not come from one particular spot on the teflon.

However, as a side note, because the teflon sample used is the step sample, changing the spot where the light hits also changed the thickness of the teflon as it hits a different step. While this effect was thoroughly studied in the previous chapter and will not be repeated here, it is interesting to note that while the shape of the data remains the same, the intensity slightly decreases on the dataset taken when the light shines off the thinnest step of 1 mm width, although not drastically.

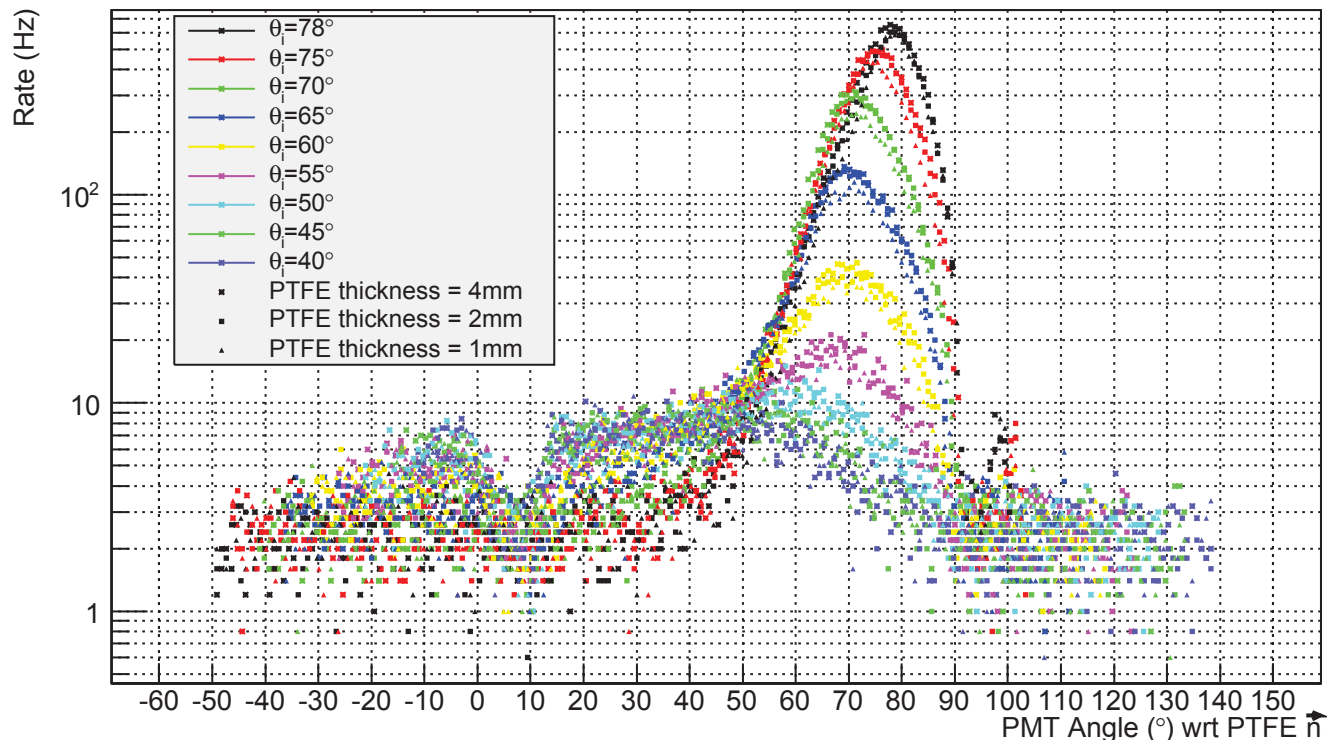


Figure 7.40: Raw data under LXe for three different teflon spots

This confirms the findings of the previous chapter where it had been established that while the other thicknesses were about the same there was a drop of intensity at 1 mm and that this teflon thickness was too thin to be used.

Going back to explaining the shape of the LXe data, the attention is now turned towards the aforementioned small convective movements in the LXe. While they were never considered to be a problem, one could postulate that they may have an impact on light propagation. There was no obvious way to test this until an accidental power outage provided the opportunity. Because of the power outage, the equilibrium in the tube was lost, some liquid bubbled, and the liquid xenon was for all purposes mixed. Once the cooling was restored, a new equilibrium point was found, which surprisingly was better than the one achieved before and no more convective or any other movements were visible. Data was then retaken. As can be seen on figure 7.41, this had no impact whatsoever on the data proving that these small motions had no impact on the shape of the data.

It has then been established that the data's behavior does not come from obvious systematic problem with the setup. Consequently, it has to be deduced that this is not a problem with the data but a real effect and that the reflection process is different in LXe than in vacuum or GXe. This will of course have an impact on the analysis which will have to be modified to match the data.

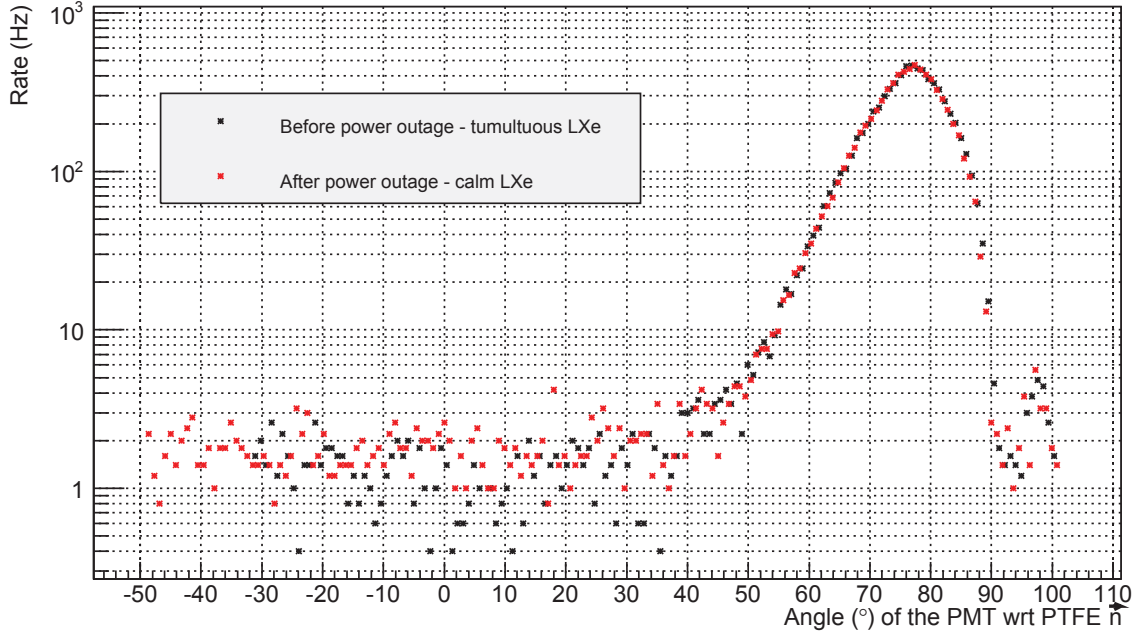


Figure 7.41: Raw data comparison before and after an accidental power outage which changed the state of the LXe

### Analysis

*Fitting the data* With this new data, it is clear that the analysis used until now needs to be modified. While the definition of the diffuse component seems to stay the same, the specular component seems to be convoluted with some sort of a step function, making it indeed present at high reflected angles and disappear at low reflected angles. Consequently the fit function 6.17 needs to be modified. In this case, convoluting the specular component with an error function such that the specular reflection is suppressed beyond the cutoff angle, seems to match the data rather well. The fit function thus becomes equation 7.4 where  $\theta_{rot}$ ,  $\theta_{PMT}$ ,  $\theta_{tilt}$  are defined as on figure 6.34,  $R_1$  is the intensity of the specular component,  $\theta_r$  is the reflected angle described by equation 6.16,  $\alpha$  is described by equation 6.10,  $\sigma$  is the width of the specular component,  $R_2$  the intensity of the diffuse component,  $\theta_{cutoff}$  is the cutoff angle and  $\beta$  is related to the width of the error function.

$$F(\theta_{rot}, \theta_{PMT}, \theta_{tilt}) = \frac{1}{2} \left( 1 + \operatorname{erf} \left( \frac{\theta_r - \theta_{cutoff}}{\beta} \right) \right) R_1 e^{-\frac{\alpha^2}{2\sigma^2}} + R_2 \cos(\theta_r) \quad (7.4)$$

Again because there is no tilt angle ( $\theta_{tilt} = 0$ ) in the case of this setup and because the incident beam is on the plane ( $\phi_i = 0$  and  $\phi_s = 0$ ), equation 7.4 can be simplified into

$$F(\theta_{rot}, \theta_{PMT}) = \frac{1}{2} \left( 1 + \operatorname{erf} \left( \frac{\theta_{PMT} - \theta_{cutoff}}{\beta} \right) \right) R_1 e^{-\frac{\alpha^2}{2\sigma^2}} + R_2 \cos(\theta_{PMT}) \quad (7.5)$$

where  $\alpha = \arccos(\sin(\theta_{rot})\sin(\theta_{PMT}) + \cos(\theta_{rot})\cos(\theta_{PMT}))$ .

For the fit to make sense physically, the cutoff angle needs of course to be fixed. From the data alone, it seems obvious that this cutoff angle is around  $70^\circ$ . Varying this value slightly on the fits to minimize  $\chi^2$ ,  $70^\circ$  was found to be indeed the proper value to use for the cutoff angle. The other fixed parameter is of course the incident angle  $\theta_{rot}$ .  $\beta$  however is left as a free parameter that can vary for different incident angles, which in addition to  $R_1$ ,  $R_2$  and  $\sigma$  makes up a total of four fit parameters.

The fits associated to the data of figure 7.37 are shown on figure 7.42 with the associated reduced  $\chi^2$  on table 7.3. Once again, according to table 7.3, the fits seem to match the data at incident angles smaller than  $70^\circ$  much better than at high incident angles. In addition, the reduced  $\chi^2$  for the normalization data is bad. However, there are several reasons to explain this. First, the peak due to normalization and the specular peak at high incident angles are very narrow which tends to exaggerate the beam asymmetry, and so the fits perform poorly especially around the now exaggerated non-gaussian tail. In addition, for the normalization measurement, the peak is not only narrow but also has only a handful of data points to it, thus completely throwing the reduced  $\chi^2$  out of proportion. In both cases, because no better beam profile description exists and because a more precise binning is limited by the step motor itself, thus preventing to get more points in the normalization peak, this data is still used in spite of those known systematics and also because, these fits visibly match the data well. Additionally, the error function appears to properly model the attenuation of the specular component at reflection angles below  $70^\circ$ .

Incident angle ( $^\circ$ )	Reduced $\chi^2$
	255.719
78	31.8732
75	12.2194
70	3.93645
65	4.03953
60	3.32497
55	2.33258
50	1.36003
45	1.43755
40	1.16907

Table 7.3: Reduced  $\chi^2$  for the fits to the data in LXe. The first reduced  $\chi^2$  value corresponds to the normalization data (no reflection off teflon)

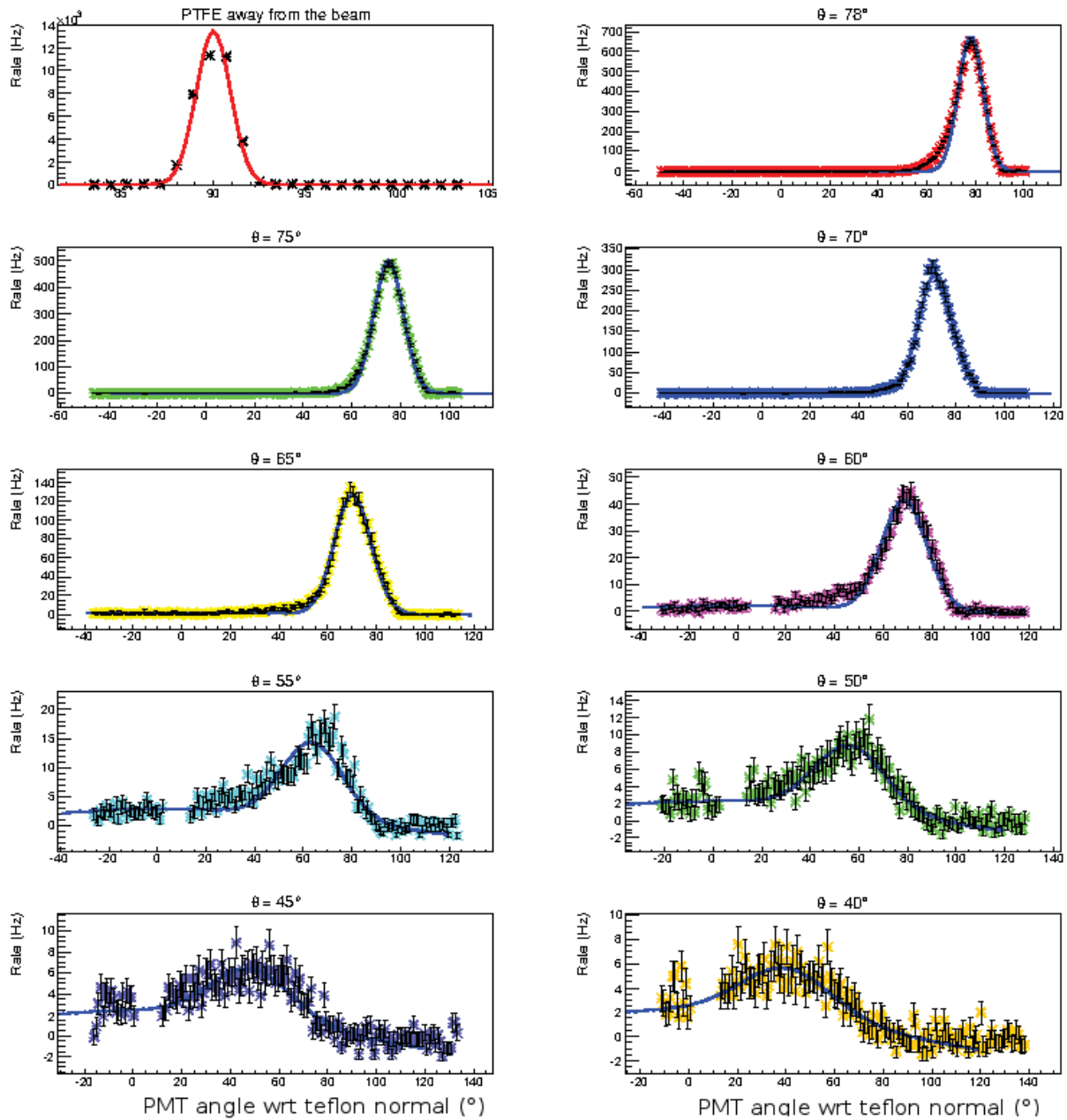


Figure 7.42: Fits to the reflectivity data in LXe

*Calculating the Reflectivity* The reflectivity is once more calculated according to equation 7.6 where  $R_s$  is the total intensity of the reflection of the teflon and  $R_0$  is the total intensity of the light without reflection, corresponding to a position where the teflon sample is out of the way.

$$R = \frac{R_s}{R_0} \quad (7.6)$$

Again, to calculate both  $R_0$  and  $R_s$  the fits must be integrated according to equation 7.7.

$$R_s = \int_0^{2\pi} \int_0^{\frac{\pi}{2}} \left( \frac{R_1}{2} (1 + \operatorname{erf}(\frac{\theta_r - \theta_{cutoff}}{\beta})) e^{(-\frac{\alpha^2}{2\sigma^2})} + R_2 \cos(\theta_r) \right) \sin(\theta_r) d\theta_r d\phi_r \quad (7.7)$$

Unfortunately while this was previously doable analytically via a change of coordinates, the erf distribution now makes this impossible. Consequently, the integrals are now calculated numerically using the ROOT integral functions. But because of this, the errors on the reflectivity will be slightly higher than for the other analysis.

### Reflectivity

Applying this new analysis method, the obtained reflectivity is shown on figure 7.43.

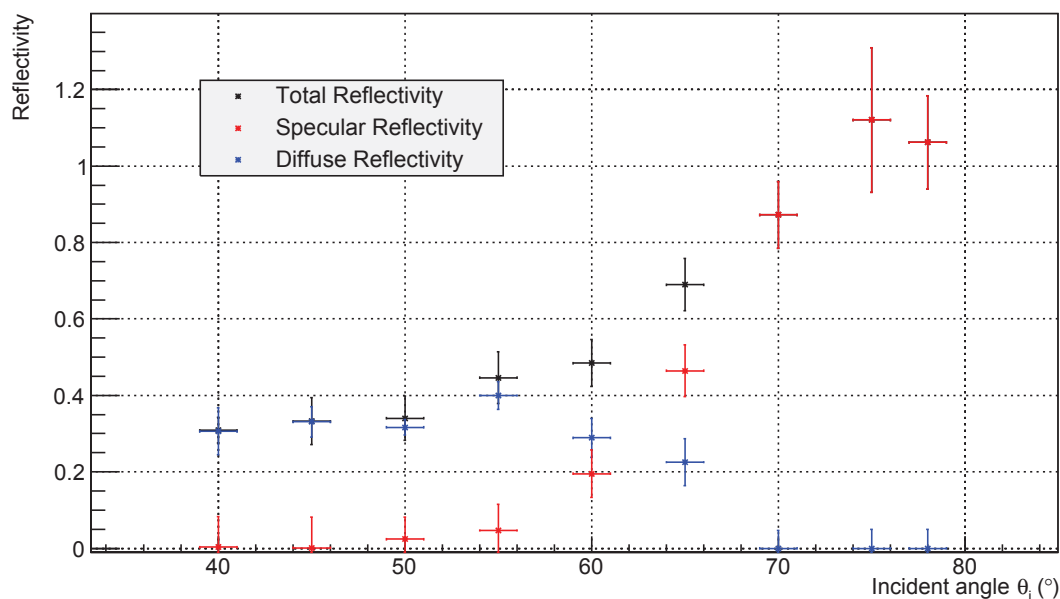


Figure 7.43: Reflectivity of 178 nm light in LXe

This is rather different than what was previously obtained. While it is obvious that the total reflectivity is much higher at high incidence angles as expected, it is also now much lower at low incident angles, where the specular component is so small that it cannot be resolved with this setup resolution. The average reflectivity is found to be  $70 \pm 9\%$ , however, this single parameter is insufficient to describe the reflectivity of the teflon because the reflection process has so much angular dependence. Until now, as a model for reflectivity, the XENON100 and XENON1T Monte-Carlo (MC) simulation only used the diffuse component which was set very high until it matched the data. This cannot be the case anymore and the MC will have to be modified to account for the dependency on the incident and reflected angles of the reflectivity.

## 7.4 Conclusion

The reflectivity setup in LXe has led to unexpected and very interesting results. The setup was tested and yielded the same results in vacuum as its predecessor (see previous chapter) with an average reflectivity of  $70 \pm 10\%$ , confirming that it works as designed and can be used for further measurements. New measurements in GXe and LXe were carried out. In GXe the data yielded about the same results as in vacuum with an average reflectivity of  $56 \pm 7\%$  for both cold and warm gas. The surprise came from the LXe measurements, which, while leading to the same average reflectivity as in vacuum, showed the reflection process to be drastically different. In LXe the reflectivity cannot be just taken as an average value but must be taken as a value highly dependent on the incident and reflected angles, with a reflectivity close to 100% at high incident angles and around 20% at low incident angles. Consequently, new simulations can be performed to match the light response of XENON100, but more importantly simulations can now include the reflectivity model described in this work to accurately model XENON1T and other large scale liquid xenon detectors.

While the setup is ready to be used routinely to scan new samples and determine the optimum teflon to use for the XENON1T TPC, a few shortcomings and consequent improvements to be made should be noted. First of all, the origins of this difference between LXe and vacuum measurements is unknown and has not been investigated. However, the underlying cause is thought to be the microstructures of the teflon. Because xenon acts as a lens, it is conceivable that these effects could still be there in vacuum, but non visible, while being very much exaggerated with liquid xenon. In addition, while measurements in gas are not advised as the light is usually much too attenuated to yield useful results, these measurements still made it clear that the trend is definitely due to the liquid xenon, as it doesn't appear in the gas measurements. In addition, because of the porous nature of teflon due to its fabrication from pressing a powder, it is possible that light gets caught in the pores which are filled with liquid xenon and somehow is reflected at a different angle. However, the only way to address this point precisely is to look at the teflon microstructures with a microscope and characterized them properly.

Second, a little bit more should be said about the biggest systematics of this study, namely the assumption that the specular peak follows a 2D gaussian and that the reflectivity on a plane can simply be integrated over solid angle to convert it to a sphere. Simply put, this assumption may simply be wrong. The only way to verify the validity of this assumption is to take measurements with the teflon at different tilt angles. These measurements are already being planned and will be

done in the near future by another student. Note, however, that because the analysis presented in this chapter was done accounting for a tilt angle which was simply set to zero to match the particular data of this study, it can simply be used even in the presence of a tilt angle, an advantage which can be used to obtain very fast answers on this point.

Finally, on a more technical point, the technique used to define the alignment of the teflon is definitely non optimal as it is based on the assumption that the specular peak should show up at a PMT angle with respect to the teflon normal equal to the incident angle, which may not be always true. An improved way to take such a measurement would be to use, as a reference point and instead of the specular peak position, the front rod position with respect to the teflon normal which is known to always be the same by design. This technique has already been tried with the data presented here but it turned out to be inconclusive as the rod is not point like and it is hard to determine its position with a  $1^\circ$  precision. However, if the data had been taken with more statistics thus defining the rod precisely, this technique would have worked and would have been actually better to determine the alignment. It is highly advised to take data with more statistics in the future in order to use this technique for a very precise teflon alignment.





## Chapter 8. CONCLUSION AND OUTLOOK



*Piled Higher and Deeper* by Jorge Cham [www.phdcomics.com](http://www.phdcomics.com)

WWW.PHDCOMICS.COM

The quest for dark matter is one of today's biggest challenges in physics. One of the favorite dark matter candidate is a supersymmetric particle, the neutralino. Many experiments are thus in competition to try and detect this new kind of particle, using many different technologies but until now, without success. One of the leading experiment, the XENON project uses a dual phase xenon TPC to try and discover this elusive particle. The first step of the project, XENON10, led the search worldwide until 2007 when the XENON100 experiment, a bigger and thus more sensitive version of XENON10, took over. XENON100 has now reached its designed sensitivity and is now used as a diagnostic tool for the upcoming experiment, XENON1T which is currently being built at LNGS. But the project does not stop there. Indeed, a new step, XENONnT is now being planned.

The work presented in this thesis overlaps both the XENON100 and XENON1T experiments.

In a first part, analysis on XENON100 data was presented which ultimately was used to reach the world's best sensitivity for a dark matter experiment at the time [23]. This analysis of the light yield of the detector, which is the number of photoelectrons detected by the PMTs per keV recoil energy, was necessary in order to get the smallest possible energy resolution for the detector. To do this 3D maps and associated correction function for the light yield of the entire detector were created from calibration data with a  $^{137}\text{Cs}$  gamma source. This had a direct impact on the nuclear energy scale used to determine the recoil energy of an event and necessary to calculate the sensitivity of the detector at different WIMP masses. These 3D maps are still in use for the XENON100 experiment and have been used in other parallel analyses [95] [103] [104] [105]. These maps have been checked for the new run of XENON100 and found that they are still valid and so will be used in the upcoming

analyses of the new data. The strategy of this light yield analysis will also be used for the upcoming XENON1T experiment, however the maps will of course have to be updated.

In a second step, R&D studies were made for the upcoming XENON1T experiment.

First, based on the XENON100 simulation package, a GEANT4 simulation of a small TPC which was built at Muenster University was implemented, thus allowing this TPC to be characterized and its response to light and other parameters predicted. This is indirectly linked to XENON1T as this TPC is itself an R&D tool for XENON1T and has already, for example, been used to look for an internal beta calibration which could be used on XENON1T. Now that this MC simulation is in place, this tool is available for anyone who wishes to study any parameters of the TPC, and should prove a valuable help in the future.

Second, direct R&D for XENON1T was performed by upgrading a setup in Muenster which now allows the reflectivity of xenon's UV scintillation light off of teflon to be measured in liquid xenon. This is a crucial parameter to investigate as the side walls of the XENON1T TPC, just like XENON100, is made of teflon which needs to be as highly reflective as possible in order to get the highest possible amount of light in the detector. This study was done in two parts.

It started by using a setup built by Karen Bokeloh to measure the reflectivity of teflon in vacuum [99]. In this work, measurements were made with this setup and using a teflon sample from XENON100 to verify the impact of the teflon thickness on the reflectivity, which appeared to be negligible for thicknesses above 3 mm. These measurements were thus a major contributing factor to the choice of teflon thickness for the XENON1T experiment. Finally, using these measurements, the average teflon reflectivity in vacuum for this sample from XENON100 was found to be  $73 \pm 7\%$ .

In a second step, this setup was modified and adapted to work under liquid xenon as, ultimately, the results from vacuum measurements are not directly applicable to the XENON project as the reflection of light in these detectors happens in liquid xenon and not in vacuum. Indeed, teflon being a porous material made by pressing teflon powder, LXe could fill in the spaces between the teflon pores, depending on teflon's wetting properties, thus possibly changing the surface properties like UV light reflection. The same sample from XENON100 that was used in the vacuum chamber was used in this new setup. In order to compare with the results from the vacuum setup and ensure that the upgraded setup worked properly, measurements were first taken in vacuum. These measurements yielded a teflon reflectivity in vacuum of  $70 \pm 10\%$  which was in complete agreement with the results from the original setup. Once that it had been confirmed that the upgraded setup worked as it should, measurements were then taken in liquid xenon. While the expectation was that the reflectivity would

simply be higher in liquid xenon than in vacuum, the results were in fact quite different. Indeed, it was found that the reflectivity in liquid xenon off of teflon behaved very differently than in vacuum and was in fact very dependent on the incident angle with a reflectivity ranging from around 25% at low incident angles to 100% at high incident angles. Consequently a new reflectivity model in liquid xenon was devised. This result had a direct impact on the MC simulation for XENON1T and this new model is now being implemented in the XENON1T simulation package. In addition, this setup is already being used by the collaboration as a routine tool to test many different teflon samples with different machining techniques, in order to select the best possible teflon to build the XENON1T TPC with. A new PhD student, Basho Kaminsky, from Bern University has already been trained by the author of this work to use the setup and has taken over and scanned several different samples with this setup which are already leading to very different and interesting results, which will ultimately allow the selection of an optimized reflector for the XENON1T TPC.



# APPENDIX

## Derivation of $\alpha$

This appendix covers the derivation of equation 6.10 to describe the angle  $\alpha$  between the direction of reflection as well as the derivation of equation 6.15 to describe the direction of perfect specular reflection and the angle of observed reflection  $\theta_r$  in terms of measured coordinates in the laboratory frame. Indeed, the problem with using equations 6.8 and 6.9 to compute  $F_1$  and  $F_2$  is that they depend on variables given in the reference frame of the teflon, while when doing measurements, the measured angles are in the reference frame of the laboratory. Consequently, to be useful, these equations need to be rotated in the reference frame of the laboratory and so the angles  $\theta_i$ ,  $\phi_i$ ,  $\theta_r$  and  $\phi_r$  must be related to the measured angles  $\theta_{rot}$ ,  $\theta_{tilt}$  and  $\theta_{PMT}$ , which are dependent on the rotation and tilt angles of the teflon and the PMT angle respectively (see figure 6.34). These latter angles and the two reference frames are represented on figure A.1 where  $(x,y,z)$  is the reference frame of the teflon and  $(x',y',z')$  is the reference frame of the laboratory.

The first step is thus to define a rotation matrix  $\mathbf{R}$  which allows to transform between the two reference frames such that:

$$\begin{bmatrix} \mathbf{x} \\ \mathbf{y} \\ \mathbf{z} \end{bmatrix} = R \begin{bmatrix} \mathbf{x}' \\ \mathbf{y}' \\ \mathbf{z}' \end{bmatrix} \quad (\text{A.1})$$

with

$$R = \begin{bmatrix} 1 & 0 & 0 \\ 0 & \cos(\theta_{tilt}) & -\sin(\theta_{tilt}) \\ 0 & \sin(\theta_{tilt}) & \cos(\theta_{tilt}) \end{bmatrix} \quad (\text{A.2})$$

and consequently the inverse matrix  $R^{-1}$ :

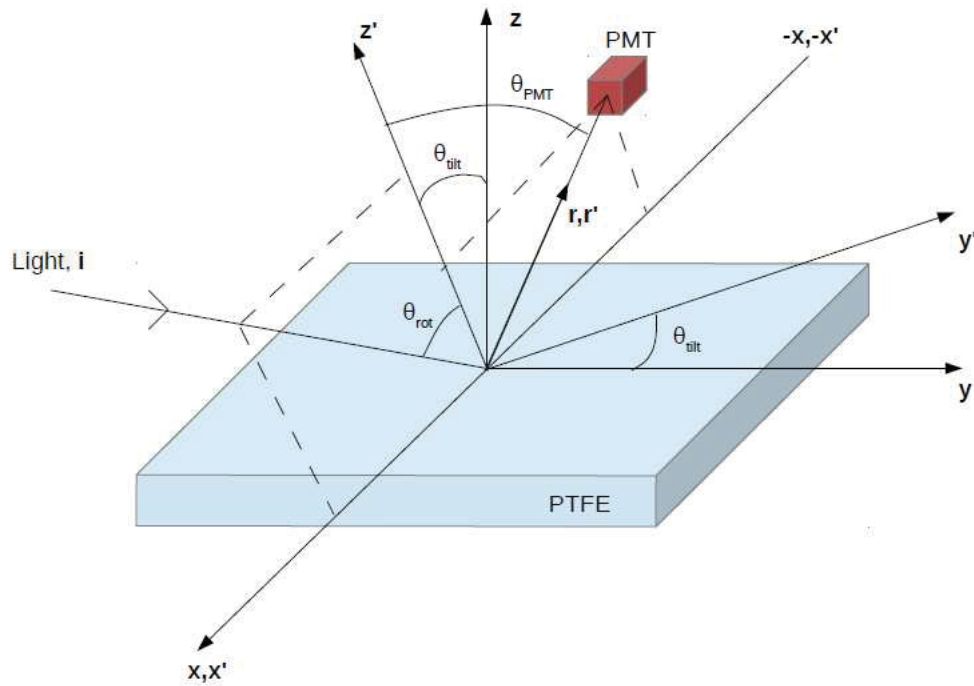


Figure A.1: The change in reference frame and the measured angles. The coordinate system is chosen such that a the tilt angle is described by a rotation about the x axis.

$$R^{-1} = \begin{bmatrix} 1 & 0 & 0 \\ 0 & \cos(\theta_{tilt}) & \sin(\theta_{tilt}) \\ 0 & -\sin(\theta_{tilt}) & \cos(\theta_{tilt}) \end{bmatrix} \quad (\text{A.3})$$

Note that from now on, prime letters correspond to the reference frame of the laboratory and non prime letters to the teflon reference frame. Also, the coordinate system is chosen such that the tilt angle is described by a rotation about the x axis.

Now that the rotation matrix between the two frames has been laid out, to find  $F_1$ , the angle  $\alpha$  needs to be expressed as a function of the measured angles  $\theta_{rot}$ ,  $\theta_{PMT}$  and  $\theta_{tilt}$ . In a second step, finding  $F_2$  will also require  $\theta_r$  to be expressed as a function of the measured angles.

The angle  $\alpha$  is a scalar, and can be calculated in any reference frame. It is most easily calculated in the reference frame of the laboratory:

$$\begin{aligned} \cos(\alpha) &= \hat{\mathbf{r}}_s \cdot \hat{\mathbf{r}} \\ &= \hat{\mathbf{r}}_s' \cdot \hat{\mathbf{r}}' \end{aligned} \quad (\text{A.4})$$

with, following the notation of figure 6.33, :

$$\hat{\mathbf{r}}_s = \sin(\theta_s)\cos(\phi_s)\hat{\mathbf{x}} + \sin(\theta_s)\sin(\phi_s)\hat{\mathbf{y}} + \cos(\theta_s)\hat{\mathbf{z}} \quad (\text{A.5})$$

$$\hat{\mathbf{r}} = \sin(\theta_r)\cos(\phi_r)\hat{\mathbf{x}} + \sin(\theta_r)\sin(\phi_r)\hat{\mathbf{y}} + \cos(\theta_r)\hat{\mathbf{z}} \quad (\text{A.6})$$

So, using matrix  $R$ ,  $\mathbf{r}$  and  $\mathbf{r}_s$  can be described in the reference frame of the laboratory such as:

$$\begin{aligned} \hat{\mathbf{r}}_s' &= R \times \hat{\mathbf{r}}_s \\ &= \sin(\theta_s)\cos(\phi_s)\hat{\mathbf{x}}' + (\cos(\theta_{\text{tilt}})\sin(\theta_s)\sin(\phi_s) - \sin(\theta_{\text{tilt}})\cos(\theta_s))\hat{\mathbf{y}}' \\ &\quad + (\sin(\theta_{\text{tilt}})\sin(\theta_s)\sin(\phi_s) + \cos(\theta_{\text{tilt}})\cos(\theta_s))\hat{\mathbf{z}}' \end{aligned} \quad (\text{A.7})$$

and, following the notation of figure A.1,

$$\hat{\mathbf{r}}' = \sin(\theta_{PMT})\hat{\mathbf{x}}' + \cos(\theta_{PMT})\hat{\mathbf{z}}' \quad (\text{A.8})$$

Now that the expressions for  $r'$ ,  $r'_s$  and  $\alpha$  have been found as a function of  $\theta_s$  and  $\phi_s$  these angles need to be expressed in terms of  $\theta_{rot}$ ,  $\theta_{tilt}$  and  $\theta_{PMT}$  as shown on figure A.1.

For this purpose, the incident light unit vector  $\hat{\mathbf{r}}_i$  is expressed in terms of the measured angles. Following the angles of figures A.1, in the laboratory coordinates,  $\hat{\mathbf{r}}_i'$  can be expressed as:

$$\hat{\mathbf{r}}_i' = \sin(\theta_{rot})\hat{\mathbf{x}}' + \cos(\theta_{rot})\hat{\mathbf{z}}' \quad (\text{A.9})$$

which translates in the teflon coordinates system (where  $\phi_i \neq 0$ ) via the inverse rotational matrix  $R^{-1}$  by:

$$\hat{\mathbf{r}}_i = \sin(\theta_{rot})\hat{\mathbf{x}} + \sin(\theta_{tilt})\cos(\theta_{rot})\hat{\mathbf{y}} + \cos(\theta_{tilt})\cos(\theta_{rot})\hat{\mathbf{z}} \quad (\text{A.10})$$

Remembering that the incident angle equals the reflected angle of the specular component, from figure 6.33, which is in the teflon coordinate system, the following angle relations can be derived:

$$\begin{aligned} \theta_i &= \theta_s \\ &= \arccos(\mathbf{z}_i/|\hat{\mathbf{r}}_i|) \\ &= \arccos(\mathbf{z}_i) \\ &= \arccos(\cos(\theta_{tilt})\cos(\theta_{rot})) \end{aligned} \quad (\text{A.11})$$

$$\begin{aligned}
\phi_i &= \phi_s - 180^\circ \\
&= \arctan(\mathbf{y}_i/\mathbf{x}_i) \\
&= \arctan\left(\frac{\sin(\theta_{tilt})\cos(\theta_{rot})}{\sin(\theta_{rot})}\right)
\end{aligned} \tag{A.12}$$

where  $\mathbf{x}_i$ ,  $\mathbf{y}_i$  and  $\mathbf{z}_i$  are the components of the incident light vector  $\mathbf{r}_i$  in the teflon frame as described by equation A.10.

This leads to the final expression for  $\alpha$  (presented as equation 6.10 in chapter 6) in terms of the measured variables:

$$\begin{aligned}
\alpha &= \arccos\left( \sin(\theta_s)\cos(\phi_s)\sin(\theta_{PMT}) \right. \\
&\quad \left. + \cos(\theta_{PMT})[\sin(\theta_{tilt})\sin(\theta_s)\sin(\phi_s) + \cos(\theta_{tilt})\cos(\theta_s)] \right)
\end{aligned} \tag{A.13}$$

with  $\theta_s$  and  $\phi_s$  defined as in equations A.11 and A.12.

Now that  $\alpha$  has been expressed as a function of the measured angles,  $F_1$  can be easily computed however  $F_2$  still remains as a function of  $\theta_r$  and needs to be expressed as a function of the measured angles  $\theta_{PMT}$ ,  $\theta_{tilt}$  and  $\theta_{rot}$ .

Looking back on figure 6.33:

$$\cos(\theta_r) = \hat{\mathbf{r}} \cdot \hat{\mathbf{r}}_z \tag{A.14}$$

where  $\hat{\mathbf{r}}_z$  is the z component of the  $\hat{\mathbf{r}}$  vector in the teflon frame, which can be found from equation A.8 and the inverse matrix  $\mathbf{R}^{-1}$  such as:

$$\hat{\mathbf{r}} = \mathbf{R}^{-1}\hat{\mathbf{r}}' = \sin(\theta_{PMT})\hat{\mathbf{x}} + \sin(\theta_{tilt})\cos(\theta_{PMT})\hat{\mathbf{y}} + \cos(\theta_{tilt})\cos(\theta_{PMT})\hat{\mathbf{z}} \tag{A.15}$$

Consequently

$$\cos(\theta_r) = \cos(\theta_{tilt})\cos(\theta_{PMT}) \tag{A.16}$$

and

$$\theta_r = \arccos(\cos(\theta_{tilt})\cos(\theta_{PMT})) \tag{A.17}$$

Equations A.11, A.13 and A.17 can then be used to parametrize the fit function  $F$  in terms of the measured variables as shown on equation 6.17.



## BIBLIOGRAPHY

- [1] van Albada TS, Bahcall JN, Begeman K, and Sancisi R. Distribution of dark matter in the spiral galaxy ngc 3198. *Ap. J.* 295:305, 1985.
- [2] Joel R. Brownstein, David J. Schlegel, Daniel J. Eisenstein, Christopher S. Kochanek, Natalia Connolly, et al. The BOSS Emission-Line Lens Survey (BELLS). I. A large spectroscopically selected sample of Lens Galaxies at redshift  $z \approx 0.5$ . *Astrophys.J.*, 744:41–62, 2012.
- [3] Douglas Clowe, Marusa Bradac, Anthony H. Gonzalez, Maxim Markevitch, Scott W. Randall, Christine Jones, and Dennis Zaritsky. A direct empirical proof of the existence of dark matter, 2006.
- [4] <http://abyss.uoregon.edu/~js/ast123/lectures/lec24.html>.
- [5] Joel R. Primack and Michael A.K. Gross. Hot dark matter in cosmology. 2000.
- [6] C.L. Bennett et al. Nine-Year Wilkinson Microwave Anisotropy Probe (WMAP) Observations: Final Maps and Results. *Astrophys.J.Suppl.*, 208:20, 2013.
- [7] Alain Coc, Elisabeth Vangioni-Flam, Pierre Descouvemont, Abderrahim Adahchour, and Carmen Angulo. Updated Big Bang nucleosynthesis confronted to WMAP observations and to the abundance of light elements. *Astrophys.J.*, 600:544–552, 2004.
- [8] Robert A. Knop et al. New constraints on  $\Omega_m$ ,  $\Omega_\Lambda$ , and  $w$  from an independent set of eleven high-redshift supernovae observed with hst. *Astrophys.J.*, 598:102, 2003.
- [9] Graciela Gelmini and Paolo Gondolo. DM Production Mechanisms. 2010.
- [10] Gerard Jungman and Marc Kamionkowski. Gamma-rays from neutralino annihilation. *Phys.Rev.*, D51:3121–3124, 1995.
- [11] Stephane Coutu. Positrons galore. *Physics*, 6:40, Apr 2013.
- [12] Gerard Jungman, Marc Kamionkowski, and Kim Griest. Supersymmetric dark matter. *Phys.Rept.*, 267:195–373, 1996.

- [13] R. Bernabei, P. Belli, F. Cappella, R. Cerulli, C. J. Dai, A. D'Angelo, H. L. He, A. Incicchitti, H. H. Kuang, J. M. Ma, F. Montecchia, F. Nozzoli, D. Prospero, X. D. Sheng, and Z. P. Ye. First results from dama/libra and the combined results with dama/nai. *EUR.PHYS.J.C*, 56:333, 2008.
- [14] Georges Aad et al. Search for dark matter candidates and large extra dimensions in events with a jet and missing transverse momentum with the ATLAS detector. 2012.
- [15] E. Aprile et al. The XENON100 Dark Matter Experiment. *Astropart.Phys.*, 35:573–590, 2012. 23 pages, 27 figures/ version accepted by journal.
- [16] E. Brown. *Search for Low Mass Dark Matter with the XENON100 Detector and Simulations for 1 ton and 10 ton Dark Matter Detectors*. PhD thesis, University of California Los Angeles, 2010.
- [17] E. Aprile, C.E. Dahl, L. DeViveiros, R. Gaitskell, K.L. Giboni, et al. Simultaneous measurement of ionization and scintillation from nuclear recoils in liquid xenon as target for a dark matter experiment. *Phys.Rev.Lett.*, 97:081302, 2006.
- [18] G. Plante. *The XENON100 Dark Matter Experiment: Design, Construction, Calibration and 2010 Search Results with Improved Measurement of the Scintillation Response of Liquid Xenon to Low-Energy Nuclear Recoils*. PhD thesis, Columbia University, 2012.
- [19] E. Aprile et al. Dark Matter Results from 100 Live Days of XENON100 Data. *Phys.Rev.Lett.*, 107:131302, 2011.
- [20] <http://physics.nist.gov/physrefdata/xcom/html/xcom1.html>.
- [21] E. Aprile et al. First Dark Matter Results from the XENON100 Experiment. *Phys.Rev.Lett.*, 105:131302, 2010.
- [22] E. Aprile et al. Likelihood Approach to the First Dark Matter Results from XENON100. *Phys.Rev.*, D84:052003, 2011.
- [23] E. Aprile et al. Dark Matter Results from 225 Live Days of XENON100 Data. *Phys.Rev.Lett.*, 109:181301, 2012.

- 
- [24] M. Szydagis, N. Barry, K. Kazkaz, J. Mock, D. Stolp, M. Sweany, M. Tripathi, S. Uvarov, N. Walsh, and M. Woods. NEST: A Comprehensive Model for Scintillation Yield in Liquid Xenon. *ArXiv e-prints*, June 2011.
- [25] E. Aprile, K.L. Giboni, P. Majewski, K. Ni, and M. Yamashita. Observation of Anti-correlation between Scintillation and Ionization for MeV Gamma-Rays in Liquid Xenon. 2007.
- [26] A. Manalaysay, T.M. Undagoitia, A. Askin, L. Baudis, A. Behrens, et al. Spatially uniform calibration of a liquid xenon detector at low energies using 83m-Kr. *Rev.Sci.Instrum.*, 81:073303, 2010.
- [27] J. Schulz. Design of a 2-phase xenon time projection chamber for electron drift length measurements. Master's thesis, University of Muenster, 2011.
- [28] National Nuclear Data Center, 2014.
- [29] Wikimedia Commons. Generation of an interference pattern from two-slit diffraction, 2005.
- [30] C. Silva, J. Pinto da Cunha, A. Pereira, V. Chepel, M. I. Lopes, V. Solovov, and F. Neves. Reflectance of polytetrafluoroethylene for xenon scintillation light. *Journal of Applied Physics*, 107(6):064902, March 2010.
- [31] PGO praezisions glas and optik. Quartz glass transmission.
- [32] F. Sprenger. Set-up and test of the slow control and calibration of the photomultiplier of an apparatus to measure the reflectivity of teflon in lxe at vuv wavelengths. Bachelor's Thesis, University of Muenster, 2013.
- [33] F. Zwicky. Republication of: The redshift of extragalactic nebulae. *General Relativity and Gravitation*, 41:207–224, January 2009.
- [34] Vera C. Rubin and Jr. Ford, W. Kent. Rotation of the Andromeda Nebula from a Spectroscopic Survey of Emission Regions. *Astrophys.J.*, 159:379–403, 1970.
- [35] Gianfranco Bertone. *Particle Dark Matter, Observations, Models and Searches*. Cambridge University Press, 2010.
- [36] F. Zwicky. On the Masses of Nebulae and of Clusters of Nebulae. *The Astrophysical Journal*, 86:217, October 1937.

- [37] Barbara Ryden. *Introduction to Cosmology*. Addison Wesley, 2003.
- [38] Matthias Bartelmann and Peter Schneider. Weak gravitational lensing. *Phys.Rept.*, 340:291–472, 2001.
- [39] C. M. Baugh and G. Efstathiou. The Three-Dimensional Power Spectrum Measured from the APM Galaxy Survey - Part One - Use of the Angular Correlation Function. *MNRAS*, 265:145, November 1993.
- [40] W.J.G. de Blok. The Core-Cusp Problem. *Adv.Astron.*, 2010:789293, 2010.
- [41] P.A.R. Ade et al. Planck 2013 results. I. Overview of products and scientific results. 2013.
- [42] D.J. Fixsen. The Temperature of the Cosmic Microwave Background. *Astrophys.J.*, 707:916–920, 2009.
- [43] George F. Smoot. COBE observations and results. *AIP Conf.Proc.*, 476:1–10, 1999.
- [44] Donald Perkins. *Particle Astrophysics*. Oxford Master Series in Particle Physics, Astrophysics and Cosmology, 2011.
- [45] John R. Ellis, J.S. Hagelin, Dimitri V. Nanopoulos, Keith A. Olive, and M. Srednicki. Supersymmetric relics from the big bang. *Nucl.Phys.*, B238:453–476, 1984.
- [46] Stephen P. Martin. A Supersymmetry primer. 1997.
- [47] Nishino et al. Search for Proton Decay via  $p \rightarrow e^{+0}$  and  $p \rightarrow ^{+0}$  in a Large Water Cherenkov Detector. *Physical Review Letters*, 102(14):141801, April 2009.
- [48] Toby Falk, Keith A. Olive, and Mark Srednicki. Heavy sneutrinos as dark matter. *Phys.Lett.*, B339:248–251, 1994.
- [49] the SLD Electroweak. A Combination of preliminary electroweak measurements and constraints on the standard model. 2003.
- [50] R Aaij et al. First observation of  $CP$  violation in the decays of  $B_s^0$  mesons. *Phys.Rev.Lett.*, 110(22):221601, 2013.
- [51] J.P. Lees et al. Search for  $CP$  violation in the Decays  $D^\pm \rightarrow K_s^0 K^\pm$ ,  $D_s^\pm \rightarrow K_s^0 K^\pm$ , and  $D_s^\pm \rightarrow K_s^0 \pi^\pm$ . *Phys.Rev.*, D87(5):052012, 2013.

- 
- [52] K. van Bibber and G. Carosi. Status of the ADMX and ADMX-HF experiments. *ArXiv e-prints*, April 2013.
- [53] O. Klein. Quantentheorie und fünfdimensionale Relativitätstheorie. *Zeitschrift für Physik*, 37:895–906, December 1926.
- [54] Lisa Edelh user, Thomas Flacke, and Michael Kr dmer. Constraints on models with universal extra dimensions from dilepton searches at the LHC. *JHEP*, 1308:091, 2013.
- [55] P. Adamson et al. Search for sterile neutrino mixing in the MINOS long baseline experiment. *Phys.Rev.*, D81:052004, 2010.
- [56] Arman Esmaili and Orlando L.G. Peres. KATRIN Sensitivity to Sterile Neutrino Mass in the Shadow of Lightest Neutrino Mass. *Phys.Rev.*, D85:117301, 2012.
- [57] W.B. Atwood et al. The Large Area Telescope on the Fermi Gamma-ray Space Telescope Mission. *Astrophys.J.*, 697:1071–1102, 2009.
- [58] The Fermi-LAT high-latitude Survey: Source Count Distributions and the Origin of the Extragalactic Diffuse Background. *Astrophys.J.*, 720:435–453, 2010.
- [59] The Fermi-: M. Ackermann et al. Constraints on the Galactic Halo Dark Matter from Fermi-LAT Diffuse Measurements. *Astrophys.J.*, 761:91, 2012.
- [60] Alex Geringer-Sameth. The VERITAS Dark Matter Program. 2013.
- [61] E. Aliu, S. Archambault, T. Arlen, T. Aune, M. Beilicke, et al. Discovery of TeV Gamma-ray Emission from CTA 1 by VERITAS. *Astrophys.J.*, 764:38, 2013.
- [62] Nicola Galante. Status And Highlights Of VERITAS. *AIP Conf.Proc.*, 1505:202–208, 2012.
- [63] Thomas K. Gaisser and Denis Robertson. Icecube3—a new window on the universe. *AIP Conf.Proc.*, 1123:177–189, 2009.
- [64] *Status and first results of the ANTARES neutrino telescope*, May 2009. Comments: 6 pages, 8 figures, Proceeding for the Rencontres de Moriond 2009 EW session.
- [65] R. Abbasi et al. Multi-year search for dark matter annihilations in the Sun with the AMANDA-II and IceCube detectors. *Phys.Rev.*, D85:042002, 2012.

- [66] R. Sparvoli. Main results from the pAMELA space experiment after five years in flight. *Nuclear Instruments and Methods in Physics Research Section A: Accelerators, Spectrometers, Detectors and Associated Equipment*, 2012.
- [67] *Antimatter and Dark Matter search in space with AMS-02*, 2008.
- [68] O. Adriani, G. C. Barbarino, G. A. Bazilevskaya, R. Bellotti, M. Boezio, E. A. Bogomolov, L. Bonechi, M. Bongi, V. Bonvicini, S. Bottai, A. Bruno, F. Cafagna, D. Campana, P. Carlson, M. Casolino, G. Castellini, M. P. De Pascale, G. De Rosa, N. De Simone, V. Di Felice, A. M. Galper, L. Grishantseva, P. Hofverberg, S. V. Koldashov, S. Y. Krutkov, A. N. Kvashnin, A. Leonov, V. Malvezzi, L. Marcelli, W. Menn, V. V. Mikhailov, E. Mocchiutti, S. Orsi, G. Osteria, P. Papini, M. Pearce, P. Picozza, M. Ricci, S. B. Ricciarini, M. Simon, R. Sparvoli, P. Spillantini, Y. I. Stozhkov, A. Vacchi, E. Vannuccini, G. Vasilyev, S. A. Voronov, Y. T. Yurkin, G. Zampa, N. Zampa, and V. G. Zverev. Observation of an anomalous positron abundance in the cosmic radiation. *NATURE*, 458:607, 2009.
- [69] O. Adriani, G.C. Barbarino, G.A. Bazilevskaya, R. Bellotti, M. Boezio, et al. The discovery of geomagnetically trapped cosmic ray antiprotons. *Astrophys.J.*, 737:L29, 2011.
- [70] M. et al. Aguilar. First result from the alpha magnetic spectrometer on the international space station: Precision measurement of the positron fraction in primary cosmic rays of 0.5–350 gev. *Phys. Rev. Lett.*, 110:141102, Apr 2013.
- [71] Gianfranco Bertone, Dan Hooper, and Joseph Silk. Particle dark matter: Evidence, candidates and constraints. *Phys. Rept.*, 405:279–390, 2005.
- [72] David G. Cerdeno and Anne M. Green. Direct detection of WIMPs. 2010.
- [73] G.K. Giovanetti, E. Aguayo, F.T. Avignone, H.O. Back, A.S. Barabash, et al. Dark matter sensitivities of the MAJORANA demonstrator. *J.Phys.Conf.Ser.*, 375:012014, 2012.
- [74] Z. Ahmed et al. Search for annual modulation in low-energy CDMS-II data. 2012.
- [75] D.S. Akerib et al. First results from the LUX dark matter experiment at the Sanford Underground Research Facility. 2013.
- [76] E. Aprile et al. Implications on Inelastic Dark Matter from 100 Live Days of XENON100 Data. *Phys.Rev.*, D84:061101, 2011.

- 
- [77] G. Angloher, M. Bauer, I. Bavykina, A. Bento, C. Bucci, et al. Results from 730 kg days of the CRESST-II Dark Matter Search. *Eur.Phys.J.*, C72:1971, 2012.
- [78] E. Armengaud et al. A search for low-mass WIMPs with EDELWEISS-II heat-and-ionization detectors. *Phys.Rev.*, D86:051701, 2012.
- [79] S. Archambault et al. Constraints on Low-Mass WIMP Interactions on  $^{19}\text{F}$  from PICASSO. *Phys.Lett.*, B711:153–161, 2012.
- [80] G. Bellini et al. Cosmic-muon flux and annual modulation in Borexino at 3800 m water-equivalent depth. *JCAP*, 1205:015, 2012.
- [81] Xenon: A liquid xenon experiment for dark matter. Proposal submitted to NSF, Particle and Nuclear Astrophysics, Proposal 0201740, September 2011.
- [82] J. Angle, E. Aprile, F. Arneodo, L. Baudis, A. Bernstein, A. Bolozdynya, P. Brusov, L. C. C. Coelho, C. E. Dahl, L. DeViveiros, A. D. Ferella, L. M. P. Fernandes, S. Fiorucci, R. J. Gaitskell, K. L. Giboni, R. Gomez, R. Hasty, L. Kastens, J. Kwong, J. A. M. Lopes, N. Madden, A. Manalaysay, A. Manzur, D. N. McKinsey, M. E. Monzani, K. Ni, U. Oberlack, J. Orboeck, G. Plante, R. Santorelli, J. M. F. dos Santos, P. Shagin, T. Shutt, P. Sorensen, S. Schulte, C. Winant, and M. Yamashita. First results from the xenon10 dark matter experiment at the gran sasso national laboratory. *Phys. Rev. Lett.*, 100:021303, Jan 2008.
- [83] J.D. Lewin and P.F. Smith. Review of mathematics, numerical factors, and corrections for dark matter experiments based on elastic nuclear recoil. *Astropart.Phys.*, 6:87–112, 1996.
- [84] J.B. Albert et al. An improved measurement of the  $2\nu\beta\beta$  half-life of  $^{136}\text{Xe}$  with EXO-200. 2013.
- [85] W.L. McCabe and J.C. Smith. *Unit Operations of Chemical Engineering*. McGraw-Hill, 3rd edition edition, 1976.
- [86] E. Aprile, K. Arisaka, F. Arneodo, A. Askin, L. Baudis, A. Behrens, K. Bokeloh, E. Brown, J. M. R. Cardoso, B. Choi, D. Cline, S. Fattori, A. D. Ferella, K. L. Giboni, A. Kish, C. W. Lam, J. Lamblin, R. F. Lang, K. E. Lim, J. A. M. Lopes, T. Marrodán Undagoitia, Y. Mei, A. J. Melgarejo Fernandez, K. Ni, U. Oberlack, S. E. A. Orrigo, E. Pantic, G. Plante, A. C. C. Ribeiro, R. Santorelli, J. M. F. Dos Santos, M. Schumann, P. Shagin, A. Teymourian, D. Thers,

- E. Tziaferi, H. Wang, C. Weinheimer, M. Laubenstein, and S. Nisi. Material screening and selection for XENON100. *Astroparticle Physics*, 35:43–49, September 2011.
- [87] A. Kish. *Direct Dark Matter Search with the XENON100 Experiment*. PhD thesis, University of Zurich, 2011.
- [88] G. Plante, E. Aprile, R. Budnik, B. Choi, K.L. Giboni, et al. New Measurement of the Scintillation Efficiency of Low-Energy Nuclear Recoils in Liquid Xenon. *Phys.Rev.*, C84:045805, 2011.
- [89] A. Manzur, A. Curioni, L. Kastens, D. N. McKinsey, K. Ni, and T. Wongjirad. Scintillation efficiency and ionization yield of liquid xenon for monoenergetic nuclear recoils down to 4 keV. *Physical Review C*, 81(2), February 2010.
- [90] P. Sorensen, A. Manzur, C.E. Dahl, J. Angle, E. Aprile, et al. The scintillation and ionization yield of liquid xenon for nuclear recoils. *Nucl.Instrum.Meth.*, A601:339–346, 2009.
- [91] F Arneodo, B Baiboussinov, A Badertscher, P Benetti, E Bernardini, A Bettini, A Borio di Tiogliole, R Brunetti, A Bueno, E Calligarich, M Campanelli, C Carpanese, D Cavalli, F Cavanna, P Cennini, S Centro, A Cesana, D Cline, I De Mitri, R Dolfini, A Ferrari, A Gigli Berzolari, C Matthey, F Mauri, D Mazza, L Mazzone, G Meng, C Montanari, G Nurzia, S Otwinowski, O Palamara, D Pascoli, A Pepato, S Petrera, L Periale, G Piano Mortari, A Piazzi, P Picchi, F Pietropaolo, T Rancati, A Rappoldi, G.L Raselli, D Rebutti, J.P Revo, J Rico, M Rossella, C Rossi, A Rubbia, C Rubbia, P Sala, D Scannicchio, F Sergiampietri, S Suzuki, M Terrani, W Tian, S Ventura, C Vignoli, H Wang, J Woo, and Z Xu. Scintillation efficiency of nuclear recoil in liquid xenon. *Nuclear Instruments and Methods in Physics Research Section A: Accelerators, Spectrometers, Detectors and Associated Equipment*, 449(1&2):147 – 157, 2000.
- [92] E. Aprile, L. Baudis, B. Choi, K.L. Giboni, K. Lim, et al. New Measurement of the Relative Scintillation Efficiency of Xenon Nuclear Recoils Below 10 keV. *Phys.Rev.*, C79:045807, 2009.
- [93] J.I. Collar and D.N. McKinsey. Comments on 'First Dark Matter Results from the XENON100 Experiment'. 2010.
- [94] E. Aprile et al. Analysis of the XENON100 Dark Matter Search Data. 2012.

- 
- [95] E. Aprile et al. Limits on spin-dependent WIMP-nucleon cross sections from 225 live days of XENON100 data. *Phys.Rev.Lett.*, 111:021301, 2013.
- [96] Teresa Marrodan Undagoitia. Light yield of 122keV for run10. XENON100 Internal Note. Max Planck Institute for Nuclear Physics Heidelberg.
- [97] Marco Selvi. MC simulation (with nest) of the light yield of 122 keV. XENON100 Internal Note. INFN Bologna.
- [98] E. Aprile, M. Beck, K. Bokeloh, R. Budnik, B. Choi, H. A. Contreras, K. L. Giboni, L. W. Goetzke, R. F. Lang, K. E. Lim, A. J. Melgarejo Fernandez, G. Plante, A. Rizzo, P. Shagin, and C. Weinheimer. Measurement of the quantum efficiency of hamamatsu r8520 photomultipliers at liquid xenon temperature. 2012.
- [99] K. Bokeloh. *Eine winkelselective Photoelektronquelle fuer das KATRIN Experiment und ein Experimentierstation zum Vermessen der Reflektionseigenschaften von Teflon fuer Vakuum-UV Licht*. PhD thesis, University of Muenster, 2013.
- [100] R. Clausius. Ueber die bewegende Kraft der Wärme und die Gesetze, welche sich daraus für die Wärmelehre selbst ableiten lassen. *Annalen der Physik*, 155:500–524, 1850.
- [101] Hamamatsu. Chapter 13, environmental resistance and reliability.
- [102] S. Rosendahl. *Upcoming thesis*. PhD thesis, University of Muenster, 2015.
- [103] E. Aprile et al. Response of the XENON100 Dark Matter Detector to Nuclear Recoils. *Phys.Rev.*, D88:012006, 2013.
- [104] E. Aprile et al. Observation and applications of single-electron charge signals in the XENON100 experiment. *Journal of Physics G Nuclear Physics*, 41(3):035201, March 2014.
- [105] E. Aprile et al. The neutron background of the XENON100 dark matter search experiment. *J.Phys.*, G40:115201, 2013.